Detailed Analysis of Protein Crystallization and Aggregation Phenomena Applying Dynamic Light Scattering

Dissertation

zur Erlangung des Doktorgrades der Naturwissenschaften
an der Fakultät für Mathematik, Informatik und Naturwissenschaften
der Universität Hamburg

vorgelegt von

Dominik Oberthür

aus Duderstadt

Hamburg, 2012

Die vorliegende Arbeit wurde im Zeitraum von November 2007 bis September 2011 in der Arbeitsgruppe von Prof. Ch. Betzel im Laboratorium für Strukturbiologie von Infektion und Entzündung am Institut für Biochemie und Molekularbiologie,des Fachbereichs Chemie der Universität Hamburg, durchgeführt.

1. Gutachter **Prof. Ch. Betzel**

2. Gutachter **Prof. R. Bredehorst**

Für Birte und Lasse.

Table of Contents

List of Abbreviations

2D	*Two dimensional*
2W1R	*Two wells one reservoir*
3D	*Three dimensional*
AA	*Amino acid*
ACF	*Auto correlation function*
AFM	*Atomic force microscopy*
Am	*Ammonium-*
ANSI	*American National Standards Institute*
APD	*Avalanche photo diode*
APS	*Ammonium persulfate*
AS	*Ammonium sulfate*
ATR-FTIR	*Attenuated total reflection Fourier transformation infrared spectroscopy*
AUC	*Analytical ultracentrifugation*
B_{22}	*Second virial coefficient*
BLAST	*Basic Local Alignment Search Tool*
BSSB	*Blast server for Structural Biology*
c	*Concentration*
CAS	*Chemical abstracts service*
CD	*Circular dichroism*
CHEMS	*Cholesteryl hemisuccinate*
CLP	*Cubic lipid phase*
cmc	*Critical micelle concentration*
CPU	*Central processing unit*
cryoEM	*Cryo electron microscopy*
CSIC	*Consejo Superior de Investigaciones Científicas (Spanish National Research Council)*
D	*Diffusion coefficient*
DESY	*Deutsches Elektronen Synchrotron (German electron synchrotron)*
DLS	*Dynamic Light Scattering*

DNA	*Deoxyribonucleic acid*
D_o	*Diffusion coefficient at infinite dilution*
DPI	*Dual Polarization Interferometry*
DTT	*Dithiothreitol*
EMBL	*European Molecular Biology Laboratory*
EQ	*Equation*
EU	*European Union*
EXAFS	*Extended X-ray absorption fine structure*
FAD	*Flavin adenine dinucleotide*
FOS 14	*Fos-Choline-14 (n-Tetradecylphosphocholine)*
FOS 18	*Fos-Choline-18 (n-Octadecylphosphocholine)*
GCB	*Granada Crystallization Box*
GCB-D	*Granada Crystallization Box Domino*
GHS	*Global harmonized system*
GST	*Glutathione S-transferase*
HCV	*Hepatitis C virus*
HEPES	*4-(2-Hydroxyethyl)-1-piperazineethanesulfonic acid*
HEWL	*Hen egg-white lysozyme*
HIV	*Human immunodeficiency virus*
HOAc	*Acetic acid*
HTS	*High throughput screening*
HZDR	*Helmholtz Zentrum Dresden-Rossendorf*
I	*Intensity*
k	*Boltzmann constant*
k_D	*Interaction factor*
kDa	*Kilo Dalton (1 kDa = 1000 g/mol)*
kHz	*Kilo Hertz*
M	*Molar*
MME	*Monomethyl ether*
MO	*Monoolein (1-Oleoyl-rac-glycerol)*
MOPS	*3-(N-morpholino)propanesulfonic acid*
MPD	*2-Methyl-2,4-pentanediol*
M_W	*Molecular weight (1 g/mol or 1 Da)*
N_A	*Avogadro's constant*

NAMS	*Nucleic acid mini screen*
NaOAc	*Sodium acetate*
NDSB	*Non-detergent sulfobetaine*
NMR	*Nuclear Magnetic Resonance*
OAc	*Acetate-*
OptiCryst	*Optimization of Protein Crystallization for European Structural Genomics*
PAGE	*Polyacrylamide gel electrophoresis*
PCR	*Polymerase chain reaction*
PCT	*Pre-crystallization test*
PDB	*Protein data bank*
PEG	*Polyethylene glycol*
Pf	*Plasmodium Falciparum*
PMT	*Photo multiplier tube*
q	*Wave vector*
R_g	*Radius of gyration*
R_H	*Hydrodynamic radius*
RNA	*Ribonucleic acid*
SANS	*Small angle neutron scattering*
Sap	*Surface array protein*
SAXS	*Small angle X-ray scattering*
SBS	*Society for Biomolecular Screening*
SCWP	*Secondary cell wall polysaccharides*
SDS	*Sodium dodecyl sulfate*
SLAC	*Stanford Linear Accelerator Center*
S-Layer	*Surface Layer*
SLH	*Surface layer homology domain*
SLP	*Surface layer Protein*
SLS	*Static Light Scattering*
t	*Time (in seconds)*
T	*Temperature (in Kelvin)*
Tar	*-Tartrate*
TEMED	*Tetramethylethylenediamine*
Tris	*Tris(hydroxymethyl)aminomethane*

UV	*Ultra violet*
v/v	*Volume to volume (for concentrations)*
VIS	*Visible*
w/v	*Weight to volume (for concentrations)*
Wb	*Wucheria bancrofti*
XANES	*X-ray Absorption Near Edge Structure*
XFEL	*European X-ray Free Electron Laser*
x *g*	*Relative centrifugal force (rcf) as multiples of the gravitational acceleration on earth (g)*
β-OG	*n-Octyl-β-D-Glucopyranoside*

1. Introduction

1.1. Biological Systems and Proteins

To understand the way biological systems work is fundamental for the treatment and prevention of diseases and thus essential for modern societies. The function of biological systems is closely related to the atomic structure and the interaction of their components. Even though lipids, (poly-)glycosides and secondary metabolites cannot be neglected if one strives to understand the function of living matter, proteins are by far the most important particles in the biological world. Built from only a small set of amino acids, chemically different only in their side chains, proteins exist in a massive structural variety and diversity maybe only being excelled by that of secondary metabolites – which themselves are all produced by complex arrangements of enzymes. Proteins are essentially the molecules that transform inorganic and simple organic matter into the molecules that form biological systems. To understand the function of biological systems one has to understand the function of proteins and their interaction with each other and other molecules within the observed system. Since the function of proteins depends on their three dimensional atomic structure it is necessary to gain structural information. And since very little changes in structure can lead to drastic changes in function the elucidation of structure should be as accurate and detailed as possible. Within the last 60 years various methods to gain structural information from molecules have been developed, e.g. Nuclear Magnetic Resonance (NMR) **[1, 2]**, cryo Electron microscopy (cryoEM) **[3-5]**, Atomic Force Microscopy (AFM) **[6-8]**, X-Ray Scattering Methods (SAXS) **[9, 10]** and Electron- **[11]**, Neutron- **[12]** and X-Ray crystallography **[13, 14]**.

1.2. X-Ray Crystallography and Protein Crystallization

To date X-Ray crystallography is the method best applicable to proteins of any size that can yield three dimensional structure information at atomic resolution. At present the protein database (**PDB**) **[15]** consists of approx. 80’000 protein structures that have been elucidated by this method. Yet this is only a small number compared to the proteins that have been purified from biological samples or produced in genetically modified organisms **[16]**. Especially for many proteins crucially for the understanding of the way biological systems interact – membrane bound receptors from eukaryotes – no structures at atomic level are available even though they have

been successfully produced, solubilized and purified. On the other hand, if diffracting crystals could be gained from purified proteins it is very probable to obtain the three dimensional structure **[16]** (see **Table 1**)

Table 1: Status of structural genomics projects. Less than one third of all purified target proteins could be crystallized **[16]**

Status	Total Number of Targets	(%) Relative to "Cloned" Targets	(%) Relative to "Expressed" Targets	(%) Relative to "Purified" Targets	(%) Relative to "Crystallized" Targets
Cloned	193473	100.0	-	-	-
Expressed	121300	62.7	100.0	-	-
Purified	45469	23.5	37.5	100.0	-
Crystallized	14547	7.5	12.0	**32.0**	100.0
Diffraction-quality Crystals	7093	3.7	5.8	15.6	48.8
Diffraction	7564	3.9	6.2	16.6	52.0
Crystal Structure	4989	2.6	4.1	11.0	34.3

Besides the efforts of the last 50 years to improve the methods, crystallization of proteins is now – in the post-structural genomic era **[17]** – the rate limiting step **[16, 18]** to get structural information at atomic resolution from biological macromolecules (see **Table 1**). In the past twenty years the concept of high-throughput crystallization **[19-23]** with the aid of pipetting robots has been widely accepted as the method of choice (see **Figure 1** for robots used for crystallization of proteins in this work).

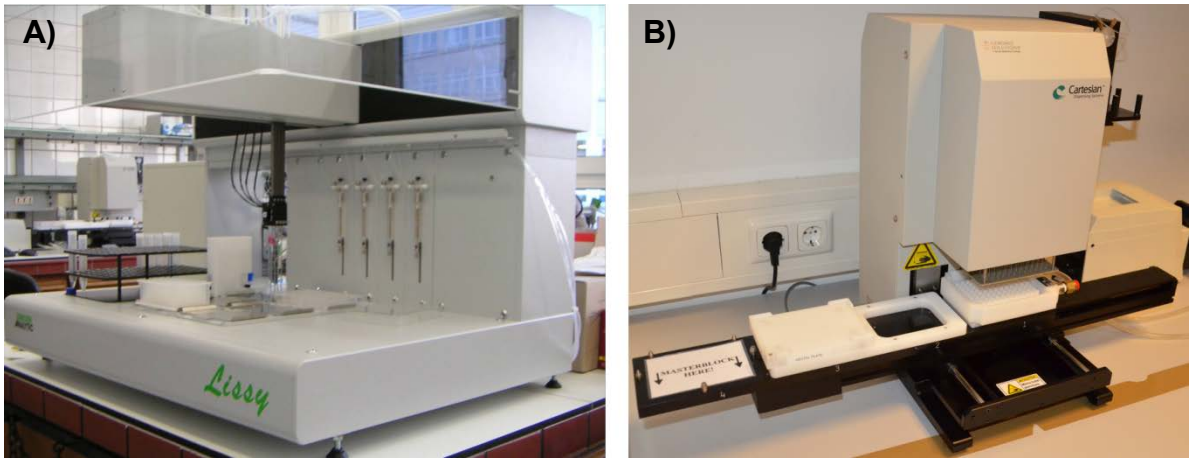

Figure 1: Robots used for preparation of crystallization experiments in the course of this work. **A)** Lissy (Zinsser, Germany), was used to prepare crystallization solutions. **B)** Honeybee 961 (Genomic solutions, USA) a robot for high throughput crystallization.

Vapor diffusion has emerged as the major method of protein crystallization since it was until recently suited best for high throughput approaches. Today high throughput screening can be applied as well to the method of free interface diffusion **[24]** in microfluidics **[25, 26]** (see **Figure 2 A** for a comparison of crystallization methods in a protein crystallization phase diagram). Together with the minimization to nanolitre volumes per crystallization droplet high throughput screening led to a higher quantity in crystallization experiments, narrowing down the crystallization space unattended (see **Figure 2 B**), but also to a higher quality since robots can carry out crystallization experiments highly reproducible. Moreover the large number of solved structures in the PDB was used for statistical evaluation of crystallization conditions resulting in improved sparse matrix **[27]** screens (see **Figure 2B**) that are commercially available (and thus reproducible) by various manufacturers (e.g. Hampton Research, Jena BioScience, Molecular Dimension or Qiagen). On the other hand did high-throughput not lead to the hoped high (structural-)output **[20]**, still the attempts to crystallize fail for the majority of purified proteins (see **Table 1**) and the question why a protein crystallizes under certain conditions and another not, remained unanswered. In future single molecule structure elucidation applying X-ray lasers **[28]** – such as the XFEL **[29]** currently under construction at DESY, Hamburg – might prove as the method of choice for the investigation of protein structures if it can yield as detailed information as X-Ray crystallography. First results applying soft X-ray pulses at FLASH (Hamburg) **[30]** and the first X-ray laser SLAC in Stanford (California, USA) are promising **[31, 32]**. The structure of the membrane protein Photosystem I was solved at SLAC by injecting nanocrystals into the X-ray laser beam **[32]**. The resolution of eight Angstroms is still quite moderate but even such a result only a few years back was thought to be impossible. Recently *in vivo* grown microcrystals of the protein Cathepsin B from *Trypanosoma brucei* were subjected to this method and diffraction patterns could be obtained **[33]**. Moreover it could be shown that even though the imaged particle (molecule or set of molecules such as protein complexes or virus particles) is destroyed by the X-ray pulse diffraction and structural information can be detected before destruction **[34, 35]**. The strength of X-Ray crystallography – in comparison with single molecule techniques – is the averaging over billions of molecules, minimizing statistical errors. Thus the investigation of crystallization phenomena and the subsequent rationalization of protein crystallization are

necessary to overcome the above described bottleneck and to be able to get diffracting crystals from the majority of solubilized and purified proteins.

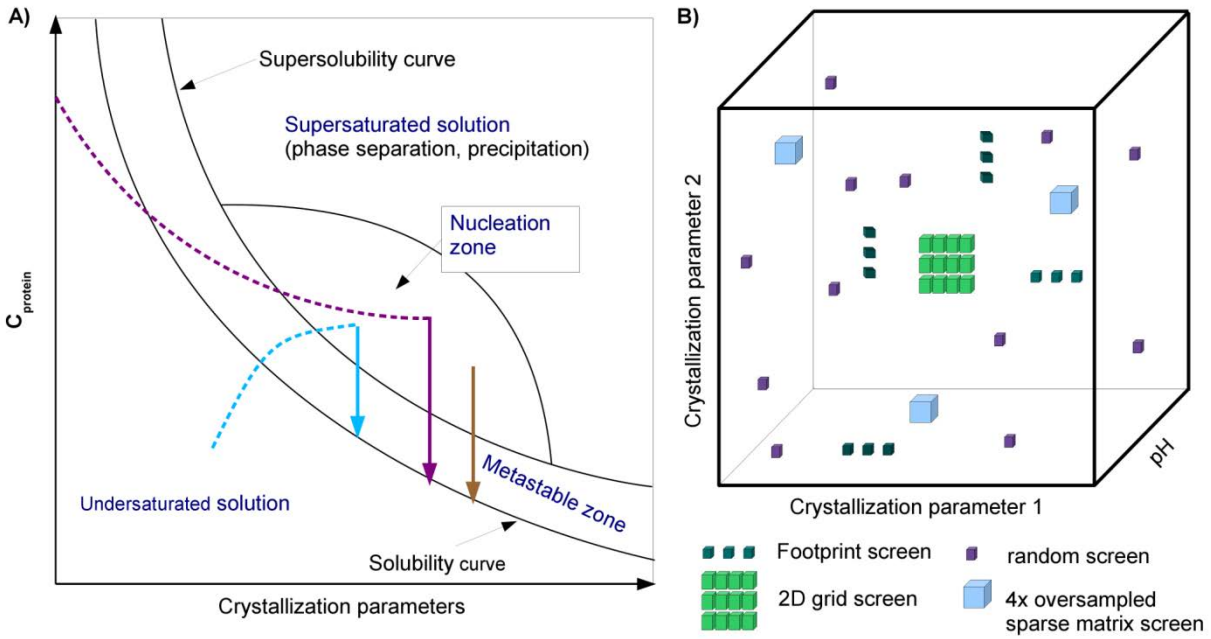

Figure 2: A) schematic protein crystallization phase diagram **[36]**, **B)** Comparison of different protein screening techniques **[14]**. **A)** shows idealized pathways of the three major crystallization methods vapor diffusion (blue line), free interface diffusion (purple line) and microbatch (brown line) from set-up to nucleation (dashed) and to successful crystallization (full line). The size of the nucleation zone of a protein determines its crystallizability. **B)**.The sparse matrix screens are derived from the conditions of previously crystallized proteins. Grid- and footprint screens are useful during the optimization of protein crystallization; the initial conditions are refined stepwise. It is today assumed that a combination of sparse matrix screens and 2D (wide)-grid screens yields the best results in initial screening. An example is the combination of the screens JCSG+ (sparse matrix) and PACT (wide grid) **[37]**. It has to be noted that the 2D and 3D drafts of protein crystallization space are simplifications and that the "real" crystallization space is multidimensional.

This will improve structure based drug design **[38]** efforts, since the three dimensional structure of drug targets will be much more easily accessible, but also new insights into the interaction of pathogens with their host will be gained and by this a better understanding will arise of the why and how of diseases.

1.3. Improvements in Protein Crystallization

Since the beginning of protein structure elucidation by X-Ray crystallography **[13]** the crystallogenesis of complex molecules such as proteins is being investigated **[18, 39-44]**. More and more details about how protein molecules form ordered aggregates that grow into crystals have been revealed or are being discussed **[45-47]**, but no consistent theory, no rational formula exists that can be applied to get certainly crystals from every protein. The main reason, after ruling out impurity and missing secondary structure, that protein crystallization cannot be rationalized is the complex electrostatic surface potential of proteins. Other than simple ions or small

organic molecules in proteins positive and negative charges are distributed on the surface in a complex manner, depending on the three dimensional arrangement of the amino acid sequence of the protein (and on the pH-value). Since to date no law is known that describes how the primary structure of a protein (the sequence) is translated into the three dimensional tertiary structure it is not possible to deduce the charge distribution of the protein simply by bioinformatic processing of the amino acid sequence. Approaches such as the cloud computing initiative Rosetta@home **[48-50]** or the Rosetta based computer game Foldit **[51]** had some success in determining the three dimensional structure of a protein. Recently based on a Foldit/Rosetta-model the structure of the retroviral protease M-PMV (PDB accession code: 3SQF) could finally be solved by molecular replacement **[52]**. But this quality of prediction is not enough for the prediction of crystallization conditions since a single mutation of an amino acid on the surface of the protein can result in completely different conditions under which the given protein crystallizes **[53]**. That means that even for two proteins, A and B that share a high sequence identity and even a nearly identical fold and three dimensional arrangement the conditions for the crystallization of B cannot be predicted exactly from the conditions that yielded diffracting crystals for A.

1.4. Rational Crystallization of Proteins

A more promising approach for rational protein crystallization does not take the amino acid sequence into account but relies on the biophysical properties of the protein- and crystallization solutions. Protein solutions prior to crystallization are probed using methods such as Circular Dichroism (**CD**) spectroscopy, Dynamic Light Scattering (**DLS**) **[54-56]** and absorption spectroscopy to ensure correct folding, purity and concentration of the protein. After the addition of a crystallizing agent the crystallization process can be observed *in situ* applying dual polarization interferometry (**DPI**) or DLS **[18]**. By absorption spectroscopy the concentration of protein at different crystallization conditions can be calculated and thus the solubility curve. From these measurements the phase diagram of a protein against a precipitant can be derived **[39]**. This is beneficial for the optimization of crystallization and narrows down the concentration range of protein and precipitant to be screened. An indicator for possible protein crystallization is the second virial coefficient B_{22} **[57,**

58] that can be derived from Static Light Scattering (**SLS**) experiments **[54, 57, 59]** as well as from DLS experiments **[60-62]**.

It could be shown that for slightly negative values of B_{22} there exists a crystallization window in which – by variation of protein concentration – formation of protein crystals is probable **[63]**. The value of B_{22} reflects the protein-protein and protein-precipitant interactions in solution **[58]**. If repulsive interactions dominate the B_{22} is positive, protein molecules will not form crystals since the time of contact between two molecules is minimized. For dominating attractive interactions B_{22} becomes negative. Too much attraction between protein molecules will lead to unordered aggregation. Crystallization is favored if the contact time between two molecules is sufficient for attachment but the attractive interaction is weak enough that they only stay attached if they are in a certain orientation towards each other **[61]**. The B_{22} is independent of the protein concentration **[57]**, the crystallization conditions however are a function of protein concentration **[57, 62]**. This is why at a B_{22}-value within the crystallization window the protein concentration has to be varied to obtain protein crystals.

1.5. Light Scattering

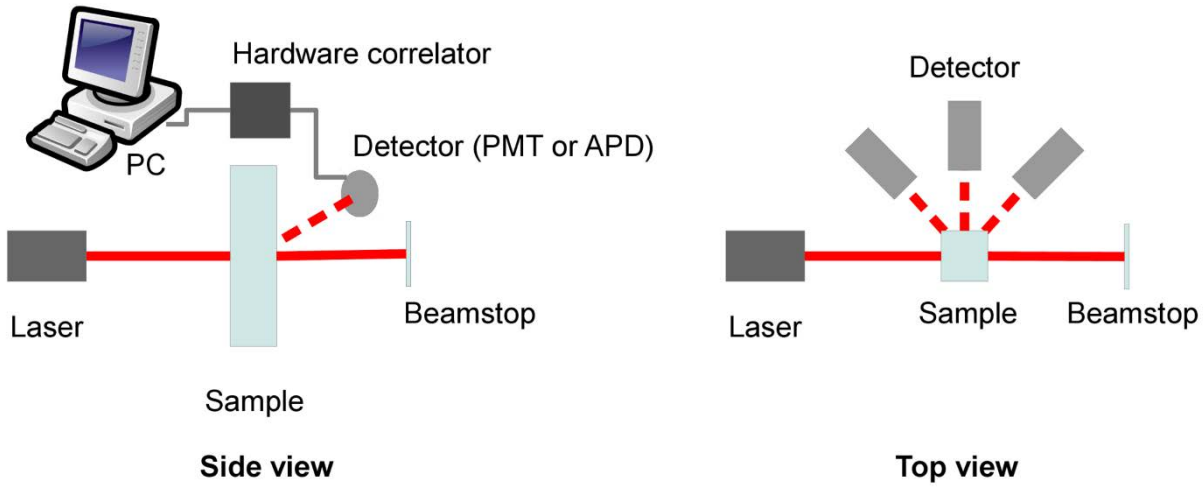

Figure 3: Scheme of DLS instrumentation. Laser light scattered by sample solution is detected by Photomultiplier Tube (**PMT**) or Avalanche photo diode (**APD**). The signal is processed by a correlator and data evaluated by a PC that also controls the laser. The top view shows that the detectors can be arranged at various angles perpendicular to the incident laser beam. Instruments with multiple detectors exist as well as set-ups where the angle of one detector can be varied

Today a light scattering experiment is carried out by probing a solution containing the solute to be investigated by a Laser (see **Figure 3**). At an angle or at multiple angles

perpendicular to this beam detectors record the scattered light from the sample. In most cases a photomultiplier tube (**PMT**) is used for that purpose but some manufacturers use an avalanche photo diode (**APD**) instead (advantages and disadvantages of both types of detectors are briefly discussed by **YADAV** *et al.* **[60]**). In the case of SLS only the intensity of scattered light is recorded whilst DLS means that the fluctuation of intensity is recorded. The signal recorded by the detector is then processed by a hardware correlator that calculates the time dependence of intensity fluctuations of scattered light. For both SLS and DLS further evaluation is carried out by a computer equipped with software for that purpose. The fluctuation of intensity is coupled to the Brownian motion of particles in solution and thus, if the viscosity of the solution is known, the hydrodynamic radius (R_H) of these particles can be estimated through the Stokes-Einstein equation (**EQ 1**) **[56, 64]**:

$$D_o = \frac{kT}{6\pi\eta R_H}$$

EQ 1

$$R_H = \frac{kT}{6\pi\eta D_o}$$

EQ 2

D_o is the diffusion coefficient at infinite dilution, k is the Boltzmann constant, T is the temperature, η is the viscosity of the solution and R_H the hydrodynamic radius. Analysis of the time dependent intensity fluctuation displayed in the auto correlation function (**ACF**) by algorithms such as CONTIN **[65-67]** or the method of cumulants **[68-70]** yields the diffusion coefficient of particles in solution. Applying **EQ 1** the R_H of particles in solution can be calculated. In the case of CONTIN, the algorithm used throughout this work, the radius distribution can be derived even if various particle sizes exist in solution. The method of cumulants has its strength in the calculation of polydispersity parameters of a single radius peak. Other methods to analyze the ACF exist (a good overview on the analysis of ACF is given in the chapter *Data analysis in Dynamic Light Scattering* in *Dynamic Light Scattering – the method and some applications* by **Wyn Brown [71]**) and some manufacturers of light scattering instruments distribute their own set of algorithms. Changes in R_H and radius distribution of a protein solution can be used for the analysis of oligomerization- and aggregation states in solution **[57]**.

When SLS is measured in macromolecular solutions that are pure and monomodal the molecular weight of particles in solution and second virial coefficient B_{22} can be calculated from the concentration- and angle-dependence of the intensity of scattered light **[64, 72]**. As described in **chapter 1.4**, B_{22} is an indicator that shows if in the probed solution repulsive or attractive interactions between the molecules dominate **[57, 73]**.

Considering the information that can be achieved applying light scattering and the non-invasive character of this methods (as long as the macromolecule contains no chromophore that can be excited by the given laser wavelength) it does not surprise that it is widely used as an analysis tool of the crystallization process and for the investigation of biological macromolecules. Already during the first years of application it was proposed **[74]** that DLS can be used to assess the crystallization probability of proteins. DLS was then used in optical cuvettes probing protein solutions prior to and during crystallization. These measurements consumed large amounts of protein solution and had – furthermore – to be carried out under non-standard conditions.

1.6. *In situ* DLS

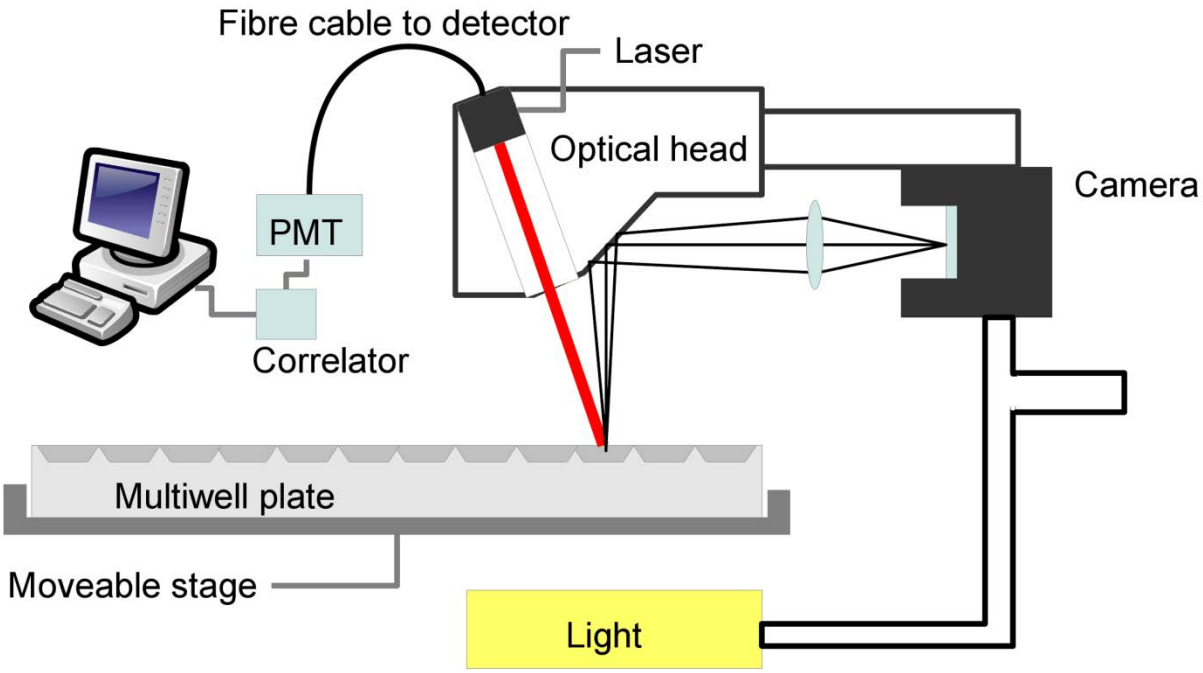

Figure 4: Scheme of an *in situ* DLS instrument. Adapted from Garcia-Caballero et al. **[18]**, figure 3.

WILSON *et al*. had the idea to measure DLS in small droplets during vapor diffusion experiments **[75]** and presented a draft of instrumentation for that purpose. Later

CASAY and **WILSON** performed the first DLS measurements in hanging crystallization droplets in a special apparatus in microgravity environment **[76]**. The first measurements in crystallization plate droplets were then performed by **RICKA** and **WESSEL** **[77]**. In parallel light scattering measurements in cuvettes under crystallization conditions using batch methods were carried out by various groups gaining insight in the complex processes during nucleation and crystallization **[57, 63, 78-86]**. The availability of DLS plate readers for micro titer plates reduced the amount of protein necessary for these experiments and DLS can now be used routinely for buffer- and additive-screening or for the observation of complex formation between two proteins **[87]**.

The scheme of instrumentation for *in situ* DLS is shown in **Figure 4**. The first commercially available DLS instrument for measurements in crystallization conditions other than batch was introduced in 2008 **[88]**. The *Spectro*LIGHT 500 system (see **Figure 5**), which was also used in this work, enables DLS measurements in standard vapor diffusion 96 well plates with SBS-footprint but also in cell culture plates **[18, 88]**. The minimum volume for DLS measurements suits the volumes normally used in high throughput crystallization approaches (~ 500 nL).

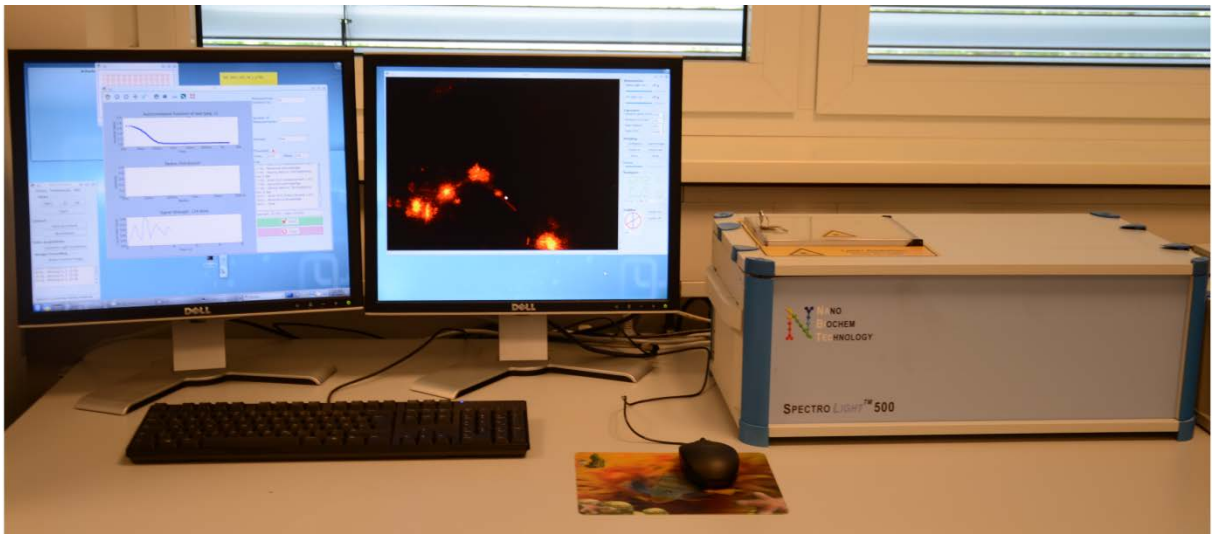

Figure 5: The *Spectro*LIGHT 500 system was used to carry out *in situ* DLS measurements. On the right hand side is the plate reader box in which also the DLS optics are included and on the left hand side the control terminal, displaying the software *SPECTRO*, can be seen.

The *Spectro*LIGHT 500 **[18]** is controlled by the *SPECTRO* software. The software on the one hand evaluates the DLS raw data coming from the hardware correlator, it interprets the ACF **[55, 56]** using the CONTIN algorithm **[65]** to then display the radius distribution of the measured solution. On the other hand it has an included

camera window in which the position of the optical head relative to the plate, the laser and image properties can be controlled. These properties furthermore can be controlled automatically by the use of small scripts written in Python **[89]**. Using these scripts complex operations such as imaging and DLS of selected wells are possible.

1.7. Theory of Dynamic and Static Light Scattering

If a sample is illuminated by a laser beam and the particles in solution are small compared to the laser wavelength the light is scattered at the particles in all directions. Since the laser light used is approximately coherent and monochromatic and the particles in solution are constantly in motion (Brownian motion) a detector perpendicular to the incident laser beam observes a fluctuation of intensity of scattered light (depending on the complex pattern of destructive- and constructive interferences of the scattered light at all the particles in the observation space in a defined time interval). The time dependence of the intensity function is related to the viscosity of the solution, particle size and temperature, since Brownian motion depends on these variables. To obtain information from the Brownian motion of particles by DLS the ACF of the time dependent intensity of light is evaluated **[64]**.

$$\boldsymbol{g_2(q;\tau)} = \frac{\langle \boldsymbol{I(t)I(t+\tau)} \rangle}{\langle \boldsymbol{I(t)} \rangle^2}$$

EQ 3

In **EQ 3** $g_2(q; \tau)$ is the second order ACF at a wave vector q and delay time τ. I is the measured intensity and t is time. At very short delay times (τ_1) there is a high correlation of intensity between t_0 and t_1 (time between t_0 and t_1 is τ) since the particles in the observed space have had no time for translational movement yet. At longer delay times (τ_2) the particles have positions different from their original position (relative to each other and the laser beam) thus there is only a low correlation of intensity between t_0 and t_1. In the case of only one particle population present in the solution and no interaction between the particles (monomodal solution of hard coils) the decay of correlation between the observation points τ_1 and τ_2 is exponential. In DLS measurements the intensity of scattered light is recorded for many delay times (τ_n) over a certain period of time. Different than the second order correlation function (**EQ 3**) which is related to the intensity, the first order correlation function $g_1(q;\tau)$:

$$\boldsymbol{g_1(q;\tau)} = \boldsymbol{e^{-\Gamma\tau}}$$

EQ 4

is related to the auto-correlation of the electric field in the above described case of a monomodal solution of hard coils that are small relative to the laser wavelength. *Γ* is the decay rate of the electric field. The electric field on the other hand cannot be measured directly. Both **EQ 3** and **EQ 4** can be related **[64]** by the Siegert relation:

$$g_2(q;\tau) = 1 + \beta[g_1(q;\tau)]^2$$

EQ 5

Where *β* is a correction factor for instrumentation non-ideality (in an ideal case β = 1). Thus the decay rate of the electric field can be related to the measurable intensity fluctuation. This decay rate on the other hand can be described as a function of the wave vector *q* and the diffusion coefficient *D* **[64]**:

$$\Gamma = \frac{D}{q^2}$$

EQ 6

$$q = \frac{4n_0\pi}{\lambda}\sin\left(\frac{\theta}{2}\right)$$

EQ 7

The wave vector *q* is a function of the wavelength *λ*, the angle between laser and detector *θ* and the refractive index of the solution n_0. Other than in a SLS experiment where usually the angle between laser and detector and hence *q* is varied to obtain a ZIMM plot for the calculation of molecular mass and B_{22}, *q* is normally kept constant during DLS measurements. Combining **EQ 4**, **EQ 5** and **EQ 6** it is clear that in the case of a monomodal solution of hard coils the diffusion coefficient *D* can be obtained by an analysis of the time dependent intensity fluctuation:

$$g_2(q;\tau) = 1 + \beta e^{-2Dq^2\tau}$$

EQ 8

As described in **chapter 1.5** this intensity fluctuation can be recorded by a detector, either a PMT or an APD. Following the detection the resulting electric signal is usually evaluated into the autocorrelation function **EQ 3** by a hardware correlator that suit this purpose better than software using a computer CPU. An exponential fit over the autocorrelation plot of $g_2(q;\tau)$ against *τ* yields – if scattering angle, wavelength of the laser and refractive index of the solution are known and hence *q* – the diffusion coefficient *D* **(EQ 8).**

If the solution is composed of interacting particles or if more than one type of particles is present in solution (polydispersity), *D* cannot be derived by a simple

exponential fit. In general all protein solutions can be considered polydisperse even though in literature and in this work the term *monodisperse* is sometimes used to describe the properties of a protein solution. Monodisperse in this sense points to a solution of low polydispersity, but in all solutions containing polyelectrolytes – such as proteins – molecule-molecule interaction exists, as well as temporary complexes, such a solution is never ideally monodisperse. The decay of the ACF will hence always deviate from an ideal exponential decay. If the ACF resulting from these measurements is fitted simply exponential the fit will not match the observation. Hence to evaluate the ACF a more complex fit is necessary. As mentioned earlier the algorithm CONTIN, developed and written by **S.W. PROVENCHER [65-67]** was used to fit the autocorrelation function and to derive *D* from DLS measurements throughout this work. CONTIN can fit an ACF derived from polydisperse solutions and not only derive the radius of the main component but also, if the species of particles in solution vary enough in size, can display the radius distribution. This is very useful if aggregation-, oligomerization- or crystallization phenomena should be studied by DLS since in these cases often two distinct particle ensembles exist in solution. The algorithm of CONTIN fits the ACF by performing the inverse Laplace Transform, starting from an unsmoothed solution **[64]**. This solution is then regularized based on statistics yielding the optimal solution **[67]**.

It is known from **EQ 2** that the hydrodynamic radius R_H can be directly calculated from the diffusion coefficient. Since *D* depends on the protein concentration in **EQ 1**and **EQ 2** D_0 is used, the diffusion coefficient at infinite protein dilution. In practice *D* can be used for the calculation of R_H but one has to bear in mind that this R_H is, as *D*, thus a function of protein concentration ($c_{protein}$).

Furthermore *D* is a function of protein-protein- and protein-solute interaction in solution **[61]**. If the protein concentration is constant changes in *D* are due to changes in protein-protein- or protein-solute interaction. It could be shown **[61, 71]** that this dependence – the interaction factor k_D – is closely related to the second virial coefficient B_{22}:

$$\boldsymbol{D = D_0\left(1 + k_D c_{protein} + \ldots\right)}$$

EQ 9

$$\boldsymbol{k_D = 2B_{22}M_W - \zeta_1 - v_{sp}}$$

EQ 10

In **EQ 10** M_W is the solute molecular weight, v_{sp} is the specific volume of the solute and ζ_1 is the first order concentration coefficient of the friction coefficient **[61]**. A deduction of **EQ 9** and **EQ 10** was presented by **WYN BROWN** and **PU ZHOU [90]**. It is assumed **[61]** that for a given solvent and solute v_{sp} and ζ_1 are constants. Then B_{22} can be calculated from the measurement of D at different protein concentrations (if D_0 is known, B_{22} can be calculated directly from a measured D and the protein concentration at that point). Still v_{sp} and ζ_1 remain uncertainties in the calculation of B_{22} based on DLS measurements. The first order concentration coefficient of the friction coefficient ζ_1 can be derived from pulsed field gradient NMR **[90]** but this is not applicable for daily routine work and thus not useful for rational crystallization of proteins. As compared by **YADAV** *et al.* **[60]** k_D can be used instead of B_{22} to describe the quality of protein-protein interaction. Since k_D is derived directly from DLS measurements its application towards rational crystallization of proteins is more straight forward as that of the second virial coefficient.

In the case of static light scattering (SLS), only the absolute intensity of scattered light at different angles is recorded by a PMT. The dynamic information about the movement of particles within the sample is lost but SLS is better suited than DLS when it comes to the analysis of M_W and B_{22} within a sample. **ZIMM [72]** could show that the intensity of scattered light recorded at different angles and concentrations of a sample is related to the M_W of the sample, to radius of gyration R_g and to the B_{22} of the examined solution **[64, 91]**:

$$\frac{\boldsymbol{Kc}}{\boldsymbol{R_\theta}} = \frac{\mathbf{1}}{\boldsymbol{M_W}}\left(\mathbf{1} + \frac{\mathbf{1}}{\mathbf{3}}\boldsymbol{q_s}^2\langle \boldsymbol{R_g}\rangle_z + \ldots\right) + \mathbf{2}\boldsymbol{B_{22}c} + \mathbf{3}\boldsymbol{C_{33}^2} + \ldots$$

EQ 11

With the optical constant K:

$$\boldsymbol{K} = \frac{\mathbf{4}\boldsymbol{\pi}^2\boldsymbol{n_o^2}(\frac{\boldsymbol{dn}}{\boldsymbol{dc}})^2}{\boldsymbol{N_A}\boldsymbol{\lambda}^4}$$

EQ 12

And the Rayleigh ratio:

$$\boldsymbol{R_\theta} = \frac{\boldsymbol{d}^2}{\sin^2\boldsymbol{\theta_z}}\frac{\boldsymbol{I_s}}{\boldsymbol{I_0}}$$

EQ 13

The SLS scattering vector q_s is nearly identical with the scattering vector in DLS (**EQ 7**) with the exception that the refractive index n_o is absent in q_s. C_{33} is the third virial

coefficient and omitted in most considerations regarding the evaluation of light scattering experiments. In **EQ 12** (dn/dc) is the refractive index increment and N_A is Avogadro's constant. I_0 in **EQ 13** is the intensity of incident light, I_s the intensity of scattered light and d is the distance of the detector from the scattering volume. The determination of I_0 is challenging. Normally this is solved by calibration with a standard of know calibration power. Solvents such as toluene can be used for this purpose. Then just protein concentration and the scattering angle (and thus q_s) must be varied in order to obtain information of the sample M_W, R_g and B_{22} according to **EQ 11** by plotting KC/R_θ against (q_s^2+const.*c) (ZIMM plot) **[72, 91]**.

However, the variation of angle is not possible in the case of *in situ* measurements within crystallization plates. Moreover do these environments not provide the freedom of dust necessary for valid SLS measurements. This is why in this work "pseudo-SLS" is used for the analysis of on-going crystallization rather than SLS. In pseudo-SLS the development of the intensity of scattered light (countrate) over time is analyzed and the relative changes of countrate between measurements are then attributed to changes in protein concentration and crystallization/nucleation/oligomerization events to complement the information derived from the analysis of changes in R_H.

2. Aim of this Work

In terms of this thesis crystallization phenomena of biological macromolecules should be analyzed utilizing light scattering methods. Particularly *in situ* DLS methods should be applied to analyze and score the most common crystallization techniques: vapor diffusion, counter diffusion and microbatch under oil, with aim to identify procedures to optimize crystallization of biomolecules and to monitor and control the most critical step within crystallization experiments, the formation of crystalline nuclei. Another aspect of the thesis was to identify and to design automatic procedures to adapt the *in situ* DLS method to high throughput crystallization techniques used most commonly today.

Further the possibility to perform DLS measurements within particularly small and low volume crystallization compartments such as microfluidics devices should be analyzed considering also complex conditions, as the cubic lipid phase system, used to crystallize membrane proteins.

In terms of these investigations the interaction and oligomerization of two human membrane proteins, CD81 and Claudin-1, both proteins are essential in the course of the HCV infection should be analyzed. In parallel crystallization experiments of native CD81 and another human membrane protein from the tetraspanin family, CD82, were intended. Finally *in situ* DLS should be applied to characterize the surface layer protein SlfB from *Lysinibacillus spaericus* strain JGA12 in solution to identify appropriate crystallization conditions and to obtain X-ray suitable crystals for further structure analysis, as so far no full length 3D structure of a surface layer protein has been presented.

3. Dynamic Light Scattering *in situ* in common Crystallization Environments

3.1. General Considerations

Even though described for the first time more than twenty years ago (see **chapter 1.6**) *in situ* DLS in droplets or other crystallization environments else than the measurement cuvette never emerged the theoretical or physical niche. Even though the physical processes within a solution of biological macromolecules during crystallization were studied **[74, 75, 78]** only few efforts were made to investigate the differences between the various methods and set-ups. These differences (mainly the time interval in which supersaturation of the solution is achieved **[45]**) were deduced from basic physical parameters such as diffusion (counter- and free interface diffusion methods) or partial vapor pressure of the solutes (vapor diffusion crystallization). The processes at super saturation were deduced from batch experiments within the above described cuvettes. A combination of both considerations together with theoretical assumptions on the influences of kinetics, thermodynamics, hydrodynamics and the electrostatic surface potentials was then the most accurate description of protein crystallization. The difference between t_0 (were the experiment was started) and t_{super} (where super saturation was achieved) ($\Delta(t_s\text{-}t_0)$) and the approximation curve to super saturation within the phase diagram were described **[36]** but not the biophysical processes taking place during this approximation. It is obvious that $\Delta(t_s\text{-}t_0)$ and the curve of approximation to super saturation in a phase diagram influence crystallization at molecular level, since these are the main differences between the methods and it could be shown that at a same level of super saturation different results in crystallization can be obtained **[45]**. Probing a crystallization experiment, whether a small droplet or solution within a thin capillary, with DLS from the start to the formation of microscopically observable crystals, can give insight into the biophysical processes during the first stages of crystallization. Changes of calculated R_H from DLS (see **chapter 1.7**) can be attributed to changes of the diffusion coefficient D. Since D depends on the protein concentration ($c_{protein}$) and protein-protein interaction over protein-solute interaction (k_D) (see **EQ 9**) depending on the kind of experiment changes in k_D (counter- and free interface diffusion, were protein diffusion is assumed to be negligible compared to precipitant diffusion; microbatch, were $c_{protein}$ = const.) or in k_D and $c_{protein}$ in parallel

can be monitored (vapor diffusion experiments). If the total intensity of scattered light (pseudo-SLS) is monitored as well during the crystallization experiment and the sample is free of dust, changes in the intensity can be compared to changes in R_H and a combination of both measurements can be used for a relative or absolute analysis of crystallization experiments. If a monomodal protein solution is considered, then under normal vapor diffusion conditions the R_H at t_0 should be larger than at t_{-p} (before addition of precipitant) since the addition of the precipitant leads to attractive protein-protein interaction, therefore D decreases **[61]** and with D being inversely proportional to R_H (**EQ 2**), R_H increases. The dependence of R_H and as well D on $c_{protein}$ is considered to be lower than that on k_D, hence the dilution to $c_{protein}$ /2 at t_0 does not influence R_H as much as the changes in k_D due to addition of precipitant. Between t_0 and t_{super} R_H will increase further depending on the equilibration rate between reservoir and crystallization drop. If at all times during t_0 and t_{super} $c_{protein}$ is known (such as in the instrument **ARNE MEYER** developed **[92]**) changes in k_D can be treated independently of changes in $c_{protein}$. If $c_{protein}$ at a certain point in time t is not known exactly (it has to be between $c_{protein}$ and $c_{protein}/2$) which is true in crystallization experiments in crystallization plates, changes in R_H between t_0 and t_{super} have to be examined as changes of k_D and $c_{protein}$. In a successful vapor diffusion crystallization experiment super saturation is achieved short before or latest at the point of equilibrium between reservoir and drop. If super saturation of protein at equilibrium is not achieved no crystals will grow from the experiment, if supersaturation is achieved far before equilibrium the chance is high that unordered aggregates form instead of X-ray suitable single crystals. At the point of super saturation attractive interaction between protein molecules will increase rapidly whilst $c_{protein}$ will increase at a normal rate. Then, if nucleation takes places, protein is either built into nuclei or assembles in mesoscopic phases **[47]**. In both cases $c_{protein}$ decreases and the rate of change in k_D will remain constant, resulting in a slower increasing R_H.

When equilibrium is achieved (with super saturation being achieved before) k_D will become constant, at still decreasing $c_{protein}$ and hence R_H will decrease slowly. The decrease of R_H will continue until decrease of $c_{protein}$ leads to an undersaturated solution. Then $c_{protein}$ will also remain constant and as such will R_H. **Figure 6** gives an overview of the theoretical development of R_H in the above described circumstances and in the case of equilibrium before super saturation.

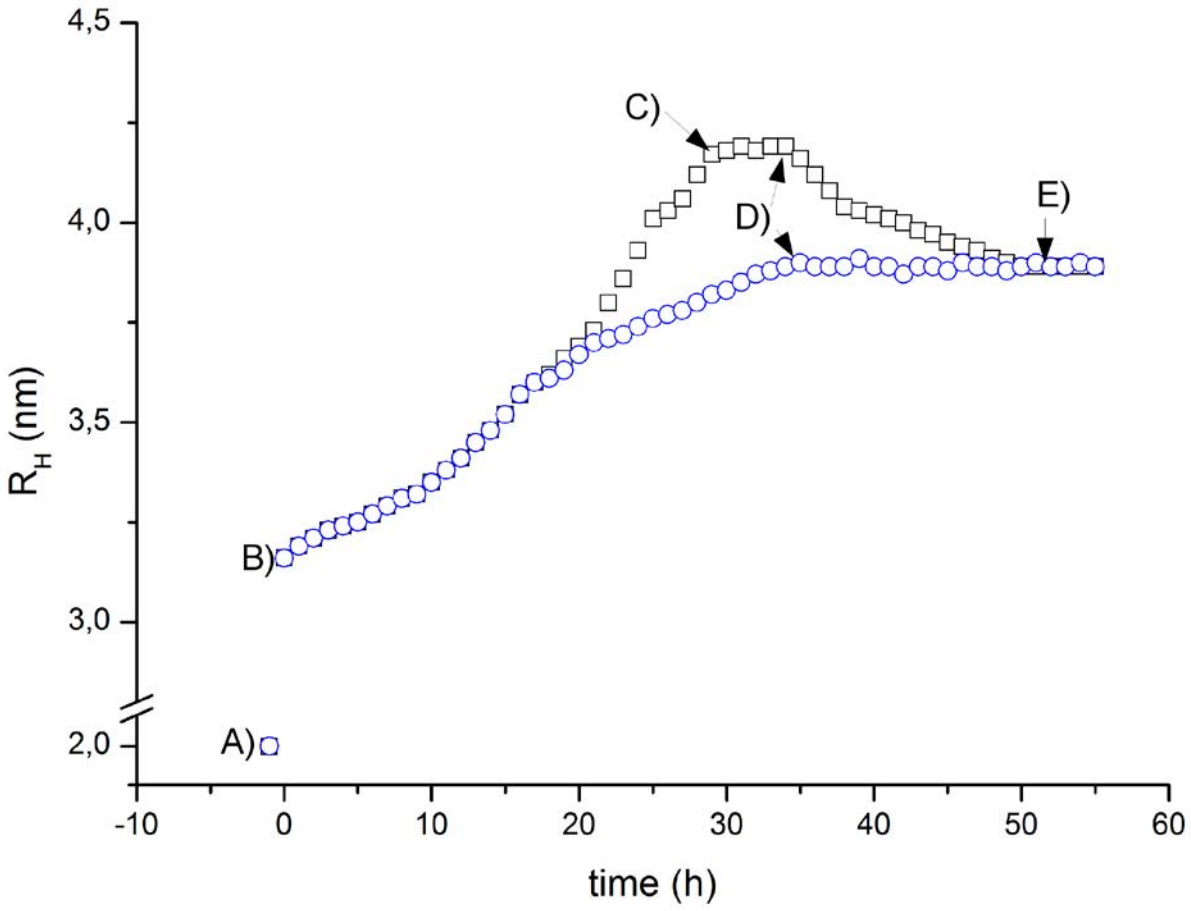

Figure 6: Scheme of an idealized R_H development (derived from a *Gedankenexperiment*) during a successful (boxes) and unsuccessful (circles) vapor diffusion crystallization experiment. A) R_H of the protein without precipitant, B) R_H of protein after addition of precipitant, C) R_H at achieved super saturation, D) vapor diffusion equilibrium E) final R_H, protein solution under saturated.

In **Figure 7** the results of a real crystallization experiment in a Linbro plate monitored by in situ DLS are shown. The development of radius distribution over time behaves as theoretically predicted for the two cases (a) crystallizing system (boxes) and (b) non crystallizing system (circles). The here applied method was hanging drop vapor diffusion. The theoretical and experimental radius distributions over time in the case of a microfluidic set-up were described by **AARON M. STREETS** and **STEPHEN R. QUAKE** **[93]**. They attributed the changes in R_H to Oswald ripening of pre-crystalline clusters following the theory of a two-step nucleation **[46]**. In the model they developed, the increased R_H after addition of precipitant is already a sign of the formation of a mesoscopic phase **[93]**. They apply a strict thermodynamic approach to protein nucleation and crystallization not taking into account the kinetics, electrostatics and hydrodynamics of protein crystallization.

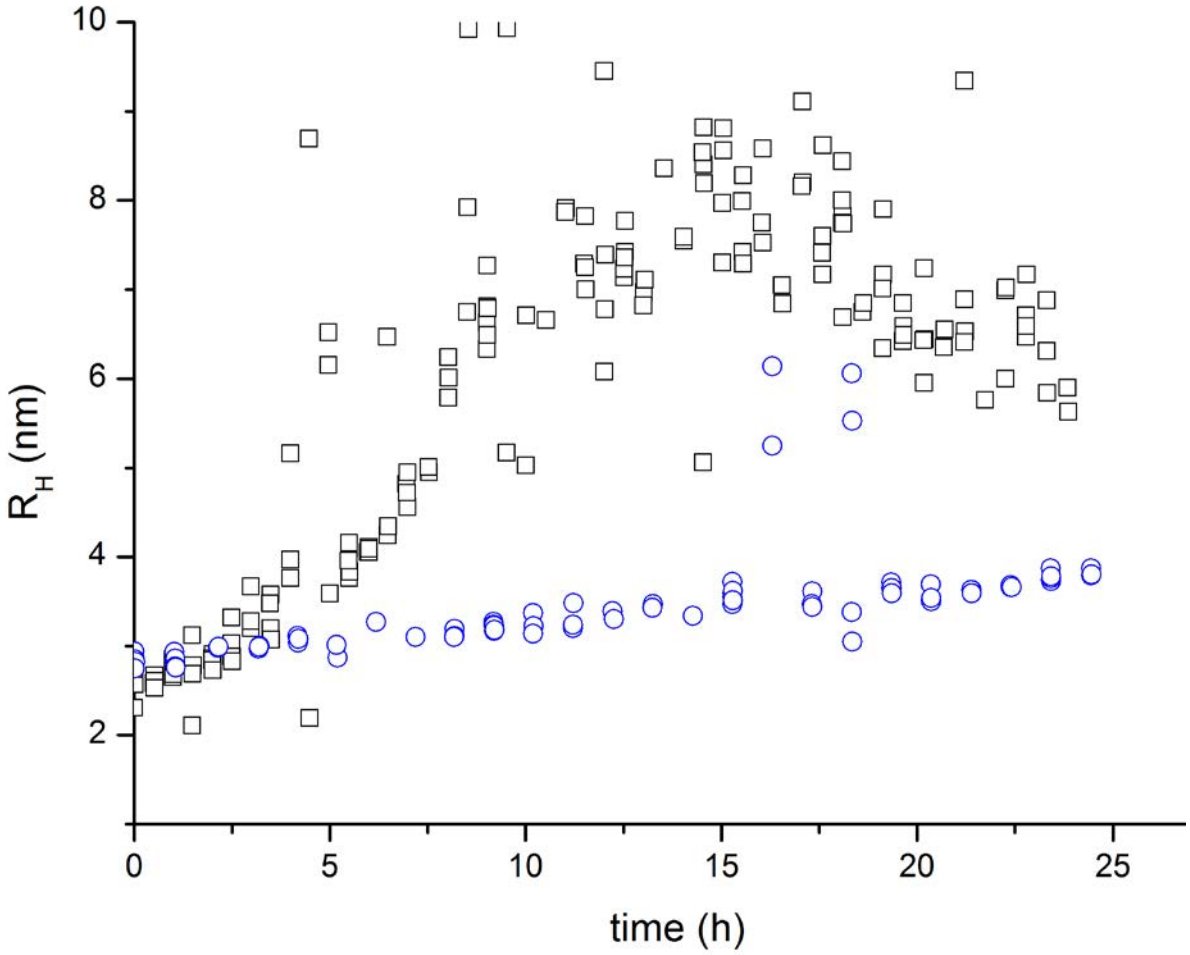

Figure 7: Development of radius distribution over time for a real vapor diffusion experiment in a Linbro24 plate. Circles: non-crystallizing conditions, 30 mg/mL hen egg white lysozyme vs. 0.125 M NaCl. Boxes: conditions that gave crystals, 30 mg/mL lysozyme vs. 1 M NaCl.

However their results could be reproduced applying *in situ* DLS within the CrystalFormer HT microfluidic system (see **chapter 3.3**). Moreover they also related the drip of R_H in systems with growing crystals to the decrease of $c_{protein}$.

From the observation of a crystallization experiment by DLS alone already a lot of information can be obtained. The relative changes of R_H (coupled to the diffusion coefficient *D*) show whether the observed system is super saturated, at equilibrium or if it is again under saturated and no further crystal nucleation can be expected. It is important to note, that it is the relative changes of R_H that matter and less the absolute changes. The absolute changes of R_H are only valuable if the observed system is known very well, e.g. for lysozyme where D_0 is known not only for the pure protein but also at various precipitant conditions. Then absolute values of R_H can be used to deduce the state of crystallization in a droplet. In all other cases the experiment has to be monitored by DLS constantly or at smallest possible Δt in the

case of multiple experiment monitoring. Hence automation and velocity of *in situ* DLS measurements matter if this method comes to application for the purpose of rationalization and optimization of protein crystallization.

3.2. Granada Crystallization Box

3.2.1. Introduction

The Granada Crystallization Box Domino (**GCB-D**) was first developed and presented in the course of a space experiment **[94]**. It is an enhancement of the previously developed crystallization environments GCB and GCB-II **[95]**. As the name denotes all types of GCB were developed in Granada at the CSIC/ Laboratorio de Estudios Cristalográficos. The here presented experiments were carried out in collaboration with **JOSÉ A. GAVIRA** and **EMILIO MELERO GARCIA** (both from CSIC/ Laboratorio de Estudios Cristalográficos) during the EU FP6 project *OptiCryst* **[18]**.

In all types of GCB super saturation of protein solutions is achieved through the method of counter diffusion **[96]**. Protein solution in thin capillaries (500 – 100 µm inner diameter) is brought in contact with precipitant concentration in a reservoir. Protein and precipitant start to diffuse against each other with the precipitant in the case of e.g. here used ammonium sulfate diffusing one order of magnitude faster than the protein. The velocity of diffusion in and out of the capillary can be further slowed down by blocking the capillary entrance by agarose layers. These are thick in the case of the GCB – here the agarose is the bottleneck **[92]** – and thin in the case of a GCB-D. In the GCB-D the inner diameter of the capillary is the bottleneck of precipitant diffusion. At some time after inserting the protein filled capillary into a GCB-D super saturation is achieved close to the open end of the capillary. With time the point of initial super saturation moves further up the capillary until all the protein within the capillary is at super saturation conditions. The difference to e.g. vapor diffusion at the level of crystallization kinetics is the temporal pathway of crystallization **[45]**. In vapor diffusion droplets super saturation is achieved in the whole drop at nearly the same time. Any saturation gradient is equilibrated fast through diffusive mass transport. This mass transport is hindered in the GCB by the narrow inner diameter of the capillaries. Thus along the capillary super saturation is achieved at different times. The time difference $\Delta(\Delta t)$ at which super saturation is achieved can be as long as three weeks. Since every Δt can be considered as a unique crystallization condition each capillary in a GCB can be viewed as a screen

with a large amount of conditions that are continuously self-screened **[96]**. The here described results have been published previously **[97]**.

3.2.2. Materials and Methods

Glucose isomerase was used for the counter-diffusion experiments. Commercial glucose isomerase (Hampton Research, USA) was dialyzed against Hepes (0.1 M, pH 7.0, Sigma Aldrich, Germany) and then concentrated in order to obtain a final stock solution of 50 mg/ml, as determined by spectrophotometry at 280 nm. GCB-D reactors **[94]** (see **Figure 8**) containing ammonium sulfate (3.0 mol/L) and Hepes (0.1 mol/L) at pH 7.0 were obtained from Triana S&T and used to set up the crystallization experiments.

Capillaries of 0.1, 0.2 and 0.3 mm inner diameter were filled with protein solution. Additionally, a fourth capillary of 0.3 mm was filled with a mixture of protein solution, buffer and low melting point agarose (0.075% w/v, Serva).

A *Spectro*LIGHT 500 instrument (Nabitec, Germany, see **Figure 5**) **[18, 88]** was used to carry out the DLS measurements. The system was adapted to be able to observe experiments in capillaries (e.g. GCB-D). The GCB-Ds were obtained in a configuration where they come prefilled with any desired cocktail of additives to be used as precipitant, topped with a layer of agarose gel through which the protein-filled capillaries are punctured for mechanical stability (see **Figure 8**).

The intensity fluctuation of scattered light was recorded by a photomultiplier tube and the autocorrelation function **[55, 56]** calculated by a hardware correlator. The ACF was interpreted using the CONTIN algorithm **[65-67]**. Results obtained through CONTIN were evaluated using the software *SPECTRO* (Nabitec, Germany). For the measurement procedure the capillaries were first loaded with protein solution, then one end of each capillary was sealed with wax and punctured - open-end first - through the gel of the GCB-D. Immediately afterwards the box was fixed inside the DLS instrument. By using the instrument's optical camera it was possible to record the coordinates at the beginning and at the end of the capillary and thus convert the distance along the capillaries to the coordinate system of the motorized stage. Seven positions were chosen to record the DLS signal according to followed the precipitation front from the entrance of the capillary as a function of time (see **Figure 8**).

Figure 8: Schematic drawing and figure of a GCB-D alone and inside the *Spectro*LIGHT 500. A schematic set up of a counter-diffusion experiment is shown on the left side. The open end of the capillary allows the precipitant to diffuse against the much slower diffusive protein solution, thereby inducing the precipitation of the protein. Each mark (*) represents a DLS measurement position, at 0.7, 2.2, 5.1, 9.9, 11.8, 18.7 and 24.5 mm from the open end. In the middle a GCB-D used for *in situ* DLS experiments is shown and on the right side a GCB-D within the *Spectro*LIGHT 500 is shown.

At the beginning of the measurements minute displacements in x, y and z directions were performed at each position to optimize the DLS signal (optimized position means: the largest countrate at which a valid ACF with high intercept could be obtained). Subsequently a cycling series of measurements was set-up (a script was written in Python and given as input for the autopilot of *SPECTRO*) in which the DLS signal was detected for 60 seconds at each of the positions in sequence, and then paused for a defined amount of time until the beginning of the next cycle. In total, the interval between two successive measurements at the same position was 122 minutes and the experiment was monitored during 14 days.

3.2.3. Results and Discussion

The volume of solution analyzed by the DLS system (crossing space of laser and detector) has been estimated to be around 1 pL **[88]**, which is equivalent to a sphere of approximately 12.5 micrometers in diameter. This volume is not negligible for sub-millimeter diameter capillaries, especially in the case of 0.1 mm capillaries that, on the other hand, are the most widely used because of its small sample consumption (approximately 400 nL). It is therefore required to ensure that no spatial distortions occur during measurement to obtain a clean DLS signal, similar to that obtained in quartz cuvettes, considering the geometry of the capillary and the plastic walls of the GCB-D. Capillaries of 0.1, 0.2 and of 0.3 mm, with and without agarose,

were filled with the supernatant of a centrifuged protein solution of 50 mg/mL in its buffer. The concentration of the supernatant was measured to be of 49 mg/mL (Absorption at 280 nm). After this, the different capillaries were punctured in GCB-D's filled with 3 M ammonium sulfate. DLS signals were acquired at 30 mm from the open end of the capillary (**Figure 9**). To make sure that the precipitant concentration in the observed volume was negligible, the DLS measurements were performed 5-15 minutes after puncturing the GCB-D. An aliquot of the protein sample in its buffer without precipitant was also measured by DLS in a quartz cuvette for comparative purposes. For all the capillaries, DLS signals were measured for 30 seconds, 30 consecutive times and 2 seconds interval between measurements. The results of the size distributions obtained from the DLS signals are shown in **Figure 9**. **Figure 9C** shows how the focus of the DLS laser beam fits inside the capillary, being sufficiently away from the flares caused by the reflection of the laser on the walls of the GCB-D, even in the case of the smallest 0.1 mm capillaries. **Figure 9A** shows an overlay plot of the radius distribution of glucose isomerase in capillaries and the optical cuvette. **Figure 9A** indicates that the size distributions calculated from DLS measurements inside the cuvette and those taken inside the capillaries are comparable. In all cases a monomodal size distribution was observed in which the only peak evident is that corresponding to the hydrodynamic radius of glucose isomerase in the buffer without precipitant.

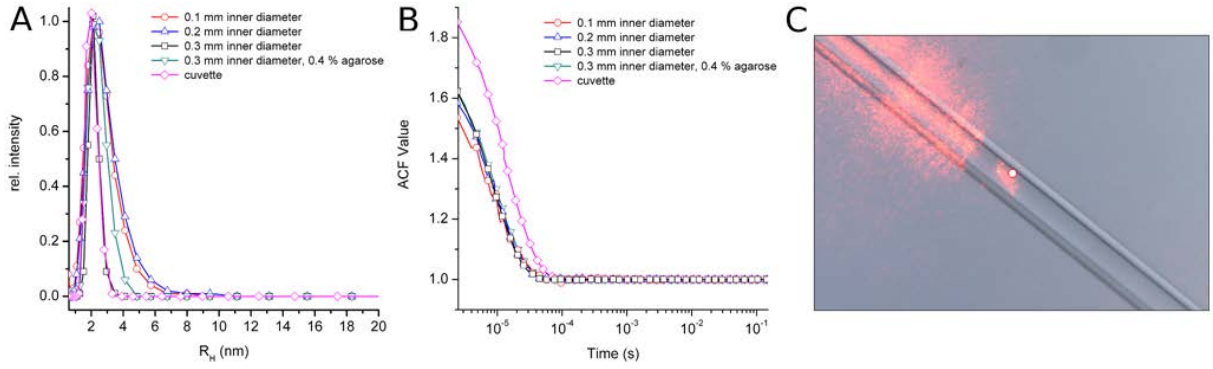

Figure 9: Results of the DLS measurements in capillaries. **A)**. Comparison of the size distributions obtained from DLS measurements of the same protein solution in standard quartz cuvettes and inside capillaries. The measured radius was approximately 2 nm in all 5 cases. **B)** ACF of the respective measurements, **C)** shows the focus of the laser inside a 0.1 mm capillary: the white dot marks the focus of the collecting optics and is slightly off for the sake of clarity, of 0.1 mm 0.2 mm, 0.3mm and 0.3mm with agarose.

Figure 9B shows an overlay of the auto correlation functions from which the radius distributions were derived. One can see that the signal to noise ratio for DLS

measurements in the cuvette is a bit better than for measurements in capillaries but all the ACF are shaped as expected **[54, 56, 91]** for monomodal solutions. These results clearly demonstrate that DLS measurements can be performed inside capillaries with an inner diameter as small as 100 µm. Moreover it could be shown that it is possible to measure DLS in standard commercial counter-diffusion devices.

After proving that DLS measurements can be performed inside capillaries a counter-diffusion crystallization experiment was set-up and the evolution of size distribution of the protein as a function of time and distance inside the capillary was monitored by DLS. A 0.1 mm capillary was filled with glucose isomerase solution at a concentration of 50 mg/mL in buffer, then punctured it in a GCB-D box containing 3 mol/L ammonium sulfate as precipitant and proceeded as described in the experimental section. The results of this experiment can be seen in **Figure 10**.

As soon as the open-end capillary is put in contact with the precipitant solution, the protein and the mixture start to counter-diffuse against each other. The precipitant diffuses faster than the protein due to its larger diffusion coefficient (approximately one order of magnitude). As the precipitant travels through the capillary, the solubility of the protein decreases and precipitation takes place. The calculated size distributions seem to react to this process in two different ways. At first, the increasing concentration of the precipitant causes an increase in the hydrodynamic radius of the protein (from 2 nm to approximately 5 nm).

A possible explanation for this observation is that the higher number of ions in the solution, their interaction with the protein and the protein-protein interactions mediated through the electrostatic conditions of the solution influence the measured diffusion coefficient, which is used by *SPECTRO* to calculate the hydrodynamic radius R_H using the Stokes-Einstein Equation **[91]**. The difference of theoretical R_H and measured R_H is, at constant protein concentration, a function of precipitant concentration (see **chapter 1.7**). Thus by relating measured R_H with theoretical R_H of the Protein it is in principle possible to determine the concentration of precipitant **[61]**. The second effect is that, at a certain time during the counter-diffusion, there is a perturbation of the size distribution consisting in the prompt extinction of the peak corresponding to the protein in solution and in the appearance of broad peaks at larger diameters.

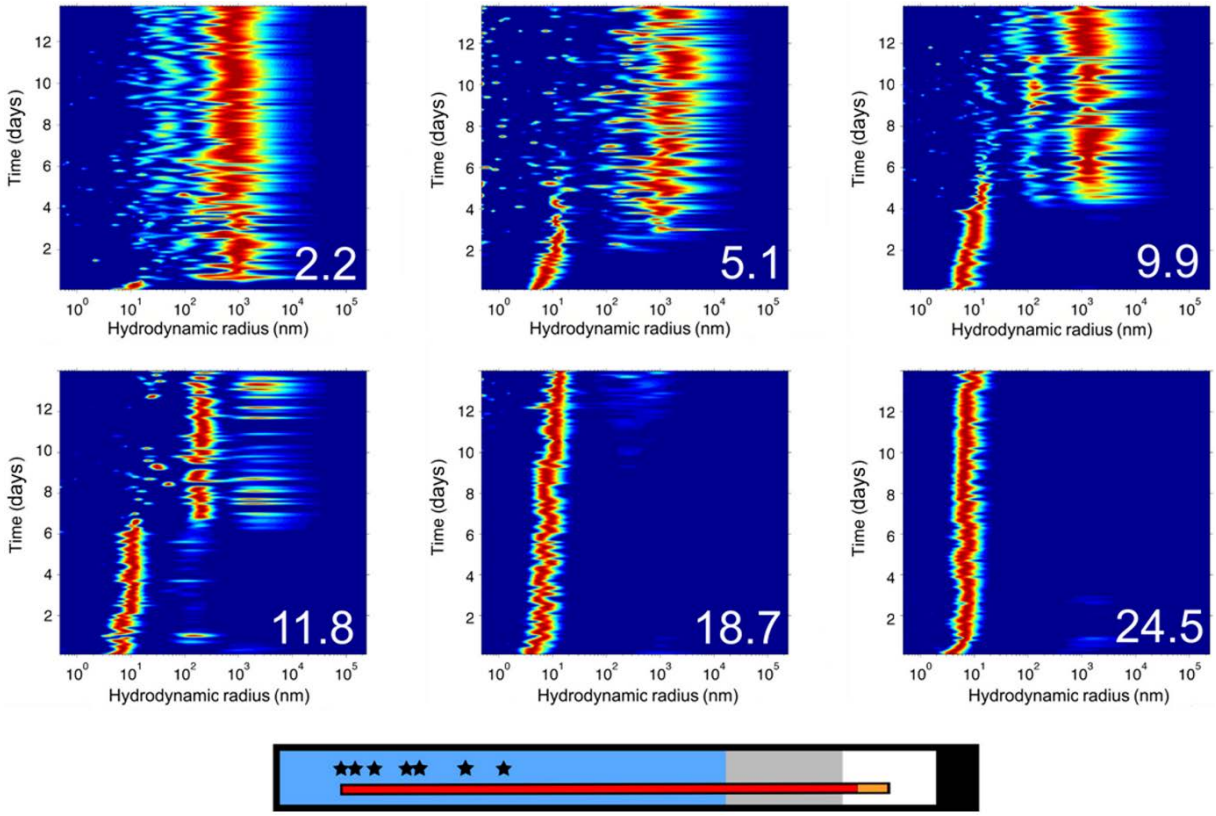

Figure 10: Size distribution (X-axis) as a function of time (Y-axis) obtained from DLS measurements in a single capillary. The number at the bottom right corner of each picture indicates the distance of the measurement in mm from the open end of the capillary. The picture at the bottom shows an overview of the capillary and the position of the measurements (*) in the GCB-D.

The fast disappearance of the initial protein peak is indicative of crystallization events **[88]** that seem to take place progressively later in time at larger distances from the entrance of the capillary, as expected from the experimental observation and the simulation results. The irregular size distributions at larger hydrodynamic radii correspond to the perturbation of the DLS signal by the appearing crystals. This is consistent with the expected formation and evolution of the already described advancing supersaturation wave **[98]** produced by the continuous diffusion of the precipitant. At the largest distances investigated it can be seen that the crystallization is not so clearly observed from DLS data. The reason for this may be that the process of nucleation and crystal growth at those positions occur at lower super saturation conditions than for points closer to the entrance. Since those processes are the cause of the depletion of the protein, it can be concluded that, at longer distances within the capillary, they are not fast and/or intense enough to counteract the restoration of the consumed protein by diffusion from the rest of the capillary.

Nevertheless, the rise in concentration of the precipitant due to diffusion can be clearly observed in the increase of R_H.

3.2.4. Conclusions

The experimental results presented here show clearly that the *in situ* DLS technique can be used inside capillaries for analysis of counter-diffusion crystallization experiments. The obtained DLS signals were equivalent to the one obtained using a quartz cuvette, yielding similar values for the hydrodynamic radius of glucose isomerase in its buffer without precipitant, even when it was measured inside capillaries of inner diameter as small as 0.1 mm.

Also a real counter-diffusion experiment in standard GCB-D systems was successfully followed by *in situ* DLS. The DLS signal is sensitive to super saturation changes inside the capillary, through the increase of the apparent protein hydrodynamic radius, which reflects the salt-dependent protein-protein and protein-salt interactions **[60, 61, 91, 99]**.

3.3. CrystalFormer HT

3.3.1. Introduction

The CrystalFormer HT (Microlytic, USA) is a microfluidic crystallization device (see **Figure 11**), utilizing the method of free interface diffusion for crystallization of biological macromolecules **[25]**. On a SBS-footprint **[100]** plate 96 channels are arranged. Each channel has a length of 1 cm and an inner diameter of 100 µm.

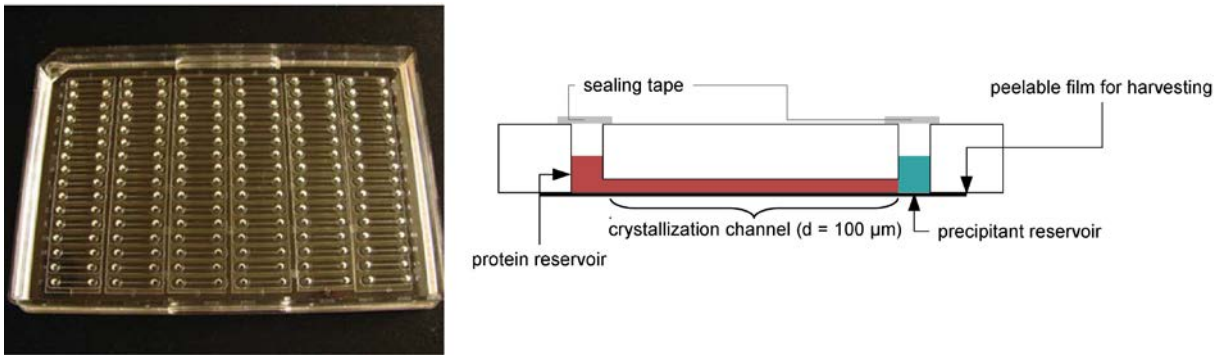

Figure 11: Left: CrystalFormer HT (Photo taken from http://www.microlytic.com), right: schematic draw of the side view of one CrystalFormer channel (Figure adapted from Stojanoff et al. **[25]).**

The CrystalFormer HT can be filled by crystallization robots such as the Mosquito or manually using microliter pipettes **[101]**. Its channels are on one hand similar to those of the GCB-D but on the other hand the set-up differs drastically. The length of the channel is only one fourth of the length of a capillary within the GCB-D. Moreover

are protein- and precipitant reservoir in the CrystalFormer HT of the same volume, whilst in the GCB-D the reservoir volume is more than 1000x larger than the protein volume. A thin layer of agarose is blocking diffusion at the tip of each capillary in a GCB-D, the channels of the CrystalFormer HT are free of any substance slowing down diffusion. In combination a faster approximation to super saturation should be expected and fewer “screening points” along the capillary due to the shorter length. After super saturation is achieved at one point along the capillary, $c_{protein}$ will remain constant (and not decrease as in vapor-diffusion or microbatch experiments) since protein being built into nuclei will be replaced by protein from the reservoir. This process is only inverted when super saturation is achieved within the protein reservoir. Since diffusion from the protein reservoir is at distances far from it limited as in the GCB a similar behavior of crystallization as in the GCB-D can be expected. At distances close to the protein reservoir deviation from the crystallization processes observed within the GCB-D are to be expected. Since at these distances super saturation is delayed they are most interesting and after assessing the general possibility of DLS in the CrystalFormer HT the focus will be on measurement positions close to the protein reservoir.

3.3.2. Materials and Methods

A CrystalFormer HT was received as a gift from Microlytic. For *in situ* DLS measurements in the scope of this work the channels were filled manually, following the instructions of the CrystalFormer user manual **[101]**. Into the protein reservoir of a channel 1 – 1.5 µL of protein were pipetted in a way that the channel was completely filled. Then carefully the chosen precipitant was pipetted in the opposite reservoir. To avoid evaporation of solvent the wells were sealed with tape provided by Microlytic. For DLS measurements the plate was inserted in the *Spectro*LIGHT 500 right after the last pipetting step. For measurements three points along the capillary were chosen (close to the protein reservoir, in the middle, close to the precipitant reservoir). The coordinates of these points were saved in the plate definition files in the *Spectro* database. Thus reproducibility of measurements was enabled. For optimization of the DLS signal a deviation from these positions of no more than 1 – 2 % relative to the channel length was used. The DLS signal was tested and through movement in x, y, z-direction using the camera and robotics of the

SpectroLIGHT 500 this signal was optimized. The measurement position was saved and DLS measurements were performed.

3.3.3. Results and Discussion

Since the CrystalFormer HT is a plate with SBS-format **[100]** footprint the adaptor for 96-well plates was used for measurements within the *Spectro*LIGHT 500. Based on the plate dimensions a plate definition file was created in the instruments database. Three points of measurement per channel were created. For the first measurements hen egg-white lysozyme (**HEWL**, Merck, Germany, 100 mg/mL, dissolved in 250 mM NaOAc/HOAc buffer, pH 4.75, dialyzed against 250 mM NaOAc/HOAc buffer, pH 4.75 buffer to remove NaCl) was used. In the protein well of the channel 2 µL of lysozyme were pipetted and assured that the channel was completely filled with protein solution. In the precipitant well 2 µL of a 1 M $CaCl_2$ (Merck, Germany) solution were pipetted and both wells were sealed with tape. The plate was inserted in the *Spectro*LIGHT 500 instrument, the plate definition file chosen and channel and point of measurement selected. The laser and detector position was then adjusted in a similar manner as described for the GCB-D (**chapter 3.2.2**) Due to the small inner diameter of the channel fine adjustments (20 µm steps) had to be carried out in order to optimize the DLS signal. Reflections of the laser at the walls of the channel and the plastics of the plate made this challenging but then a DLS signal of good quality could be obtained. The quality of a DLS signal is given by a) the ACF b) Intensity and c) radius distribution. The ACF should have an intercept of at least 1.4, ideally it is 2. Most of the times for measurements in cuvettes an intercept of 1.8 – 1.9 can be achieved. For the first DLS measurement in the CrystalFormer HT an intercept of approx. 1.8 could be obtained (see **Figure 12**). Moreover the form of the ACF is critical: the ACF obtained in these initial measurements was shaped as to be expected for a monomodal protein solution. The signal intensity of a measurement is important for signal-to-noise considerations and it tells if the laser beam or scattered light is blocked by the measurement environment. Moreover diffuse reflections will add to the intensity. A good measurement in non-standard environments has an intensity of scattered light that does not deviate too much from the intensity measured in a cuvette. The average countrate of 555 +/- 10 kHz obtained for this measurement is high but the deviation from standard DLS is not too much.

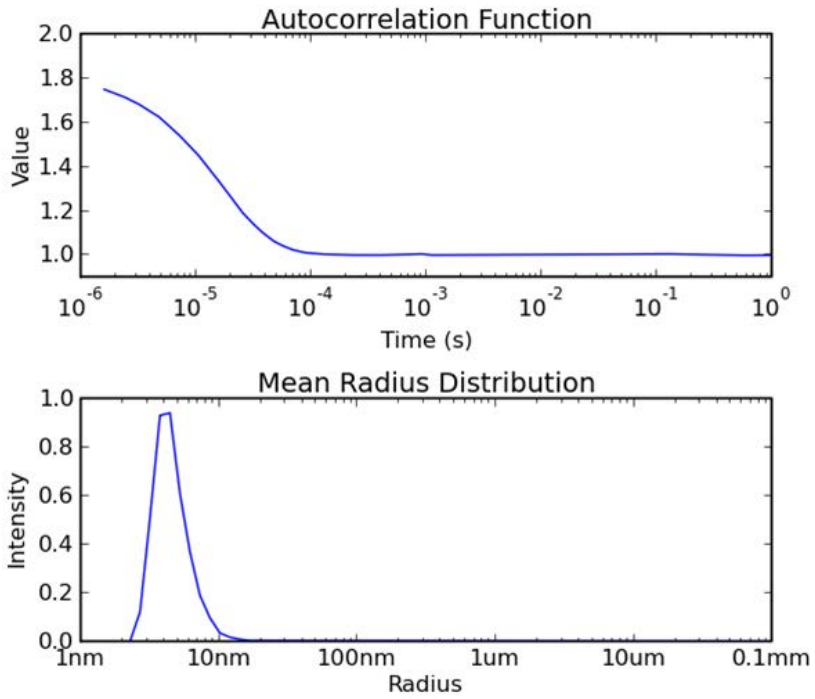

Figure 12: Results of first DLS measurements within the CrystalFormer HT. In the upper box the ACF is shown. The intercept of approx. 1.8 indicates a good measurement. The radius distribution derived from the ACF by CONTIN is shown in the lower box. The lysozyme solution at this initial stage of crystallization is as expected monomodal.

In **Figure 13** more results of initial DLS measurements within the CrystalFormer HT are presented. In the case of lysozyme, the ACF obtained in the CrystalFormer are compared with an ACF obtained by conventional DLS in optical cuvettes. As can be seen the quality of DLS measurements in the microfluidic device is comparable with that in the optical cuvette. The same applies for DLS measurements with the protein *Pf*GST (Glutathione s-transferase from *Plasmodium falciparum*, **[102]**), received from **RAPHAEL EBERLE** (University of Hamburg). Here the ACF obtained from DLS measurements within the CrystalFormer HT was compared with a measurement in a Terazaki-plate under oil (see **chapter 3.5**). Both ACF are nearly identical. This also shows that the application of DLS for measurements within this device is not limited to model proteins such as lysozyme.

Based on these results it is clear that DLS measurements within the CrystalFormer HT are not only possible but qualitatively equal to those in optical standard environments. From this point on the next step was to investigate crystallization processes within the microfluidic device *in situ* by DLS. It was chosen to investigate the crystallization of lysozyme at three different conditions (1 M NaCl,

0.6 M NaCl and 50% PEG 400). Measurements were prepared as described above but continued at position 1 on the selected channel for at least 60 hours.

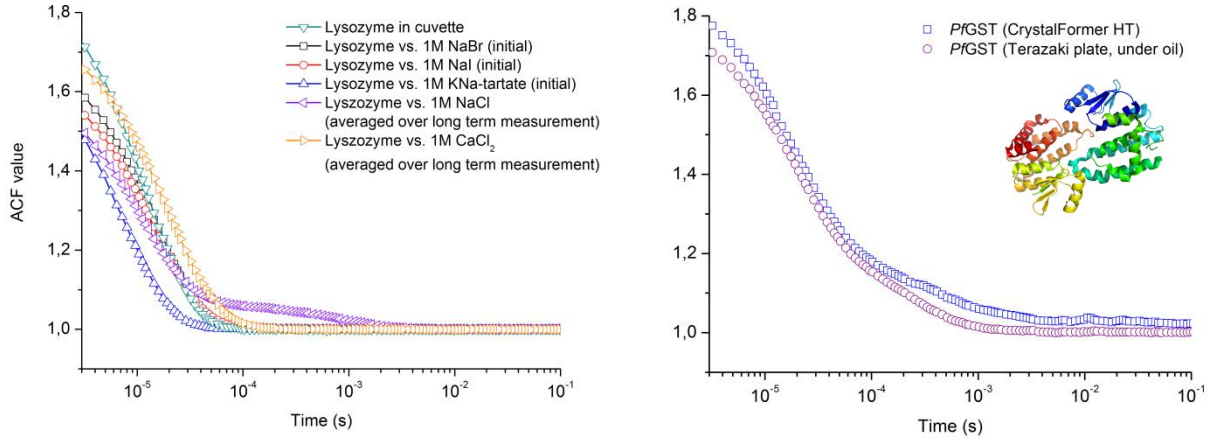

Figure 13: ACF obtained by DLS measurements in the CrystalFormer HT. On the left hand side different conditions of lysozyme are compared with an ACF of lysozyme obtained from measurements in an optical cuvette. On the right hand side the ACF of *Pf*GST (protein expressed and purified by **RAPHAEL EBERLE,** its structure is displayed as a cartoon plot on the right hand side, PDB-accession code: **1PA3, [102]**) in the CrystalFormer is compared with the ACF of the same protein in Terazaki-plates under oil.

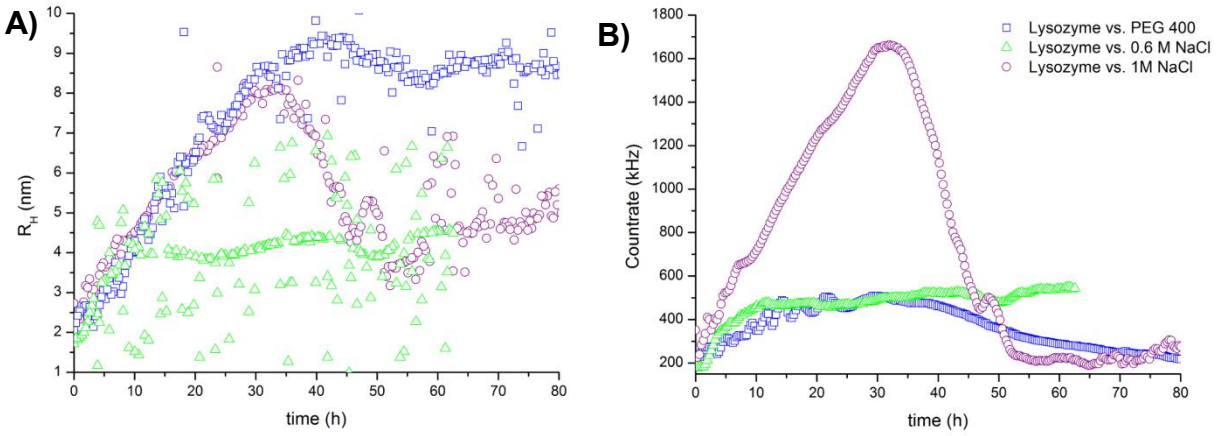

Figure 14: Results of *in situ* DLS monitoring of crystallization experiments within the CrystalFormer HT. A) an overlay of the development of radius distribution over time for the three conditions is shown. B) the corresponding pseudo-SLS measurements.

(A) Lysozyme vs. 1 M NaCl: Lysozyme (95 mg/mL) was crystallized within the CrystalFormer HT against a solution containing 1 M NaCl solved in the lysozyme buffer (250 mM NaOAc/HOAc, pH 4.75). 1 M NaCl was chosen because in previous crystallization experiments in 96-well plates and cell culture plates this was the condition that in most cases resulted in the growth of lysozyme crystals. DLS was recorded within the *Spectro*LIGHT 500 at position 1 during 80 h. Whilst this period

the solution at the selected point was monodisperse with only one particle species in solution. The R_H of lysozyme increased rapidly from approx. 2 nm to a maximum of 8.4 nm after 32 hours (for the development of R_H see **Figure 14 A**, violet circles). Within the next 20 h the hydrodynamic radius decreased nearly as fast as it previously increased: the R_H after 51 hours was just 3.5 nm. From 51 to 80 h of the observed experiment R_H increased to about 5 nm but being at the same time fluctuant, changing from measurement to measurement. Increase and decrease, similar in the time range as for the R_H, could also be observed for the intensity of scattered light (see **Figure 14 B**): Initially a countrate of 250 kHz was recorded. A maximum of countrate (~ 1700 kHz) was observed after approx. 30 – 32 hours. After 32 hours the countrate decreased within 14-16 hours from 1700 kHz to approx. 220 kHz and remained more or less constant for the next 12 h. Between hour 62 and 74 the countrate increased slightly to 300 kHz then it finally decreased again to a final value of approx. 200 kHz after 80 hours.

Developments of countrate and R_H in the course of this experiment are typical for an occurring crystallization and are in concordance with theoretical considerations (see **chapter 3.1**) and experimental results obtained previously by **AARON STREETS [93]**. The diffusion of NaCl leads to stronger attractive interaction between protein molecules in solution.

Since the R_H depends on protein concentration, protein size and solution properties and the first two are assumed to be constant throughout the experiment changes of R_H are due to changes of solution properties. Since R_H is inversely proportional to the diffusion coefficient *D* (**EQ 1**) and it is known **[61]** that *D* will become smaller if there is an increase of attractive protein-protein interactions, the correlation of increasing NaCl concentration and increasing R_H for lysozyme becomes clear. On the other hand decreases the lysozyme concentration during crystallization whereas the NaCl concentration increases further. The R_H decreases, this means that the change in $c_{protein}$ is dominates of changes of k_D during crystallization. The fluctuations in R_H visible after approx. 47 h can be explained by fluctuations in protein concentration due to crystallization along the capillary or in the protein or precipitant reservoir relatively far away from the point of measurement causing a local protein concentration gradient and a flow of protein molecules and thus a local change of protein concentration.

(B) Lysozyme vs. 0.6 M NaCl: Experimental procedures were the same as for the experiment with 1 M NaCl. A 0.6 M NaCl solution in NaOAc/HOAc buffer was used. The lower NaCl concentration should shed light on the precipitant concentration dependence of R_H and countrate development during a crystallization experiment. DLS was recorded *in situ* for 65 hours. As in the experiment with 1 M NaCl R_H increased rapidly with time: from 1.72 nm at t_0 to 4.13 nm after 10 h of incubation (see **Figure 14 A**, green triangles). Within the next 55 hours only a slight increase of R_H to 4.6 nm could be observed. Moreover fluctuations of R_H occurred. Whilst the majority of the measurements yielded values of R_H that did not deviate from a range of 4 – 4.6 nm frequently R_H were recorded much smaller (down to 1 nm) or bigger (up to 7 nm). These fluctuations may be associated with deviations from ideal diffusion. However, within these 65 hours of observations no peak of R_H as for crystallization with 1 M NaCl could be observed. The slight increase of R_H after 10 hours reflects an on-going increase of NaCl concentration. The NaCl concentration present after 65 h was more or less equal to that present in the 1 M NaCl experiment after approx. 10 to 11 hours (R_H = 4.6, t = 10.5 h). The R_H can be used for comparison of NaCl concentration since all other parameters of the experiment have been kept the same. This NaCl concentration present after 10 – 11 hours (1 M NaCl experiment) and 65 hours (0.6 M NaCl experiment) does not result in a supersaturated lysozyme solution. Crystals only grew in the 0.6 M NaCl experiment about one week after *in situ* DLS was finished. Within the 65 hours there was no peak in R_H since no crystallization occurred yet. This demonstrates that the measured R_H is highly sensitive to changing precipitant concentrations and that DLS can be used to compare precipitant concentrations at different points in time in counter diffusion experiments.

The development of the intensity of scattered light over time for this experiment (see **Figure 14B**, green triangles or **Figure 15** for details) was analogous to the development of R_H: a strong increase within the first 10 – 12 hours (from approx. 175 kHz to 475 kHz) of measurement followed by a slight increase in intensity in the following 55 hours of observation. Fluctuations in the countrate could be observed, but not as strong as in the radius distribution. Other than in the previous experiment with 1 M NaCl there is no clear peak in the countrate. In conjunction with the radius development this is a clear sign for no supersaturation at any point of measurement within the observed period of time.

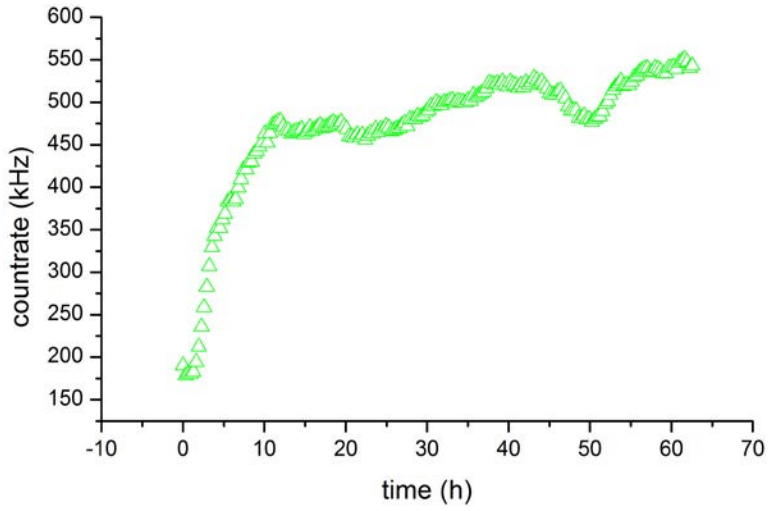

Figure 15: Detailed view on the development of the intensity of scattered light in case of the crystallization experiment of lysozyme vs. 0.6 M NaCl.

(C) Lysozyme vs. PEG 400: Lysozyme was crystallized against a solution containing 50 % PEG 400 (v/v) in 0.2 M sodium citrate (pH 4.5). The solution was obtained from a counter diffusion training kit (Triana, Spain) and thus it was verified that this solution will crystallize lysozyme with a high probability. DLS was recorded at position 1 for approx. 80 hours (see **Figure 14**). Throughout the 80 h a monomodal solution was present. The R_H of the particles in solution increased from initially 2 nm to approx. 9 nm after 80 h. The increase occurred rapidly during the first 30 h. From hour 30 to 60 a slight decrease of R_H could be observed and during the last 20 h it remained nearly constant.

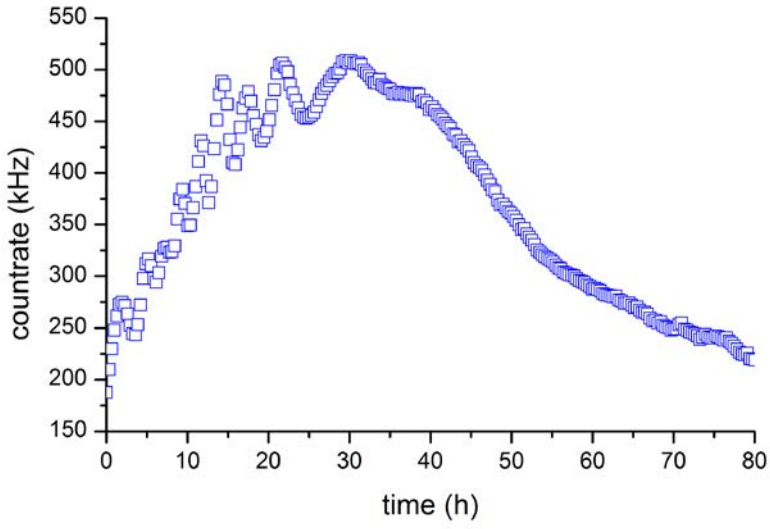

Figure 16: Detailed view on the development of the intensity of scattered light in case of the crystallization experiment of lysozyme vs. 50% (v/v) PEG 400.

Intensity of the recorded scattered light increased during the first 30 h from 250 to 500 kHz (see **Figure 16**). From 15 h to 30 h sinus like fluctuation of the intensity could be observed. After 30 h the intensity decreased to approx. 300 kHz within 20 h. Within the last 30 h of measurement it decreased further to 200 kHz. Observation of the channel after 80 hours revealed that crystals had grown not within the channel but close to the point of measurement within the lysozyme reservoir (**Figure 17**).

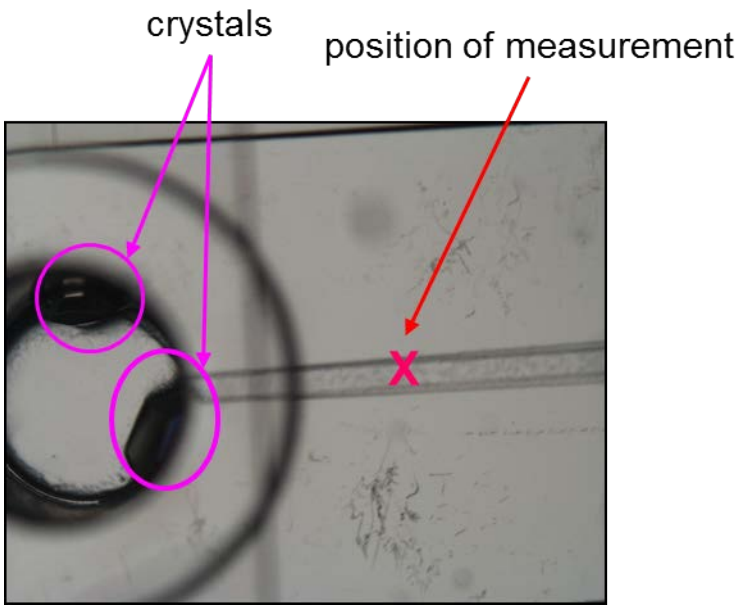

Figure 17: Lysozyme crystals grown in the protein reservoir of the CrystalFormer HT during crystallization with 50% (v/v) PEG 400 as precipitant.

The initial increase of both R_H and countrate can be explained by the diffusion of precipitant along the capillary, as it was described above for the experiments with 1 M and 0.6 M NaCl. Increasing concentration of PEG 400 cause increased R_H and countrate for two reasons: first, the higher viscosity of the PEG solution in comparison with the lysozyme solution in buffer and second, PEG mediates attractive interaction between lysozyme molecules. Since a change of viscosity leads to slower particles these appear to be bigger than they actually are: in the Stokes-Einstein equation used by *SPECTRO* the viscosity is kept constant. A smaller diffusion coefficient *D* reflects directly in a bigger R_H. This change of viscosity on the other hand does not explain the increasing countrate since the intensity of scattered light is independent of the viscosity and only coupled with the concentration and size of molecules in solution. On the other hand acts PEG 400 as precipitant: it causes attractive interaction between lysozyme molecules. Both countrate and R_H are sensitive to changes in the protein-protein and protein-solutes interaction. Thus an

increase of protein-protein interaction leads to increased countrate and R_H. After the onset of crystallization protein molecules are built into the growing crystals and are no longer in solution: the protein concentration decreases. This decrease in concentration causes the decrease in countrate. The R_H depends on protein size, protein concentration and solution properties (see **chapter 1.7**and **3.1**). Since the PEG 400 concentration stays constant after 1.5 days or increases slowly to 50% (v/v) the viscosity of the solution remains constantly high in comparison to a solution of lysozyme in its buffer. The apparent R_H depends strongly on the viscosity and due to this, decreases only slowly or rather remains constant after 30 h. This comes clear when comparing the development of R_H with that of the experiment with 1 M NaCl as precipitant (**Figure 14**). For the latter case R_H decreases after approx. 30 h from 8 nm to approx. 4.5 nm after 55 h. The increase of viscosity for a 1 M solution of NaCl is only small compared with 50% PEG 400 thus changes in protein concentration and protein-protein interaction are more visible in the experimental data in the case of NaCl. It also shows that for a correct interpretation of *in situ* DLS experiments both development of intensity of scattered light and R_H have to be analyzed.

3.3.4. Conclusions

It could be shown for the first time that DLS measurements within the CrystalFormer HT are possible and that the quality of these measurements is comparable to that of DLS in conventional optical cuvettes. Moreover it could be shown that it is possible to follow the crystallization process in situ within this microfluidic device. In the course of the DLS monitoring results obtained by **AARON STREETS [93]** could be verified and new insights into the processes that occur when salt is replaced by PEG as precipitant could be gained.

It is now clear that by the observation of crystallization processes one can distinguish between supersaturation/crystallization and undersaturated conditions within microfluidic crystallization environments even if no nuclei can be observed (as was demonstrated for vapor diffusion in **chapter 3.1**). This is important because the appearance of nuclei in the radius distribution is considered to be a clear sign of too harsh crystallization conditions **[63]**.

3.4. DLS in 96-Well Plates

3.4.1. Introduction

The most common crystallization plates today have a SBS-footprint **[100]** and are designed to screen for 96 precipitant conditions. These plates can have one, two or three crystallization wells per precipitant reservoir and are optimized for automated high-throughput screening (**HTS**) **[19-21, 23, 103-106]** vapor diffusion crystallization applying pipetting robots. In our lab a Honeybee 961 robot (Genomic Solutions, USA) is used to set up crystallization plates. For robotic screening with a total volume of 600 or 1200 nL applying the Honeybee 961 the NextalQia1 plate (Qiagen, Germany) was used. The bottom of its wells is conical hence even at nanolitre volumes the crystallization drop is always situated at the same place. This is important for the automation of imaging and *in situ* DLS as well as for the reproducibility of experiments.

The other 96-well plate finally used for *in situ* DLS experiments is the MRC Crystallization Plate™ (**MRC**, Swissci, Switzerland). As the NextalQia1 it has two crystallization wells per precipitant reservoir. Its wells are hemispherical und thus were not suitable for HTS with the Honeybee robot. They were chosen for manual pipetting and buffer screening since the design of the plate seemed promising for *in situ* DLS.

First DLS experiments within 96-well plates (Nextal Qia1) have been carried out by **ARNE MEYER [92]** showing that it is possible to get an ACF from measurements in small sitting droplets. On the other hand these first experiments showed a non-satisfactory signal-to-noise ratio and the countrate was low in comparison with measurements in cuvettes or culture plate hanging drops. This was especially the case if the wells were sealed with tape, necessary to prevent evaporation of the drop. Without the tape signal-to-noise ratio was better but experiments could only be carried out for a few minutes until the drop fell dry.

Besides the mentioned plates other plates from manufacturers such as Corning or Greiner have been tested but no good DLS signal could be obtained. Since also the first experiments using the NextalQia1 were not promising focus was laid on the MRC-1 plates.

One reason for the unsatisfactory DLS measurements within the wells of a NextalQia1 plate were the geometrical properties of the plate. Each two well – one

reservoir compartment (named **2W1R**) is separated from the next by relatively high walls close to the wells. Since the *Spectro*LIGHT 500 uses not an x-y-stage but a rotating table with polar coordinates for positioning of the laser and the optics the relative position of laser and detector on a well varies depending on the position of the well on the plate. Hence not on all wells of the plate *in situ* DLS measurements are possible because either laser or detector are blocked by the high walls. Since the body of the MRC plate does not come with high walls between the 2W1R compartments it was thought that these plates would be best for in-depth *in situ* DLS analysis of vapor-diffusion crystallization.

3.4.2. Materials and Methods

Both the NextalQia1 and MRC are 96 reservoir, 192 well crystallization plate with SBS footprint **[100]** designed for high throughput crystallization. For *in situ* DLS observation of crystallization experiments between 0.6 and 1.5 µL protein solution were mixed with equal amounts of precipitant unless noted else. The reservoir was filled with 40 – 80 µL of precipitant solution. In the case of additive or buffer screening the reservoirs were either kept empty or filled with 90 µL paraffin oil to prevent shrinkage of the drop due to evaporation during long-time experiments. The wells were always sealed with AMPLIseal (Greiner Bio one, Germany) to prevent evaporation of the drop.

For initial experiments 2 µL of hen egg-white lysozyme (Merck, Germany, 45 mg/mL in 250 mM NaOAc/HOAc buffer, pH 4.75) were filled in both wells of a 2W1R compartment on a MRC plate. The reservoir was filled with 50 µL of the protein buffer and the 2W1R compartment was sealed with tape to prevent evaporation. The plate was inserted in the *Spectro*LIGHT500 and the plate type “MRC1” and the wells containing the protein solution were chosen from the database. The laser beam was positioned within the first well and by variation of x-, y- and z-coordinates laser beam and (virtual) detector position were brought into accordance. Then DLS measurements were recorded.

For *in situ* DLS monitoring of crystallization experiments instead of protein buffer 40 – 80 µL of precipitant solution were pipetted in the reservoir and in the well protein solution was mixed with precipitant to yield a final drop volume ranging from 1 – 4 µL. Besides lysozyme the Erv1-fragment ΔN (FAD-binding sulfhydryl oxidase,13.4 kDa, received from **KYRIAKOS PETRATOS**, IMBB-FORTH, Crete, Greece,

in the terms of a research collaboration) was used in initial *in situ* DLS studies in MRC1 plates.

For integration of *in situ* DLS in the evaluation of high throughput crystallization experiments a NextalQia1 plate was filled by a Honeybee 961 (Genomic Solutions, USA) robot: 600 µL protein (lysozyme, Merck, Germany, 45 mg/mL in 250 mM NaOAc/HOAc buffer, pH 4.75) were mixed in each well with 600 µL precipitant (columns 1-6 of the plate: 500 mM NaCl; columns 7-12: 1 M NaCl). Each reservoir was filled with 60 µL of the respective precipitant solution. The laser beam was positioned within the first well and by variation of x-, y- and z-coordinates laser beam and (virtual) detector position were brought into accordance. This was repeated in all 96 wells. An autopilot file was written (Python script, see **Appendix, chapter 9.1**) and automated measurements started in all 96 wells.

3.4.3. Results and Discussion

Else than in preliminary experiments within the wells of NextalQia1 plates the laser trace was good visible during positioning of laser and detector within the first well of the MRC plate. From this point it was clear that in well 1 the laser beam was not blocked by the plate. Positioning however was challenging since due to the round drop surface distorted signals were obtained in most parts of the drop. The position chosen was close to the side of the drop (see **Figure 21A**). DLS was then recorded and a good ACF with an intercept of approx. 1.7 could be obtained. Radius distribution showed that the solution was monomodal with a R_H of 2.1 nm and being in good concordance to that measured in an optical cuvette (R_H: 1.8 nm) (see **Figure 18**). In the course of the preparation of *in situ* DLS measurements to investigate membrane protein interaction (see **chapter 6.3.2**) DLS was measured in wells of the MRC plate to see if a good signal can be obtained in the case of membrane proteins and investigate the protein quality prior to further experiments. Since these proteins are solved in a detergent containing buffer they tend to form a flat surface rather than round droplets. CD82 **[107]** a human membrane protein from the tetraspanin family (see **chapter 6.1**) was cloned and expressed in yeast cells and received as purified protein from **NICKLAS BONANDER** (Aston University, UK, OptiCryst). Two different preparations of CD82 (each 1 µL) were pipetted into wells of a MRC plate, measurements were carried out as described above.

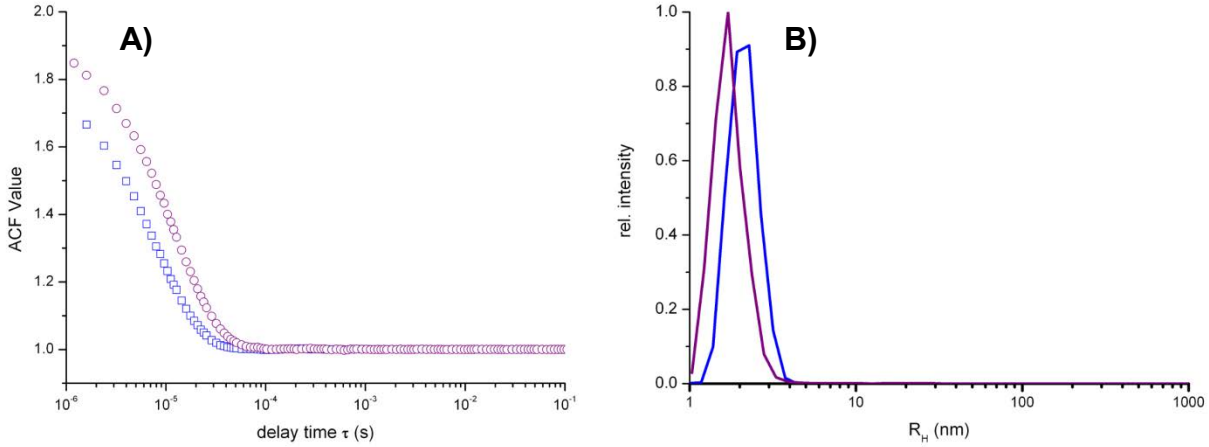

Figure 18: First DLS measurements in a MRC plate (blue boxes / blue line) compared with a measurement of the same protein solution in an optical cuvette (purple circles / purple line). A) The ACF is of good quality in the case of DLS in a small droplet though the intercept is higher when DLS is measured within a cuvette. B) Small differences are also visible in the radius distribution. But it is clear that the obtained results deviate not too much from that within a cuvette.

The results of *in situ* DLS (**Figure 19**) show that even in the case of extremely flat droplets containing detergent solution valid measurements can be carried out. Moreover does the ACF show that the quality of measurement in the case of CD82 is even better than for lysozyme. Further measurements showed that DLS can be measured within all wells of a MRC plate and that the quality of measurements does not deviate too much from measurements within optical cuvettes. The possibility to measure DLS within the MRC was exploited for buffer screening (see **chapter 5.2.1**) and to investigate membrane protein interaction and oligomerization (**chapter 6.3.2**).

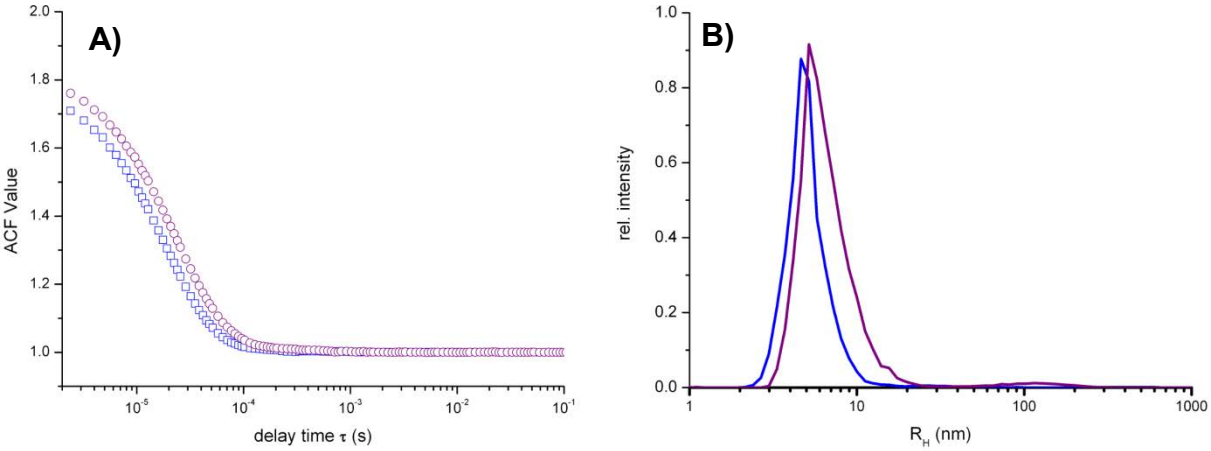

Figure 19: *In situ* DLS within small (1 µL) droplets of the CD82 preparations X (blue) and Y (purple).Even though the solutions formed no droplet but a thin flat layer covering all the protein well good DLS measurements were possible, as can see from the ACF of both solutions (A). The obtained R_H between 3 and 4 nm (B) is in concordance with a monomer in solution (29.6 kDa protein in β-OG micelles).

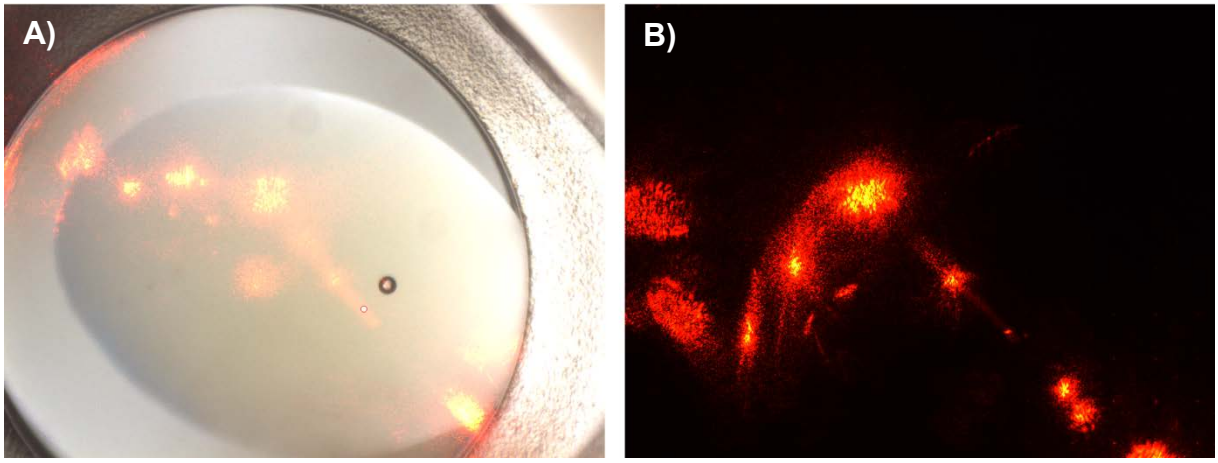

Figure 20: DLS measurements within a well of a MRC plate. A): under white light illumination to show well and drop, B): real conditions, reflections of the laser on the round surface of the droplet are visible but the trace through the drop itself remains undisturbed.

3.4.3.1. *In situ* DLS to Monitor Crystallization Experiments

Based on the previously described experiments to prove that DLS measurements in small droplets in the MRC plate are possible crystallization experiments were set-up to be monitored by DLS. In well A1_2 (second well of the 2W1R compartment A1) of a MRC plate 1.5 µL lysozyme was mixed with 1.5 µL NaCl solution (1 M, both in 250 mM NaOAc/HOAc buffer, pH 4.75), the reservoir was filled with 50 µL of 1 M NaCl solution in the same buffer. Measurements were started right after the introduction of the plate into the *Spectro*LIGHT500. First a series of measurements (10x20 s) was recorded to monitor the initial radius distribution. The experiment was then monitored by DLS over a period of 50 h (see **Figure 21 A**), all five minutes a measurement of 20 seconds length was recorded. The initial R_H of lysozyme is with approx. 2.5 nm larger than that for lysozyme alone (1.9 nm). This is caused by the initial NaCl concentration of 0.5 M. Addition of any soluble molecule, such in this case NaCl, changes the chemical potential in solution **[108, 109]**. Moreover attachment of chloride and sodium ions to the surface of the protein can result in protein-salt-protein bridges. This yields at certain concentrations to attractive interactions between protein molecules. The motion of particles in solution is not anymore purely Brownian. This is represented in the diffusion coefficient *D* and hence in the R_H derived by DLS measurements (**EQ 1**). With increasing salt and protein concentration caused by vapor diffusion R_H increases further from 2.5 nm to 3.2 nm within 24 hours. Then, as expected in the case of nucleation and growing crystals (see **chapters 3.1** and **3.3**) R_H remains constant and decreases slightly within the next 10

hours to a R_H between 3 and 3.1 (see **Figure 21 A**). After approx. 35 h the results of DLS start to get diffuse this is either caused by a diffusion gradient due to crystal growth close to the point of measurement or because large nuclei are diffusing through the point of measurement causing distortions of the signal.

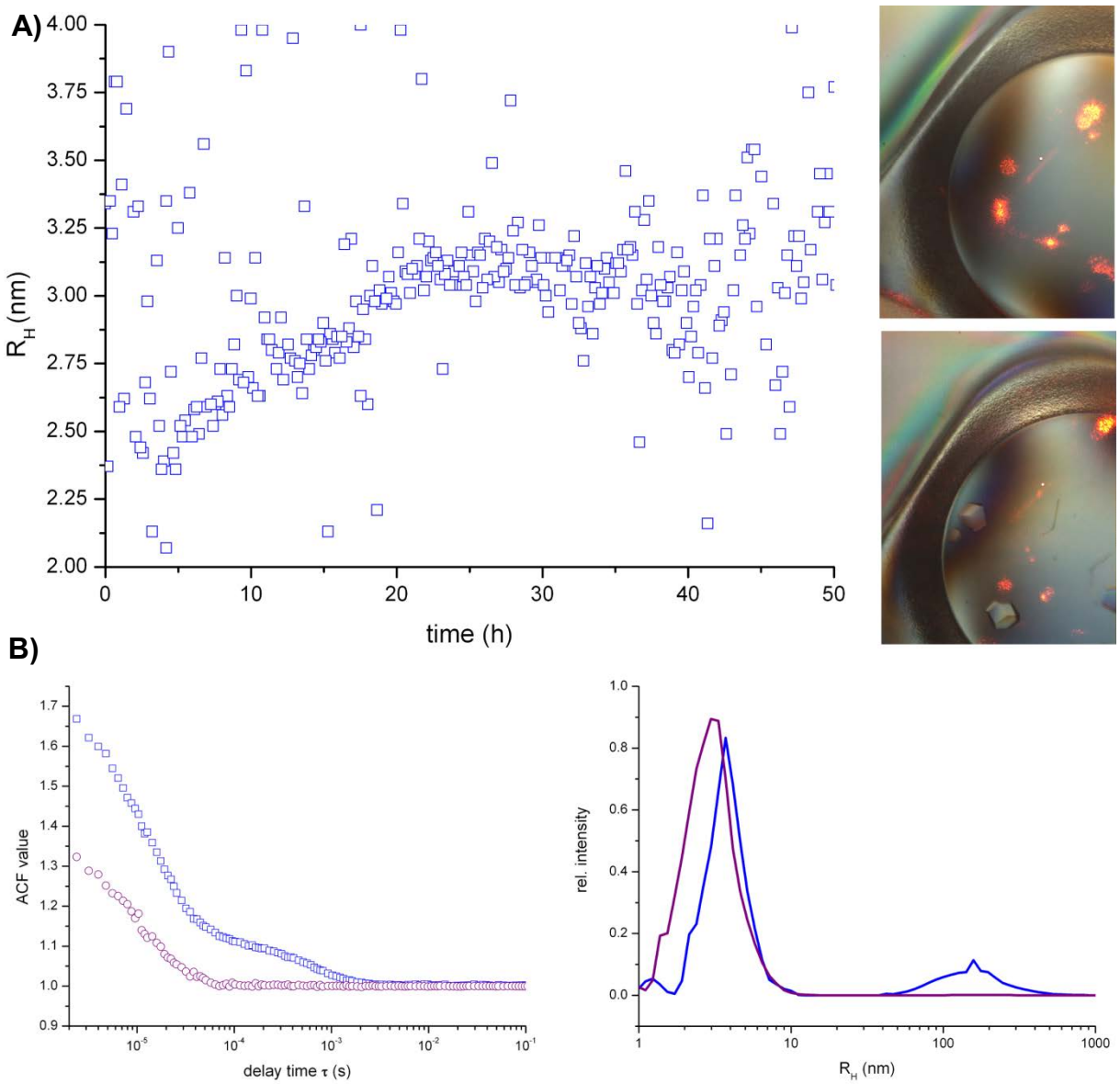

Figure 21: *In situ* DLS monitoring of a crystallization experiment. A) left hand side: development of radius distribution of monomeric lysozyme over time under vapor diffusion crystallization. Right hand side: drop before crystallization with DLS laser (upper image) and after 50 hours with crystals of lysozyme being visible (lower image, at different position to enable DLS measurement. B) ACF and radius distribution of the monitored drop before (blue boxes) and after (purple circles) crystallization. The reduced protein concentration leads to a lower R_H of the monomer after crystallization.

Evaluation of the droplet after DLS monitoring shows that crystals grew under these conditions (see **Figure 21 A**). A comparison of DLS results before and after crystallization (**Figure 21 B**) showed that the nucleation peak at 100-200 nm in the

radius distribution in the initial measurement is not present after crystallization. Moreover is the monomeric R_H after crystallization approx. 1 nm smaller than in the initial series of measurement. This is related to the reduced protein concentration after crystallization. In comparison with results obtained from similar experiments in the CrystalFormer HT (see **chapter 3.3.3**) or in Linbro plates (see **chapter 3.1**) the small increase of R_H during the crystallization experiment attracts attention. An explanation might be that nuclei formed directly after addition of NaCl to the protein due to local super saturation. These nuclei withdrew protein from solution and the lower protein concentration then led to lower R_H.

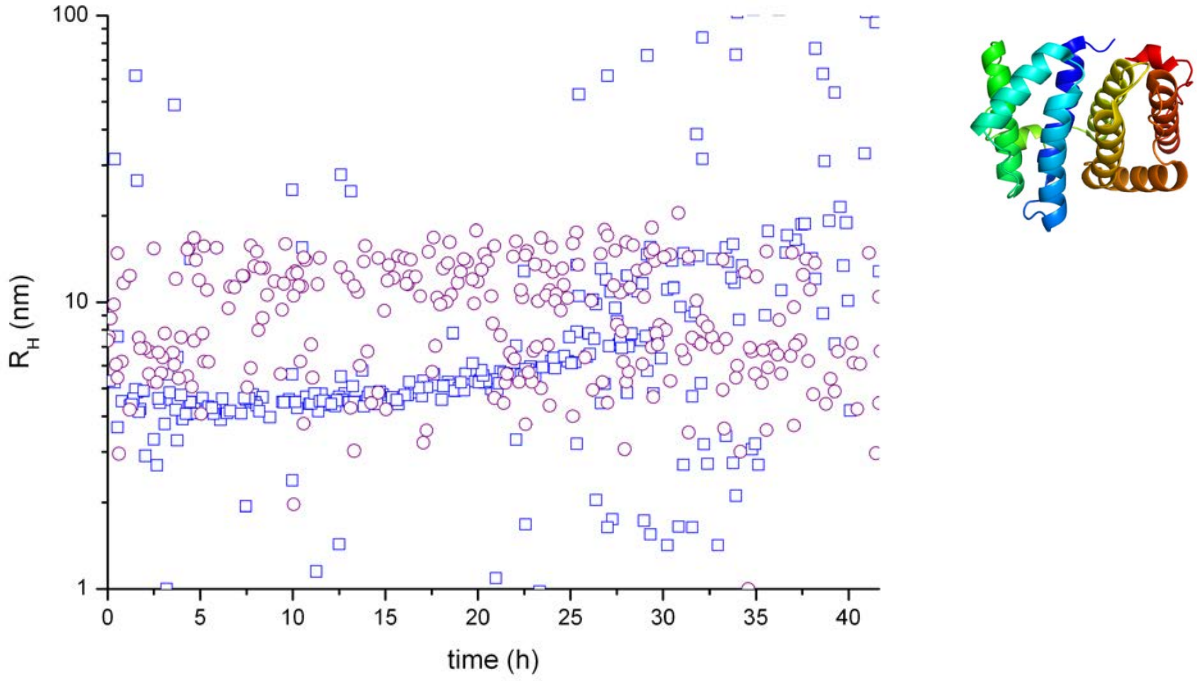

Figure 22: *In situ* DLS monitoring of two crystallization experiments with ΔN. In both cases a mixture of 8% (w/v) PEG 4000 and 100 mM ammonium sulfate was used as precipitant. In the experiment represented by boxes in the radius distribution 1.7 µL protein was mixed with 0.7 µL precipitant. In the experiment represented by circles a mixture of equal amounts of protein and precipitant was used. The cartoon plot in the upper right side displays the structure of a sulfhydryl oxidase similar to ΔN (PDB-accession code: **2HJ3**).

In **Figure 22** *in situ* DLS monitoring of two crystallization experiments of ΔN (FAD-binding sulfhydryl oxidase,13.4 kDa, received from **KYRIAKOS PETRATOS**, IMBB-FOTH, Crete, Greece, in the terms of a research collaboration) is shown. In both experiments the same precipitant solution was mixed with protein (8% (w/v) PEG 4000, 100 mM ammonium sulfate). The only difference is that in one well (blue boxes) 0.7 µL precipitant solution was added to 1.7 µL of protein whilst in the other well (purple circles) equal amounts of protein and precipitant were mixed.

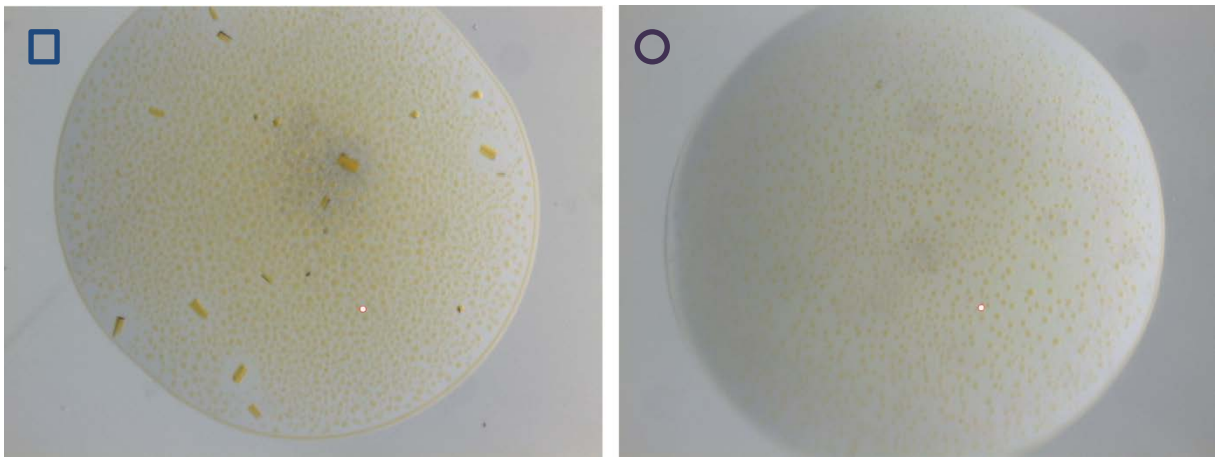

Figure 23: Results of crystallization experiments of ΔN that were monitored by DLS (**Figure 22**).Crystals could only be obtained in the case of boxed (left). In the case of circles (right) only phase separation is visible.

It can be seen that the R_H of the latter case is > 10 nm and shows a broad distribution. In the other case the radius distribution is narrow in the first 25 hours and grows constantly from approx. 5 nm to 7-8 nm. After 25-27 hours also this radius distribution becomes broader and some nuclei can be monitored (at R_H > 100 nm, omitted in the figure) by DLS. This difference in DLS between both monitored experiments corresponds with the macroscopic results of the experiment (**Figure 23**): only in the experiment represented by blue boxes grew crystals (next to phase separation) whilst in the other case only phase separation could be observed. Applications of *in situ* DLS monitoring of crystallization experiments within the MRC plate are also described in **chapter 6.2.1**.

For in situ DLS measurements within the wells of a NextalQia1 plate filled by a Honeybee 961 robot, laser and detector position were adjusted manually in all 96 wells**.** After adjustment DLS was measured in these wells. **Figure 24** shows the results of two of these measurements. In both wells lysozyme (45 mg/mL) was mixed with an equal volume of NaCl (0.5 M) solution. A shoulder – typical sign of a bimodal solution – is visible in the ACF in the DLS measurement right after preparation of the crystallization experiment. Even though the experiment was set-up by a pipetting robot and the DLS positions were adjusted carefully the ACF are not identical, indicating that even with high accuracy statistical errors cannot be avoided in crystallization. However, after 14 days (no macroscopic crystals grew in neither droplet) both ACF are nearly identical showing that DLS positioning and robotic pipetting were indeed carried out accurately.

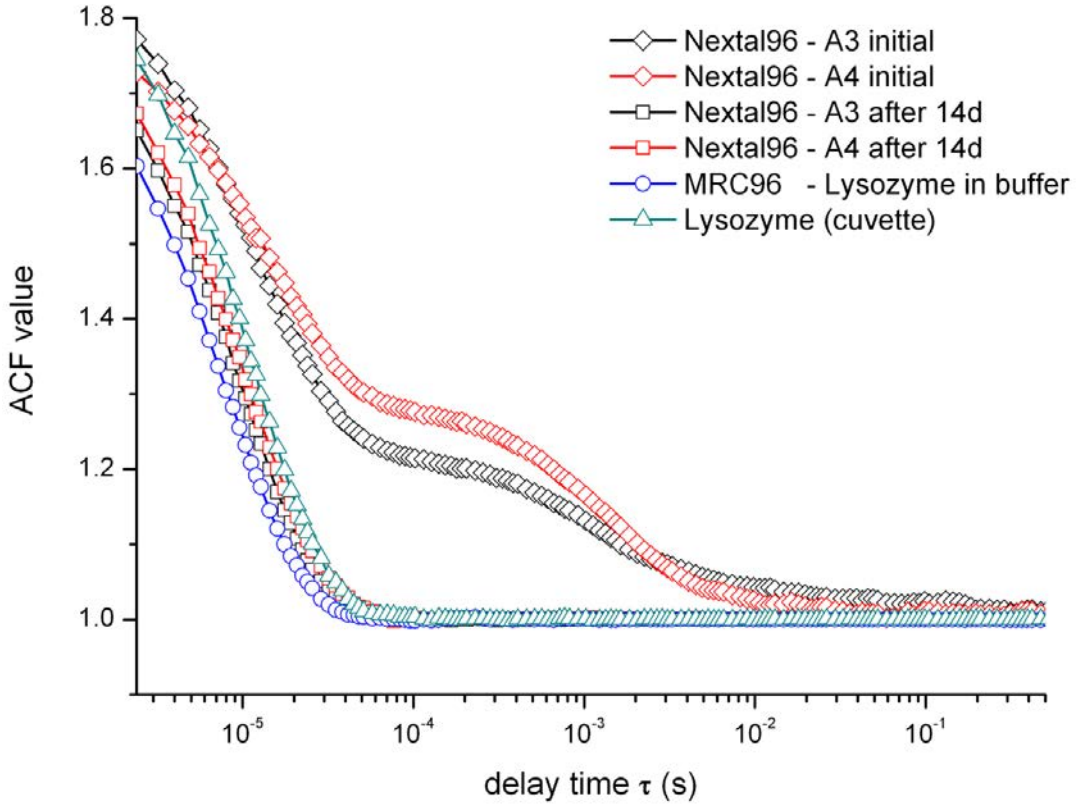

Figure 24: DLS measurements within wells A3 and A4 of a NextalQia1 plate (boxes) in comparison with measurements in a MRC plate (circles) and in an optical cuvette (triangles). Also displayed are results from *in situ* monitoring of crystallization (diamonds, initial) in the same wells of a NextalQia1 plate.

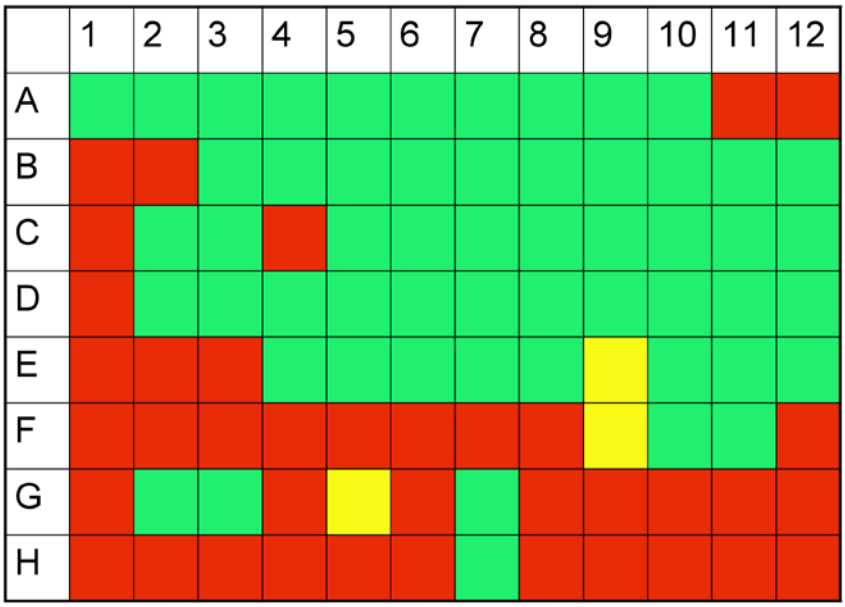

Figure 25: Schematic drawing of a NextalQia1 plate showing in which positions DLS measurements in droplets (1.2 µL volume) are possible (green), restricted (yellow) and not possible (red).

A comparison with DLS measurements in a MRC plate and a cuvette shows that the quality of DLS within the NextalQia1 plate at well A3 and A4 is a bit better as in a MRC plate and not as good as in an optical cuvette. **Figure 25** shows – based on the DLS measurements carried out – in which of the wells of a NextalQia-1 plate DLS measurements are possible (green). In the other wells DLS measurements are restricted (E and F9, G6) or impossible. DLS measurements are impossible when laser or detector is blocked by the high walls separating the 2W1R compartments within this type of plate. When using smaller volumes (< 1.2 µL) DLS will become impossible in nearly all wells. The distribution of red on the plate indicates a problem stemming from the polar stage. Since the relative position of laser and detector to the walls varies due to the way positioning is carried out by the stage not all wells are affected from blocking of the DLS optics. To overcome this problem the polar stage – being beneficial in the case of capillaries – should be coupled with a x-y-stage that would allow better measurements in the case of plates such as the NextalQia1.

3.4.4. Conclusions

It could be shown for the first time that valid DLS measurements in droplets in 96well plates such as the MRC plate are possible. This is important since 96well plates are the plates used most for high throughput protein crystallization. Moreover it could be shown that monitoring and scoring of *in situ* DLS measurements in such plates is possible. Furthermore for the first time DLS measurements could be carried out in crystallization droplets within a NextalQia1 plate that were prepared by a pipetting robot. It was assessed in which wells DLS measurements are possible and in which not.

3.5. DLS under Oil

3.5.1. Introduction

Besides vapor diffusion **[110]** and counter diffusion/free interface diffusion **[96, 111]** the microbatch approach **[112-114]** is the third major method for protein crystallization. Other than for conventional batch methods crystallization volumes used are comparable to that in vapor diffusion approaches. Robots are available for high throughput screening applying the microbatch method **[114, 115]**. Usually the system during crystallization under microbatch conditions is sealed with paraffin oil to prevent evaporation. A combination of microbatch and vapor diffusion conditions can

be achieved by replacing paraffin oil with other oils that are permeable for water vapor **[112]**. Most known is the commercially available “Al´s Oil”, a 1:1 mixture of paraffin oil and silicone oil. In this chapter the application of in situ DLS towards both methods will be described. So far no DLS monitoring of droplets in microbatch plates had been reported.

Interesting about the DLS monitoring within microbatch plates under oil is the fact that the droplets are contained in a stable environment. If pure paraffin oil is used the drop size will be stable for weeks and thus a once adjusted DLS signal will be stable for a very long time. Any change of the recorded ACF can hence be attributed to changes in the drop making DLS results very reliable. Furthermore the oil layer forms a flat surface that should cause no distortions of the laser light (as it is the case with the laser on the round surface of sitting drop vapor diffusion droplets). The path of light through the oil towards onto the round drop bears not such a strong risk of distortions and flares that can deteriorate the DLS signal since the refractive index of paraffin oil (1.47, **[116]**) and water (1.33, **[117]**) differ not as much as it is the case between water and air (1.00). Another reason for expected good results of light scattering experiments within droplets under oil is that most of the dust that always resides on a plate is adsorbed in the oil layer, since the oil is poured onto the plate prior to the protein droplets. Moreover the remaining dust in the system will be enriched over time in the viscous oil rather than in water.

3.5.2. Materials and Methods

For initial experiments lysozyme (Merck, Germany, 2 µL, 45 mg/mL in NaOAc/HOAc buffer pH 4.75) was centrifuged at 16’100 x *g* for 30 minutes and pipetted manually into wells of a Terazaki plate (Nunc, Denmark). The plate was treated previously with paraffin oil (Applichem, Germany) in a way that all wells were filled with oil. Measurements were carried out using a custom designed adaptor for the *Spectro*LIGHT 500. The optical head was moved relatively to the plate in order to obtain a valid DLS signal in a similar manner as described for the adjustment of measurements in the case of 96 well plates. Furthermore *Pf*GST **[102]** (Glutathione s-transferase from *Plasmodium falciparum*, M_W: 25 kDa, PDB accession code: **1PA3**) in its buffer (0.1 M Tris pH 8.0, 10 mM glutathione) was obtained from **RAPHAEL EBERLE**, who had expressed and purified the protein, in terms of a collaborative work to analyze protein quality and monitor crystallization. Droplets were prepared as

described for lysozyme. All non-protein solutions were filtered through a 0.22 µm syringe filter (VWR, Germany) prior to use.

3.5.3. Results and Discussion

From the initial DLS measurements in lysozyme solutions within Terazaki plates an ACF typical for monomodal solutions with an intercept of 1.7 could be obtained. Radius distribution analysis showed one particle species in solution with a R_H of 2.2 nm (**Figure 26**).

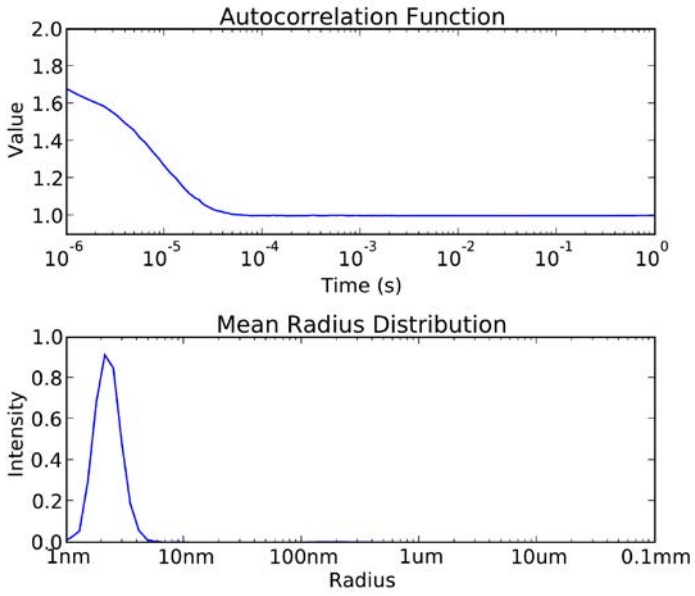

Figure 26: Results of initial DLS measurements within a small droplet under oil in a Terazaki plate. A 45 mg/mL solution of lysozyme was used as sample.

After the possibility to obtain valid DLS measurements within small droplets under oil was assessed, a crystallization experiment was monitored by DLS. 2 µL Lysozyme were pipetted into the well of a pre-oiled Terazaki plate and small volumes of 1 M NaCl solution were added stepwise. Between the additions DLS measurements were recorded.

As can be seen in **Figure 26** the first addition of NaCl (1 µL) led to an increase of protein radius from approx. 2 to 4 nm. After another 1 µL of 1 M NaCl solution was added the monomer radius increases further to approx. 6-7 nm. Moreover a second particle species appears in solution at roughly 90 nm. This second species represents either nuclei or – following the two step nucleation hypothesis **[47]** – the dense mesoscopic phase from which then macroscopic nuclei emerge. After nucleation appeared the drop was diluted by 2 µL of buffer. The second particle

species immediately starts to vanish. However the monomer R_H shows only slow decrease.

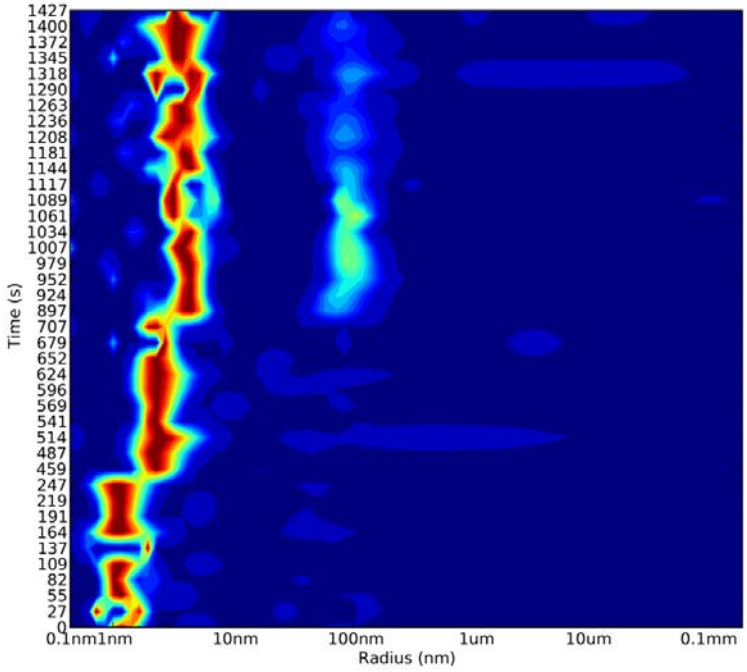

Figure 27: Contour plot of the development of radius distribution over time derived by *in situ* DLS within a Terazaki plate. Stepwise precipitant addition led to stepwise growth of protein monomer R_H. The colors of the contour plot indicate the relative intensity of the particle, with blue being zero and dark red being maximum.

After these initial measurements, automation of DLS within Terazaki plates was achieved (see **chapter 3.6**). Moreover it could be shown that droplets under oil bear ideal conditions for DLS measurements thus this method was used to replace the conventional DLS measurements in optical cuvettes in the case of e.g. buffer optimization. The advantage over MRC plates is that the wells within a Terazaki plate are automatically sealed by the oil. Additionally the straight oil surface reduces flares and laser reflections to a minimum (see **Figure 28**). The crystallization of *Pf*GST **[102]** under batch conditions was optimized for crystallization of the protein in a containerless environment in levitated drops **[118]** in Xi'an, China. In the course of this optimization *in situ* DLS was applied to optimize conditions rationally. In **Figure 29** the results of such an experiment are presented. The clear difference in ACF and radius distribution between pure *Pf*GST and *Pf*GST at crystallizing conditions showed that even if the pure protein is not monomodal in solution the crystallization process could be investigated by *in situ* DLS.

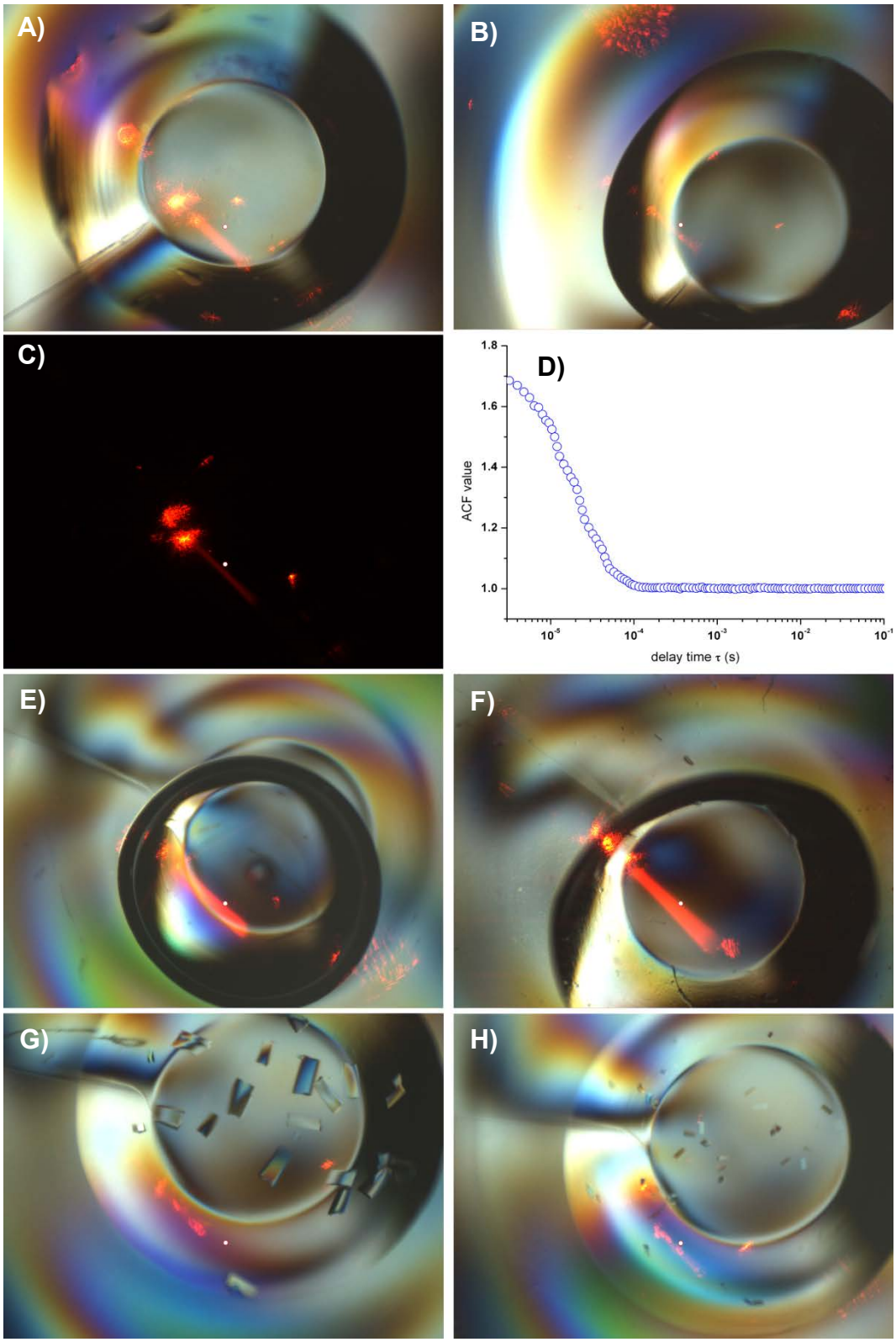

Figure 28: DLS within Terazaki microbatch plates under oil. **A)** and **B)** DLS laser within a normal crystallization droplet. **C)** Laser trace within such a drop without additional illumination, **D)** ACF of an *in situ* DLS measurement within the drop displayed under C), **E)** and **F)** Laser trace in non-perfect droplets. Nearly no flares distortions can be observed, DLS measurements are possible. **G)** and **H)** at the end of an *in situ* DLS monitored crystallization experiment of the protein *Pf*GST. DLS does not influence the crystal growth when applying microbatch under oil conditions.

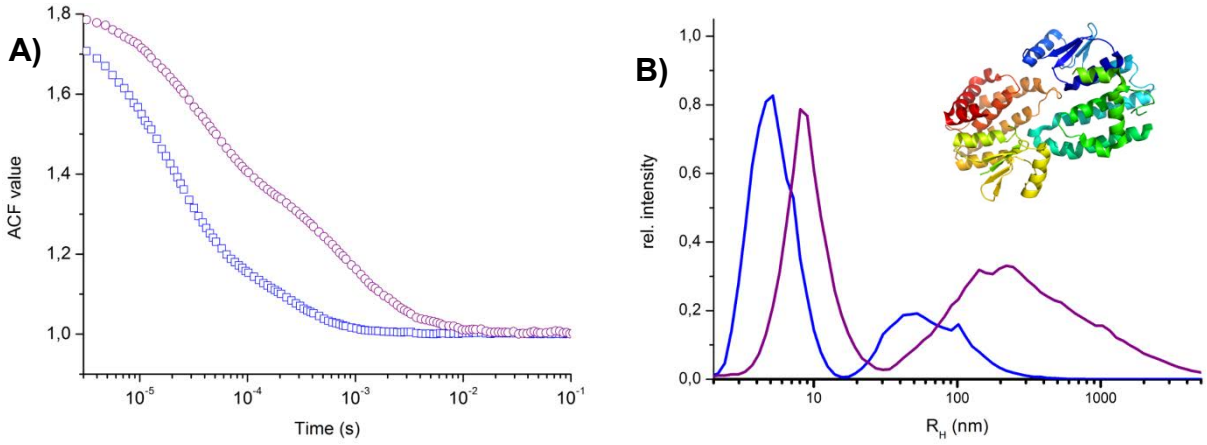

Figure 29: Comparison of ACF (A) and radius distribution (B) of *Pf*GST (the cartoon plot in the upper right side shows the structure of *Pf*GST,) in its buffer (blue, 0.1 M Tris pH 8.0, 10 mM Glutathion) and during crystallization (violet) after mixing 2 µL of ammonium sulfate solution (2.6 M, 0.1 M Tris pH 8.0, 10 mM Glutathion) with 1 µL of *Pf*GST. From this set up crystals grew after 12 hours (see **Figure 28 G**).

3.5.4. Conclusions

It could be shown for the first time that DLS measurements within small droplets under oil in Terazaki plate are possible and can deliver information to optimize the crystallization process. Moreover the quality of DLS measurements in droplets under oil proved to be good enough to replace optical cuvettes or MRC plates in the case of pre-crystallization DLS (e.g. buffer optimization). An example for the application of DLS towards droplets under oil can be found in **chapter 5.3.7**.

3.6. Automation of Measurements

3.6.1. Introduction

For application of *in situ* DLS as a standard method to monitor and score crystallization experiments automation is necessary. The rise of HTS methods results in a huge number of crystallization trials. *In situ* DLS has to have the ability to be applied to many conditions at the same time. The *Spectro*LIGHT 500 was built as an UV/VIS imager with added *in situ* DLS instrumentation **[18, 88, 92, 119]**. It was known that the accuracy of its mechanical components was good enough for imaging purposes. But from initial *in situ* DLS measurements it was clear that occasionally a deviation of just 20 µm could cause a distortion of the DLS signal, hence a much higher accuracy is required. For automated *in situ* DLS monitoring of a 96-well plate for 24 hours and three measurements per well and per hour the plate and optics head would have to move approx. 7'000 times. And even after 7'000 movements the

deviation of measurement position should be as small as possible, preferably < 20 µm. DLS automation was tested for vapor diffusion- (MRC plate) and microbatch crystallization and within the GCB-D.

Automated *in situ* DLS would be possible if a) measurements with many movements and b) with highest precision could be carried out. Requirement a) was tested using a MRC plate and for b) DLS was recorded for two weeks on seven positions along a capillary within the GCB-D.

3.6.2. Materials and Methods

Measurements within the *Spectro*LIGHT 500 were prepared as described before (see e.g. **chapter 3.4.2**). After manual adjustment of laser and detector at every measurement position an autopilot file was generated as Python script. In this file the total number of measurements per well, the interval between measurements and the duration of a single measurement within the respective experiment were saved. The automated measurement was then started by reading this script-file (e.g. autopilot.py, see **Appendix, chapter 9.1** for examples of such scripts) into the DLS software *SPECTRO*. DLS was then recorded as described in the file.

All plates in the case of MRC plates were prepared manually. To avoid evaporation during preparation only one third of a plate was pipetted at a time. During the preparation of the other parts of the plate it was temporarily covered with AMPLIseal (Greiner Bio One, Germany). When the preparation was complete this seal was removed and a new sheet of AMPLIseal used to seal the whole plate.

The preparation of measurements within the GCB-D is described in **chapter 3.2.2.** For automated experiments in Terazaki plates under oil an IMPAX robot (Douglas Instruments) was used to prepare the droplets under oil. A matrix of 6x6 drops was pipetted, applying 6 different protein (lysozyme Merck, Germany): 7.5 – 25 mg/mL, dissolved in 250 mM NaOAc buffer, pH 4.75) and precipitant concentrations (NaCl: 0.4 – 1.0 M, dissolved in the same buffer as the protein). The overall drop volume was 2 µL. Measurements were carried out in the *Spectro*LIGHT 500 using the autopilot function. DLS was recorded at each well for 15 seconds; this was repeated 140 times during 20 hours.

All protein solutions used were centrifuged for at least 20 minutes prior to use and all other buffers, precipitants, detergents used in these experiments were filtered through 0.22 µm syringe filters (Milipore, USA) before mixing with protein solutions.

3.6.3. Results and Discussion

An initial test for automation requirement a) was carried out while monitoring experiments on the interaction of membrane proteins (see **chapter 6.3.2**). There two times 20 wells (1. A1 – A5 to D1 – D5; 2: E1 – E5 to H1 – H5) were observed, each time 118 measurements per well have been monitored (2380 movements per experiment). In most of the wells a valid DLS signal could be obtained during the entire observation. And no significant deterioration of DLS signal could be observed in both experiments.

To test if this would still hold true on a completely filled plate Well 2 of all 96 2W1R compartments was filled with 1 µL protein (Columns 1-4: CD81 **[120]**, columns 5-8: CD82 **[121]** and Columns 9-12: Proteorhodopsin **[122]**, all proteins being membrane proteins and were cloned, expressed and purified by **NICKLAS BONANDER**) and 1 µL of a selection of 32 different detergents at each 10x their critical micelle concentration (**cmc**). The reservoir was filled with 16 µL protein buffer (1 % (w/v) β-OG, 20 mM MOPS, pH 8.0) to avoid any vapor diffusion. DLS measurements started after insertion of the plate into the *Spectro*LIGHT 500 and adjustment of all 96 wells for best DLS signal. An autopilot file was written in Python (see **chapter 9.1, Appendix 3**) in a way that DLS was measured in each well for 60 seconds and that in each well DLS was measured once all 100 minutes. At all 6240 measurements were recorded within 80 hours, the plate and optical head were moved 6240 times during this experiment. Initially 89 of 96 wells yielded a valid DLS signal (94 % success rate) but after approx. 10 measurements results from some wells showed distortion in DLS that was clearly result of mechanical drift. However, from most of the wells valid measurements could be obtained throughout the experiment.

During the first automated DLS measurements in Terazaki plates, monitoring microbatch crystallization experiments under oil, in 20 of 36 wells (56 %) a valid DLS signal could be recorded during the entire time, in all but two wells this was the case for at least the first 20 measurements. Imaging of the wells right after finishing the DLS measurements revealed that in most of the cases distortion of the DLS signal could be assigned to crystal growth. The growing crystals either block the laser or detector or cause light reflections that are more intense than the scattered light from solution. There are though some wells in which no crystal growth was observed but the DLS signal appeared distorted after 20 – 60 measurements. In these cases shrinkage of the drop (Al´s oil was used in this experiment) or mechanical drift could

be the cause of the distortion. Since not all drops were perfectly formed and the relative position of laser towards the droplets depends on the position of the well on the plate mechanical drift may not affect all wells. Thus the distortion can be explained.

If requirement b) for automation could be achieved in the course of experiments regarding *in situ* DLS in small capillaries (see **chapter 3.2**). The capillaries within the GCB-D only have an inner diameter of 100 µm. It is in this environment critical to be continuously on the same position. Even a deviation of just 20 µm will lead to a complete decline of the DLS signal. DLS was recorded at seven positions along a 100 µm inner diameter capillary during a counter diffusion experiment. The capillary was filled with glucose isomerase (50 mg/mL, in 0.1 M Hepes, pH 7.0), 3 M solution of ammonium sulfate was used as counter diffusion precipitant. In two weeks a total of 1022 measurements was recorded (146 per position), thus plate and optical head were moved 1022 times. It can be clearly seen from the results in **chapter 3.2.3** that at positions at which no crystals grew within two weeks a valid ACF could be obtained throughout the experiment. This proves that automated *in situ* DLS measurements even in such critical environments as a 100 µm diameter glass capillary are possible.

3.6.4. Conclusions

The first automated DLS measurements within crystallization plates and thin capillaries could be carried out and it could be shown that even in the case of the GCB-D where highest accuracy is required automated monitoring of crystallization processes could be carried out. These results show that the integration of *in situ* DLS as a standard method within high throughput screening is possible and can be used to score and analyze crystallization droplets. However it is still required to adjust the position of laser and detector manually at all positions prior to the measurement. This needs to be automated as well in the future.

3.7. *In situ* DLS: Overview, Conclusions and Outlook

As shown in the previous chapters that DLS measurements can be carried out in all major crystallization environments and that automation of these measurements is possible. This opened the possibility to investigate the submicroscopic processes taking place during protein oligomerization, aggregation and crystallization.

For the first time ever *in situ* DLS monitoring within Terazaki plates under oil, in 100 µm inner diameter capillaries within the Granada crystallization box domino (GCB-D) and in the channels of the CrystalFormer HT was established. Moreover the initial experiments in 96well-plates carried out by **ARNE MEYER [92]** could be improved. Choosing seals (AMPLIseal, Bio Greiner One) and the plates best suited for *in situ* DLS (MRC Crystallization Plate™, Swissci) a better signal to noise ratio could be achieved and even more important: DLS is now possible in all 192 wells of the plate making it possible in the future to integrate *in situ* DLS as a standard step in high throughput screening, just as today imaging is carried out. The information gained by DLS surely will help to refine the crystallization experiments and facilitate optimization of crystal growth in order to obtain X-ray suitable crystals. However, application of *in situ* DLS towards different target proteins showed the complexity of this approach: in most cases the derived radius distributions over time showed a very complex pattern that was not comparable with the results obtained for model proteins (own results and results obtained by **ARNE MEYER [92]** and **KARSTEN DIERKS** *et al.* **[88]**). This opens the question if the use of model proteins leads to any scientific progress if it comes to the development of novel methods.

What target proteins often show (in the course of this work it was observed for SlfB (see **chapter 5**) and ΔN) is precipitation before crystallization. In these cases crystals grew out of the precipitate. If the conditions of the solution are altered to prevent precipitation no crystals appear at all. The application of *in situ* DLS could not reveal why this is the case.

Especially for *in situ* DLS within vapor diffusion crystallization experiments the shrinking drop size is a problem. An initially perfectly adjusted position of measurement can due to changes in the drop size eventually become a position at which DLS measurements are not or not good possible due to reflections and flares of the laser. The interpretation of data after such an experiment is then very difficult since CONTIN produces always a radius distribution and if the ACF is not interpreted manually such false positive results could easily be taken for real.

Promising are *in situ* DLS measurements in capillaries. Here the environment is stable; a once adjusted position will stay adjusted during the whole experiment. Hence interpretable results can be obtained. Based on reflections of **WILLIAM WILSON [63]** that if nucleation can be detected by DLS already to many nuclei exist in solution (which is not desired **[40]**) and of **PETER G. VEKILOV** that nucleation rather occurs

from a dense protein phase called the mesoscopic phase than directly from the dilute solution of protein molecules **[47]** monitoring of crystallization processes was focused to the analysis of the development of the R_H of monomeric (or low oligomeric) particles. The same approach was proposed by **AARON STREETS [93]** and within the CrystalFormer HT comparable results, as first described by him in 2010, could be obtained for the time dependent development of R_H in the case of a crystallizing and non-crystallizing systems.

In the course of this work the crystallization of various target proteins could be improved by *in situ* DLS:

- Jack Bean Urease **[123]** was obtained from Sigma as lyophilized powder for structure-function relation studies with inhibitors by **AFSHAN BEGUM** (University of Hamburg). All crystals only showed diffraction to approx. 3.5 Angstroms. *In situ* DLS revealed that the protein was oligomerized and that this oligomerization could not be removed. **AFSHAN BEGUM** then purified Jack Bean Urease from Jack Bean meal and could then grow crystals from the naturally occurring hexamers. These crystals proved to be X-ray suitable and showed diffraction up to 1.8 Angstroms. Inhibitor studies by **AFSHAN BEGUM** are in progress.
- *Wb*GST, a glutathione-s-transferase from *Wucheria bancrofti* **[124]** was expressed and purified by **PRINCE PRABHU** (Centre for Biotechnology, Anna University, Chennai). No crystals could be obtained. An analysis of the most promising conditions and of variations of these conditions by *in situ* DLS showed rapid aggregation taking place inside the crystallization droplet. Analysis of the protein without precipitant showed that its stability was highly temperature dependent. All crystallization processes were then carefully carried out at 4°C. X-ray suitable crystals could be obtained and the structure was solved by **PRINCE PRABHU** (to be published).
- ΔN, a recombinant protein construct of full length yeast ERV1 which is a sulfuryl hydroxylase **[125]**, was investigated in terms of a cooperation with **KYRIAKOS PETRATOS** from IMBB Forth (Crete). Petratos and co-workers could only obtain tiny crystals. *In situ* DLS revealed that the used PEG concentrations were too high. Applying in situ DLS crystallization conditions were altered rationally. Reducing the concentration of PEG 4000 from 20% to 5% and addition of 5-8 % of PEG 400 resulted for the first time in the growth of

larger (300 – 400 µm) crystals that showed diffraction pattern. However the conditions need to be further optimized.

- The Spiegelmer NOXE36 was developed by NOXXON (Berlin, Germany) as an inhibitor of the monocyte chemoattractant protein (MCP-1) **[126]**. In the course of her scientific work **BARBORA SCHMIDT** (University of Hamburg) aimed at crystallizing the complex of NOXE36 and MCP-1. *In situ* DLS studies revealed that the initial crystallization conditions resulted in aggregation short after preparation of the crystallization experiments. Improvement of conditions led to the growth of X-ray suitable crystals that showed diffraction up to 2.2 Angstroms. Solution of the three dimensional structure is on-going.

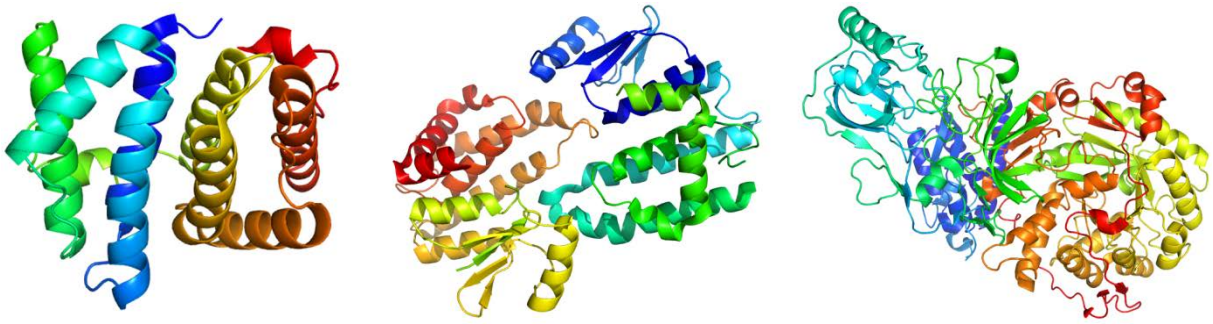

Figure 30: A) Erv1 from *Arabidopsis Thaliana* (PDB-accession code: **2HJ3**) as an example for sulfuryl hydroxylases. A recombinant fragment of Erv1 – ΔN – was crystallized with the help of *in situ* DLS. **B)** *Pf*GST (PDB-accession code: **1PA3, [102]**) as an example for Glutathione S-transferases such as *Wb*GST from *Wucheria bancrofti*. The structure of *Wb*GST was solved by the method of molecular replacement with *Pf*GST as search model (33% sequence identity). **C)** Cartoon plot of the asymmetric unit of Jack bean urease (PDB-accession code: **3LA4**, **[123]**), the assumed biological molecule is composed of six monomers.

Three proteins were investigated as part of the EU FP6-funded OptiCryst **[18]** consortium. The results of these investigations are presented as studies on the application of *in situ* DLS on target proteins in **chapters 5** and **6**.

- CD81 and CD82 two human membrane proteins of the Tetraspanin-family **[127]**, were expressed and purified by **ROSLYN BILL** and **NICKLAS BONANDER** (Aston University, UK). Applying *in situ* DLS crystals of both CD81 and CD82 could be obtained. Moreover interaction and oligomerization between and of CD81 and the tight junction protein Claudin-1 **[128]** was investigated by in droplet DLS. These studies are thoroughly discussed in **chapter 6**.

- SlfB from *Lysinibacillus spaericus* strain JGA12 **[129]**, was purified directly from JGA12 by **JOHANNES RAFF** (Helmholtz-Zentrum Dresden-Rossendorf, **HZDR**) and co-workers. *In situ* DLS was applied to optimize buffer conditions

(**chapter 5.3.1**), investigate initial crystallization experiments (**chapter 5.3.4**) and to evaluate the influence of bivalent cations on the stability of SlfB (**chapter 5.3.7**).

In conclusion it can be stated that *in situ* DLS has a high potential to facilitate the rationalization of protein crystallization and to gain further insight into the submicroscopical processes within crystallizing solutions of biological macromolecules. In future light scattering methods *in situ* and prior to crystallization will help delivering the desired nano-crystals for structure elucidation of target proteins with X-ray lasers such as the XFEL currently being built at the DESY site.

4. Light Scattering Experiments in Special Hardware

4.1. Introduction

Today most of the crystallization plates are standardized and follow the measures of the SBS footprint **[100]**. Other crystallization techniques such as counter diffusion in capillaries or microfluidics tend also towards the usage of SBS footprint devices since imagers and robots are designed to handle this format. It could be shown that the DLS instrument used in this work, the *Spectro*LIGHT 500 is capable to handle also non-SBS crystallization hardware (see **chapter 3.2** and **3.5**). Sometimes it is desired to monitor crystallization, protein oligomerization or protein-protein interaction in devices that are non-standard and were certainly not designed to suit the optical properties required for DLS measurements. In this chapter initial DLS measurements in special environments, such as containers for crystallization in space, small reaction tubes or in cubic lipid phases (**CLP**) **[130]**, are carried out and the applicability of DLS is discussed.

4.2. Materials and Methods

Protein material was centrifuged prior to the experiments to remove dust and other residuals. In the case of DLS within small reaction tubes (tubes typically used for polymerase chain reaction, **PCR**) and cubic lipid phases, hen egg-white lysozyme was used to demonstrate the possibility of DLS monitoring.

HEWL (Merck, Germany) was solved in NaCl-free NaOAc-buffer (250 mM, pH 4.75) and dialyzed against this buffer to remove any NaCl carried in from the lyophilized protein powder. Concentration and purity of the protein was estimated prior to the experiment by absorption spectroscopy applying a Nanodrop 2000c (Thermo Fisher, USA).

For measurements in small reaction tubes a 1.5 M solution of NaCl in NaOAc-Buffer (250 mM, pH4.75) was prepared and filtered through a 0.22 µm syringe filter prior to use. Equal amounts (10 µL) of HEWL (45 mg/mL) and 1.5 M NaCl solution were mixed inside a clear PCR tube. The tube was placed into the *Spectro*LIGHT 500 in a similar manner as the GCB-D (see **chapter 3.2**). Minute displacements were carried out to find a position of optimized DLS signal quality. DLS was recorded and evaluated with *SPECTRO*.

Cubic lipid phases were prepared in small reaction tubes with and without addition of protein. In the latter case the CLP was prepared as follows:

14.8 mg rac-Glycerol 1-monooleate (MO, monoolein, Sigma, Germany), 14 µL NaCl solution (1 M in in 250 mM NaOAc-Buffer, pH 4.75), 0.9 µL MPD (100 % (v/v), Carl Roth, Germany) and 7.8 µL HEWL solution (45 mg/mL, in 250 mM NaOAc-Buffer, pH 4.75) were added together in this order and mixed with a vortex shaker for 3 minutes. After waiting for 15 minutes the opaque emulsion was centrifuged for 150 min at 10'000 x *g*. Every 20 minutes the tube was turned inside the centrifuge around 180° to achieve a straight surface within the small reaction tube. The CLP without protein was prepared in the same manner by replacing protein solution by 250 mM NaOAc-Buffer at pH 4.75.

The resulting clear solid mixture was inserted into the *Spectro*LIGHT 500 and DLS measurements were prepared and carried out as described for measurements in small reaction tubes.

For DLS measurements in capillaries within a space box designed for the Chinese space mission Shenzhou8 the protein ThiM (5-(hydroxyethyl)-4-methylthiazole kinase; EC 2.7.1.50, from *Staphylococcus aureus* **[131]**) was used. ThiM was cloned, expressed and purified by **JULIA DREBES** (University of Hamburg). After purification it was dialyzed in a buffer containing 100 mM TRIS (pH 8.0) and 150 mM NaCl. The protein was concentrated using 3 kDa cut-off centrifugal filters (Millipore, USA) to approx. 12 mg/mL. Concentration and purity of the protein was estimated prior to the experiment by absorption spectroscopy applying a Nanodrop 2000c (Thermo Fisher, USA), quality of the sample was assessed by DLS measurements (Terazaki plate under oil, *Spectro*LIGHT 500)

The concentrated monomodal protein (~ 10 µL) was injected into a capillary (10 mm long, 1 mm inner diameter) applying a 100 µL gas-tight syringe (Hamilton, USA) to avoid formation of bubbles. The capillary was closed with a 2% (w/v) solution of low melting point agarose (Serva) and placed into a well of a space box. The well was then filled with precipitant solution (18-20 % (w/v) PEG 3350, 7% 2-propanol, 0.25 M magnesium formate) and sealed with AMPLIseal (Greiner Bio One) to prevent evaporation and leaking of the precipitant. The Growth-box was placed into the *Spectro*LIGHT 500 in a similar manner as the GCB-D (see **chapter 3.2**). A search for the box and its capillaries was performed and the capillary position saved in the database of *SPECTRO*. Minute displacements were carried out to find a position of optimized DLS signal quality. An autopilot-file was generated as Python script and automated measurements were started.

4.3. Results and Discussion

4.3.1. DLS in Capillaries for Space Experiments

Measurements were carried out similar to those in the GCB-D and the CrystalFormer HT. Initial DLS measurements after adjustment of laser and detector position showed a typical ACF with an intercept of 1.7 (see **Figure 31**). A crystallization experiment was then monitored automatically for 60 hours at five positions within the capillary.

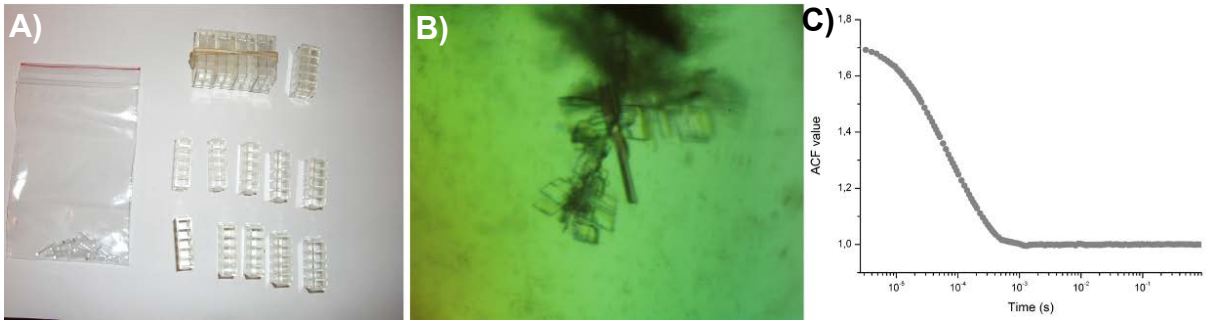

Figure 31: Growth box for crystallization during Shenzhou8 mission and results of crystallization and *in situ* DLS. **(A)** The crystallization system for Shenzhou8, on the left hand side the capillaries are displayed, the containers are shown on the right hand side **(B)** crystals of ThiM grown in the capillaries (bearing the same crystal morphology as described by **JULIA DREBES** *et al*. **[131]**), **(C)** ACF of initial DLS measurements within the capillary inside a container

The results of DLS measurements within the first 14 hours are displayed in **Figure** 32. At first, a bimodal solution is present in all positions along the capillary. The smaller particle species grows from R_H= 6-9 nm to 15 nm within the first 6 h. But after 4 h it can only be detected at position 2. Meanwhile the larger particle species grows from approx. 30 nm to 50 nm. Between 6 and 8 hours the size of this particle species at positions 5 and 6 increases faster than at the other positions. After 7-8 hours the size of these particles exceeds 1 µm.

The same happens to this particle species at position 3 after 9 hours, at position 2 after 12 h and at position 1 after 13-14 hours. This points to a correlation between position and radius distribution stemming from a gradient of precipitant within the capillary. The differences between the positions can be related to the diffusion velocity within the capillary. Compared with the results from DLS measurements inside the GCB-D it can be seen that the diffusion takes place much faster. This is due to the larger inner diameter of the capillary.

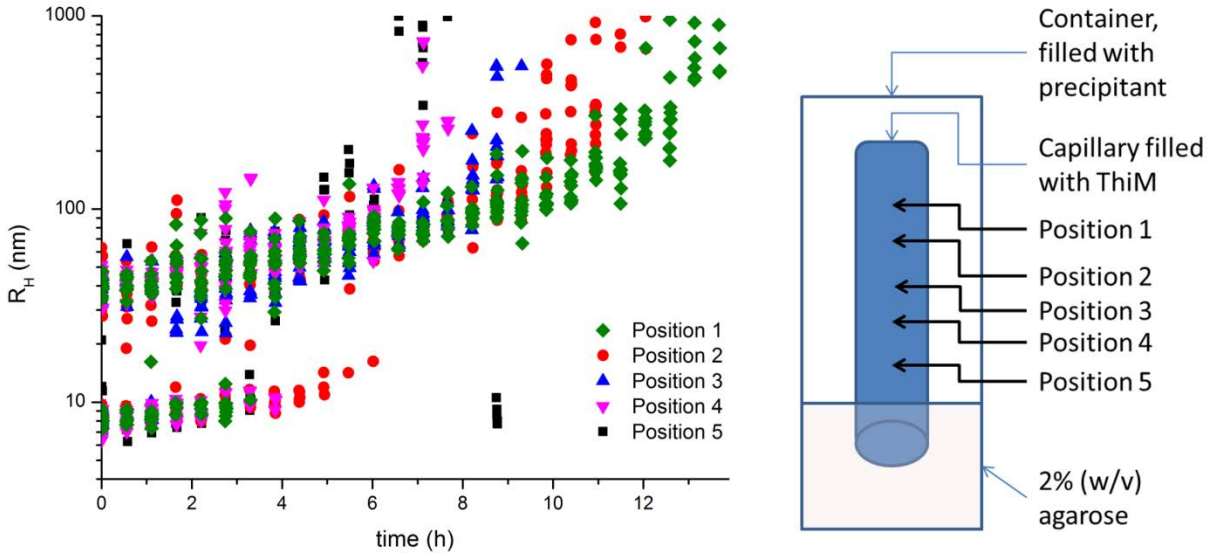

Figure 32: Results of *in situ* DLS in the crystallization box designed for Shenzhou8. A strong correlation between the position of measurement and growth of the aggregates can be seen in the radius distribution. At positions close to the entry (4, magenta and 5, black) the aggregates grow to a R_H over 1 µm after 7 h, at position 3 (blue) this is the case after 9 hours, at position 2 (red) after 12 hours and at position 1 after 13-14 h. This displays the concentration gradient within the capillary.

4.3.2. DLS in Small Reaction Tubes

Since to enable first DLS measurements the CLPs had to be prepared in small reaction tubes the general quality of DLS measurements within these tubes had to be assessed. Lysozyme- and NaCl-solutions were mixed inside a small reaction tube and the tube then inserted into the *Spectro*LIGHT 500 instrument. The laser and detector position were adjusted and an ACF recorded and evaluated. As can be seen in **Figure 33** it is possible to measure DLS within PCR tubes. Even though, comparison with a measurement at equal conditions in a MRC plate shows that the ACF has a lower intercept (1.4 to 1.7) the quality of measurement is comparable. The ACF is formed as expected for a nucleating lysozyme solution and it approximates 1 at large delay times. In delay times > $4x10^{-5}$ s both ACF are nearly identical. The lower intercept at small delay times can be attributed to reflections and the non-ideal environment leading to a deviation from ideal intensity fluctuation over time. The radius distribution shows the typical bimodality expected for lysozyme. The differences in radius distribution between the measurement in a MRC plate and the PCR tube can be explained by the ACF: The relative ACF value at delay times between 10^{-4} and 10^{-3} s compared with the intercept is higher in the case of PCR tubes hence the intensity in the radius distribution as calculated by CONTIN is higher as in the case of the measurement in a MRC plate.

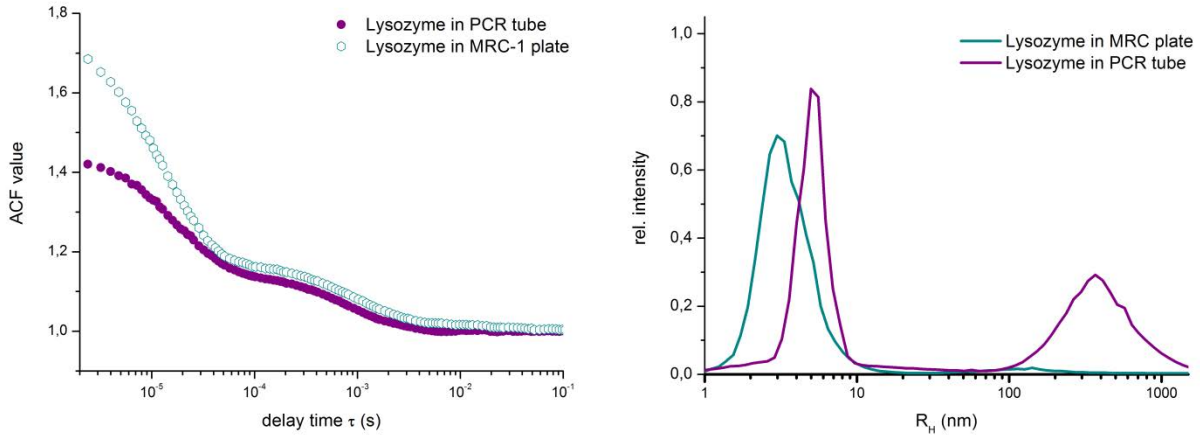

Figure 33: DLS in PCR tubes, on the left hand side the ACF is shown, the radius distribution is displayed on the right hand side.

4.3.3. DLS in Cubic Lipid Phases

Cubic lipid phases **[130]** can be regarded as liquid crystals with a regular arrangement of water and lipid molecules ranging throughout the space the CLP is prepared in. CLPs are clear, show no birefringence when illuminated with polarized light and have viscous, solid-like, texture. Because of their property to keep lipophilic molecules encapsulated for a certain time depending on the way the CLP is prepared and the type of caged molecule, their use in drug delivery systems is discussed **[132, 133]**. With regards to Structural Biology most important is their role in the crystallization of membrane proteins **[134-136]**. Due to their lipophilic properties within a hydrophilic environment CLPs mimic biological membranes **[134]**. Else than these membranes they are arranged in a regular and connected three dimensional pattern **[135]**. The membrane protein molecules are incorporated in the lipid structure just as in their natural environment, membranes. The structural properties of CLPs facilitate crystallization of the membrane proteins **[135]**. Channels within the CLPs deliver precipitant molecules towards the protein and CLPs are liquid crystals – the arrangement is always dynamic. This dynamic within the CLP provides contacts between membrane proteins. If the solution properties favor attractive protein interaction this can lead to nucleation and crystal formation **[137]**. Most important, the three dimensional structure of the CLP leads to the growth of three dimensional crystals and not to the typical crystals of membrane proteins composed of layers of two-dimensional crystals. Bearing this and the high importance of membrane proteins in nearly all biological processes in mind, it is very interesting to investigate the crystallization phenomena within a CLP by light scattering methods in order to

rationalize and facilitate crystallizability. Here the first DLS measurements in CLPs with and without protein are presented.

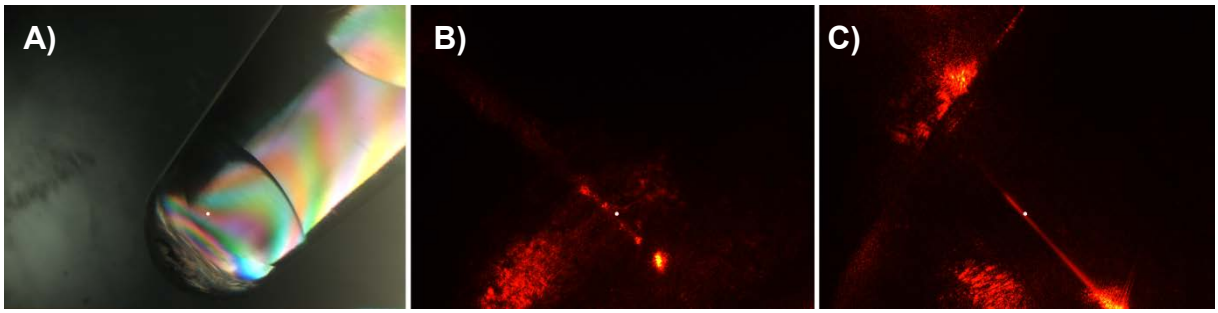

Figure 34: (A) CLP in a small reaction tube, **(B)** DLS laser in CLP without protein, **(C)** laser passing through CLP with lysozyme

In **Figure 34** the CLP within a PCR tube (A) and the laser trace in the case of CLP without- (B) and with protein (C) are displayed. It can be seen that especially in the CLP with protein the laser passes the PCR tube walls and the CLP without any major flares and reflections. The ACF (**Figure 35**) in the case of CLP without protein has an intercept of 1.4 and has a shape typical for a valid measurement although the countrate is low (11 kHz). If lysozyme is present the ACF is smoother and has an intercept of 1.6. Moreover the countrate is more than ten times higher (127 kHz). Thus the background signal of the CLP does not disturb DLS measurement of protein samples.

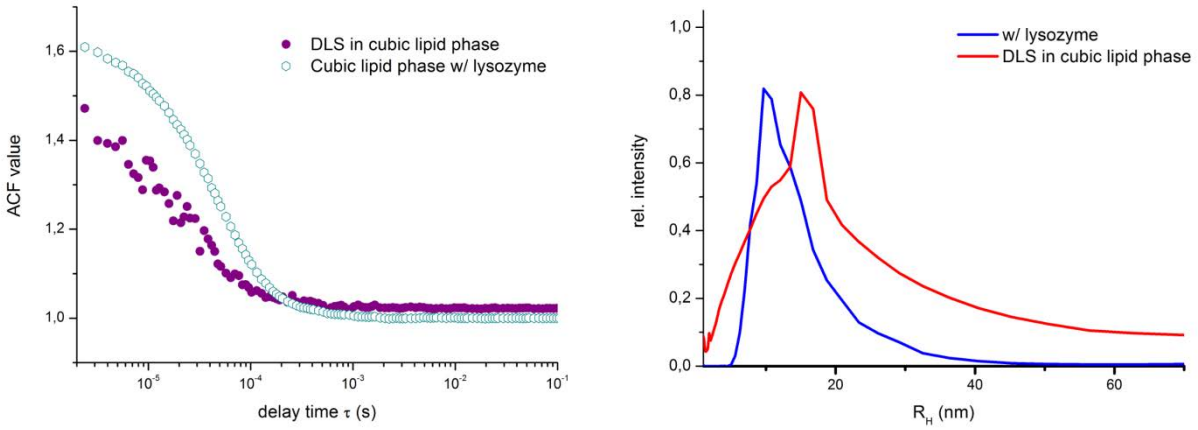

Figure 35: Results of DLS measurements within cubic lipid phases.

This clearly shows that valid DLS measurements within CLPs are possible. Since the CLP as such is viscous and – compared with e.g. buffers – rigid and DLS measurements are based on the Brownian motion of particles this was not to be expected.

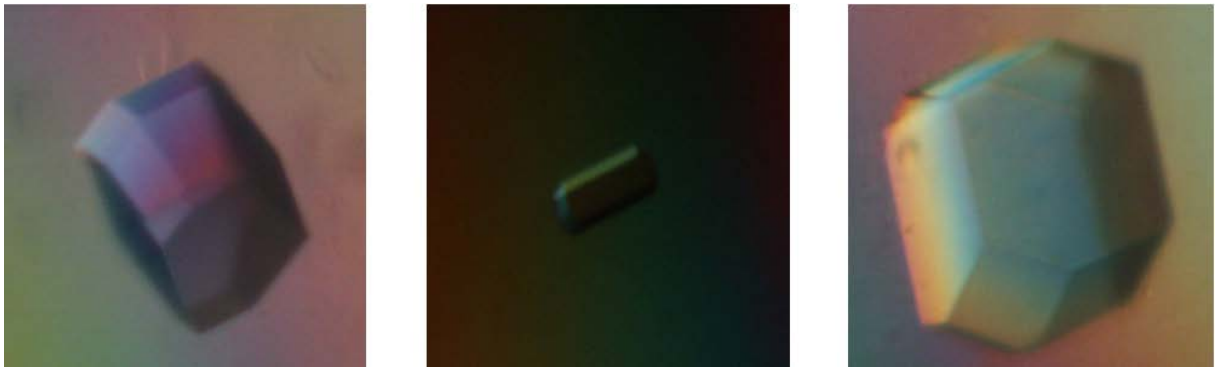

Figure 36: Lysozyme crystals grown in a CLP within a small reaction tube

The results of *in situ* DLS with lysozyme show that lysozyme behaves as a Brownian particle inside a CLP. It still needs to be assessed whether this is the case if instead of lysozyme a membrane protein is placed within the CLP. Since membrane proteins are placed between the lipid molecules and not in the connecting channels its movement may be hindered.

Figure 36 shows lysozyme crystals grown in a CLP. For soluble proteins such as lysozyme a CLP provides an environment such as agarose: the high viscosity of the CLP protects the crystal during growth, whilst protein molecules are transported to the growing crystal via channels present in the CLP.

4.4. Conclusions and Outlook

It could be shown that DLS measurements are possible even in special crystallization hardware and that the quality of measurements can be compared to those in optical cuvettes or crystallization plates. Most interesting is the possible potential of *in situ* DLS in the case of cubic lipid phases. Sometimes up to 50’000 crystallization experiments are necessary to obtain membrane protein crystals and in many cases even these ultra-high through put approaches fail to produce X-ray suitable crystals. DLS within CLPs might help in future to narrow down the number of experiments and facilitate successful membrane protein crystallization.

5. Application of *in situ* DLS – JGA12 / SlfB

5.1. Introduction

SlfB from *Lysinibacillus spaericus* strain JGA12 **[129]** is a surface layer protein (S-Layer protein, **SLP**) **[138-141]** first isolated and described by **JOHANNES RAFF** (HZDR, Dresden) and co-workers from uranium mine waste piles in eastern Germany **[129]**. The protein consists of 1207 amino acids and has a molecular weight of approx. 120 kDA. As a surface layer protein it has the tendency to self-arrange to two dimensional crystal like structures **[142]**. Protein used within this work was obtained from **JOHANNES RAFF** and co-workers who isolated and purified the protein directly from *Lysinibacillus spaericus* strain JGA12 **[129]**. BLAST **[143]** search revealed that no protein structure with more than 28% sequence homology exists in the PDB. This fact, possible industrial applications **[144, 145]** of S-layer protein coated surface and the need to enlighten the structural basis of s-layer formation are making the three dimensional structure determination of SlfB / JGA12 a challenging and interesting aim. Previous work of **JOHANNES RAFF** included AFM characterization of surface layer formation as well as EXAFS (Extended X-Ray Absorption Fine Structure), XANES (X-ray Absorption Near Edge Structure) and ATR-FTIR (Attenuated Total Reflectance Fourier Transform Infrared Spectroscopy) measurements to determine the metal binding properties of SlfB, especially the ability to complex uranium and palladium **[144, 146, 147]**. In the PDB, besides the ubiquitous occurrence of S-Layer proteins in the bacterial world, to date no full length structure of a SLP is present. The structure of single domains of SLPs were solved and complete structures predicted by arrangement of these domains **[148]**. The structure of the surface layer homology (**SLH**) domains of the surface array protein (**Sap**) from *Bacillus anthracis* (the pathogen that causes anthrax) was solved **[149]**. These SLH domains are characteristic for many S-layer proteins and are necessary for binding to secondary cell wall polysaccharides (**SCWP**) of Gram-positive bacteria **[149]**. These SLH domains are also present in SlfB from *Lysinibacillus spaericus* strain JGA12 **[129]** although the sequence similarity (approx. 40%) and identity (22 %) with the respective domains in **Sap** is low.

5.2. Materials and Methods

5.2.1. Buffer and Salt Optimization

The received first two charges (**JGA12-A** and **JGA12-B**) of protein were produced and purified by **JOHANNES RAFF** and dissolved in water at pH 7.0 and free of bivalent cations. The concentration as determined by **JOHANNES RAFF** was approx. 13 mg/mL **[150]**. Solution properties were assessed with DLS. 2 µL of protein were transferred into the wells of a MRC-plate. The plate was sealed to avoid evaporation of the droplets and a series (20x20 s) of DLS measurements was recorded using the *Spectro*LIGHT 500 (Nabitec, Germany). For buffer optimization the pH-Screen (Hampton Research) was used. Protein (1.5 µL) and the solutions from the screen (1.5 µL) were mixed in the wells of a MRC-plate. DLS measurements were carried out as for the protein alone. Further optimization of protein buffer was carried out using custom made buffers and salt solutions (see **Table 2**). Solution properties were monitored with DLS as described above. Additionally all solutions were monitored after 24 h and 7 days to gain insight into the long-time stability of JGA12 in the respective buffers.

Table 2: List of compounds used for buffer optimization.

Compound	**Concentration in drop**	**Compound**	**Concentration in drop**
MOPS (pH 8.0)	10 mM	TRIS (pH 7.4), NaCl	25 mM, 150 mM
MOPS (pH 8.0), β-OG	10 mM, 0.5 %	TRIS (pH 7.4), NaCl, Anion-Mix[1]	28 mM, 135 mM, 10%
$MgSO_4$	500 mM	MOPS (pH 7.1), NaCl	100 mM, 150 mM
NaCl	500 mM	TRIS (pH 7.4), NaCl, $(NH_4)_2SO_4$	28 mM, 70 mM, 135 mM
TRIS (pH 7.4), NaCl, ethylene glycol	50 mM, 150 mM, 2.5 %	TRIS (pH 7.4), NaCl, ethylene glycol	25 mM, 75 mM, 2.5 %
TRIS (pH 7.4), NaCl, NDSB256[2]	50 mM, 150 mM, 200 mM	TRIS (pH 7.4), NaCl, NDSB256	25 mM, 75 mM, 200 mM
TRIS (pH 7.4), NaCl	25 mM, 75 mM	TRIS (pH 7.4), NaCl, EDTA	28 mM, 135 mM, 5 mM

[1] Anion-Mix: 80 mM NaI, 40 mM of NaF, NaCl, NaBr and Na_2SO_4, [2]NDSB256 was obtained from Hampton Research

5.2.2. Crystallization

Two different solutions of JGA12-B were prepared for crystallization experiments:

1. **JGA12-B_DIL**

   Equal amounts of JGA12-B and buffer (**SLP1**, 150 mM NaCl, 50 mM TRIS, pH 7.4) were mixed and centrifuged for 1 h at 16'100 x *g*. The protein was stored at 4°C all the time.

2. **JGA12-B_DIAL**

   JGA12-B (400 µL) was dialyzed for 21h in a dialysis box (Slide-A-Lizer, 10 kDa cut off) against 400 mL of buffer (**SLP2**, 300 mM NaCl, 50 mM TRIS, pH 7.4). After dialysis the protein was centrifuged for 1 h at 16'100 x *g* and stored at 4°C constantly.

Solution properties of both JGA12-B_DIL and JGA12-B_DIAL were monitored before crystallization experiments with DLS following the procedure described for buffer optimization. Before the initial crystallization experiments the protein concentration necessary for crystallization was estimated applying the pre-crystallization test (**PCT**, Hampton Research) **[151]**.

Initial screening for crystallization conditions was carried out with JGA12-B_DIL. The pipetting robot Honeybee 961 (Genomic solutions) was used to transfer protein and precipitant solution onto a 96 well *Nextal Qia1* plate (Qiagen, Germany). The commercially available premixed screens *JCSG+*, *Classic* and *Cryo* (all Qiagen, Germany), containing a total of 284 unique precipitant mixtures, were chosen for the first crystallization experiment. 300 nL protein were mixed with 300 nL of the respective precipitant in one of the two wells per reservoir. Each reservoir was filled with 55 µL of the respective precipitant mixtures. The plates were sealed and stored at 4°C or 20°C in a vibration free incubator (Rubarth, Germany) and monitored once a week with an optical microscope (Olympus, Japan) and the imager *CrystalScore* (Diversified Scientific, USA).

Further screening was carried out with JGA12-B_DIL and JGA12-B_DIAL using the above described procedure but applying the screens *PACT*, *Morpheus*, *PGA* (all by Molecular Dimensions, UK), *MPD Suite*, *pHClear I & II Suite*, *Anions Suite* and *AmSO4 Suite* (all Qiagen, Germany). The plates were stored at 20°C in a vibration free incubator (Rubarth, Germany) and monitored once a week.

Optimization of crystallization conditions was based on the observations of the initial screenings. The most promising conditions were varied systematically. Input

Excel-sheets containing information of the optimization mixtures (see **Appendix, chapter 9.2**) were created for the pipetting robot *LISSY* (Zinsser, Germany). *LISSY* was used for the automated generation of optimization screens. The deepwell blocks filled by *LISSY* were used to carry out screens with the *Honeybee 961* robot as described above. Both protein solutions (_DIL and _DIAL) were subjected to the custom made optimization screens. Storage and monitoring of the screens was carried out as described above. The first optimization screen (PPEG) was analyzed and evolutionary optimization carried out, taking into account information derived from all previous screens. Such the screens PPEG2 and PPEG3 (optimization step 2), PPEG7 and PPEG8 (optimization step 3) and PPEG9 (optimization step 4) were designed and used in crystallization experiments.

5.2.3. New JGA12

The third batch of JGA12 protein, **JGA12-N** (13 mg/mL), was dissolved in buffer **SLP4** (75 mM NaCl, 25 mM TRIS, pH 7.4) during purification by **JOHANNES RAFF**. Solution properties of JGA12-N were assessed by DLS as described above. Crystallization experiments were carried out using the optimization screens PPEG 1, 2, 3, 7, 8 and 9 as described above – with the difference that 600 nL protein was mixed with 600 nL precipitant in the well – was used for automated pipetting with the Honeybee 961 robot. The plates were stored at 20°C in a vibration free incubator (Rubarth, Germany) and monitored once a week.

5.2.4. *In situ* DLS

Protein (JGA12-B_DIL and JGA12-B_DIAL) was mixed in the wells of a MRC-plate with an equal amount of precipitant and equilibrated against 30-50 µL of the respective precipitant. The plate was sealed and inserted into the *Spectro*LIGHT 500 for DLS measurements. Precipitant solutions were selected that yielded crystals in the initial screening. Moreover precipitant solutions were prepared where the conditions that yielded crystals initially were varied for optimization of crystal growth.

DLS was measured in all droplets after the preparation of the crystallization set-ups. Selected wells were monitored by DLS throughout the experiment. Between measurements the wells were inspected applying the built in camera or a microscope to monitor crystal growth. *In situ* DLS was also applied to crystallization experiments of JGA12-B under oil. DLS measurements were evaluated using the software *SPECTRO* and *Origin*.

5.2.5. SAXS Measurements

Concentration of SlfB (JGA12-N) was determined using a Nanodrop 2000c (Thermo Fisher) and theoretical values for Absorption-coefficient (ProtParam, http://web.expasy.org/protparam/). Four dilutions were prepared (5, 4, 3 and 2 mg/mL) by mixing protein solution with its buffer, centrifuged and stored at 4°C until the measurements. SAXS measurements **[9]** were carried out at X33 beamline (HASYLAB/EMBL). Results were evaluated using the ATSAS software *GNOM* **[152]** and ATSAS online server **[153]**. *Ab initio* modeling was carried out using *DAMMIN* **[154]** and *DAMMIF* **[155]**, *CRYSOL* and *SASREF* **[156]** were used for comparison of SAXS data and PDB-data of homologous structures.

5.2.6. *In situ* Proteolysis

Monodisperse SlfB (JGA12-N) in its buffer was subjected to four proteases (subtilisin, papain, trypsin and chymotrypsin) at two protease concentrations (0.1 and 0.01 mg/mL) according to the instructions of the *floppy choppy* kit (Jena Bioscience). The proteolysis was monitored by DLS and SDS-PAGE **[157]**. SAXS measurements of the products of proteolysis with trypsin and chymotrypsin were carried out as described in **chapter 5.2.5**. For DLS 2.5 µL of the centrifuged proteolysis solution were pipetted into a well of a MRC 96-well plate, the reservoir was filled with 50 µL paraffin oil and the 2W1R compartment was sealed. DLS measurements (20 x 20s) of all proteolysis experiments and full length SlfB as reference were recorded in the *Spectro*LIGHT 500 at 150° scattering angle. The software SPECTRO was used to evaluate the results from DLS. For SDS-PAGE **[157]** aliquots of the proteolysis solution were denatured using the following protocols:

a) 1.5 µL of proteolysis solution were diluted with 8.5 µL buffer, mixed with 10 µL DTT solution (0.5 mol/L) and 20 µL sample buffer (66 mmol/L Tris, pH 6.8, 26% (v/v) glycerol, 2.2% (w/v) sodium dodecyl sulfate (**SDS**), 0.01% (w/v) bromphenol blue). The mixture was heated for five minutes at 96°C using a ThermoMixer comfort (Eppendorf, Germany). Final concentration of SlfB: approx. 0.09 µg/µL.
b) 2 µL of proteolysis solution were diluted with 8 µL buffer. Of this diluted solution 4 µL were taken and further diluted with 6 µL buffer, 10 µL DTT solution (0.5 mol/L) and 20 µL sample buffer were added. The mixture was

heated for five minutes at 96°C using a ThermoMixer (Eppendorf, Germany). Final concentration of SlfB: approx. 0.06 µg/µL.

For SDS-PAGE a reducing gel containing 7% acrylamide was used.

5.2.6.1. Crystallization

Concentration of the *in situ* proteolysis solutions were adjusted applying the PCT (Hampton) prior to crystallization. Crystallization screening was carried out as described above using the Honeybee 961 robot (Genomic Solutions, USA) and the premixed commercial screens JCSG+, Cryo (both Qiagen, Germany), PACT, PGA-screen and Morpheus (all Molecular Dimension, UK). Crystallization plates were stored at 20°C in a vibration free incubator (Rubarth, Germany) and monitored once a week.

Crystals of SlfB digested by subtilisin (at 0.01 mg/mL of subtilisin) grew after two month in a mixture of 1 µL protein solution (concentration estimated by A_{280} approx.) and 1 µL of solution A1 from PCT (Hampton Research, USA) equilibrated in a Linbro24 plate against 500 µL solution A1 (2.0 M ammonium sulfate and 0.1 M Tris hydrochloride, pH 8.5). UV-Imaging of the crystallization droplet applying a *Crystal*LIGHT 100 (Nabitec, Germany) light source showed fluorescence of the crystals indicating them being protein crystals.

For X-ray data collection one crystal (approx. 150x100x60 µm) was flash frozen in a stream of nitrogen at 100 K. To avoid crystal damage and water ice formation the crystal was transferred with a Micromount (Mitegen, USA) loop in a drop containing 2.0 M ammonium sulfate, 0.1 M Tris hydrochloride (pH 8.5) and 20% (v/v) glycerol as cryoprotectant and incubated there for approx. 20 s before mounting on the goniometer head. Diffraction images were recorded with a MARCCD165 detector (Marresearch, Germany) at the consortiums beamline X13 (HASYLAB/DESY) at a wavelength of 0.8180 Å. The software DNA **[158]** was used for initial indexing.

5.2.7. Influence of Selected Bivalent Cations

SlfB-batches (JGA12-B and JGA12-B_DIAL) were centrifuged (16'100 x *g*, 60 minutes, 4°C), citrate buffer (200 mM, pH 4.0) was prepared from sodium citrate and citric acid, 20 mM solutions of $Mg(OAc)_2$, $Ca(OAc)_2$, $SrCl_2$, $BaCl_2$, $ZnSO_4$ and $CuSO_4$ were prepared from 1 M stock solutions. All solutions were filtered through 0.22 µm syringe filters prior to use. 20 µL of JGA12-B and JGA12-B_DIAL were mixed with 20

µL citrate buffer (JGA12-B_CIT and JGA12-B_DIAL_CIT). For DLS measurements 1.5 µL of JGA12-B, JGA12-B_DIAL, JGA12-B_CIT and JGA12-B_DIAL_CIT were mixed directly in the wells of a MRC1 plate with 1.5 µL of the respective solutions of bivalent cations. Moreover for comparative measurements 3 µL of each protein solution were pipetted into wells of the same plate. The reservoir was filled with 60 µL of paraffin oil and the plate was sealed with AmpliSEAL to avoid evaporation. DLS measurements in all 28 wells (4 protein solutions vs. 6 cation solutions plus 4 protein solutions alone) were carried out in the SpectroLIGHT 500 as described before. A series of 20x20 s was recorded per well immediately after mixing.

More detailed investigation of the influence of bivalent cations was conducted with SlfB (JGA12-N). The protein was centrifuged (16'100 x *g*, 60 min, 4°C) and 15 µL of protein were mixed with an equal amount of the respective cation solution. For each cation (chlorides of Mg, Ca and Sr) 21 solutions were prepared, seven different concentrations (final concentration of Cat^{2+} after mixing with protein: 500, 100, 50, 5, 1, 0.5 and 0.1 mmol/L) in three different buffers (Protein buffer; NaOAc/HOAc, pH 4.75, 250 mM and glycine-HCl, pH 2.0, 200 mM). Solutions were prepared from stock solutions (2 mol/L in deionized water) of $MgCl_2$, $CaCl_2$ and $SrCl_2$. Stock solutions were diluted with the respective buffers 1:1 (Stock 2: 1 mol/L), the pH adjusted with NaOH and the remaining concentrations prepared by dilution with the respective buffers at half their original concentration (thus assuring that all solutions at a pH shared the same buffer concentration). All solutions were filtered through 0.22 µm syringe filters prior to use.

The protein-cation mixtures were centrifuged for 20 minutes at 16'100 x *g* and kept on ice. For DLS measurements 3 µL of each mixture were pipetted into the pre-oiled wells of a Terazaki plate (NunC, Denmark). To prevent evaporation of the droplets paraffin oil (Applichem, Germany) was used. DLS measurements were carried out within the *Spectro*LIGHT 500 (Nabitec, Germany). For each mixture a series of measurement (10x10 s) was recorded directly after pipetting and after nine days at room temperature. Moreover a second plate was loaded with protein-cation mixtures one day after the first measurements to test the stability of SlfB with different cations at 4°C. DLS measurements were carried out as described for the first plate. To evaluate the effect of bivalent cations three mixtures of SlfB with the buffers were prepared, to yield a buffer and protein concentration as in the above described protein-cation experiments. DLS was measured right after preparing the solutions,

after one day and after nine days at room temperature. DLS measurements were evaluated using the software *Spectro* and *Origin*.

5.3. Results and Discussion

5.3.1. Buffer and Salt Optimization

The received first two charges (JGA12-A and JGA12-B) of protein were dissolved in water at pH 7.0 and free of bivalent cations. The concentration as determined by **JOHANNES RAFF** was approx. 13 mg/mL. Initial DLS of the protein solutions showed that both solutions were polydisperse. Besides the monomer at approx. 10 nm a broad peak representing particles with a R_H of 20 – 80 nm was present (see **Figure 37**). Neither by filtration nor by centrifugation could this be removed. Different buffers were tested using the Hampton pH-Screen. A MRC-plate (Swissci, Switzerland) was used for DLS measurements. In a well 1.5 µL of protein solution was mixed with 1.5 µL of the respective buffer and a series of DLS measurements was recorded (20 x 20s) with the *Spectro*LIGHT 500. In none of the buffers a significant optimization of the solution properties could be achieved. In all cases the polydispersity of the solution persisted. It was then assumed that not the pH value of the solution causes the polydispersity, but the lack of salt or other additives. Besides typical additives such as ethylene glycol, non-detergent sulfobetaine (**NDSB**) or detergent, NaCl was tested in the same manner as the pH screen before.

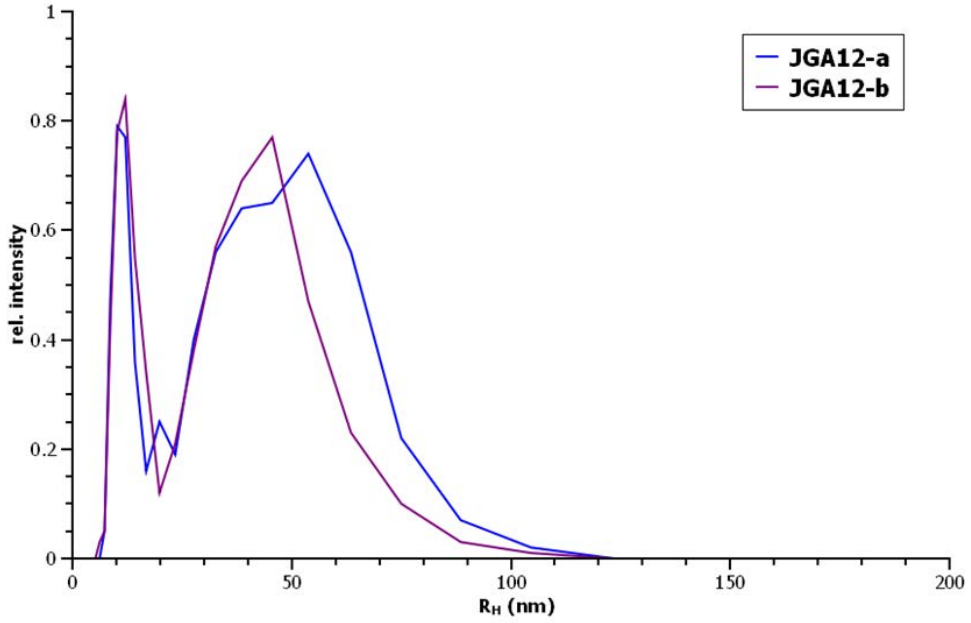

Figure 37: Radius distribution of the two SlfB solutions JGA12-A and JGA12-B as received.

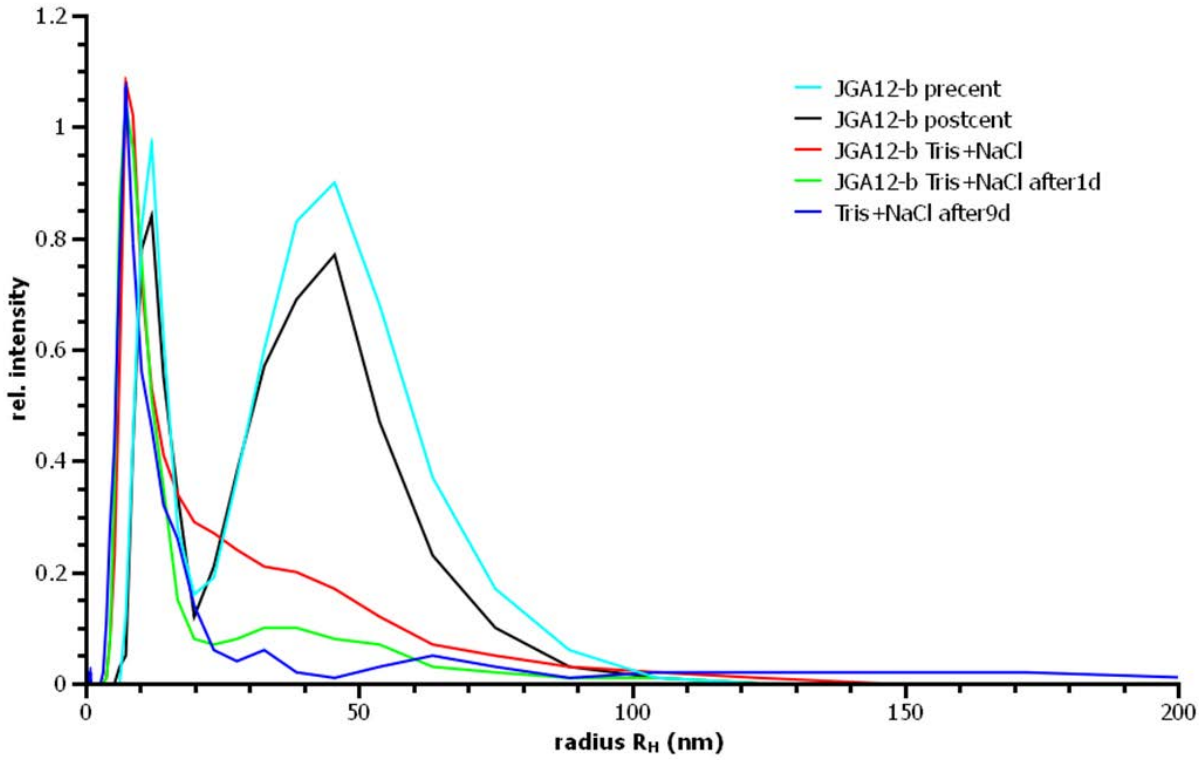

Figure 38: Results of buffer optimization for the SlfB solution JGA12-b. The slow decay of the aggregated fraction over time can be seen as well as the shift of the monomer- or small oligomer-peak from 10 to 7 nm.

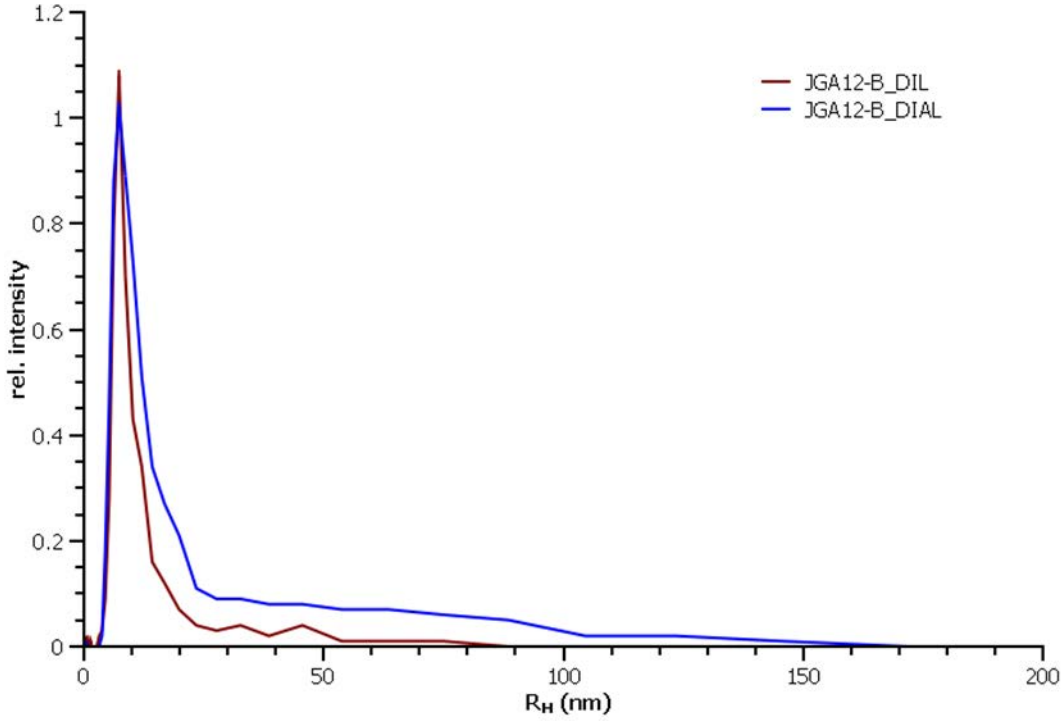

Figure 39: Comparison of the radius distributions of the SlfB solutions JGA12-B_DIL and JGA12-B_DIAL, the latter one showing a more polydisperse radius distribution.

A combination of 50 mM Tris buffer at pH 7.4 and 300 mM NaCl added to the protein solution resulted finally in a slow decay of the broad peak (**Figure 38**). At the same time the monomer or small oligomer peak was shifted from approx. 10 nm to 7 nm, representing either a dimer of SlfB or a non-globular monomer. Comparison of JGA12-A and JGA12-B nine days after addition of the buffer showed that JGA12-A was still polydisperse in solution whilst the JGA12-b solution was nearly monomodal. For all further experiments only JGA12-b was used. For initial crystallization trials two buffers were used for SlfB (for DLS results see **Figure 39**): a) SlfB was dialyzed against a buffer containing 300 mM NaCl and 50 mM Tris, pH 7.4 (JGA12-B_DIAL) and b) SlfB was mixed with a buffer containing 150 mM NaCl and 50 mM Tris, pH 7.4 resulting in a solution containing the protein at half the concentration in a buffer of 75 mM NaCl and 25 mM Tris at pH 7.4 (JGA12-B_DIL).

5.3.2. Crystallization

Applying the PCT (Hampton Research, USA) showed that the concentration of JGA12-B_DIL was better suited for crystallization trials. Protein concentration in JGA12-B_DIAL was to high according to the PCT. JGA12-B_DIL was screened with the Honeybee 961 against three screens: Nextal Classic, Nextal Cryo and JCSG+. For each screen two plates were pipetted: one was stored at 20°C and the other at 4°C to assess the temperature dependence of the protein phase diagram. After one week of incubation plates were analyzed automatically using the CrystalScore system and manually under a microscope. Three possible crystallization conditions could be identified, all from plates stored at 20°C:

(1) 30% PEG2000 MME, 0.2 M $(NH_4)_2SO_4$

(2) 12% PEG8000, 0.4 M Li_2SO_4

(3) 25% PEG3350

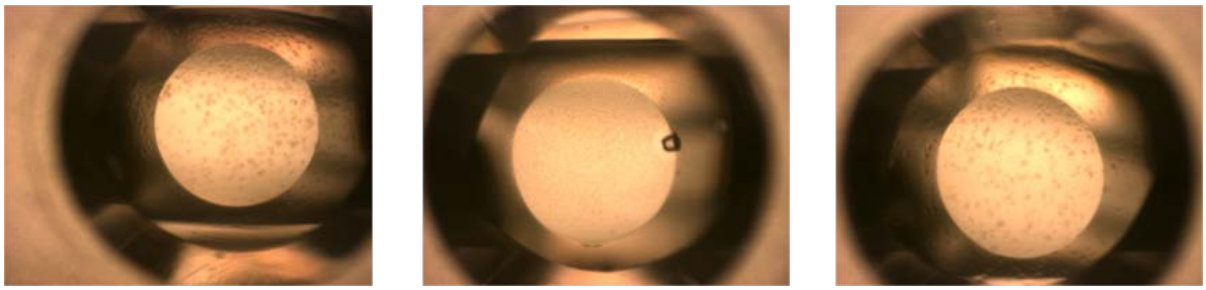

Figure 40: Results from initial crystallization screening of SlfB. On the left hand side the clusters of small needles derived from condition (1) can be seen. In the middle the crystal grown from condition (2) is visible and on the right hand side the cluster of small needles grown under condition (3) are displayed.

All initial conditions contained PEG, reproduction of crystals was carried out under *in situ* DLS monitoring. Condition 1 (30% PEG 2000MME, 0.2 M ammonium sulfate) yielded small needles as in the screen, the DLS analysis however showed (see **chapter 5.3.4**) that even lower concentrations of PEG 2000MME (22% w/v) induced aggregation followed by precipitation. Hence, based on the results from *in situ* DLS and initial screening, an optimization screen was designed (see **Appendix, chapter 9.2**), PPEG1, containing variations of the conditions that initially gave crystals at slightly lower PEG concentrations. After incubation for one week the plate was analyzed and the most promising results (all at lower PEG concentrations of approx. 16-20% PEG, see e.g. **Figure 41**) were optimized applying again self-designed screens (PPEG2 and PPEG3, see **Appendix, chapter 9.2**). As precipitants various concentrations of PEG 3350 (c (w/v): 19 – 16%), 8000 (c (w/v): 16 and 14%) and 10000 (c (w/v): 14 and 12%) were used. The PEGs were combined with ammonium sulfate, citrate buffer at pH 4.0 or NaOAc/HOAc buffer at pH 4.75 and various additives.

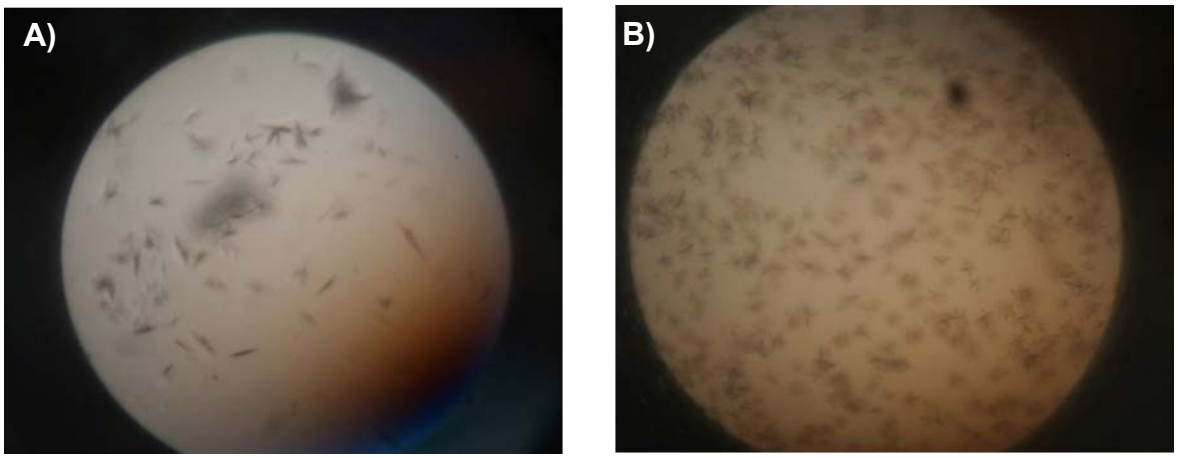

Figure 41: Improved crystals grown in the PPEG1 optimization screen. Conditions: **(A)** 18% PEG 8000 (w/v), 0.2 M ammonium sulfate, 0.1 M Na-citrate (pH 4.0), 10% Anion-Mix (Anions of Na, 0.08 M I^-, 0.04 M of Br^-, Cl^-, F^- and SO_4^{2-}), **(B)** 18% PEG 3350 (w/v), 0.2 M ammonium sulfate, 0.1 M NaOAc-buffer (pH 4.75), 10% Anion-Mix (Anions of Na, 0.08 M I^-, 0.04 M of Br^-, Cl^-, F^- and SO_4^{2-})

Based on the analysis of crystallization results within PPEG2 and PPEG3 (see **Figure 42**) crystallization screens PPEG7 and PPEG8 were prepared and screened using the Honeybee robot. Other than in the previous screens in PPEG7 and 8 only PEG 10000 was used since the best results in PPEG2 and 3 were obtained with PEG 10000. In screen PPEG7 only Na-citrate at pH 4.0 was used as buffer, variation of conditions was achieved by variation of salts and salt concentration. In PPEG8 the most promising results from PPEG7 were further optimized by pH-variation

(additionally pH 4.75 and NaOAc-buffer was used) and variation of ammonium sulfate concentration. Moreover only two salts besides ammonium sulfate were used in the screen: ammonium iodide and ammonium nitrate. Further improvement of crystallization could be observed (**Figure 42**). The best crystals obtained by screening with PPEG8 can be seen in **Figure 42 F**, these thin plates have a maximum size of 150 µm but were still too small for DORIS III. UV-analysis of the crystals with a *Crystal*LIGHT 100 (Nabitec, Germany, **[119]**) could not clarify whether the crystals are protein crystals or not. This is quite common for such thin crystals, their fluorescence being too weak against a strong background due to the plastic crystallization plates used. However test experiments with droplets without protein did not yield such crystals thus it is very probable that these crystals are protein crystals.

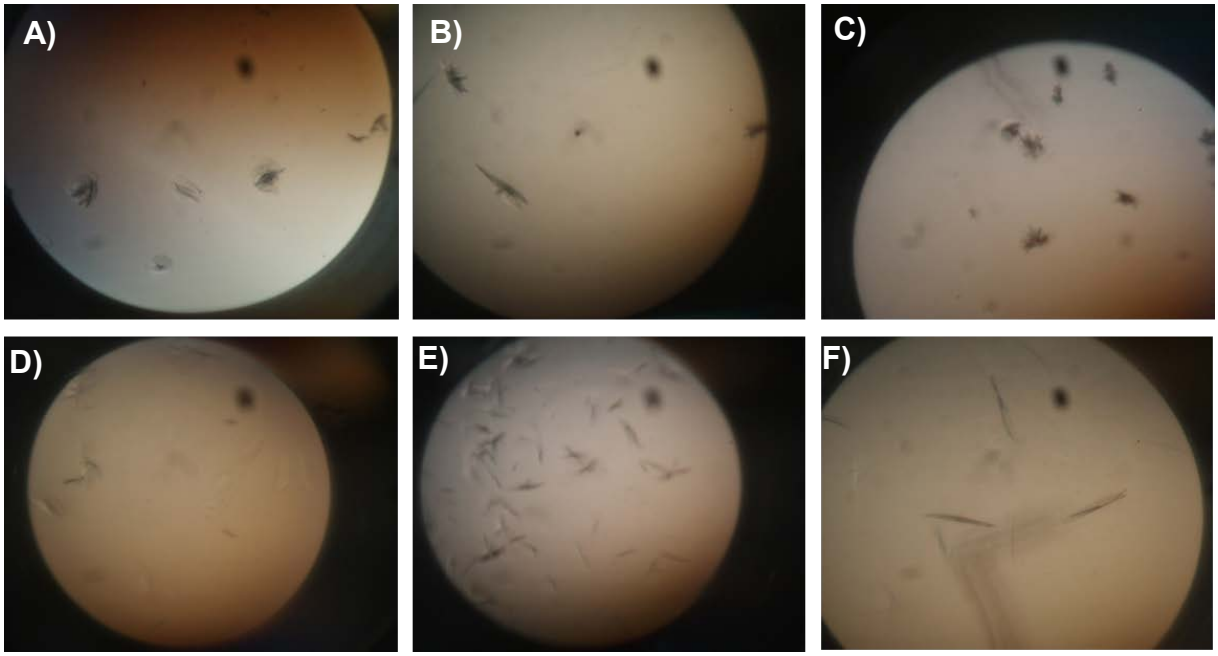

Figure 42: Optimized crystals of SlfB grown in screens PPEG2 - PPEG8. **(A)** crystals grown from PPEG2, conditions: 15% (w/v) PEG10000, 0.1 M Na-Citrate (pH 4.0), 0.2 M $(NH_4)_2SO_4$, 10% Anion-Mix (Anions of Na, 0.08 M I^-, 0.04 M of Br^-, Cl^-, F^- and SO_4^{2-}); **(B)** crystals grown from screen PPEG2, conditions: 14% (w/v) PEG10000, 0.1 M Na-Citrate (pH 4.0), 0.2 M $(NH_4)_2SO_4$, 10% Anion-Mix3 (Anions of Na, 0.05 M of each anion: I^-, Br^-, Cl^-, NO_3^- and tartrate); **(C)** crystals grown from screen PPEG3, conditions: 14% (w/v) PEG10000, 0.1 M Na-Citrate (pH 4.0), 0.2 M $(NH_4)_2SO_4$, 20% Anion-Mix3 (Anions of Na, 0.05 M of each anion: I^-, Br^-, Cl^-, NO_3^-, malonate and tartrate); **(D)** crystals grown from screen PPEG7, conditions: 15% (w/v) PEG10000, 0.1 M Na-Citrate (pH 4.0), 0.18 M $(NH_4)_2SO_4$, 10% AnionMix 6 (0.08 M NH_4Br and 0.07 M NH_4I); **(E)** crystals grown from screen PPEG7, conditions: 15% (w/v) PEG10000, 0.1 M Na-Citrate (pH 4.0), 0.2 M $(NH_4)_2SO_4$, 0.1 M NH_4NO_3; **(F)** crystals grown from screen PPEG8, conditions: 15% (w/v) PEG10000, 0.1 M NaOAc (pH 4.75), 0.17 M $(NH_4)_2SO_4$, 0.2 M NH_4NO_3.

5.3.3. New batch of SlfB

Since DLS measurements showed that for monomodal solutions of SlfB NaCl and buffer at pH 7.4 are required the co-operation partner (**JOHANNES RAFF**, Helmholtz Zentrum Dresden) decided to use the buffer **SLP1** already during purification. DLS upon arrival of the purified protein (JGA12-N) showed (see **Figure 43**) that this optimized purification led to an improvement of solution properties. SlfB in solution is now monomodal with a R_H of 6.41 nm.

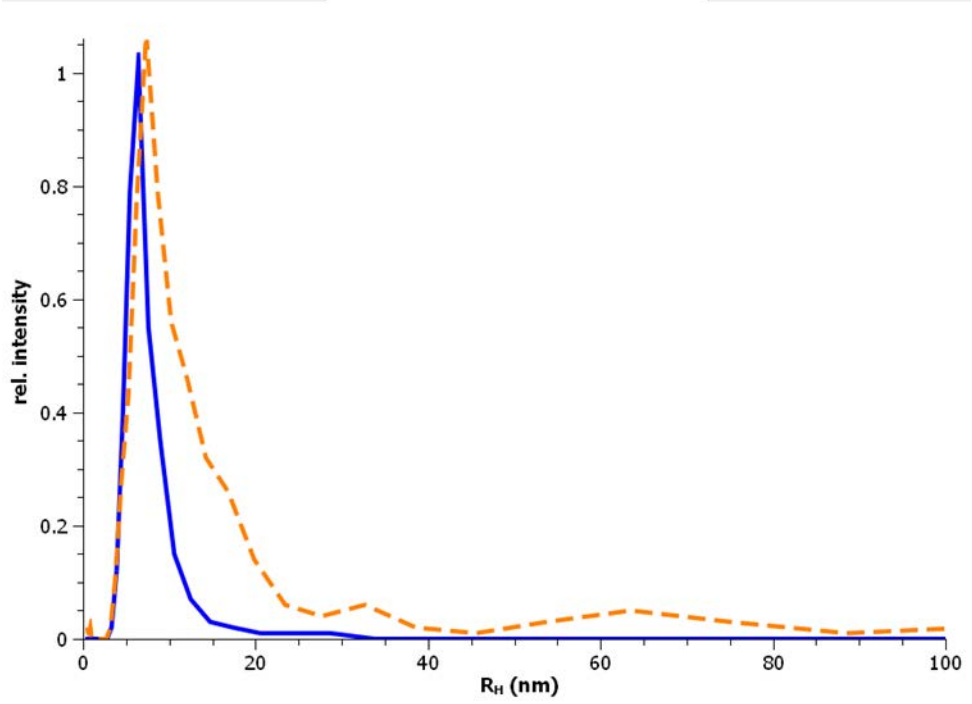

Figure 43: Radius distribution of SlfB (JGA12-N, blue) in comparison with SlfB solution JGA12-B_DIL (orange, dashed). It can clearly be seen that JGA12-N is less polydisperse.

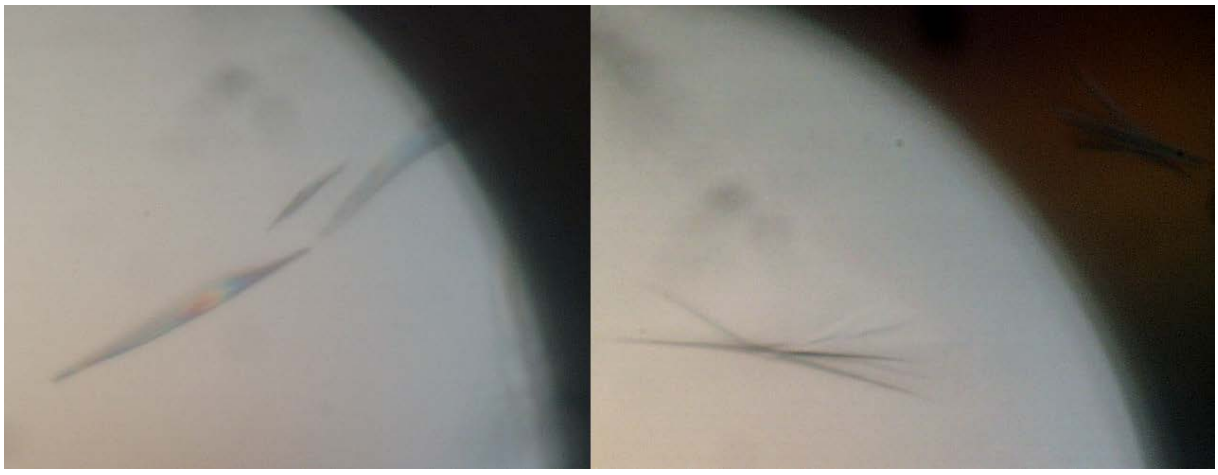

Figure 44: Crystals of SlfB grown from a screening of JGA12-N against PPEG7. Conditions: 15% (w/v) PEG10000, 0.35 M NH_4NO_3, 0.1 M Na-Citrate (pH 4.0), 8 mM NH_4I, 7 mM NH_4Br.

The new batch of SlfB was then screened against PPEG screens 2, 3, 7, 8 and the newly designed PPEG9 (see **appendix, chapter 9.2**). There was no general improvement in crystallization but in PPEG7 thin plates (**Figure 44**) with a length of approx. 200 µm could observed after two weeks. These are the biggest crystals obtained for SlfB so far. Still these crystals appeared as very thin plates and were preserved for further investigation of the crystals at beamline P11 (PETRA III).

5.3.4. *In situ* DLS

Directly after first crystals of SlfB could be observed in the initial screens it was tried to reproduce and optimize crystal growth manually. Conditions that yielded crystals were prepared and selected crystallization experiments monitored by DLS. The best initial crystals could be obtained with PEG 2000 MME as precipitant hence in these initial optimizations under *in situ* DLS observation it was focused on conditions containing PEG 2000 MME. From the first measurements on it was clear that the conditions were too strong: No more monomeric SlfB could be detected by DLS. Instead a slowly growing fraction at initially 20 – 30 nm could be observed, accompanied by larger aggregates at over 100 nm. It can be seen in **Figure 45** that the radius distribution during the first 25 hours of crystallization depends on the crystallization conditions. The aggregates are smaller at 18% PEG 2000 MME (blue circles) than at 22%. But also the concentration of ammonium sulfate has an influence, the green triangles (corresponding to 0.2 M ammonium sulfate, 22% PEG 2000MME) have initially a radius comparable to that of SlfB at 18% PEG, from 12 hours on however their radius distribution is similar to that of SlfB at 22% PEG and 0.18 M ammonium sulfate. The initially not so strong aggregation at higher ammonium sulfate concentrations was exploited in the PPEG screens were in most cases ammonium sulfate concentrations between 0.20 and 0.22 M were used. These initial *in situ* DLS experiments also showed that a lower PEG concentration may yield better crystals. This was also considered during the design of the first optimization screen PPEG. The results of *in situ* DLS presented in **Figure 46** show the importance of protein concentration in successful crystallization. Even though the differences in precipitant concentration are large (20% difference), it can clearly be seen that the radius distribution during the 55 hours of automated observation depends strongly on the protein concentration ($c_{DIL} = c_{DIAL}/2$) whilst the radius distribution at a certain protein concentration is nearly identical. The crystals obtained from this experiment

were bigger in the case of JGA12-B_DIL. Optimization of crystallization was then, also based on the results of *in situ* DLS, continued with this protein solution.

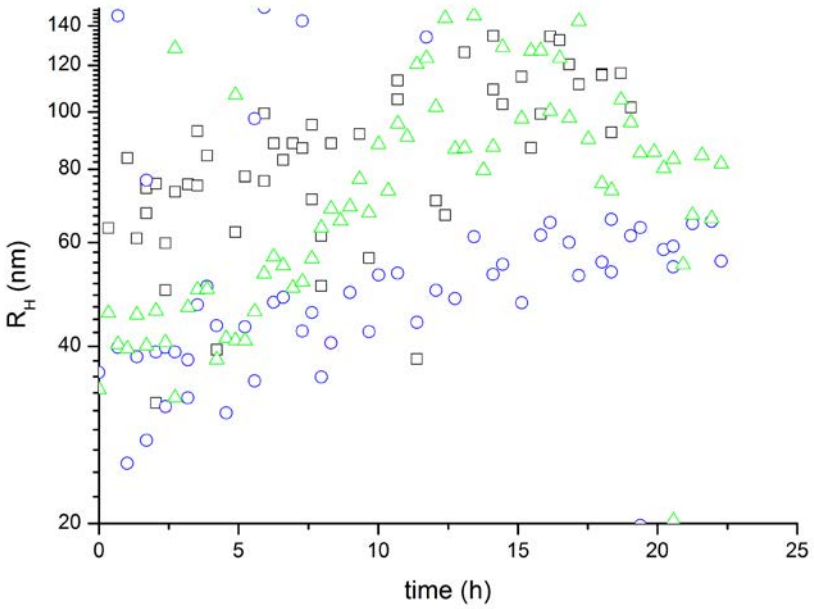

Figure 45: *In situ* DLS during a crystallization experiment of SlfB vs. PEG 2000MME.Conditions are:(A) black boxes: 22% PEG 2000MME, 0.15 M ammonium sulfate, 0.1 M NaOAc-buffer (pH 4.75), 15 % glycerol; (B) green triangles: 22% PEG 2000MME, 0.2 M ammonium sulfate, 0.1 M NaOAc-buffer (pH 4.75), 15 % glycerol and (C) blue circles: 18% PEG 2000MME, 0.15 M ammonium sulfate, 0.1 M NaOAc-buffer (pH 4.75), 15 % glycerol.

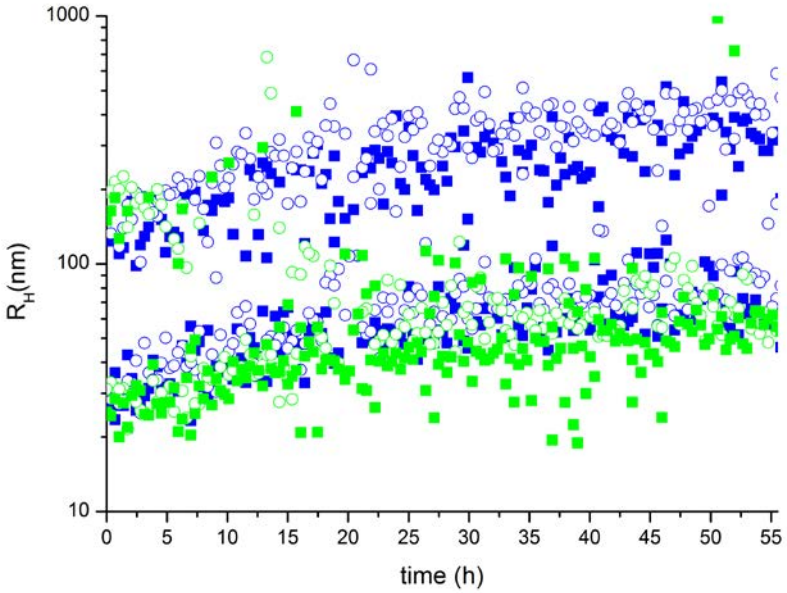

Figure 46: Comparison of the influence of protein concentration and precipitant concentration on submicroscopic processes during crystallization. In all conditions 15% glycerol, 86 mM NaOAc-buffer (pH 4.75) and 0.25 M ammonium sulfate are present. Conditions marked with circles contain 16% PEG 2000MME and those marked with a box contain 20% PEG 2000MME. Blue is SlfB solution JGA12-B_DIAL and green represents SlfB solution JGA12-B_DIL.

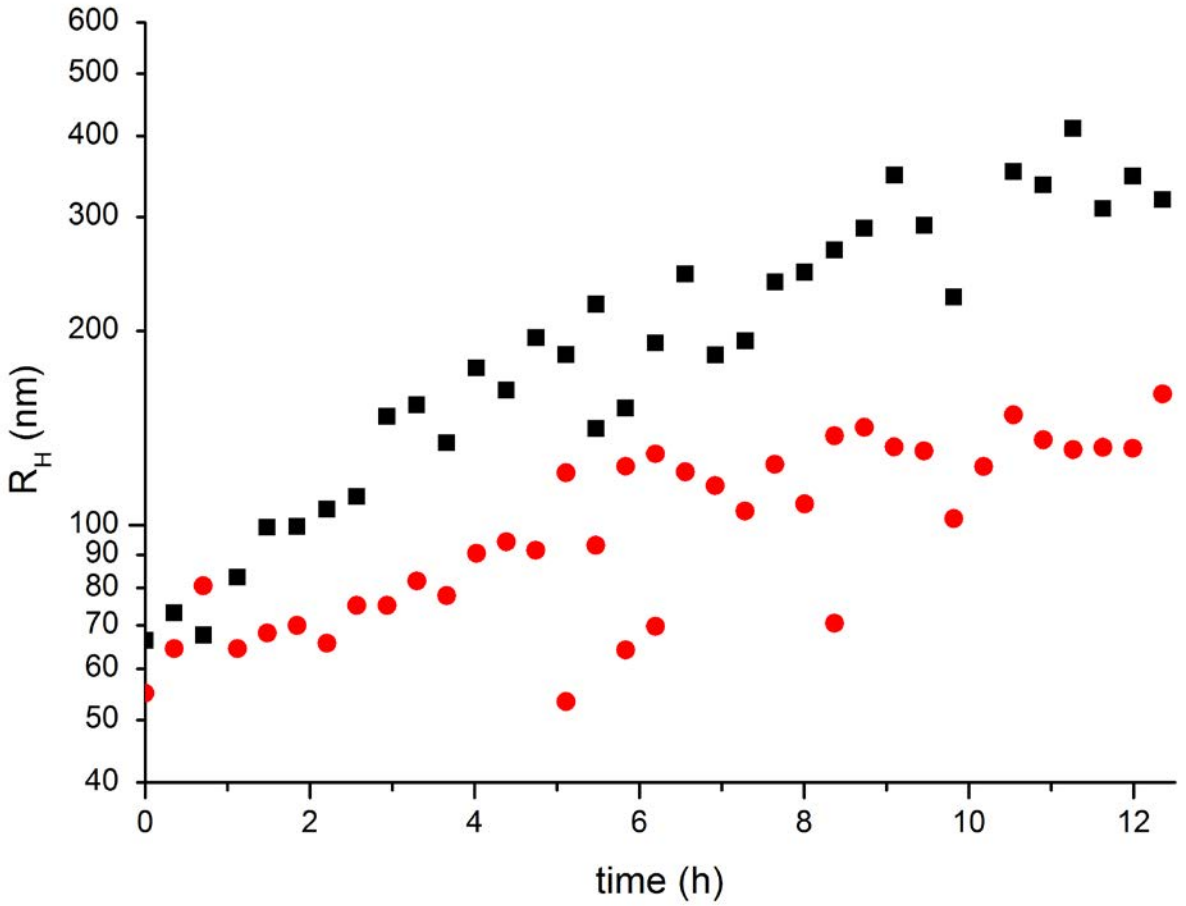

Figure 47: In parallel to the on-going crystallization experiments also new conditions were tested. Here the crystallization of SlfB with PEG 4000 is investigated. (A) black boxes: 10% (w/v) PEG 4000, 10% ethylene glycol, 50 mM TRIS (pH 7.4) and 300 mM NaCl; (B) red circles: 8% (w/v) PEG 4000, 10% ethylene glycol, 4% 2-propanol, 50 mM TRIS (pH 7.4) and 300 mM NaCl.

Statistics from the PDB show that PEG 4000 is one of the most used precipitants in successful crystallization experiments **[159]**. Thus a small set of conditions with PEG 4000 was prepared and the crystallization experiments monitored by automated *in situ* DLS within a MRC1-plate. In **Figure 47** the results of such an experiment are displayed. The rapid growth of particles indicates in case (A) – 10% (w/v) PEG 4000, 10% ethylene glycol, 50 mM TRIS (pH 7.4) and 300 mM NaCl – aggregation. After five days precipitation could be observed in the crystallization droplet. The reduction of PEG 4000 concentration (from 10% to 8%) and addition of 4 % 2-propanol (case (B)) led to a slower increase in particle growth. However: in this droplet still precipitation could be observed, but three days later as in case A. The reason for non-successful crystallization may be attributed to the high pH-values (7.4) relative to the pH-values at successful crystallization (pH 4 - 4.75) and to the missing ammonium sulfate. Thus during the design of the optimization screens PPEG to

PPEG3 the pH of all conditions was kept below pH 7.0 and ammonium sulfate was added to all conditions. *In situ* DLS applied to monitor crystallization experiments of SlfB improved the quality of the optimization screens and thus facilitated optimization of protein crystallization.

5.3.5. SAXS of SlfB

The evaluation of SAXS data with the program *GNOM* **[152]** showed that SlfB in solution is monomodal. The radius of gyration (R_g) as calculated from the SAXS data by GNOM of SlfB is 6.13, the calculated M_W is approx. 115 kDa which is in good concordance with the molecular weight expected from the sequence of SlfB (~ 120 kDa). This clarifies that SlfB in solution is a monomer. This information was then used in *ab initio* modeling of the low-resolution structure of SlfB. Applying *ATSAS* **[153]** programs *DAMMIF* **[155]** and *DAMMIN* **[154]** on the SAXS data processed by *GNOM* showed that SlfB in solution exists as an elongated molecule in solution (**Figure 48**) with several domain-like structure elements. This confirmed the results from DLS that the R_H (as calculated from DLS measurements) is too large for the present molecular weight hence an elongated shape of the molecule rather than globular and internal flexibility was assumed.

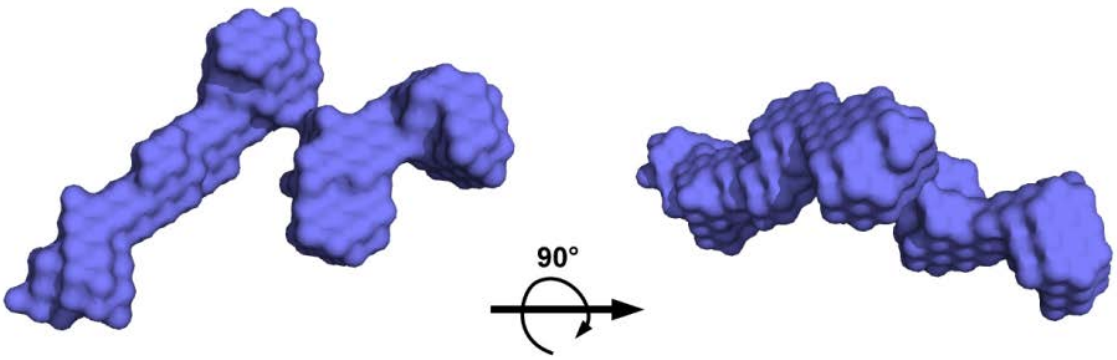

Figure 48: DAMMIN-model of SlfB as determined from SAXS-data.

Protein BLAST **[143]** search with the sequence of SlfB revealed the existence of a three dimensional structure (PDB accession code: **3PYW**, **[149]**) of the SLH domains of Sap *Bacillus anthracis*. Sap is a surface layer protein and bears an overall homology with SlfB of 28%. Alignment of the sequence of the crystallized fragment of Sap with the SlfB sequence using the BSSB server **[160]**, shows a homology of 41% and identity of 22% for the N-terminal region of SlfB (Residue 2 – 185). It is known **[149]** that most S-layer proteins, including SlfB **[129]**, share three SLH domains at

the N-terminal region. Moreover it was proposed **[149]** that albeit the sequence homology might vary, most SLH domains should share a high structural homology. Therefore the crystal structure of the SLH region of Sap was used for modeling of the N-terminal region of SlfB with the data derived from SAXS measurements applying *CRYSOL* and *SASREF* (ATSAS online server) **[156]**. However these programs failed to model the crystal structure of the SLH domains of Sap into the SAXS-model of SlfB. The SLH domain is either to small compared to the rest of the protein or the 3D structure of Sap differs too much from the SAXS low resolution N-terminus of SlfB. **Figure 49** shows a manual overlay – created with PyMol **[161]** - of the Sap crystal structure (derived from the PDB, accession code: **3PYW**) and the DAMMIN-model of SlfB. It should be noted that this is just a possible orientation of the molecule and that the sequence homology between the SLH domains from Sap and SlfB is rather low (homology modeling with SWISS-MODEL **[162]** showed no good result). Still as can be seen in **Figure 49** the crystal structure of the SLH domains of Sap from *B. anthracis* **[149]** fits quite well into the terminal domain of the DAMMIN-model of SlfB.

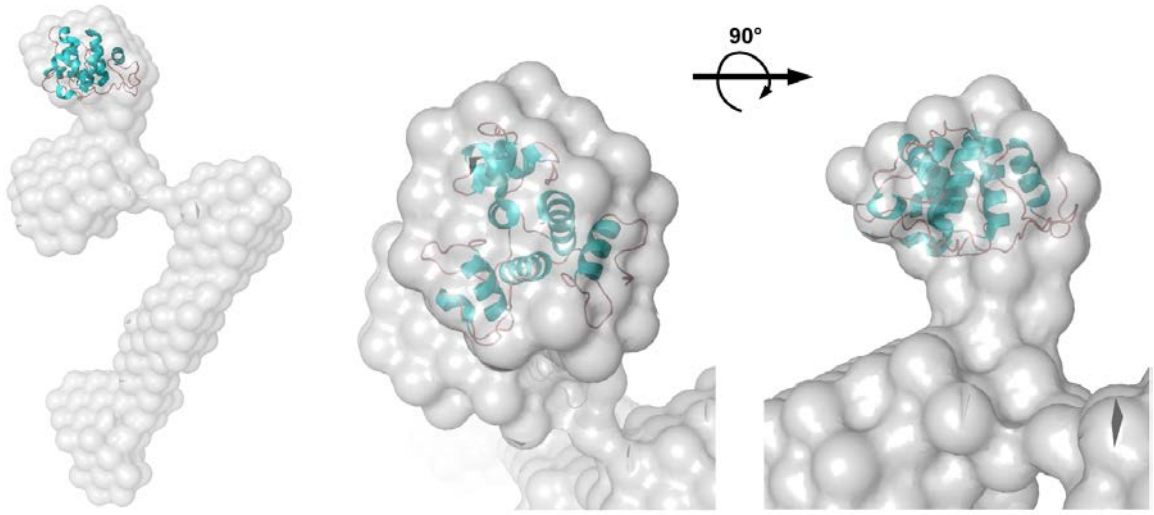

Figure 49: Overlay of the DAMMIN-model of SlfB and the X-Ray structure of the SLH domains of Sap from *B. Anthracis* (PDB accession code: **3PYW**, **[149]**)

5.3.6. *In situ* Proteolysis of SlfB

Initially the Floppy Choppy-kit (Jena Bio Science) was applied for *in situ* proteolysis **[163, 164]** of full length SlfB from JGA12. This method was chosen after crystallization experiments only yielded small crystals even after extensive screening and optimization of buffer- and crystallization conditions. Moreover DLS and SAXS

measurements showed that SlfB has an elongated shape in solution (see **chapter 5.2.5**) which points to the possibility of highly flexible domains that – without further modification – would resist attempts to form large crystals. It could be shown **[163, 164]** that the method of in situ proteolysis provides a good way to get at least X-ray structures of single domains of large and/or flexible proteins.

In situ DLS monitoring of the proteolysis experiments was carried out directly after mixing SlfB and the respective protease solutions and afterwards in selected intervals during two weeks. DLS has the advantage over SDS-PAGE **[157]** that it directly yields information of the non-denatured status of the protein. Still SDS-PAGE was used to gain additional information on the state of proteolysis. For both DLS and SDS-PAGE undigested JGA12-N in its buffer and in the proteolysis buffer conditions were used as reference. In the course of the DLS monitoring conclusions were drawn and new *in situ* proteolysis experiments were started with larger volumes. In the initial experiments (see **Figure 50**) a fast decrease of R_H (from the 6.8 nm of pure SlfB) could be observed at 100 µg/mL subtilisin (1:10 dilution), in all other solutions except subtilisin at 1:100 dilution and papain at 1:10 – where a slow decrease could be observed – the R_H remained nearly constant. These observations hold true during the two weeks, the hydrodynamic radius of the sample digested by 100 µg/mL subtilisin decreased to approx. 3.8 nm while the intensity of scattered light vanished more and more. At this concentration it seems that subtilisin digests SlfB almost completely.

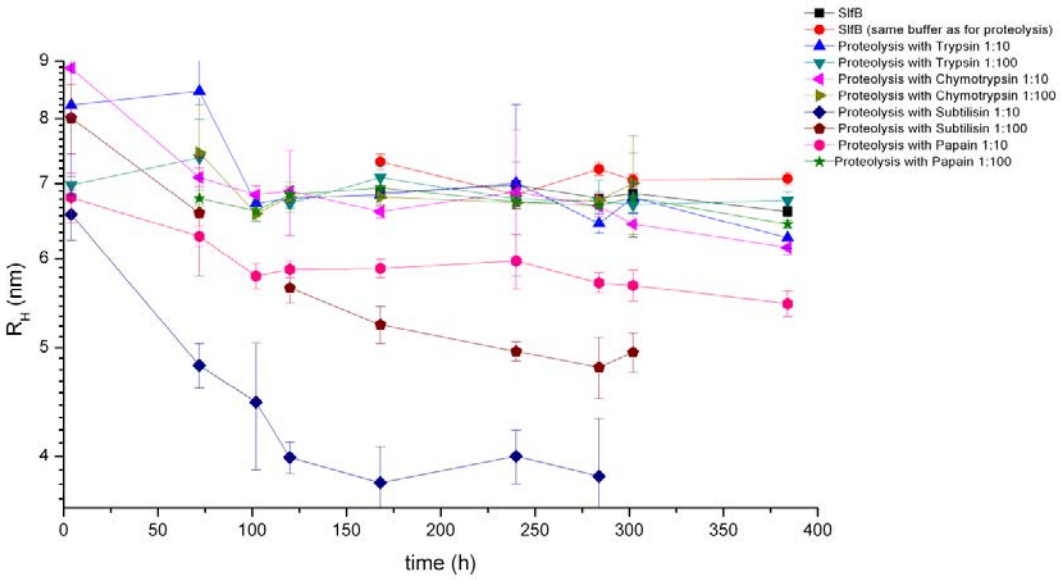

Figure 50: DLS monitoring of *in situ* proteolysis experiments for two weeks.

At a higher dilution of subtilisin (1:100 dilution, 10 µg/mL) the R_H decreased slowly to about 5 nm after two weeks. If papain at 1:10 dilution (100 µg/mL) was used the R_H after two weeks was 5.5 nm. For all other *in situ* proteolysis experiments (papain at 1:100 dilution, trypsin and chymotrypsin at 1:10 and 1:100 dilution) no significant change of R_H could be observed. Based on these initial results large scale proteolysis set-ups applying subtilisin at 1:100 and papain at 1:10 dilution were carried out.

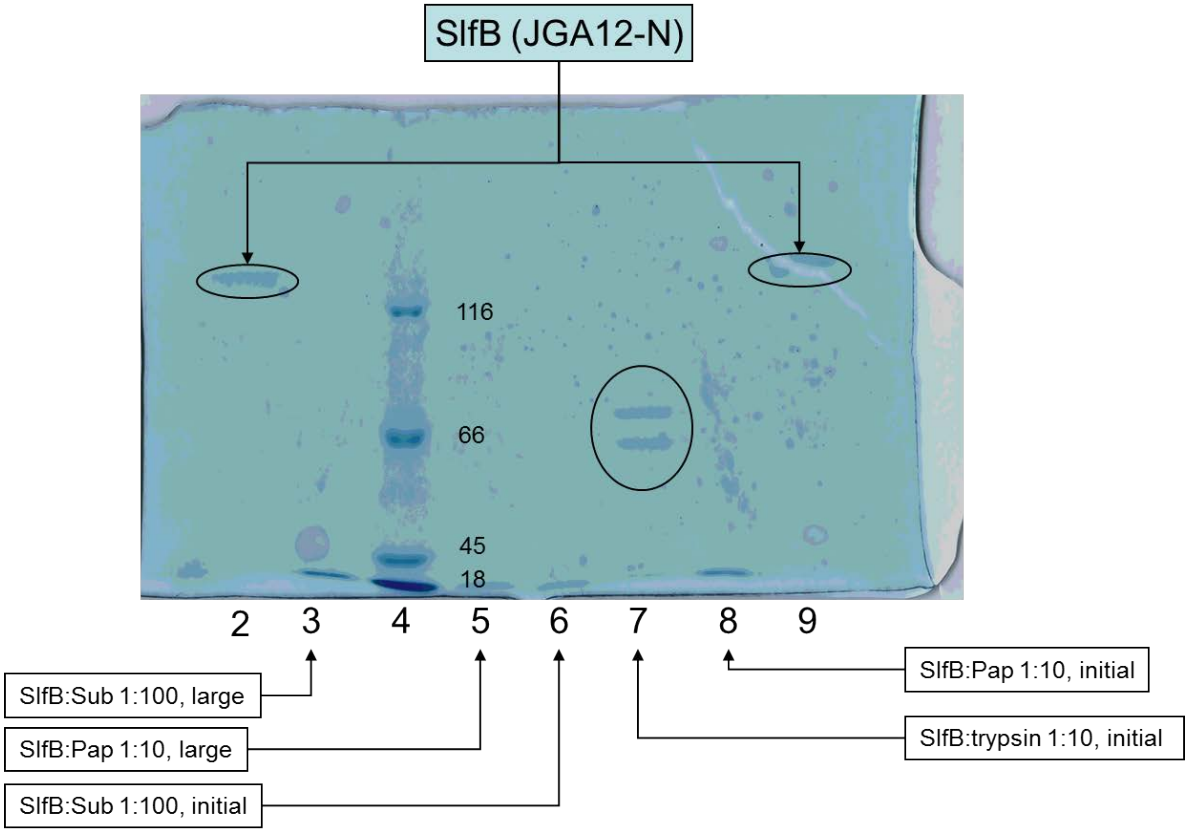

Figure 51: SDS-PAGE to monitor *in situ* proteolysis of SlfB. Whilst digestion of SlfB with 1:10 trypsin shows only little change of R_H in the DLS measurements it appears in the gel as two bands representing two fragments (Sub = subtilisin, Pap = papain).

Further analysis of these experiments by SDS-PAGE (**Figure 51**) showed that no fragments larger than 18 kDa were present in the digested sample in the case of digestions with papain and subtilisin, whilst in DLS particles with a R_H between 4.5 and 5.5 nm could still be detected. The SLH domains of SlfB have an estimated M_W of 16 kDa, it is possible that proteolysis by papain of subtilisin leads to a digestions of all SlfB, but the SLH domains. Crystallization experiments were carried out with both (subtilisin 1:100 and papain 1:10) proteolysis solutions. The concentration of the samples was adjusted applying the pre crystallization test (**PCT**, Hampton) and both solutions containing SlfB digested by subtilisin at 1:100 and by papain at 1:10 dilution were screened against 480 conditions applying the Honeybee 961 robot. After three

weeks of incubation at 20°C crystals of SlfB digested by papain grew in condition C10 (10% w/v PEG 8000, 20% v/v ethylene glycol, 0.03 M of each NPS (sodium nitrate, disodium hydrogen phosphate, ammonium sulfate), 0.1 M bicine/Trizma base pH 8.5) of the MORPHEUS screen **[165]**. These crystals (**Figure 52**), however are too small for UV-analysis and X-ray diffraction and need further optimization.

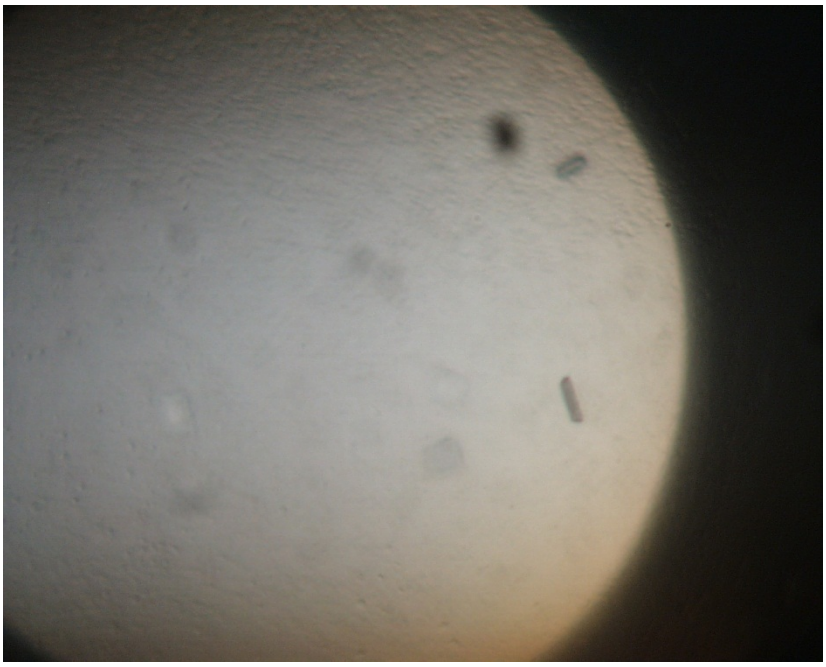

Figure 52: Crystals of SlfB digested with papain (1:10 dilution). Crystals were grown in condition C10 (10% w/v PEG 8000, 20% v/v ethylene glycol, 0.03 M of each NPS (sodium nitrate, disodium hydrogen phosphate, ammonium sulfate), 0.1 M bicine/Trizma base pH 8.5) of the MORPHEUS screen.

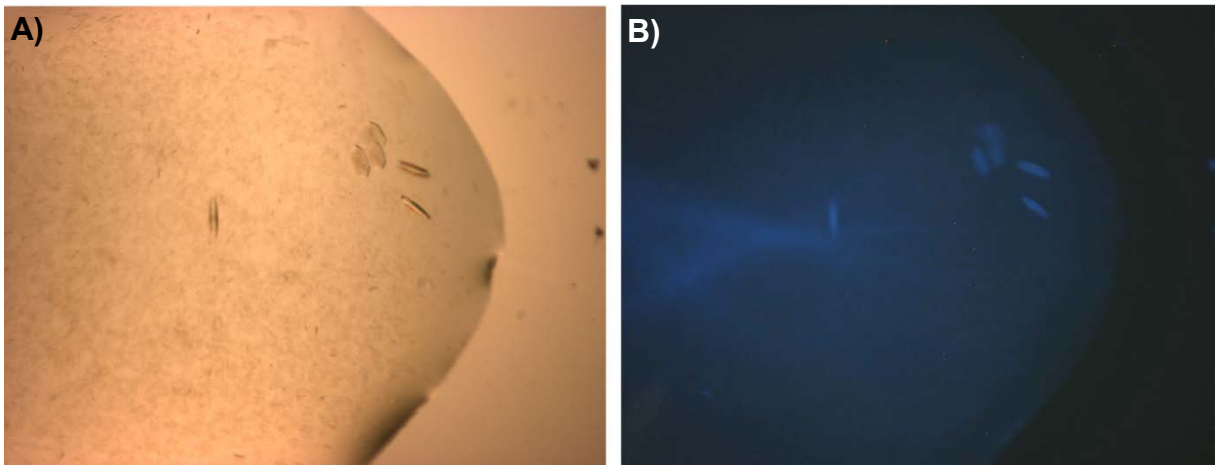

Figure 53: Crystals of SlfB digested by subtilisin grown in solution A1 of the PCT (Hampton). The strong UV-fluorescence (**B**) shows that the crystals are protein crystals.

After two month crystals (**Figure 53**) of SlfB digested with subtilisin could be observed in the PCT drop A1, containing 2.0 M ammonium sulfate and 0.1 M TRIS

hydrochloride (pH 8.5). UV-Imaging **[119]** of the crystallization droplet applying a *Crystal*LIGHT 100 (Nabitec, Germany) light source showed fluorescence of the crystals (**Figure 53**) indicating them being protein crystals. Crystals were analyzed at the consortiums beamline X13 (HASY- LAB / DESY) and proved to be X-ray suitable (see **Figure 54**). However the diffraction was too weak applying synchrotron radiation at DORIS III to estimate cell constants. Crystals are stored at 100 K for further investigation at the P11 beamline of PETRA III.

Since SDS-PAGE showed fragmentation of SlfB by trypsin (**Figure 51**) that could not be observed by DLS, a large scale approach of digestion with trypsin and chymotrypsin at 1:10 dilution was set-up. After one week of incubation the concentration of the samples was adjusted as described for the digestions with subtilisin and papain. The concentrated samples were screened against 480 conditions applying the Honeybee 961 robot. No crystals could be obtained.

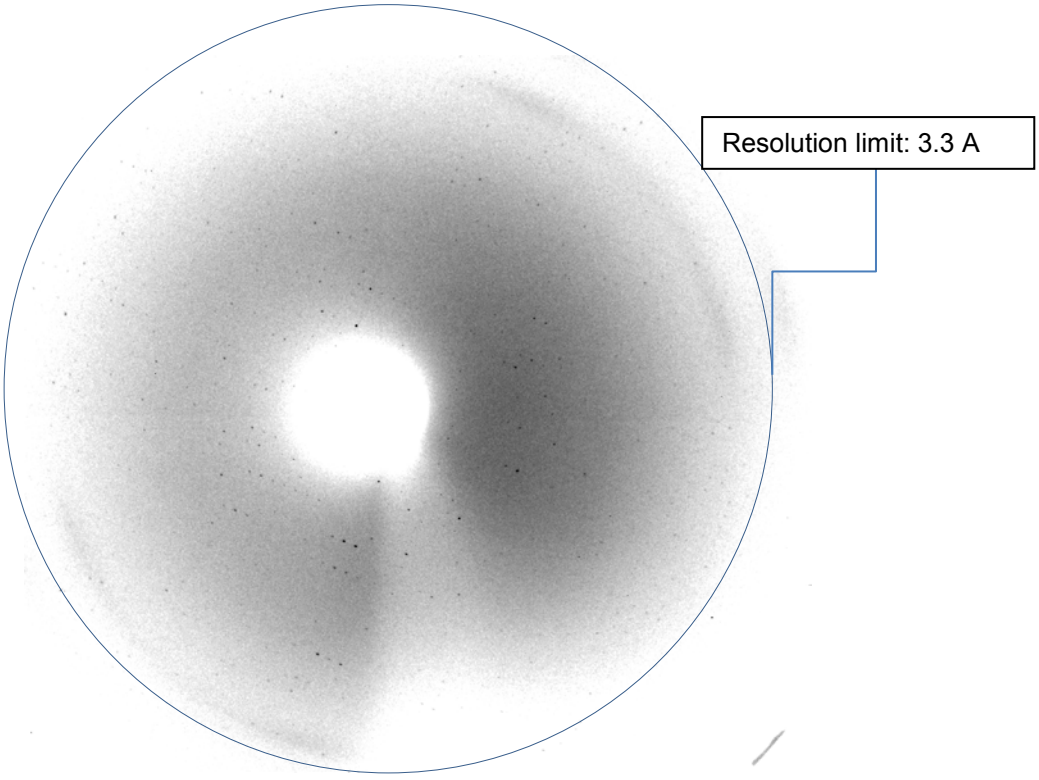

Figure 54: Diffraction image of one of the crystals shown in **Figure 53**. However, the spots visible were too weak to index the crystals. But it proves that the crystals are indeed protein crystals.

To analyze the digestion of SlfB by trypsin and chymotrypsin further SAXS was applied. As described in **chapter 5.3.5** SAXS data were processed by *GNOM* **[152]**. For digestion with trypsin at 1:10 dilution the radius of gyration (R_g) was determined to be approx. 5.9 nm (undigested: R_g = 6.13 nm), which is in concordance with the

DLS results showing only minor changes in R_H. However the M_W determined by SAXS is with about 62 kDa much smaller as for undigested SlfB (115 kDa) but similar to the M_W obtained by SDS-PAGE. For digestion with chymotrypsin at 1:10 dilution R_g was determined to be approx. 5.9 nm thus being very similar to the digestion with trypsin. Also the M_W determined by SAXS is approx. 64 kDa nearly identical with the results obtained for digestion with trypsin.

Table 3: *In situ* proteolysis of SlfB with trypsin and chymotrypsin, comparison of DLS and SAXS results.

	R_H (nm) (DLS)	R_g (nm) (SAXS)	M_W (kDa) (SAXS)
SlfB	*6.61±0.07*	*6.14±0.12*	*115*
SlfB digested with trypsin	*6.26±0.13*	*5.93±0.18*	*62*
SlfB digested with chymotrypsin	*6.14±0.09*	*5,92±0.27*	*64*

DAMMIF **[155]** was used from the ATSAS online server **[153]** for *ab initio* modeling of the digested fragments of SlfB and comparison with the full length protein. Alignments of the DAMMIF-models with PyMol show that digestion with trypsin results in a branched and elongated molecule bearing not many similarities with SlfB. This is different for chymotrypsin here an alignment with full length SlfB shows that both molecules are nearly identical.

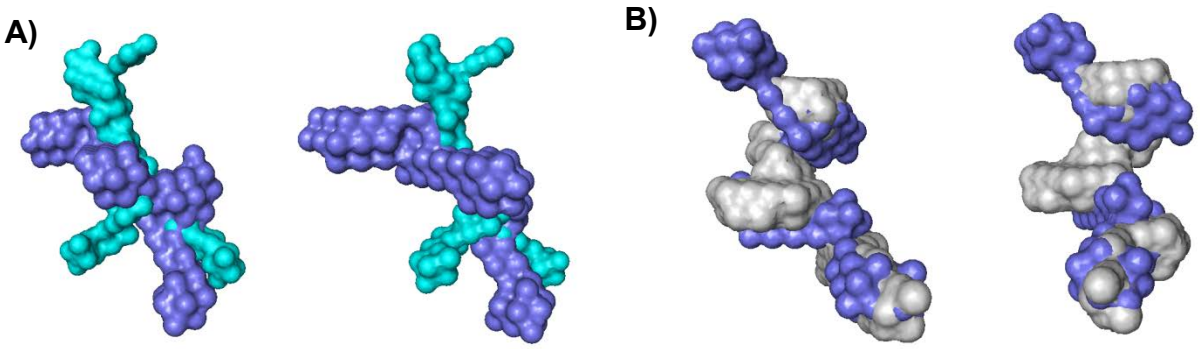

Figure 55: Alignment of DAMMIF models of **(A)** full length SlfB (blue) and trypsin digested SlfB (cyan) and **(B)** full length SlfB (blue) and chymotrypsin digested SlfB (grey).

The model obtained by *DAMMIF* from SAXS data for SlfB after digestion with chymotrypsin lacks only a terminal domain. It was proposed in **chapter 5.3.5** that the here missing part of SlfB consists of the SLH domains. Thus one possibility is, that chymotrypsin digests these N-terminal domains of SlfB. However the M_W of the remaining fragment is with – as determined by SAXS –approx. 62 kDa lower than the

expected M_W of SlfB without the SLH domains (approx. 100 kDa: SlfB: 115 kDa, SLH domains of SlfB approx. 16 kDa).

5.3.7. Influence of Bivalent Cations on SlfB Stability

It could be shown **[146]** that SlfB from JGA12 as other SLPs has binding sites for bivalent cations. From first crystallization experiments it was known, that SlfB tends to form small and irregularly shaped crystals (see **chapter 5.3.2**). Furthermore SlfB in its Cat^{2+} free state showed instability during DLS measurements at room temperature. Assuming that instability at room temperature and the growth of small and unshaped crystals are correlated it is necessary to stabilize the protein for improved crystal growth. This stabilization on the other hand should not lead to a favored 2D over 3D crystallization. To find the best conditions SlfB at two different pH-values was initially mixed with 20 mM solutions of magnesium- and calcium acetate, strontium- and barium chloride and zinc- and copper sulfate in water and after evaluation of the DLS results of these initial experiments an improved set-up was designed where monodisperse SlfB of the JGA12-N batch was mixed with various concentrations of $MgCl_2$, $CaCl_2$ and $SrCl_2$ at three different pH-values. The mixtures were observed by *in situ* DLS directly after preparation, after one day and after nine days.

Based on initial DLS experiments with 20 mM solutions of various bivalent cations (magnesium- and calcium acetate, strontium- and barium chloride and zinc- and copper sulfate) and SlfB JGA12-B_DIL and JGA12-B_DIAL at pH 4.0 (200 mM sodium citrate buffer) and pH 7.4 it was expected that the addition of calcium- and strontium-ions would not improve the solution properties but lead to protein aggregation. For magnesium acetate a slight improvement of solution conditions could be observed. The presence of barium-, copper-, and zinc-ions led to strong aggregation at both pH-values (pH 7.4 and pH 4.0) of JGA12-B_DIL (SlfB).

Already during the recording of the DLS measurements of the experiments it could be observed that at 500 mM concentration of Cat^{2+} and pH 7.4 or 4.75 the solution was monodisperse with a R_H slightly shifted from 6.2 nm for JGA12-N to 8.04 nm. This shift in R_H is not surprising taking the high ion concentration into account. Completely unexpected was the monodispersity and total absence of aggregation at this concentration of bivalent cations.

At pH 2.0 with 500 mM Sr^{2+} or Ca^{2+} JGA12-N was still monodisperse in solution but as a defined oligomer with R_H of approx. 26 nm (**Figure 57B** and **Figure 58B**). Addition of 500 mM Mg^{2+} led to formation of a broad peak at approx. 70 nm, indicating the presence of an ensemble of oligomers. The protein alone at pH 2.0 showed a broad and diffuse signal in DLS (**Figure 56 A**). For all three bivalent cations strong concentration dependence could be observed: the R_H for the dominant particle in solution was bigger for 500, 100 and 50 mM than for the lower concentration. Especially at these lower concentrations (1, 0.5 and 0.1 mM Cat^{2+}) the solution was oligomeric but monodisperse, indicating that defined oligomers exist in solution.

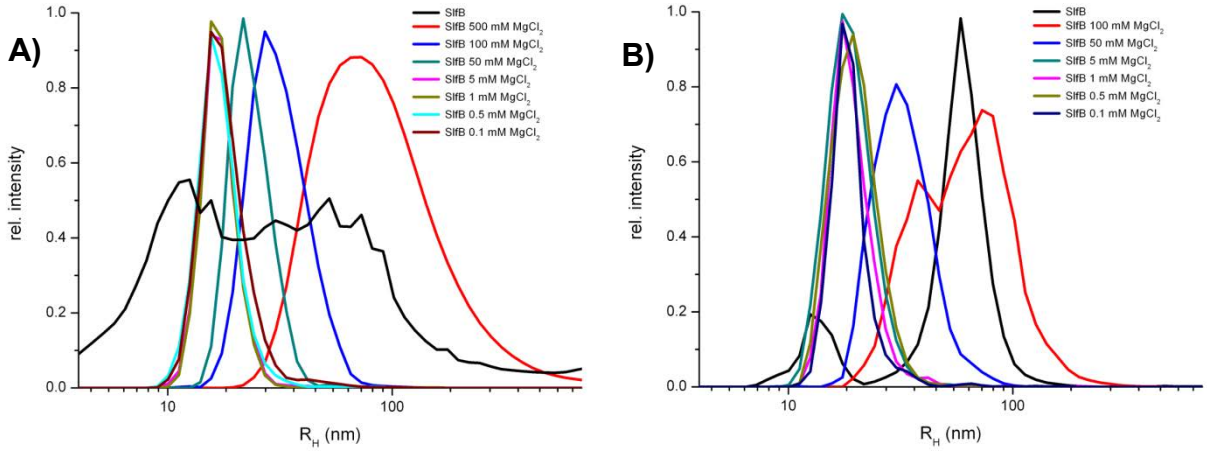

Figure 56: Radius distribution of SlfB at pH 2.0 with (colored curves) or without (black curve) Mg^{2+} directly after preparation of the samples (**A**) and after nine days at ambient temperature (**B**).

After nine days no DLS signal could be recorded in the wells containing 500 mM Mg^{2+}, Ca^{2+} or Sr^{2+}, a thick opaque crystalline like layer had formed in the droplets. This was not the case for JGA12-N at pH 2.0 without bivalent cations; here two defined particle species coexist in solution with a R_H of approx. 12 and 58 nm. A possible explanation is that the defined oligomers are building blocks of 2D-crystals that form in the course of nine days. Since the surface layer also protects the bacteria from low pH-values and bivalent cations are required for its formation, it is obvious that surface layer formation can be induced at low pH in the presence of high concentrations of bivalent cations. For all concentrations below 500 mM and all three cations DLS could be measured after nine days. For 100 mM of the respective bivalent cations polydisperse radius distributions were calculated from DLS measurements. For Sr^{2+} and Ca^{2+} particles with a radius of about 100 nm coexisted with those detected in the initial measurements (see **Figure 57 B** and **Figure 58 B**)

whilst for Mg^{2+} the initially derived broad peak was now split into two peaks (**Figure 56 B**). Nothing changed for SlfB solutions with bivalent cations at concentrations below 50 mM: monodisperse radius distribution with a R_H of approx. 20 nm was observed by DLS.

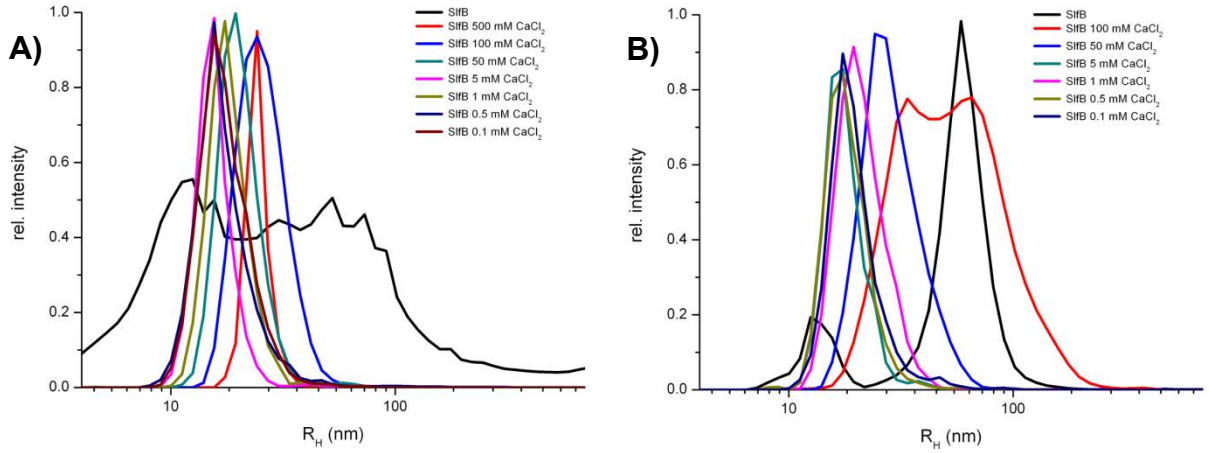

Figure 57: Radius distribution of SlfB at pH 2.0 with (colored curves) Ca^{2+} (results of pure SlfB (black) are shown for comparison of results) directly after preparation of the samples (**A**) and after nine days at ambient temperature (**B)**

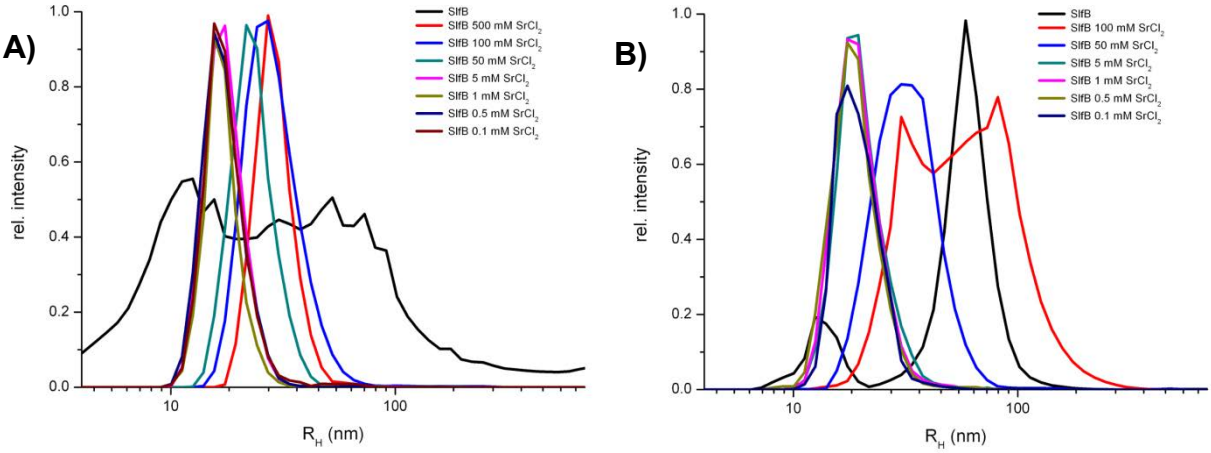

Figure 58: Radius distribution of SlfB at pH 2.0 with (colored curves) Sr^{2+} (results of pure SlfB (black) are shown for comparison of results) directly after preparation of the samples (**A**) and after nine days at ambient temperature (**B)**

The shifts in R_H observed within nine days for 50 and 100 mM of Ca^{2+} and Sr^{2+} in addition to the formation of an opaque protein layer at 500 mM of Mg^{2+}, Ca^{2+} or Sr^{2+} at pH 2.0 indicates a concentration dependence of the velocity of surface layer formation in vitro. It can be speculated that even a critical value of bivalent cation concentration exists below which no 2D-crystals form but the protein is preserved in stable oligomers. At all Ca^{2+} and Sr^{2+} concentrations between 100 and 0.1 mM in

protein buffer (pH 7.4) a disturbed DLS signal was recorded during the measurements directly after mixing protein and cation solution together indicating on-going aggregation at room temperature at these conditions.

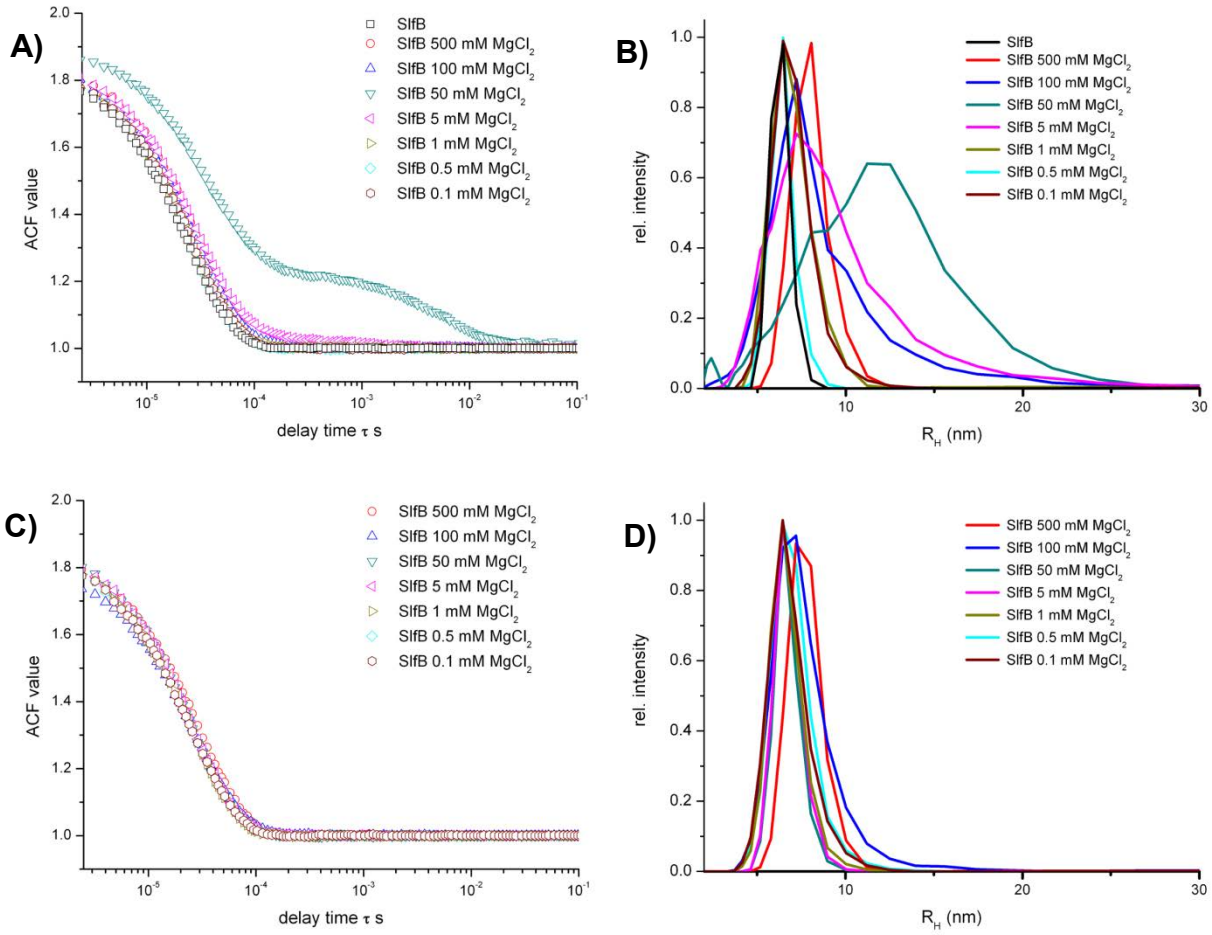

Figure 59: Results of DLS measurements directly after the addition of $MgCl_2$ at pH 7.4 (**A** and **B**) and pH 4.75 (**C** and **D**). The ACF in A shows that only the addition of 50 mM of Mg^{2+} leads to a strong deviation from the curve obtained for the pure protein at this pH. At pH 4.75 however all solutions containing Mg^{2+} deviate strongly from the pure protein at that pH: DLS in SlfB at pH 4.75 without bivalent cations resulted in a non-regular ACF. Mg^{2+} has here a stabilizing effect right after the addition to the protein solution.

As can be seen in the ACF overlay for these concentrations (**Figure 60 A** and **E**) this is especially the case for Ca^{2+} were only measurements at 100 and 0.5 mM concentration give an ACF that corresponds to a evaluable measurement. For Sr^{2+} concentrations between 5 and 0.5 mM a valid ACF can be obtained although the fitted curves show no asymptotic approach to 1 at higher relaxation times. The resulting radius distributions, which are calculated from the non-regular ACF, are biased and thus will not be evaluated further.

This was different for Mg^{2+} where at pH 7.4 only for 50 mM Mg^{2+} aggregation could be observed (**Figure 59 A** and **B**). At all other conditions the solutions were monodisperse in DLS. This confirmed the initial experiments where Mg^{2+} was the bivalent cation that stabilizes SlfB most at pH 7.4. For all three cations DLS measurements showed much better results at pH 4.75, the peaks in radius distribution are more defined indicating low polydispersity. Only for 50 mM $CaCl_2$ and 0.5 mM $SrCl_2$ slight aggregation of SlfB could be observed right after the preparation of the mixtures (**Figure 60 D** and **H**). This is interesting since most of the crystallization experiments have been carried out at pH values between 4.0 and 5.0. It can be seen that SlfB solutions at pH 4.75 containing bivalent cations are generally less polydisperse than SlfB without bivalent cations (see **Figure 59 D** and **Figure 60 D and H**).

For the crystallization of SlfB even more interesting is the long term stability at room temperature. All bigger crystals obtained so far grew after one to two weeks at 20°C thus SlfB needs to be stable at these conditions for at least one week. Aggregation or other forms of protein degradation can lead to minor crystal quality as in the case of SlfB. The pH dependence of SlfB stability is also interesting: the desired condition should show no degradation at pH 4.75 and pH 7.4.

Favored are conditions that proved to be stable already directly after the addition of the respective bivalent cation. This is true for all conditions with $MgCl_2$ except 50 mM $MgCl_2$. As can be seen in **Figure 61 B** and **D** the narrowest peak obtained from DLS measurements after nine days at 20±1°C with pH values of 4.75 and 7.4 is that of SlfB with 100 mM $MgCl_2$ in solution. No aggregation can be observed, the solution is monodisperse. Nearly as good results could be obtained for 50 mM $MgCl_2$ but this condition showed initially aggregation. The R_H of SlfB at 100 mM $MgCl_2$ with 6.45 nm is close to the R_H measured for SlfB without bivalent cations after centrifugation. At 500 mM Mg^{2+} this peak is shifted to 8.04 nm, probably due Mg^{2+} mediated protein-protein interaction. As shown before, directly after preparation of the solutions no valid DLS results could be obtained for SlfB at any concentration of Ca^{2+} or Sr^{2+} at pH 7.4.

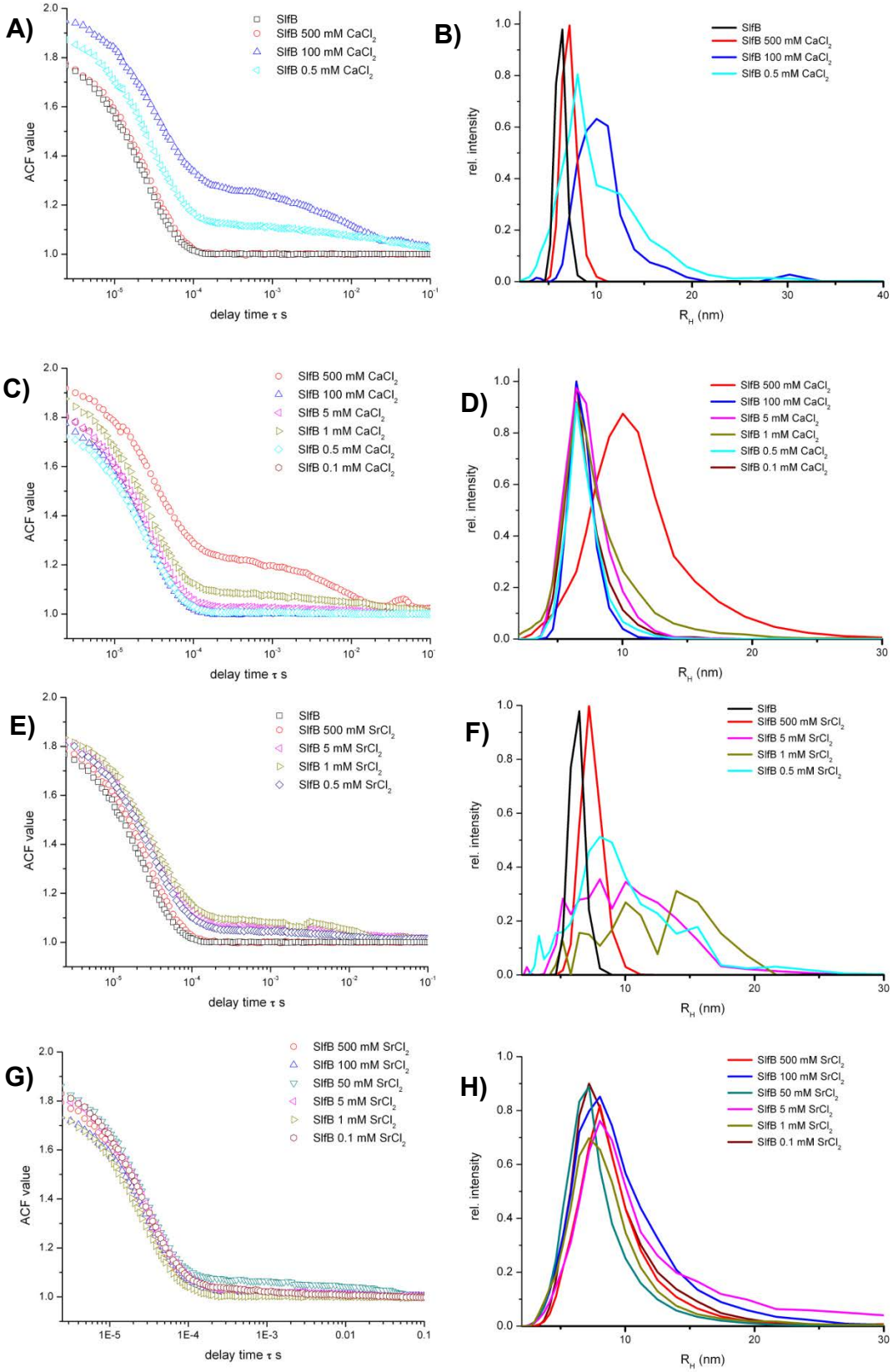

Figure 60: Results of DLS measurements directly after the addition of $CaCl_2$ at pH7.4 (**A** and **B**) and pH 4.75 (**C** and **D**) and $SrCl_2$ at pH 7.4 (**E** and **F**) and pH 4.75 (**G** and **H**).In A-B and E-F many ACF showed irregular behavior. The resulting curves were omitted. Besides the results for 500 mM of Sr^{2+} or Ca^{2+} the stability of SlfB is worse than after the addition of $MgCl_2$.

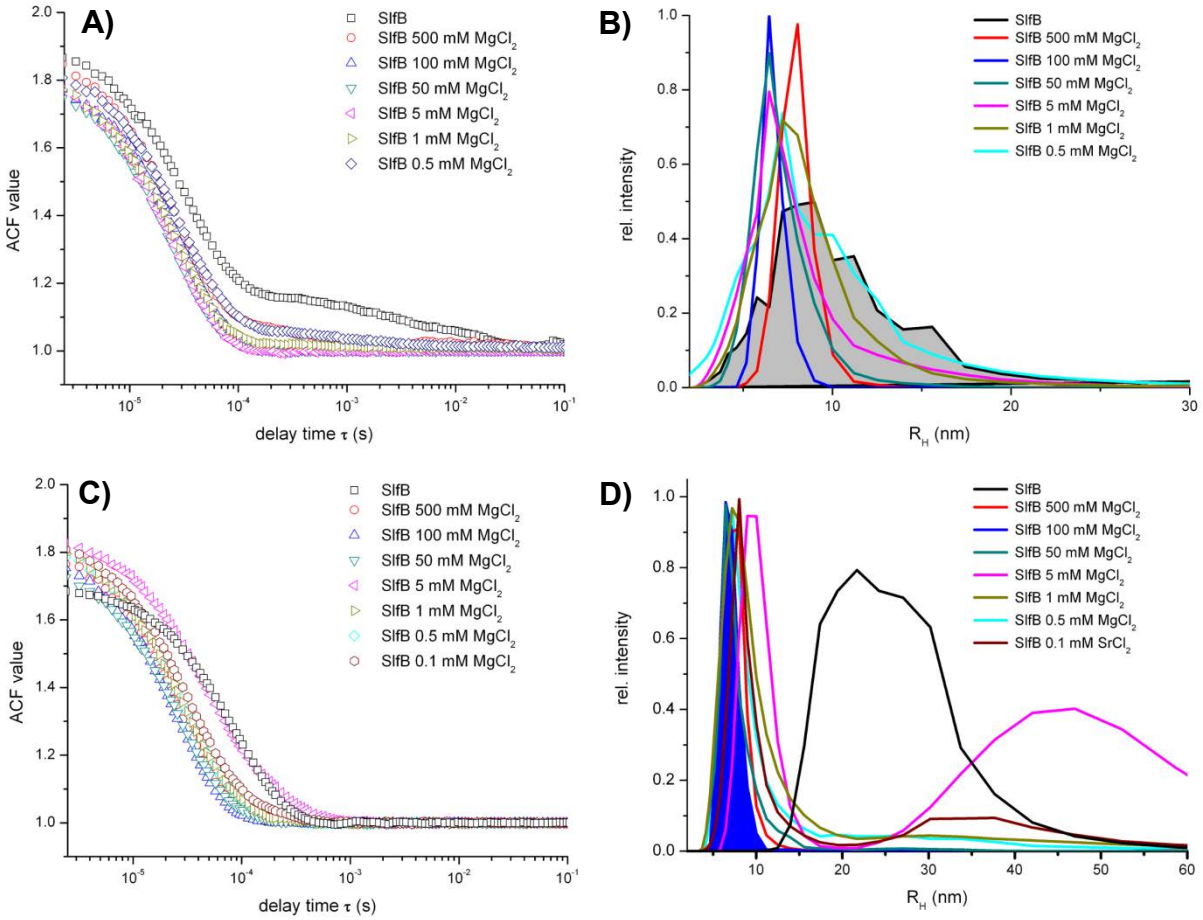

Figure 61: Results of *in situ* DLS measurements in solutions of SlfB at pH 7.4 (**A)** and **B)**) and pH 4.75 (**C)** and **D)**) with (curves in colors) and without **Mg^{2+}** (black curves) at different concentrations after nine days at 20±1°C. From comparisons of the ACF (**A)** and **C)**) and radius distributions (**B)** and **D)**) it is clear that within a defined range of concentration, Mg-ions have a stabilizing effect on SlfB. Both ACF and radius distribution show less aggregation/oligomerization with Mg^{2+} than without. The only deviation can be seen in **C)** and **D):** at 5 mM Mg^{2+} SlfB shows aggregation at higher radius than SlfB without $Mg^{2+.}$ However: pure SlfB lacks a monomeric species (see **D)**) whilst SlfB with 5 mM Mg^{2+} (magenta) shows aggregated SlfB in coexistence with monomeric protein. SlfB is most stable (at both pH values) after nine days at ambient temperature when it contains 100 mM Mg^{2+} (blue curve in **B)** and **D),** in **D)** filled for clarification). Similar results can be obtained at half the Mg concentration (curve in dark cyan).

The fact that DLS cannot be measured in solutions containing 0.1 to 100 mM of Sr^{2+} and Ca^{2+} changes after nine days. At 100 mM concentration of either $CaCl_2$ (**Figure 63 B**) or $SrCl_2$ (**Figure 62 B**) no aggregation can be observed and in the latter case the radius distribution overlay shows nearly identical solution properties with that obtained for SlfB with 100 mM $MgCl_2$ (R_H = 6.45 nm in both cases).

At pH 4.75, SlfB remains monodisperse and monomeric for nine days at 20±1°C when the solution contains 50 – 500 mM $SrCl_2$ (see **Figure 62 D**). At 5 mM, heavy aggregation can be observed, at lower concentrations of $SrCl_2$ most of the protein remains in a monomeric state but some aggregation can be observed between 20 and 60 nm. As at pH 7.4 the best results were obtained for the droplet containing 100 mM $SrCl_2$. But the difference in R_H between 100 and 500 mM of the bivalent cation is not as big as at the higher pH value (**Figure 62 B and D**). For 100 mM $CaCl_2$ at pH 7.4 the peak is a bit broader (**Figure 63 B**) than for the same concentration of $MgCl_2$ or $SrCl_2$ indicating either structural flexibility or the presence of an ensemble of oligomers, the R_H is shifted to 7.20 nm, which is equivalent to that obtained for 1 and 0.5 mM of Mg^{2+} in solution.

At pH 4.75 even the lowest Ca^{2+} concentration (0.1 mM) shows a tremendous effect on the stabilization of SlfB. Whilst the pure protein at this pH shows a broad peak at approx. 20 – 30 nm, the addition of 0.1 mM calcium ions leads to a mostly monomeric radius distribution with some minor aggregation at about 30 – 40 nm. At higher Ca^{2+} concentrations (50 – 500 nm) the solutions show a monomodal radius distribution with narrow peaks that indicate low polydispersity and low internal flexibility of the protein (**Figure 63 D**).

The different results for Sr^{2+} and Ca^{2+} at concentrations below 500 mM directly after the addition to the protein and after nine days at ambient temperature are surprising. Since the solutions were stored as droplets under paraffin oil at ambient temperature, not centrifuged prior to the measurements and no precipitation could be observed it is assumed that SlfB incorporates the relatively small Mg^{2+} ion faster than the larger Ca^{2+}- and Sr^{2+}-ions, thus a stable state with bound bivalent cations is achieved fast for Mg^{2+} whereas the internal rearrangement upon addition of the latter two cations leads to disturbed DLS signals directly after the mixtures are prepared.

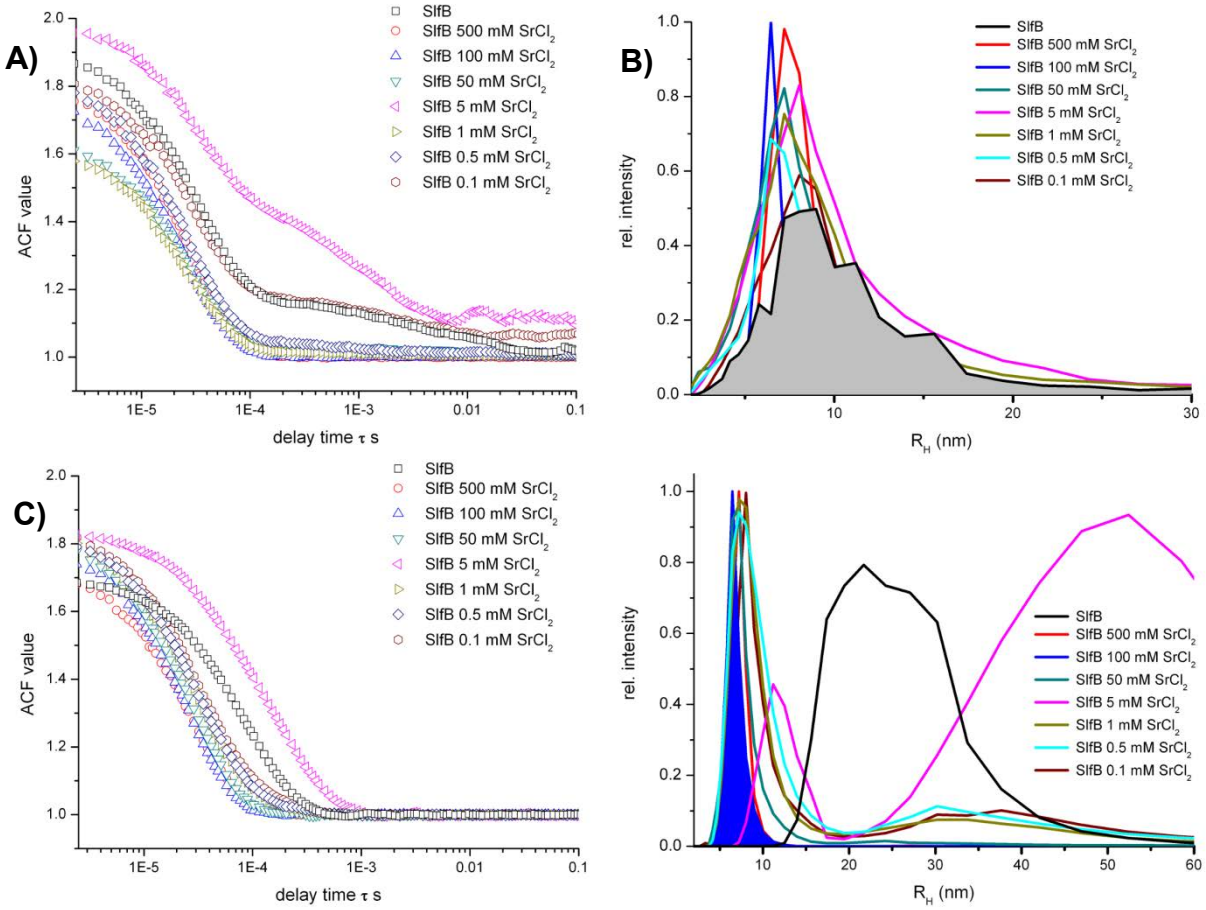

Figure 62 Results of *in situ* DLS measurements in solutions of SlfB at pH 7.4 (**A)** and **B)**) and pH 4.75 (**C)** and **D)**) with (curves in colors) and without Sr^{2+} (black curves) at different concentrations after nine days at 20±1°C. From comparisons of the ACF (**A)** and **C)**) and radius distribution (**B)** and **D)**) it is clear that within a defined range of concentration Sr^{2+}-ions have a stabilizing effect on SlfB. Both ACF and radius distribution show less aggregation/oligomerization with Sr^{2+} than without. Deviations can be seen in **A)** and **B):** the ACF of SlfB at pH 7.4 with 0.1 mM Sr^{2+} is nearly identical to that of pure SlfB. At such low concentrations the Sr^{2+}-ions have no stabilizing effect on the protein. The radius distribution in both cases is also nearly identical: the peak of 0.1 mM Sr^{2+} is almost completely hidden by the peak of pure SlfB. Moreover the ACF of 5 mM Sr^{2+} indicates a solution containing both a small oligomer and a heavily aggregated species (magenta triangles in **A)**). As in the case of Mg^{2+} SlfB with 5 mM Sr^{2+} shows aggregation at higher radius than SlfB without Sr^{2+} However: pure SlfB lacks a monomeric species (see **D)**) whilst SlfB with 5 mM Sr^{2+} (magenta) shows aggregated SlfB in coexistence with protein in a low oligomerized state (R_H ~ 12 nm). SlfB is most stable (at both pH values) after nine days at 20±1°C when it contains 100 mM Sr^{2+} (blue curve in **B)** and **D),** in **D)** filled for clarification). Similar results can be obtained at half the Sr^{2+} concentration (curve in dark cyan).

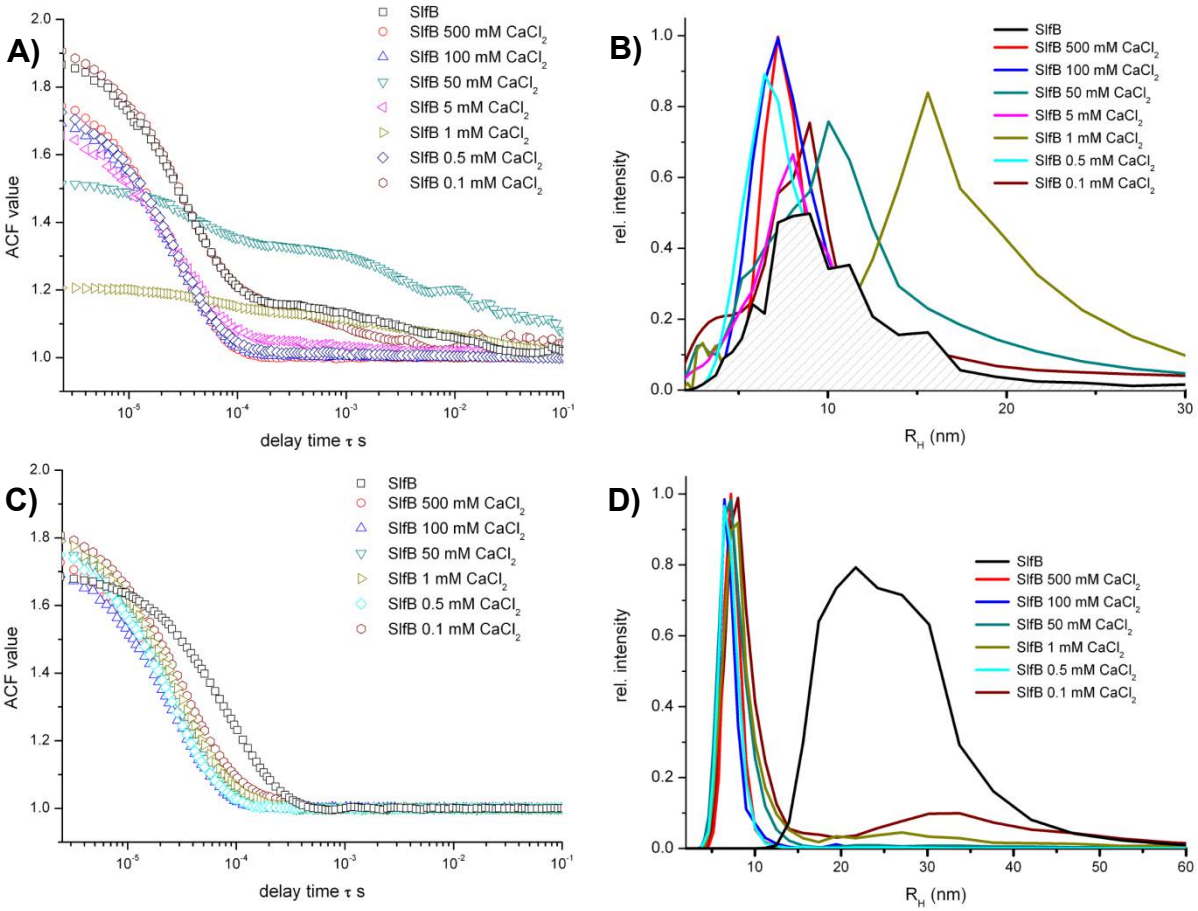

Figure 63 Results of *in situ* DLS measurements in solutions of SlfB at pH 7.4 (**A)** and **B)**) and pH 4.75 (**C)** and **D)**) with (curves in colors) and without Ca^{2+} (black curves) at different concentrations after nine days at ambient temperature.From comparisons of the ACF (**A)** and **C)**) and radius distribution (**B)** and **D)**) it is clear that at pH 7.4 Ca^{2+} has a far less stabilizing effect on SlfB than Sr^{2+} and Mg^{2+}. The monomeric form is stabilized only at 500 mM, 100 mM and – surprisingly – 0.5 mM Ca^{2+}. As for SlfB containing Sr^{2+} at this concentration, 0.1 mM of Ca^{2+} have no effect at all: the ACF of pure SlfB at pH 7.4 is nearly identical with the ACF at 0.1 mM of calcium chloride. This is totally different if the pH of the solutions is buffered at 4.75. The pure protein shows aggregation at this pH after nine days at room temperature. It appears in the radius distribution as one broad peak (R_H ~ 25 nm), whilst even at only 0.1 mM $CaCl_2$ most of the protein remains in a monomeric or low oligomeric state (R_H ~ 8 nm). At higher Ca^{2+} concentrations (50 – 500 mM) no aggregation appears, the protein solution is monomodal and the narrow peak indicates a very low percentage of polydispersity.

5.3.7.1. Stability at 4°C

Since SlfB JGA12-N is very stable at 4°C (for at least four months) this did not need to be improved, however it is necessary to assess the stability of SlfB with bivalent cations at 4°C to gain knowledge if once SlfB is mixed with them it still can be stored at 4°C and if an incubation at 4°C for 24 h after preparation will lead to improved stability of the protein at 20°C. This was especially interesting for Ca^{2+} and

Sr^{2+} at pH 7.4 were DLS measurements directly after preparation showed aggregation and instability but measurement results were much better after 9 days at 20°C. In parallel the absorption spectra of all mixtures were measured to see if addition of bivalent cations led to a significant loss of protein concentration. During these measurements no significant changes in protein concentration could be observed.

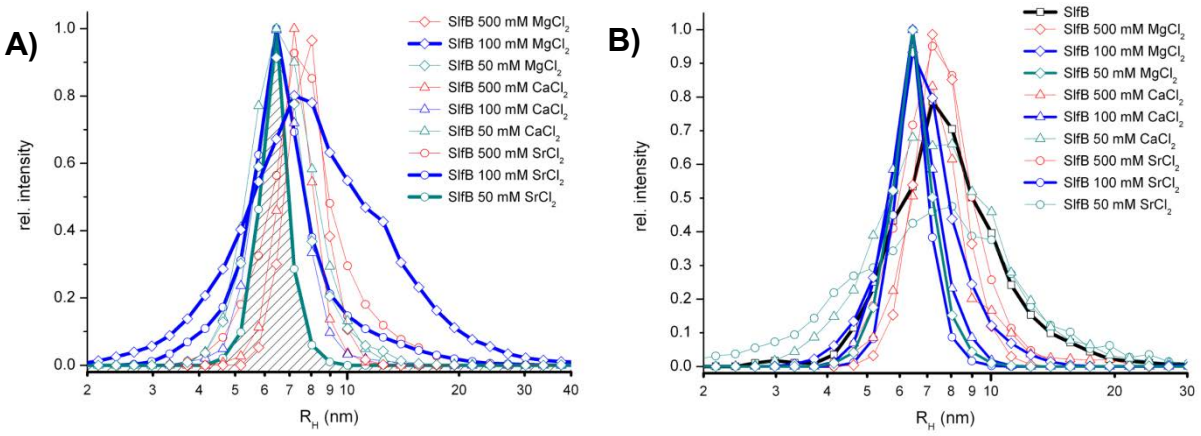

Figure 64: Stability of SlfB at 4°C after addition of bivalent cations.

DLS measurements were carried out after one day of incubation at 4°C. **A)** shows results at pH 7.4, **B)** those at a pH of 4.75.

DLS measurements revealed that at pH 7.4 after one day of incubation at 4°C almost for all concentrations of the three bivalent cations, the solutions show a monodisperse radius distribution with peaks at 6.45 nm, 7.20 nm or 8.04 nm. For low concentrations of $CaCl_2$ (0.1, 0.5 and 1 mM) some aggregation could be detected with a R_H > 1 µm. Most surprisingly the best condition after preparation and after nine days, 100 mM $MgCl_2$ (pH 7.0), showed after one day at 4°C aggregation at aprox. 500 – 600 nm. Moreover the R_H of the main peak was shifted from 6.45 to 7.20 nm and the form of the peak and its relative broadness indicate some fraction of polydispersity (see **Figure 64 A**). For Ca^{2+} and Sr^{2+} these results again showed that these cations do not generally cause instability of SlfB but incubation time is required for incorporation and eventually binding to the protein. Especially at a concentration of 100 mM the radius distributions show a high degree of monodispersity (R_H = 6.50, standard deviation for Ca^{2+} is 0.08 nm and for Sr^{2+} it is 0.11 nm) for both solutions (see **Figure 64 A**) which is comparable to the results obtained for Sr^{2+} and Mg^{2+} after nine days at 20±1°C.

In NaOAc buffer at pH 4.75 significant aggregation could only be observed for 0.5 mM $CaCl_2$ and 50 mM $SrCl_2$. Other than at pH 7.4, DLS measurement in the droplet containing 100 mM $MgCl_2$ showed a monodisperse radius distribution with a R_H of 6.45 nm (see **Figure 64 B**). The same result could be obtained for all Mg^{2+} concentrations except for 500 mM (R_H = 7.20 nm). Addition of 100, 5 or 1 mM of $CaCl_2$ to SlfB yielded monodisperse solutions with a R_H of 6.45 nm, whilst for 50 and 0.1 mM a broad radius distribution representing small oligomers or structural flexibility of the monomer (RH ~ 6-8 nm) was found. With 500 mM of $CaCl_2$, SlfB showed a R_H of approx. 7.20 nm resembling a lot the radius distribution for SlfB without bivalent cations (pH 4.75). In the case of $SrCl_2$ at all concentrations but 100 and 0.5 mM the radius distribution showed a small amount of polydispersity. The best result was obtained for 100 mM $SrCl_2$, even if compared with the best results for Mg^{2+} and Ca^{2+}. The peak is narrow (R_H standard deviation of just 0.06 nm) indicating a high degree of monodispersity and low flexibility of SlfB (see **Figure 64 B**).

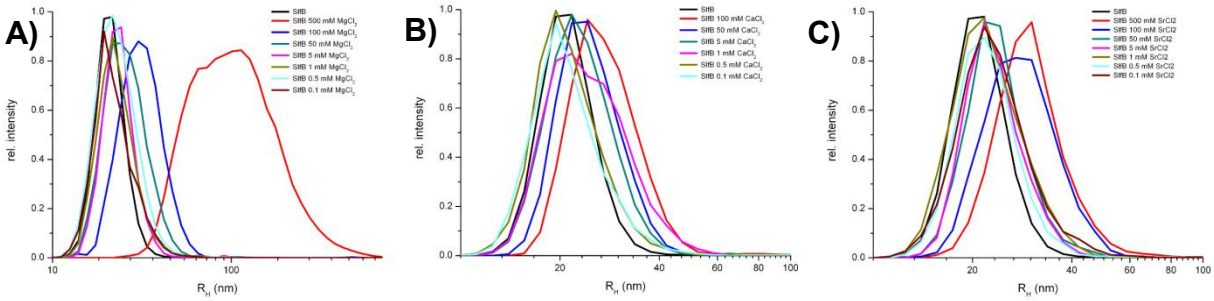

Figure 65: SlfB solutions at pH 2.0 with and without bivalent cations after one day incubation at 4°C. **A)** $MgCl_2$ was added, **B)** results after addition of $SrCl_2$ and **C)** influence of Ca^{2+}-ions at pH 2

Unlike the above discussed radius distributions of SlfB in glycine buffer at pH 2.0 initially and after nine days, a monodisperse radius distribution (R_H ~ 20 nm) resulted from DLS measurements carried out after incubating SlfB for one day at 4°C in the same buffer at pH 2.0 (see **Figure 65**). For $SrCl_2$ at concentrations below 50 mM the radius distributions were in good concordance with that of bivalent cation-free SlfB. The higher the Sr^{2+} concentration the larger was the R_H and the broader the peak. This was – with the exception of 1 mM – also the case for Ca^{2+}, although the concentration dependence was not so strong here. The concentration dependence of R_H and polydispersity could also be observed for Mg^{2+}. At concentrations below 100 mM $MgCl_2$ the radius distribution at pH 2.0 was in good accordance with that of bivalent cation-free SlfB at pH 2.0. At 100 mM of Mg^{2+} the R_H was shifted from

~20 nm to ~30 nm and at the highest tested concentration (500 mM) a very broad peak ranging from 60 – 300 nm was calculated from DLS measurements.

Based on these results $SrCl_2$ proves to be a good alternative for $MgCl_2$ to stabilize SlfB. If this improvement of protein stability should be used in protein crystallization it is recommended to add $MgCl_2$ right before the screening while on the other hand $SrCl_2$ should be added one day in advance, followed by incubation at 4°C until performing the crystallization screen. Interestingly even the addition of 100 mM Ca^{2+} to the protein solution that should result in the preferred formation of 2D crystals improved protein stability if compared with SlfB at 20°C. It seems that at 20±1°C, the temperature at which the protein might be in an active state, bivalent cations are required for its stability. Moreover it could be shown that 2D crystals, at least *in vitro*, only form within two weeks if the solution is brought to low pH-values of approx. 2.0 or below. These results certainly widen the possibilities of approaches to obtain X-ray suitable 3D crystals.

5.4. Conclusions and Outlook

Albeit the importance of S-layer proteins for the survival of many bacteria – including pathogens – and possible industrial applications in waste management, catalysis, nanotechnology and drug delivery, little is known about the 3D structure of these proteins. It is therefore of high interest to overcome these deficiencies and shed light onto the three dimensional structures of s-layer proteins at atomic resolution. The high flexibility of these proteins, their inherent tendency to form 2D but not 3D crystals makes this a challenging task. On the other hand in the course of this work, first crystals of SlfB could be presented that are a starting point for further investigations. Especially with the possibilities of PETRA III at DESY the thin plates obtained will eventually become X-ray suitable crystals. Furthermore the crystals grown from the proteolysis approach have to be investigated. Moreover investigation of the influence of bivalent cations on SlfB suggest that the addition of Mg^{2+} or Sr^{2+} to the protein buffer improves stability of the protein and thus might enhance its crystallizability. Nonetheless it may be necessary to include molecular biology approaches as it could be shown by other groups that expression, purification and structure determination of fragments of s-layer proteins by X-ray crystallography are possible. In combination with solution scattering techniques (SAXS, SANS) and CryoEM-analysis of 2D-crystals this may prove the better way to obtain a full length

structure of SlfB at high resolution. In addition to the characterization of SlfB, also other novel s-layer proteins of genetically similar bacteria but also of other bacterial families should be analyzed. Especially the structure-function analysis of S-layer proteins from human pathogens could deliver interesting insights applicable in the development of novel antibiotics.

6. Application of *in situ* DLS to Analyze Solution Properties of CD81and CD82 and Tetraspanin-Claudin-1 Interaction

6.1. Introduction

CD81 (see **Figure 66** for a scheme) is a human membrane protein from the tetraspanin family **[127]**, bearing two extra-cellular loops, EC1 and EC2 and four trans-membrane α-helices. It is involved in various host-pathogen interactions including HIV, HCV and *Plasmodium falciparum* infection **[120, 166, 167]**. Tetraspanins are known to form complexes with each other and other protein molecules such as integrins **[127]**.

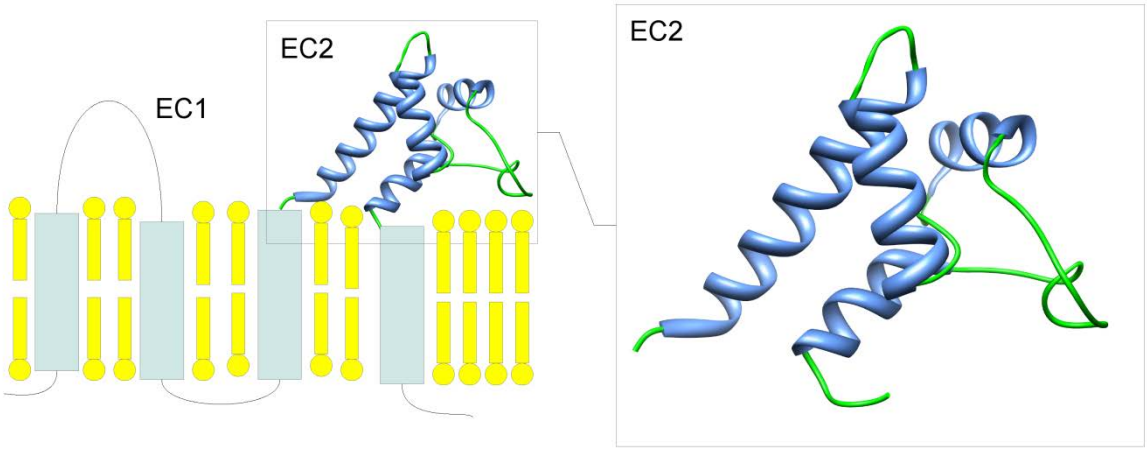

Figure 66: Scheme of CD81. Blue boxes are the trans-membrane helices, the membrane is drawn in yellow, EC2 is displayed as cartoon plot (magnified on the right side) as generated from PDB-file 1IV5.

Claudin-1 **[168-170]** is a trans-membrane protein from the Claudin superfamily **[170]**. As CD81 it has four trans-membrane helices. The structural components of cellular tight junctions are mainly formed by Claudins **[169]**. These tight junctions **[171]** are important in intercellular communication and cellular interaction during infection **[172-175]**. For HCV infection of liver cells interaction of CD81 with the E1/E2 glycoproteins on the HCV surface is essential **[167]**. But when Claudin-1 **[168-170]** is absent no infection occurs **[128]**. It was proposed that Claudin-1 and CD81 interaction plays an important role during HCV infection **[128, 176, 177]**. The investigation of this interaction and its dependence on co-factors is important for the understanding of HCV host-pathogen interaction and thus the treatment and prevention of HCV **[178]**.

CD82 **[179, 180]** is a metastasis suppressor that belongs to the tetraspanin superfamily. Its expression or the absence of CD82 expression are associated with

various human cancers **[107]**. Function **[121, 179, 181-184]** and potential use of CD82 in anti-cancer treatment **[107]** are widely discussed.

CD81 and CD82 share some characteristics **[181, 185-187]** but differ in most aspects of their cellular function and role. Important for the investigation of CD81-Claudin-1 interaction, as carried out in this work is that no interaction is reported for CD82 and Claudin-1. Hence CD82 serves as a control model for the significance of the experimental results.

Little is known about the three dimensional structures of tetraspanins. Only two structures of the EC2-loop of CD81 are deposited with the PDB **[188, 189]**. Moreover one cryoEM-structure of the tetraspanin uroplakins Ia and Ib at 6 Å resolution exists giving insight into the structure of tetraspanin complexes **[190]**. Keeping the above described importance of tetraspanins in many cellular processes in mind it is clear that to obtain more detailed information and to gain insight into structure-function relations at atomic level the determination of complete three-dimensional structures of tetraspanins by X-ray crystallography is necessary. Even the optimized expression and purification of CD81 and CD82 from yeast **[120]** only yields small amounts of pure protein. Moreover the crystallization of membrane proteins is difficult and not straight forward **[191, 192]**. In general the amount required to crystallize a membrane protein is bigger than that needed for a soluble protein. However, recent advantages in the development of synchrotron light source with the possibilities of microfocus beamlines **[193-195]** combined with increased photon intensity makes it possible to determine the structure of biological macromolecules from crystals as small as 10 µm. Thus the structure determination of membrane proteins is facilitated since the crystal size required for X-ray crystallography has decreased drastically **[195]**. Furthermore technologies are being developed that aim at better expression of membrane proteins as well as methods that facilitate membrane protein crystallization **[191, 196]**. Still to grow X-ray suitable crystals of membrane proteins and even to solve their three dimensional structure is a huge challenge **[197]**.

In the scope of this work crystallization experiments for CD81 and CD82 were designed and carried out, applying high throughput technologies and *in situ* DLS **[88]**. Moreover solution conditions and detergent properties were assessed by light scattering methods (DLS) and optimized.

6.2. Materials and Methods

6.2.1. Crystallization of CD81 and CD82

Both CD81 and CD82 were cloned, expressed and purified by **NICKLAS BONANDER** (Aston University, Birmingham, UK). The production of the recombinant proteins, as carried out by **NICKLAS BONANDER**, was described by **MOHAMMED JAMSHAD** *et al*. **[120]**. The received protein samples were clarified by centrifugation at 16'100 x *g* for 15 min, followed by DLS in a *Spectro*LIGHT 300 (Nabitec, Germany) to determine protein quality.

Buffer and detergent were optimized applying DLS in cuvettes (within the *Spectro*LIGHT 300) and *in situ* DLS within the *Spectro*LIGHT 500 in MRC-plates. DLS measurements were analyzed and evaluated with the software *SPECTRO.* Radius distributions were calculated by *SPECTRO* applying CONTIN **[65-67]**.

Protein concentrations were adjusted applying 3 kDa cut-off centrifugal filters (Millipore, USA). Protein concentrations were determined by absorption spectroscopy, applying a Nanodrop 2000c (Thermo Fisher, USA). The concentration range for crystallization was estimated by application of the PCT (Hampton Research, USA).

Protein buffer (20 mM MOPS (Sigma Aldrich, USA), pH 8.0, 1 % n-Octyl-β-D-Glucopyranoside (β-OG, Anatrace, USA)) was received by **NICKLAS BONANDER** and as all other precipitants, additives and detergents were filtered through 0.22 µm syringe filters prior to use.

For initial crystallization experiments conditions from the Molecular Dimension (**MD**, UK) screens MemGold™ and MemPlus™ containing Ca^{2+} were used since these conditions yielded small crystals in previous screens. These conditions however were varied and optimized based on initial results. A crystallization method was adapted from the Nucleic Acid Mini Screen (NAMS, Hampton Research, USA). Various concentrations of MPD or MPD/PEG 400 mixtures in the reservoir (500 µL) were equilibrated against droplets (4 µL) containing protein (at half the concentration) and 5 mM of $CaCl_2$. The mixture in the reservoir is not only hygroscopic, MPD is also volatile. This has the effect that the protein drop is dried out slowly and at the same time MPD is enriched within the drop, acting as precipitant. Further protein crystallization was carried out with a Honeybee 961 (Genomic Solutions, USA) robot applying pre-formulated screens (Classic, JCSG+, MPD-Suite, MB-Class I & II,

CryoSuite and ComPAS; all by Qiagen, Germany). Based on the results of initial and robotic screening a customized screen (Screen 8.2.G, see **Appendix, chapter 9.2**) was developed and screened against CD81 and CD82 manually in 24 well cell culture plates. Fos-Choline-14 (n-Tetradecylphosphocholine, **FOS 14**, Anatrace, USA) and Fos-Choline-18 (n-Octadecylphosphocholine, **FOS 18**, Anatrace, USA) were used in this screen as additives.

All X-ray diffraction experiments were carried out at the EMBL beamline X12 (HASYLAB/DESY).

6.2.2. *In situ* DLS Determined Interaction between CD81 and Claudin-1

Protein solutions were clarified by centrifugation at 16'100 x *g* for 15 min and then transferred to a MRC crystallization plate at 1 µL/well. Five different molar ratios of Claudin-1:CD81, Claudin-1:CD82 and CD82:Claudin-1 (9:1; 7:3; 5:5; 3:7; 1:9) were analyzed with and without the addition of 0.1 µL cholesteryl hemisuccinate (**CHEMS**, Anatrace, USA; 2.2 mg/mL in 20 mM MOPS, pH 8.0, 1 % beta-OG) to the drop. As controls, Claudin-1, CD81 and CD82 were analyzed alone with and without addition of 0.1 µL CHEMS (2.2 mg/mL in 20 mM MOPS, pH 8.0, 1 % β-OG) to the drop, as well as the same buffer without protein. The reservoirs were filled with 35 µL protein buffer (20 mM MOPS, pH 8.0, 1 % beta-OG) and the plate was sealed with AMPLIseal (Greiner Bio-One, Germany) to avoid evaporation during the measurements. DLS measurements within these droplets were carried out at 20°C using a *Spectro*LIGHT 500 instrument. Data were analyzed using *Spectro* (Nabitec, Germany). *Spectro* interprets the autocorrelation function **[54, 56]** using the CONTIN-algorithm **[65]** to obtain the distribution of particle radii. To obtain data on the time-dependent change of the hydrodynamic radius (R_H) distribution of the respective protein mixtures, DLS measurements were recorded for 23 h in all wells. From each well a series of 130 measurements at 30 s per measurement was recorded, with an interval of approximately 10 min between each measurement.

6.3. Results and Discussion

6.3.1. Crystallization of CD81 and CD82

Purified samples of the human membrane proteins CD81 and CD82, both of the tetraspanin family were received from **NICKLAS BONANDER** (Aston University, UK) in terms of the EU FP6 project *OptiCryst*.

Initially solution properties of both samples were assessed by DLS in cuvettes (see **Figure 68** and **Figure 69**). It could be shown that the received samples were in an aggregated state, with a broad radius distribution and R_H between 20 and 60 nm (CD82) and 60 nm (CD81). Centrifugation for 20 minutes at 16'100 x *g* did not lead to a significant improvement in radius distribution. However, in the case of CD81 it could now be seen that besides the aggregated state some smaller particles (R_H of approx. 7 nm) existed in solution.

Since it is known from literature that detergent micelles can be detected by DLS and that the R_H of detergent micelles depends on their concentration in solution **[198, 199]** DLS was measured in solutions containing different concentrations of β-OG in the protein buffer (20 mM MOPS, pH 8.0). Based on the results of DLS (see **Figure 67**) it is plausible that the low concentration of detergent is responsible for the broad radius distribution of both CD81 and CD82. The obtained results are nearly identical with that of 1 % β-OG without protein and the protein solutions also contain 1 % β-OG**.** For crystallization a low concentration is ideal since high concentrations of detergent inhibit concentration. On the other side a high degree of monodispersity is desired in crystallization. Already at 2 % detergent a monodisperse radius distribution could be obtained, but the results in the case of 2.5 % β-OG were even better (see **Figure 67**).

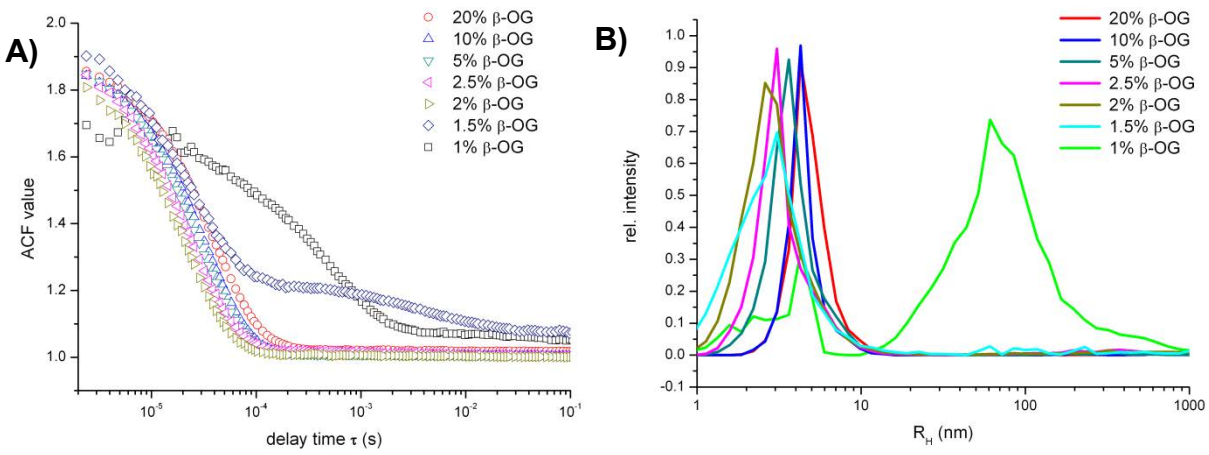

Figure 67: DLS measurements in solutions of the detergent β-OG in protein buffer (without protein). The dependence of ACF (A) and radius distribution (B) on detergent concentration can clearly be seen. At 1% concentration the radius distribution shows aggregation between 50 and 200 nm. This aggregation disappears already at 1.5% concentration of β-OG, but the peak corresponding to one detergent micelle in solution is still broad. From 2-20 % the radius distribution is monomodal and the peaks corresponding to one detergent micelle in solution are narrow. As can be seen from ACF and radius distribution the R_H increases slightly with concentration.

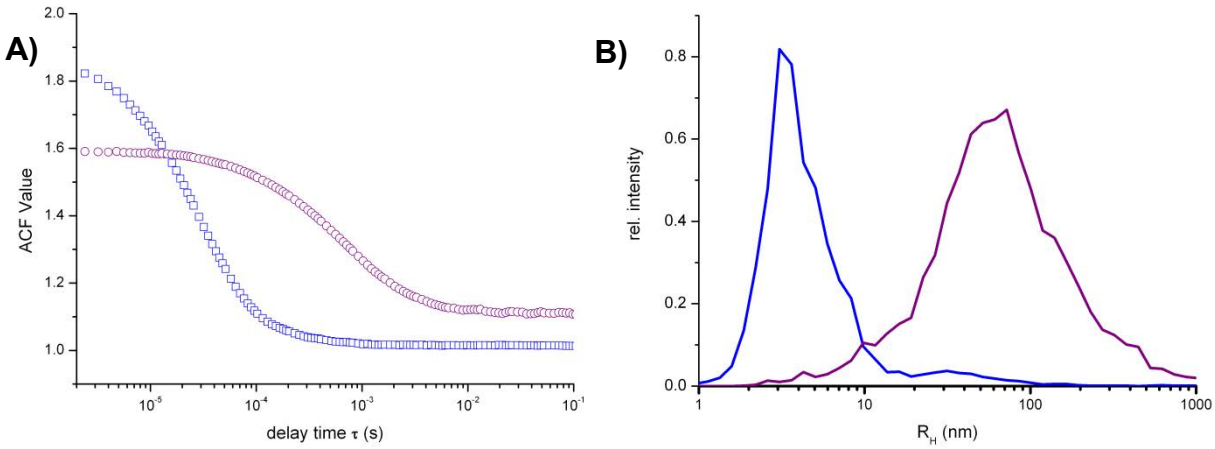

Figure 68: Results (ACF (A) and (B) radius distribution)of DLS investigation of CD81 before (purple) and after (blue) adjustment of polydispersity and aggregation. The sample shows in the latter case a low degree of polydispersity and aggregation and its R_H (B) corresponds to a dynamic mixture of monomers and dimers of CD81 in detergent micelles.

It was chosen to increase the detergent concentration to 2.5 % but to also increase protein concentration to 2.5 mg/mL to compensate the increased solubility caused by higher detergent concentration. CD81 at higher protein and detergent concentration (**Figure 68**, blue curves) is nearly monomodal in solution just showing a small fraction of aggregation at approx. 20 nm. The R_H of the major peak is 3.62 nm and corresponds to a monomer of CD81 within a detergent micelle. However the peak is broader to higher R_H than to lower indication a dynamic mixture of monomer and small oligomers such as dimers in solution.

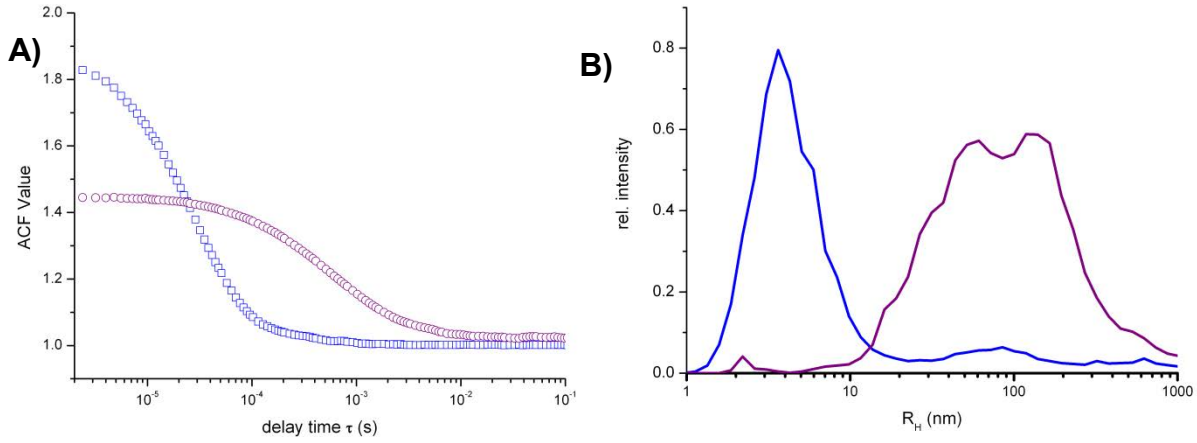

Figure 69: Results of DLS investigation of CD82 before (purple) and after (blue) adjustment of detergent and protein concentration. The sample shows in the latter case a low degree of polydispersity and aggregation and its R_H (B) corresponds to a dynamic mixture of monomers and dimers of CD82 in detergent micelles.

CD82 at higher detergent and protein concentration behaves similar as CD81 (see **Figure 69**). The radius distribution shows that the R_H of the dominant peak is at 3.5 nm. This corresponds to a monomer of CD82 within a detergent micelle. Other than in the case of CD81, CD82 at higher concentrations shows aggregation at higher R_H and intensity. Since the relation of intensity and concentration depends on the radius of the particle the fraction of aggregation can assumed to be similar. Both - CD81 and CD82 - solutions after optimization of protein and detergent concentration showed a quality in DLS that was considered to be good enough for crystallization experiments.

For initial crystallization experiments conditions from the Molecular Dimension (MDL, UK) screens MemGold™ and MemPlus™ containing Ca^{2+} were adapted, since from previous work of **NICKLAS BONANDER** a Ca^{2+} dependency of protein stability and crystallizability was proposed. However these conditions yielded no protein crystals. The drops either remained clear or precipitation occurred. A new approach followed the method of the Nucleic Acid Mini Screen where initially only a low concentration of MPD in the DNA/RNA drop is equilibrated against a high concentration of MPD. In the adaption MPD was omitted from the drop and only added to the reservoir. The drop was prepared by mixing equal amounts of protein and 10 mM $CaCl_2$-solution in 20 mM MOPS buffer (pH 8.0). Variation of the conditions was achieved by changing the concentration of MPD in the reservoir or by addition of PEG 400 to the reservoir. PEG 400 as MPD is hygroscopic but it is not volatile. Thus addition of PEG 400 instead of a higher concentration of MPD leads to a more dried out drop but not to more precipitant within the drop.

Figure 70: Initial crystals of CD81. The UV illuminated image (right hand side) shows fluorescence of the crystal-cluster.

A crystal-cluster grew in solutions containing CD81 (**Figure 70**) after two weeks of equilibration against a reservoir containing 21 % (v/v) MPD and 40 % (v/v) PEG 400. UV analysis **[119]** with a *Crystal*LIGHT 100 (Nabitec, Germany) showed fluorescence of the crystals, indicating them being composed of protein material.

These crystals however showed to be not X-ray suitable at this stage. After six weeks crystals with the morphology of thin plates and needles could be observed in conditions where the crystallization droplet was either equilibrated against 500 µL or 1 mL of 35 % (v/v) MPD. Both, plates and needles, showed UV-fluorescence (**Figure 71**). The plates were mounted and showed diffraction up to 1.9 Å (**Figure 72**).

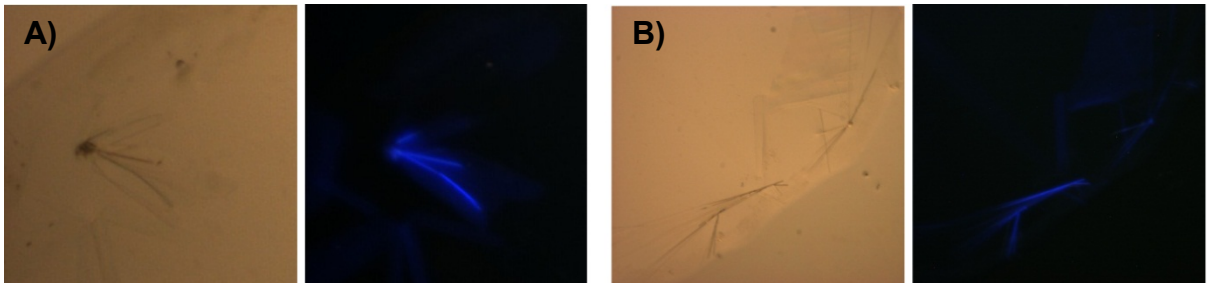

Figure 71: (A) Thin plates grown after six weeks equilibration of CD81 against 500 µL 35% (v/v) MPD; **(B)** equilibration against 1 mL of the same reservoir solution led to the growth of thin needles.

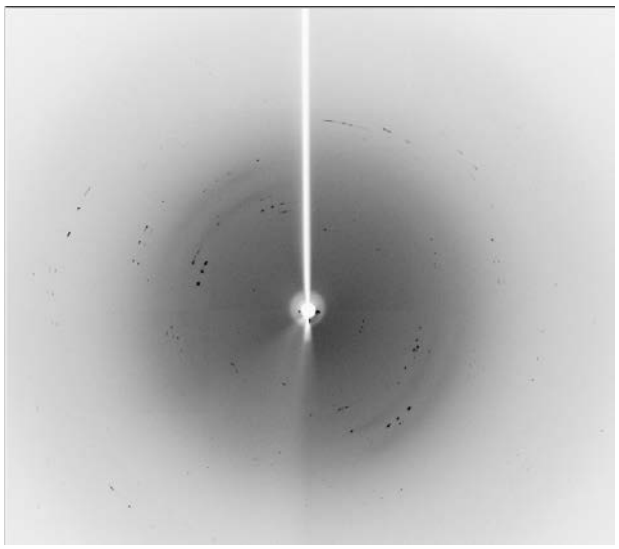

Figure 72: Diffraction image of the crystals displayed in **Figure 71 A**.

Larger thin plates could be observed after seven weeks in a CD81 drop that was equilibrated against 32 % (v/v) MPD (see **Figure 73**). These plates showed strong UV fluorescence and diffraction up to 3.2 Å, but again indexing of the crystal system is presently not possible. For CD82 in these initial crystallization experiments no crystals could be obtained. However in a later screening crystals of CD81 showing

UV-fluorescence could be obtained from condition A3 (3.4 M 1,6-hexanediol, 0.2 M $MgCl_2$, 0.1 M Tris, pH 8.5)) of the Qiagen Classic Suite.

The knowledge that the use of 1,6-hexanediol as precipitant can lead to crystals was used in a optimization screen together with the lipids FOS 14 and FOS 18 as additive. After three month crystals grew from droplets prepared by mixing equal amounts of CD81 and 0.25 mM FOS 14, 10 mM $CaCl_2$ and either (A) 3.6 or (B) 4 M 1,6-hexanediol as well as (C) 0.25 mM FOS 18, 10 mM $CaCl_2$ and 3.6 M 1,6-hexanediol and equilibration against the respective solutions (**Figure 74**).

Figure 73: Crystals grown from equilibration of a CD81 crystallization droplet against 32 % (v/v) MPD. From left to right: VIS-image, UV-image, showing strong fluorescence of the crystal, Diffraction images of the crystal.

These crystals have not yet been analyzed by X-ray diffraction experiments since they are too small for DORIS III beamlines. The crystals are kept for future X-ray diffraction studies and data collection at beamline P11 (HASYLAB/DESY) of PETRAIII.

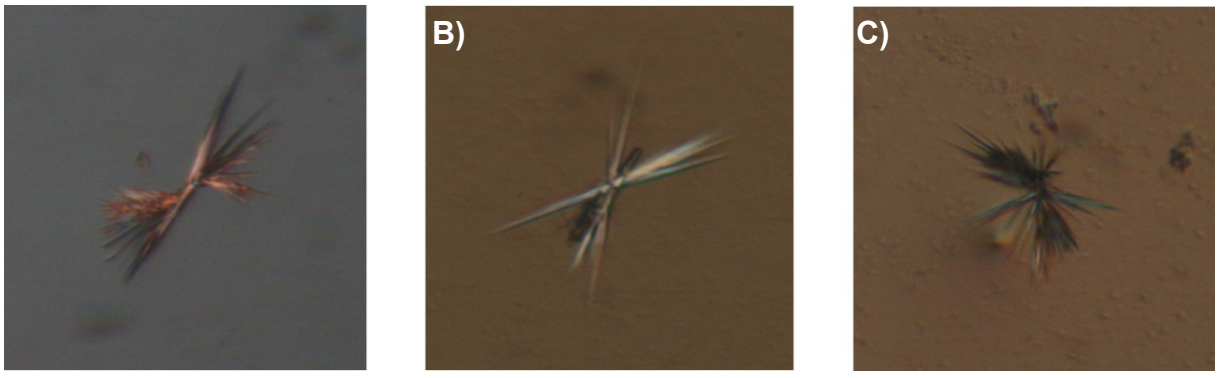

Figure 74: Crystals of CD81 grown after three month with A), B) FOS14 or C) FOS18. The maximum length of a needle is approx. 50-80 µm.

6.3.2. Protein Interaction

The particle size in solution for Claudin-1 was calculated from DLS measurements using the Stoke-Einstein-Equation (**EQ1**) and thus relating the diffusion coefficient to the corresponding hydrodynamic radius (R_H) **[56]**.

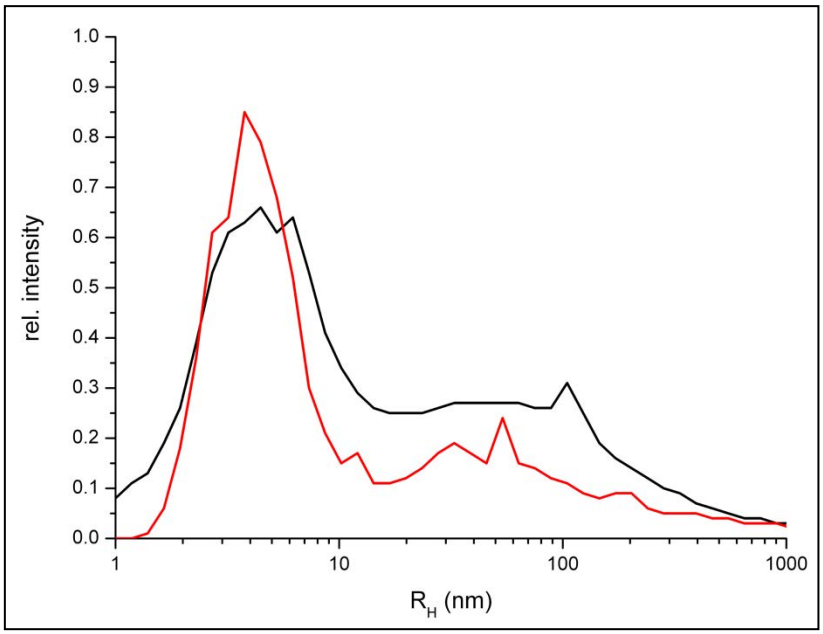

Figure 75: Radius distribution of Claudin 1 with (red) and without (black) CHEMS.

The diffusion coefficient was obtained by analysis of the ACF **[56]** using the CONTIN algorithm **[65]** within the software *SPECTRO***.** For Claudin-1 the mean particle hydrodynamic radius (R_H) for the monomer was measured by DLS to be 4.0±0.7 nm. The radius of a FOS-choline-12 micelle in solution calculated from DLS measurements is given in literature as 2.5±0.6 nm **[199]** and thus not much different than that of βOG-micelles (R_H in literature ranges from 2.3 – 3.1 nm **[198, 199]** which was confirmed by own measurements where a R_H of 2.6 – 4.4 could be obtained, see **chapter 6.3.1**). The molecular weight of the FOS-choline-12 micelle as determined by DLS is 28 kDa and that of a β-OG-micelle is 33 kDa **[199]**, respectively. The size of β-OG is 21 – 30 kDa as determined by sedimentation velocity (Analytical ultra-centrifugation, **AUC [200]**) and SLS **[198].** Claudin-1 (M_W = 23 kDa) in complex with the FOS-choline-12 detergent micelle would yield a molecular weight of approx. 51 kDa. The R_H of approx. 4 nm corresponds to a molecular weight of approx. 77 kDa which is in accordance with two molecules of Claudin-1 in complex with the detergent micelle, thus the main species in solution is a Claudin-1 homodimer. Homodimerization of Claudins was previously described for Claudin-5 **[201],** The relative broadness of the peak (± 0.7 nm in the presence of CHEMS and ±0.9 nm in

the absence) indicates a presence of other oligomers (e.g. tetramer, hexamer) in solutions as well as a small amount of monomeric Claudin-1 and detergent alone. Aggregation was observed with a radius distribution of 10 to 1000 nm (**Figure 75**).

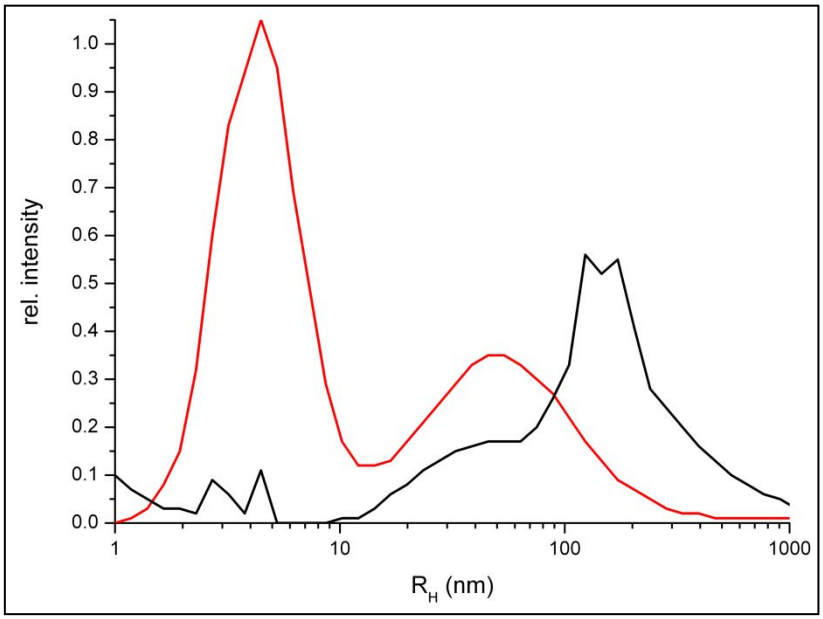

Figure 76: Radius distribution of Claudin 1 with (red) and without (black) CHEMS after 12h at room temperature.

With CHEMS added to the drop this aggregation appeared less intense in the calculated radius distribution derived from DLS measurements (**Figure 75**). Moreover the peak in the radius distribution corresponding to a particle with the mean radius of approx. 4 nm was more defined and with a higher relative intensity (0.82 to 0.65) compared with the measurement without CHEMS. Since the relative intensity is compared for the same molecule at an identical radius, it is a measure of the amount of this species of particle in solution. Thus addition of CHEMS results in a higher concentration of Claudin-1 homodimer in solution and in less aggregation: it obviously stabilizes the monomer of Claudin-1 in solution. Nonetheless DLS results show that Claudin-1 even in the presence of CHEMS has a tendency towards aggregation, as in about 12 h the aggregation peak is tighter and corresponding to a particle size of ~80 nm (**Figure 76**). For CD81 with and without CHEMS DLS measurements showed that the dominating species in solution is a detergent-protein-complex with a hydrodynamic radius of approx. 6 nm (**Figure 77**).

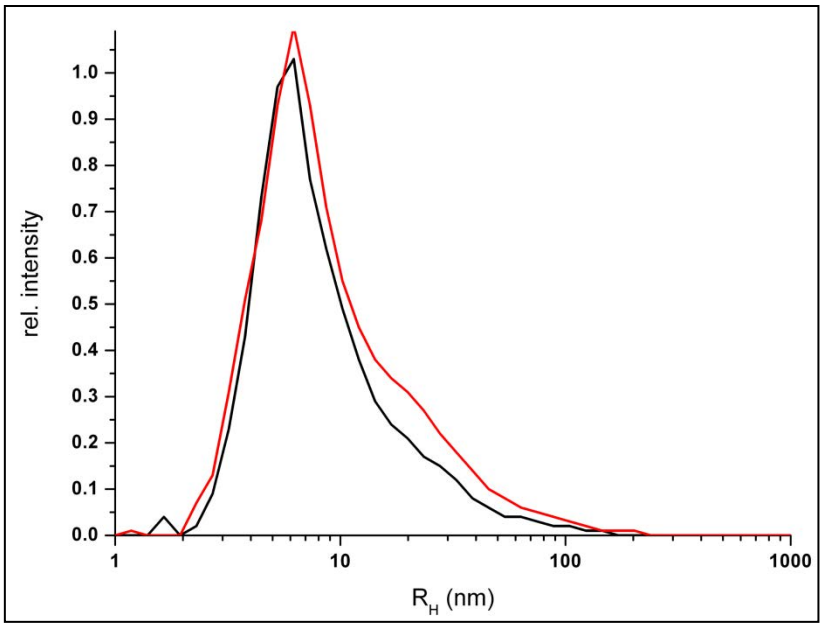

Figure 77: Radius distribution of CD81 with (red) and without (black) addition of CHEMS.

The R_H of 6 nm corresponds to an estimated molecular weight of the complex of approx. 220 kDa. This can be related to six or seven molecules of CD81 within a β-OG-micelle (M_W of approx. 190 – 220 kDa). The relatively broad peak indicates that some lower (e.g. dimeric CD81) as well as higher oligomeric states and aggregates are present in the solution, but at low concentrations relative to the dominant species. This radius distribution is in accordance with the reported tendency of CD81 to form dimers and oligomeric complexes in solution **[190, 202]**. CD81 was stable with CHEMS present in solution throughout the whole series of measurements (23 h) while in the absence of CHEMS a broadening of the peak, indicating a complex distribution of particles in solution could be observed (**Figure 78**).

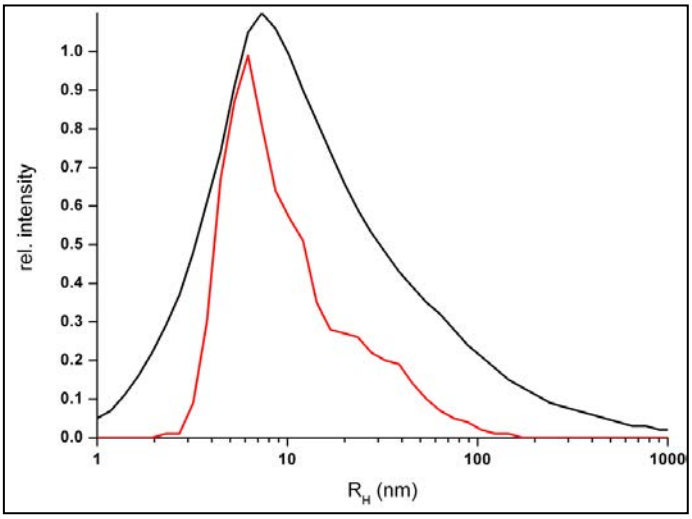

Figure 78: Radius distribution of CD81 with (red) and without (black) CHEMS after 12h at room temperature.

It is known that various tetraspanins interact with each other **[178]**, with other proteins such as tight junction proteins (e.g. CD9 with Claudin-1 **[203]** or CD81 and Claudin-1 **[127]**) or integrins **[204]** and form – in the course of this interaction – heterodimers and higher oligomer complexes **[187, 204]**. Moreover it is known that interaction between CD81 and Claudin-1 plays a critical role in HCV cell entry **[128]**. To gain information about this interaction DLS was applied to analyze the two component solutions of CD81 and Claudin-1 at different molar ratios (9:1, 7:3, 5:5, 3:7 and 1:9) (**Figure 79**) a summary of results can be found in **Table 4**. For comparative reasons DLS was also measured at the same molar ratios for mixtures of CD81 and CD82 and of CD82 and Claudin-1. All measurements were carried out with and without addition of CHEMS, since it is known that cholesterol plays an important role in tetraspanin association and host-pathogen interaction **[127, 166].** These measurements showed that for all CD81:Claudin-1 ratios, except for CD81:Claudin-1 7:3, the radius distribution was similar to the one expected from a non-interacting mixture of both proteins (**Figure 79**).

For CD81:Claudin-1 1:9, 3:7 and 5:5 without addition of CHEMS the resulting radius distribution for R_H > 10 nm was more or less equal to that of Claudin-1 alone. For CD81:Claudin-1 9:1 with and without addition of CHEMS radius distribution showed a particle with a hydrodynamic radius corresponding to that of CD81 (R_H of approx. 6nm), but the radius of the higher oligomers/aggregates corresponded to that of Claudin-1 and the mixtures of Claudin-1 and CD81 (except the molar ratio of CD81:Claudin-1 7:3).

For CD81:Claudin-1 7:3 distribution of particle radii in solution was different: with and without addition of CHEMS a defined oligomeric species at approx. 30 nm appeared within one hour after pipetting both protein solutions together (**Figure 79**). This defined oligomer was stabilized by addition of CHEMS where it is the dominating species after 12h (**Figure 80**) whilst the radius of the defined oligomer is shifted from 30 to 60 nm in the absence of CHEMS. **Figure 81** shows, that for the latter case the radius of the oligomer is growing up to approx. 80 nm within 18h while the radius of the oligomer is nearly constant during 18h of DLS monitoring with CHEMS present in the drop. For CD81 alone and for CD81:CD82 in 7:3 ratio in the presence of CHEMS a particle with a hydrodynamic radius of ~20 – 30 nm could be observed as well. But these particles where less defined and their intensity is lower than that for CD81:Claudin-1 at 7:3 ratio. This corresponds rather to an ensemble of oligomers of

different sizes at lower concentrations in solution than to a unique oligomer as could be observed for CD81:Claudin-1 in 7:3 ratio. For CD81:CD82 1:9 a defined oligomeric particle could be observed within the first ten measurements but analysis of the data showed that measurement errors had occurred here that led to such a false interpretation of the result. Neither for any other CD81:CD82 molar ratio, nor for CD82:Claudin-1 at any molar ratio, particles with a R_H of 20 – 35 nm could be observed. For all other mixtures and CD81, CD82 or Claudin-1 alone just aggregation or less defined higher oligomers (~80 nm) could be observed, but no oligomers at approx. 30 nm.

Table 4: Summary of particle radius distribution as measured by *in situ* DLS after mixing CD81 and Claudin-1 at different ratios.

Protein	**Particle radius (nm)**				**Predicted oligomeric state**
	– CHEMS		**+ CHEMS**		
	<10 nm	>10 nm	<10 nm	>10 nm	
Claudin-1 in foscholine-10	4.0 (2.5; 0.9)	40 (40; 0.2)	4.0 (1.3; 0.8)	40 (20; 0.2)	Dimer (4 nm) as well as higher oligomers/aggregates (broad peak at 40 nm)
CD81 in □OG	6.0 (3.5; 1.0)	–	6.5 (1.0; 1.0)	25 (6; 0.3)	Dimer (6 nm) plus, in the presence of CHEMS, a distinct peak at 25 nm
Claudin-1:CD81 (1:1)	4.6 (2.0; 1.0)	45 (40; 0.2)	5.0 (1.6; 1.0)	48 (23; 0.2)	Dimer (4–5 nm) as well as higher oligomers/aggregates (broad peak at >40 nm)
Claudin-1:CD81 (1:2)	4.2 (0.9; 0.9)	28 (9.0; 0.4)	4.0 (1.6; 0.4)	33 (9.0; 0.7)	Dimer (4 nm) as well as a distinct oligomer (30 nm) which is dominant in the presence of CHEMS; predicted to be hexameric
Claudin-1:CD81 (2:1)	4.3 (1.7; 0.8)	42 (10; 0.2)	5.0 (1.0; 0.9)	68 (30; 0.2)	Dimer (4–5 nm) as well as higher oligomers/aggregates (broad peak at >40 nm)
Claudin-1:CD81 (1:9)	5.2 (1.4; 0.9)	48 (48; 0.3)	6.5 (2.6; 0.9)	70 (85; 0.2)	Dimer (>5 nm) as well as higher oligomers/aggregates (broad peak at >40 nm)
Claudin-1:CD81 (9:1)	4.5 (2.5; 0.8)	75 (30; 0.2)	4.0 (0.5; 1.0)	41 (10; 0.2)	Dimer (>4 nm) as well as higher oligomers/aggregates (broad peak at >40 nm)

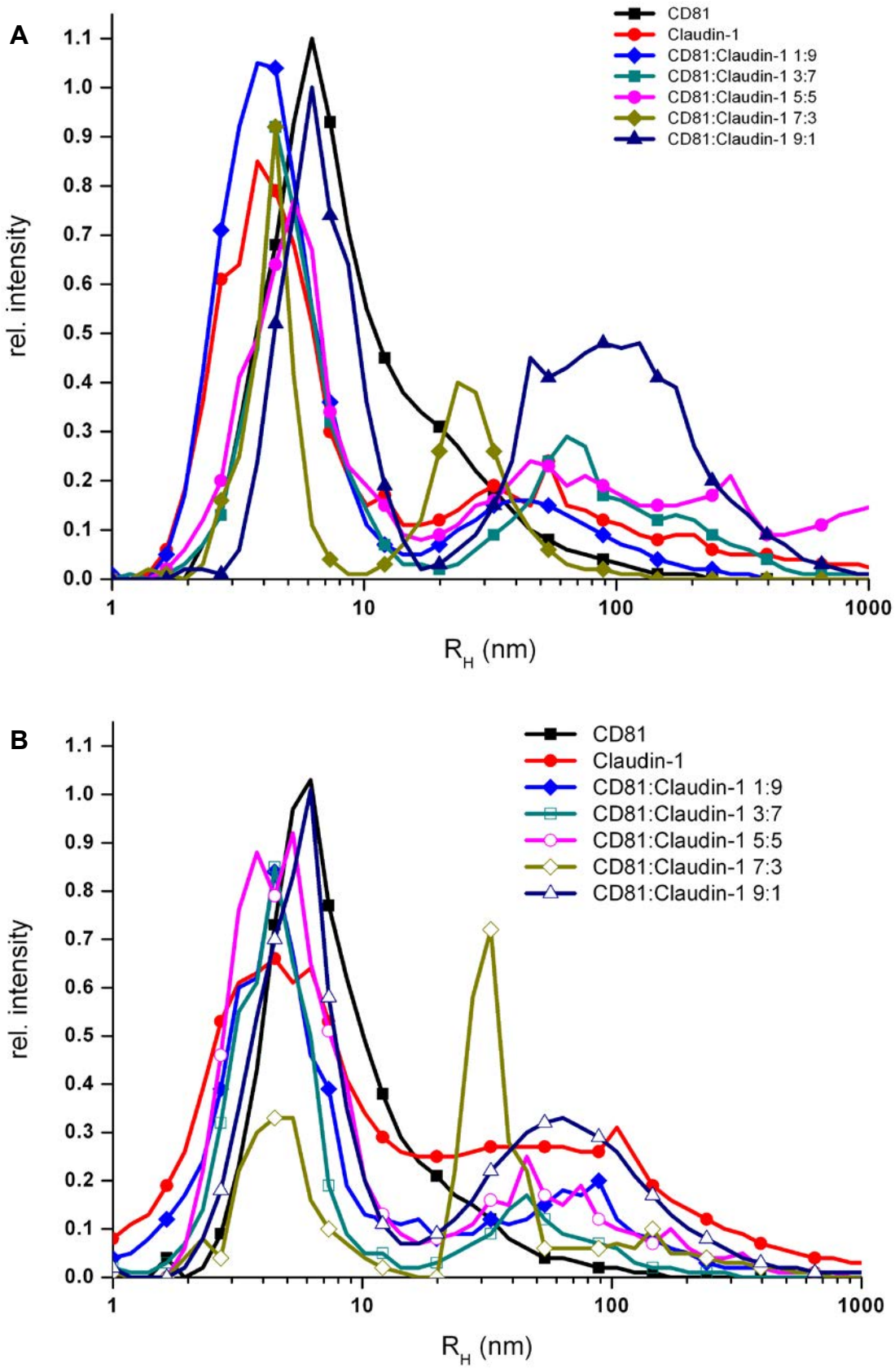

Figure 79: Comparison of radius distribution derived from DLS measurements for CD81, Claudin-1 and all mixtures of both proteins. **A)** in the absence **B)** in the presence of CHEMS.

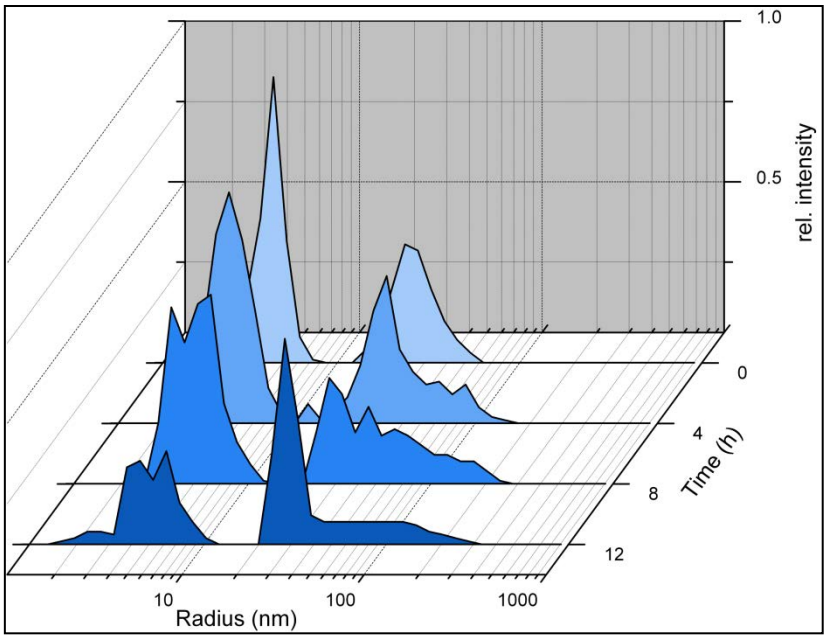

Figure 80: Radius distribution for CD81:Claudin-1 7:3 in the presence of CHEMS as measured by DLS.

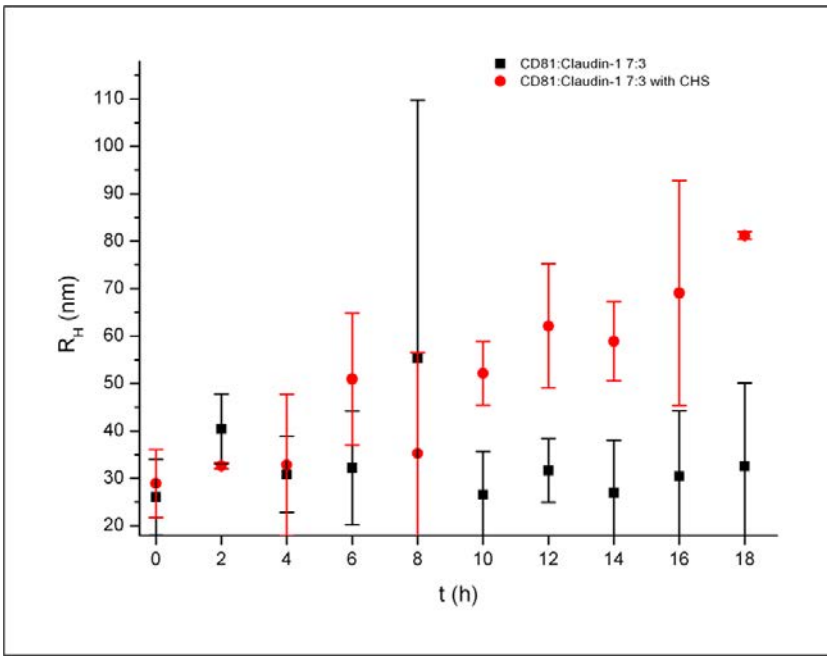

Figure 81: Radius distribution (> 10 nm) over time forCD81:Claudin-1 7:3 with (black boxes) and without (red circles) CHEMS.

It is known that the tetraspanin uroplakins Ia and Ib form defined hexagonal complexes **[190]** with a radius of approx. 8nm. Oligomerization of such a complex of six homodimers leads to a cluster of tetraspanin molecules. This could explain the less-defined particle radius of CD81 ranging from approx. 8nm to approx. 100 nm, observed in this study in the presence of CHEMS. The defined oligomeric state at a R_H of approx. 30nm that could be observed with DLS for a solution containing CD81

and Claudin-1 in a 7:3 molar ratio would then be the result of incorporation of Claudin-1 into such a complex leading to a more defined oligomerization, which is stable if CHEMS is present in the solution (**Figure 81**).

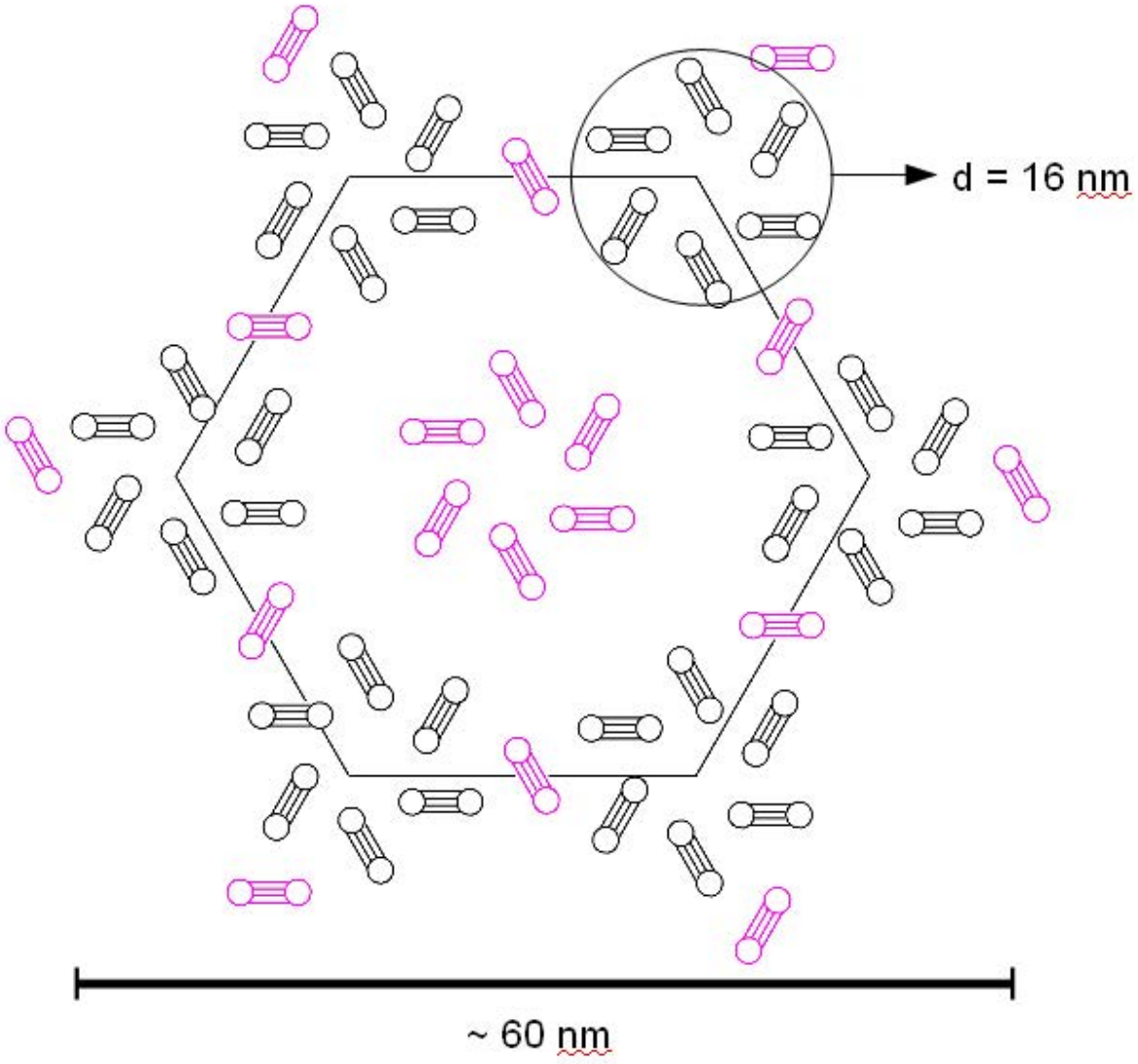

Figure 82: Proposed complex of CD81 homodimers (black) and Claudin-1 homodimers (pink). The hexagonal arrangement of CD81 homodimers is the arrangement that was found for tetraspanin uroplakins Ia and Ib by cryoEM studies.

The different DLS results for absence and presence of cholesterol is in accordance with the proposed two cholesterol binding sides of CD81 **[205]** and studies on the role of CD81 in HCV infection which showed that the entry of the virus in the host cell is dependent on the cholesterol content within the cell **[166].** One possible complex between Claudin-1 and CD81 with a diameter of about 60 nm, and therefore in concordance with the measured R_H of approx. 30 nm is displayed in **Figure 82**. As building blocks of the complex the hexagonal arrangement of dimers revealed by

CryoEM for tetraspanin uroplakins Ia and Ib was used. These hexamers of dimers were found to have a diameter of 16 nm **[190]**. These 16nm were used as a ruler for the overall complex between CD81 and Claudin-1. Claudin-1 and CD81 dimers were furthermore arranged in a way that the specific ratio of 7:3 between CD81 and Claudin-1 is reflected in the mirror. The above displayed structure has a 6:3 CD81:Claudin-1 ratio, which is within the pipetting error at this volumes to a ratio of 7:3.

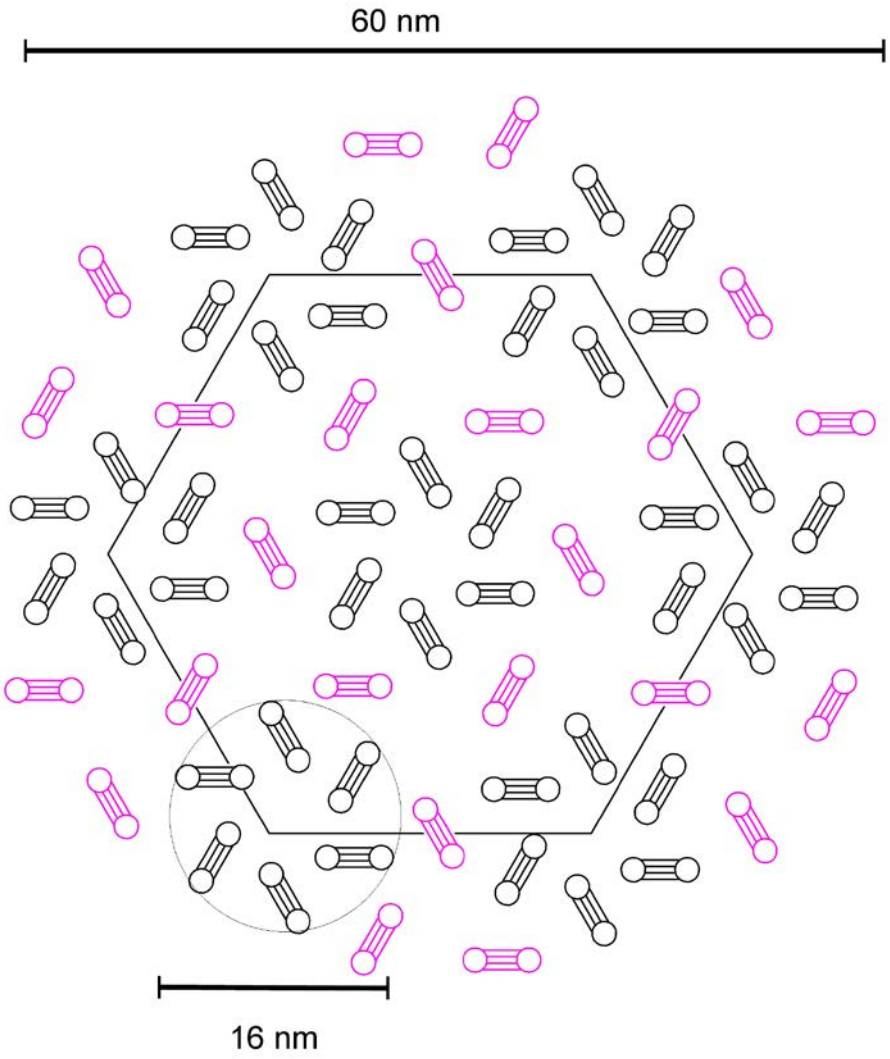

Figure 83: Most probable complex of CD81 homodimers (black) and Claudin-1 homodimers (pink).The hexagonal arrangement of CD81 homodimers is the arrangement that was found for tetraspanin uroplakins Ia and Ib by cryoEM studies **[190]**.

Attention also needed to be paid to the symmetry of the complex. In the 2D-crystals used for cryoEM of uroplakins a hexagonal symmetry was found **[190]**. Combining these restraints another complex was proposed (**Figure 83**). Here the symmetric arrangement of molecules is more logical. Seven uroplakin-like CD81 (black)

complexes (containing six homodimers each) are arranged with 24 Claudin-1 homodimers (Claudin-1). Again the known diameter of the hexamer of dimers (16 nm) **[190]** was used as a ruler to assemble the complex. The result is a complex of approx. 60 nm in diameter representing the R_H ~ 30 nm particle present in solutions containing CD81 and Claudin-1 in a 7:3 ratio. The ratio of CD81 and Claudin-1 in the complex is 7:4 which is in the range of pipetting errors at the volumes used for the DLS measurements.

6.4. Conclusions and Outlook

After improvement of initially received solutions of CD81 and CD82 based on results from DLS measurements, crystals of both proteins could be obtained. CD81 crystallized better, but diffraction studies showed that for indexing and data collection crystals need to be improved. Optimization of crystallization was challenging since even at optimized expression and purification by **NICKLAS BONANDER** only small amounts of protein were available. With larger amounts of protein and the now even further improved DLS methods it will be possible to overcome the problems during crystallization and to obtain the first crystal structure of a tetraspanin.

It could be shown for the first time that the assumed interaction of CD81 and Claudin-1 exists in solution, but only at a molar ratio of CD81 to Claudin-1 of roughly 2:1. Interesting is the dependence of the stability of this complex on the presence of CHEMS since it is proposed that CHEMS is important for HCV infection and CD81 function. This makes it necessary to further investigate the interaction of CD81 and Claudin-1 by other techniques such as CryoEM or SAXS that yield more information than DLS. Furthermore the interaction of CD81 and Claudin-1 – both alone and together – with the E1/E2-glycoproteins on the HCV surface should be investigated by DLS as well as SAXS. This should then shed light on the interaction between these proteins and thus will give new insights into HCV infection and maybe on how to prevent infection.

7. Abstract – Zusammenfassung

7.1. Abstract

Obtaining X-ray suitable crystals is to date the rate limiting step to solve the structure of biological macromolecules such as proteins at atomic resolution. Those Structures are required for the design of novel drugs and to understand the way biological systems work. Rationalization of crystallization by biophysical methods is a promising way to accelerate this process. Here Dynamic Light Scattering (DLS) was applied in order to develop novel methods for the rationalization of crystallization and to analyze crystallization and aggregation of proteins in detail.

The method of *in situ* DLS was successfully applied to all major crystallization methods used today. For the first time ever the submicroscopic processes during crystallization and nucleation could be observed within thin capillaries used in the Granada Crystallization Box Domino (GCB-D) and in the CrystalFormer HT. Furthermore for the first time DLS measurements could be carried out in small protein and crystallization droplets under oil in Terazaki plates. In this case not only the observation and scoring of the crystallization or oligomerization processes is possible, also the quality of the DLS measurements is good enough that in future optical cuvettes may be replaced by Terazaki plates, thus saving time and material. 1 µL sample solution instead of 10 µL can be used and automated measurements are possible. Also light scattering measurements in the most commonly used 96 well sitting drop vapor diffusion plates could be improved and detailed analysis and scoring of crystallization processes within these plates was enabled and demonstrated. Automation of measurements for the above mentioned crystallization environments and methods could be automated for the first time. This allows analyzing up to 192 droplets at the same time. Some of these results are published already.

Following these improvements, DLS measurements were carried out also for the first time in special environments, as a crystallization box used for microgravity experiments in space or in cubic lipid phases within PCR tubes. Especially the latter set up is valuable, since membrane proteins are mainly crystallized within cubic lipid phases today.

Based on the developed DLS methods and technical results obtained, DLS was applied to investigate the crystallization behavior of the surface layer protein SlfB

from *Lysinibacillus spaericus*. Applying DLS initial crystals could be obtained from this protein. Moreover it could be shown by DLS that the stability of SlfB depends on the presence of bivalent cations. At pH 4.75 and 7.4 the protein is stabilized by 100 mM of either $MgCl_2$ or $SrCl_2$. This information will support crystallization experiments to obtain X-ray suitable crystals and thus will facilitate the 3D structure analysis. It could be confirmed by small angle X-ray scattering (SAXS) that the elongated shape of SlfB predicted by DLS is indeed the shape of the protein.

Furthermore *in situ* DLS was applied to investigate the specific interaction of the human membrane proteins CD81 and Claudin-1, both involved in the infection of liver cells by hepatitis C virus (HCV). It could be shown by DLS that only at a CD81:Claudin ratio of 7:3 and in the presence of cholesteryl hemisuccinate a stable complex is formed. Based on these results and biochemical data a model for this complex was proposed. Finally CD81 could be crystallized after solution conditions were improved by applying *in situ* DLS.

7.2. Zusammenfassung

Die Gewinnung Röntgentauglicher Kristalle ist heute der limitierende Schritt bei der Lösung der Struktur von biologischen Makromolekülen, zum Beispiel Proteinen, bei atomarer Auflösung. Diese Strukturen werden benötigt um neue Medikamente zu entwickeln und um zu verstehen wie biologische Systeme funktionieren. Die Rationalisierung der Kristallisation unter Anwendung biophysikalischer Methoden ist ein vielversprechender Weg diesen Prozess zu beschleunigen. In dieser Arbeit wurde Dynamische Lichtstreuung (DLS) angewendet um neue Methoden der Rationalisierung der Kristallisation zu entwickeln und die Prozesse der Proteinkristallisation und –aggregation im Detail zu untersuchen.

Die Methode der Dynamischen Lichtstreuung *in situ* wurde erfolgreich an alle heute gebräuchlichen Kristallisationsmethoden adaptiert. Zum ersten Mal überhaupt konnten die submikroskopischen Prozesse während der Kristallisation in Kappilaren der auf Gegendiffusion basierenden Granada Crystallization Box Domino (GCB-D) und dem CrystalFormer HT zeitaufgelöst untersucht werden. Weiterhin konnten erstmals DLS Messungen in kleinen Protein- und Kristallisations-Tropfen unter Öl in sogenannten Terazaki Platten durchgeführt werden. In diesem Fall ist nicht nur die Überwachung von Kristallisations- oder Oligomerisierungs Prozessen möglich sondern die hervorragende Qualität dieser Messungen ermöglicht es die bislang überwiegend für DLS Messungen genutzten Küvetten in Zukunft durch Terazaki-Platten zu ersetzen. Dies spart Zeit und Material. Es reichen für eine Messung 1 µL statt bislang 10 µL Lösung. Weiterhin lassen sich die Messungen auch voll, automatisch und zeitaufgelöst in unterschiedlichen Tropfen parallel durchführen.. Lichtstreumessungen wurden auch in Tropfen mit niedrigen Volumen in Platten mit 96 Kristallisationstöpfen durchgeführt. Diese Platten sind heute die meistgenutzten in robotunterstützten Hochdurchsatz Kristallisationsexperimenten. Die Methode der *in situ* DLS Messung in diesen Platten wurde ausgearbeitet und angepasst. Eine detaillierte Analyse von Kristallisationsphänomenen in diesen Platten wurde ermöglicht und an ausgewählten Beispielen dargestellt. Diese Anwendung ermöglicht es nun bis zu 192 Kristallisationsexperimente über DLS zu überwachen und auszuwerten. Ein Teil dieser Arbeiten konnte bereits veröffentlicht werden.

Im Anschluss an diese Experimente und Arbeiten konnte gezeigt werden, dass DLS Messungen auch in einigen besonderen Kristallisationsumgebungen möglich sind. So zum Beispiel in Kapillaren in einer Kristallisationsbox für

Weltraumexperimente oder in kubisch lipiden Phasen in PCR-Behältern. Vor allem die letztere Kristallisationsumgebung gewinnt heute zunehmend an Bedeutung, da Membran-Proteine häufig in kubisch lipiden Phasen kristallisiert werden. Es ist nun im Prinzip möglich die submikroskopischen Vorgänge von kristallisierenden Membran-Protein Lösungen in kubisch lipiden Phasen mit DLS zu untersuchen und zu optimieren. Damit lässt sich die Kristallisation und die Strukturaufklärung dieser sehr wichtigen Protein-Klasse zukünftig verbessern

Basierend auf den vorab beschriebenen und im Rahmen dieser Doktorarbeit entwickelten Methoden wurde in situ DLS angewandt um das surface layer protein SlfB aus Lysinibacillus spaericus in Lösung zu analysieren. Die über DLS gesammelten Informationen ermöglichten eine erste erfolgreichen Kristallisation dieses Proteins. Zusätzlich konnte mit DLS gezeigt werden, dass die Stabilität von SlfB über die Zugabe von bivalenten Kationen optimiert werden kann. Bei pH-Werten von 4.75 und 7.4 wird das Protein durch 100 mM $MgCl_2$ oder $SrCl_2$ am stärksten stabilisiert. Dieses Erkenntnisse sollen in Zukunft genutzt werden, um röntgentaugliche Kristalle von SlfB zu erhalten und folgend die Struktur zu lösen. Durch Kleinwinkel Röntgenbeugung konnte gezeigt werden, dass die anhand von DLS Messungen bereits vermutete längliche Form von SlfB tatsächlich in Lösung vorliegt.

Des Weiteren wurde *in situ* DLS angewandt, um die spezifische Interaktion von CD81 und Claudin-1, beides menschliche Membran-Proteine, die an der Infektion von Leberzellen mit dem Hepatitis C Virus (HCV) beteiligt sind, zu untersuchen. Es konnte gezeigt werden, dass nur bei einem Verhältnis von CD81 zu Claudin-1 von sieben zu drei und unter Zugabe von von Cholesteryl Hemisuccinat ein stabiler und definierter Komplex gebildet wird. Basierend auf diesen Ergebnissen konnte ein Modell für einen möglichen CD81-Claudin-1 Komplex vorgeschlagen werden. Abschliessend konnte CD81 alleine kristallisiert werden, nachdem die Proteinlösung basierend DLS Messungen optimiert wurde.

8. References

[1] Ab, E.; Atkinson, A. R.; Banci, L.; Bertini, I.; Ciofi-Baffoni, S.; Brunner, K.; Diercks, T.; Dotsch, V.; Engelke, F.; Folkers, G. E.; Griesinger, C.; Gronwald, W.; Gunther, U.; Habeck, M.; de Jong, R. N.; Kalbitzer, H. R.; Kieffer, B.; Leeflang, B. R.; Loss, S.; Luchinat, C.; Marquardsen, T.; Moskau, D.; Neidig, K. P.; Nilges, M.; Piccioli, M.; Pierattelli, R.; Rieping, W.; Schippmann, T.; Schwalbe, H.; Trave, G.; Trenner, J.; Wohnert, J.; Zweckstetter, M.; Kaptein, R., NMR in the SPINE Structural Proteomics project. *Acta Crystallographica Section D* **2006,** 62, (10), 1150-1161.

[2] Kremer, W.; Kalbitzer, H. R.; Thomas L. James, V. D. t.; Uli, S., Physiological conditions and practicality for protein nuclear magnetic resonance spectroscopy: Experimental methodologies and theoretical background. In *Methods in Enzymology*, Academic Press: 2001; Vol. Volume 339, pp 3-19.

[3] David, D.; Grant, J. J., Historical Perspective - 3D Reconstruction from Electron Micrographs: A Personal Account of its Development. In *Methods in Enzymology*, Academic Press: 2010; Vol. Volume 481, pp 1-24.

[4] Pawel A, P.; Grant, J. J., Chapter One - Fundamentals of Three-Dimensional Reconstruction from Projections. In *Methods in Enzymology*, Academic Press: 2010; Vol. Volume 482, pp 1-33.

[5] Schenk, A. D.; Castano-Diez, D.; Gipson, B.; Arheit, M.; Zeng, X.; Stahlberg, H.; Grant, J. J., Chapter Four - 3D Reconstruction from 2D Crystal Image and Diffraction Data. In *Methods in Enzymology*, Academic Press: 2010; Vol. Volume 482, pp 101-129.

[6] Osmulski, P. A.; Gaczynska, M.; Raymond, J. D., Atomic Force Microscopy of the Proteasome. In *Methods in Enzymology*, Academic Press: 2005; Vol. Volume 398, pp 414-425.

[7] Patrick, V.; Nejat, D., Chapter 3 - Liposome Characterization by Quartz Crystal Microbalance Measurements and Atomic Force Microscopy. In *Methods in Enzymology*, Academic Press: 2009; Vol. Volume 465, pp 43-73.

[8] Yamamoto, D.; Uchihashi, T.; Kodera, N.; Yamashita, H.; Nishikori, S.; Ogura, T.; Shibata, M.; Ando, T.; Nils, G. W., Chapter Twenty - High-Speed Atomic Force Microscopy Techniques for Observing Dynamic Biomolecular Processes. In *Methods in Enzymology*, Academic Press: 2010; Vol. Volume 475, pp 541-564.

[9] Mertens, H. D. T.; Svergun, D. I., Structural characterization of proteins and complexes using small-angle X-ray solution scattering. *Journal of Structural Biology* **2010,** 172, (1), 128-141.

[10] Rambo, R. P.; Tainer, J. A., Bridging the solution divide: comprehensive structural analyses of dynamic RNA, DNA, and protein assemblies by small-angle X-ray scattering. *Current Opinion in Structural Biology* **2010,** 20, (1), 128-137.

[11] Henderson, R.; Baldwin, J. M.; Ceska, T. A.; Zemlin, F.; Beckmann, E.; Downing, K. H., Model for the structure of bacteriorhodopsin based on high-resolution electron cryo-microscopy. *Journal of Molecular Biology* **1990,** 213, (4), 899-929.

[12] Blakeley, M. P.; Langan, P.; Niimura, N.; Podjarny, A., Neutron crystallography: opportunities, challenges, and limitations. *Current Opinion in Structural Biology* **2008,** 18, (5), 593-600.

[13] Kendrew, J. C.; Bodo, G.; Dintzis, H. M.; Parrish, R. G.; Wyckoff, H.; Phillips, D. C., A Three-Dimensional Model of the Myoglobin Molecule Obtained by X-Ray Analysis. *Nature* **1958,** 181, (4610), 662-666.

[14] Rupp, B., *Biomolecular Crystallography: Principles, Practice, and Application to Structural Biology*. 1st ed.; Garland Science: New York, 2009; p 850.

[15] Berman, H. M.; Westbrook, J.; Feng, Z.; Gilliland, G.; Bhat, T. N.; Weissig, H.; Shindyalov, I. N.; Bourne, P. E., The Protein Data Bank. *Nucleic Acids Research* **2000,** 28, (1), 235-242.

[16] TargetDB. http://targetdb.sbkb.org/statistics/TargetStatistics.html#table1 (20.09.2011),

[17] Burley, S. K.; Almo, S. C.; Bonanno, J. B.; Capel, M.; Chance, M. R.; Gaasterland, T.; Lin, D.; Sali, A.; Studier, F. W.; Swaminathan, S., Structural genomics: beyond the Human Genome Project. *Nature Genetics* **1999,** 23, (2), 151-157.

[18] Garcia-Caballero, A.; Gavira, J. A.; Pineda-Molina, E.; Chayen, N. E.; Govada, L.; Khurshid, S.; Saridakis, E.; Boudjemline, A.; Swann, M. J.; Shaw Stewart, P.; Briggs, R. A.; Kolek, S. A.; Oberthuer, D.; Dierks, K.; Betzel, C.; Santana, M.; Hobbs, J. R.; Thaw, P.; Savill, T. J.; Mesters, J. R.; Hilgenfeld, R.; Bonander, N.; Bill, R. M., Optimization of Protein Crystallization: The OptiCryst Project. *Crystal Growth & Design* **2011,** 11, (6), 2112-2121.

[19] Joachimiak, A., High-throughput crystallography for structural genomics. *Current Opinion in Structural Biology* **2009,** 19, (5), 573-584.

[20] Chayen, N. E., Protein crystallization for genomics: throughput versus output. *Journal of Structural and Functional Genomics* **2003,** 4, (2), 115-120.

[21] Weselak, M.; Patch, M. G.; Selby, T. L.; Knebel, G.; Stevens, R. C.; Charles W. Carter, Jr.; Robert, M. S., Robotics for Automated Crystal Formation and Analysis. In *Methods in Enzymology*, Academic Press: 2003; Vol. Volume 368, pp 45-76.

[22] Patrick J, L., Membrane protein structural biology: the high throughput challenge. *Journal of Structural Biology* **2003,** 142, (1), 144-153.

[23] Fogg, M. J.; Alzari, P.; Bahar, M.; Bertini, I.; Betton, J.-M.; Burmeister, W. P.; Cambillau, C.; Canard, B.; Carrondo, M.; Coll, M.; Daenke, S.; Dym, O.; Egloff, M.-P.; Enguita, F. J.; Geerlof, A.; Haouz, A.; Jones, T. A.; Ma, Q.; Manicka, S. N.; Migliardi, M.; Nordlund, P.; Owens, R. J.; Peleg, Y.; Schneider, G.; Schnell, R.; Stuart, D. I.; Tarbouriech, N.; Unge, T.; Wilkinson, A. J.; Wilmanns, M.; Wilson, K. S.; Zimhony, O.; Grimes, J. M., Application of the use of high-throughput technologies to the determination of protein structures of bacterial and viral pathogens. *Acta Crystallographica Section D* **2006,** 62, (10), 1196-1207.

[24] May, A. P.; Segelke, B. W., Efficient Macromolecular Crystallization Using Microfluidics and Randomized Design of Screening Reagents. In *Structural Proteomics : High-Throughput Methods*, 2008; Vol. 426, pp 387-402.

[25] Stojanoff, V.; Jakoncic, J.; Oren, D. A.; Nagarajan, V.; Navarro Poulsen, J.-C.; Adams-Cioaba, M. A.; Bergfors, T.; Sommer, M. O. A., From screen to structure with a harvestable microfluidic device. *Acta Crystallographica Section F* **2011,** 67, (8), 971-975.

[26] van der Woerd, M.; Ferree, D.; Pusey, M., The promise of macromolecular crystallization in microfluidic chips. *Journal of Structural Biology* **2003,** 142, (1), 180-187.

[27] Jancarik, J.; Kim, S.-H., Sparse matrix sampling: a screening method for crystallization of proteins. *Journal of Applied Crystallography* **1991,** 24, (4), 409-411.

[28] Neutze, R.; Wouts, R.; van der Spoel, D.; Weckert, E.; Hajdu, J., Potential for biomolecular imaging with femtosecond X-ray pulses. *Nature* **2000,** 406, (6797), 752-757.

[29] Altarelli, M., The European X-ray free-electron laser facility in Hamburg. *Nuclear Instruments and Methods in Physics Research Section B: Beam Interactions with Materials and Atoms* **2011,** 269, (0), 2845-2849.

[30] Chapman, H. N.; Barty, A.; Bogan, M. J.; Boutet, S.; Frank, M.; Hau-Riege, S. P.; Marchesini, S.; Woods, B. W.; Bajt, S.; Benner, W. H.; London, R. A.; Plonjes, E.; Kuhlmann, M.; Treusch, R.; Dusterer, S.; Tschentscher, T.; Schneider, J. R.; Spiller, E.; Moller, T.; Bostedt, C.; Hoener, M.; Shapiro, D. A.; Hodgson, K. O.; van der Spoel, D.; Burmeister, F.; Bergh, M.; Caleman, C.; Huldt, G.; Seibert, M. M.; Maia, F. R. N. C.; Lee, R. W.; Szoke, A.; Timneanu, N.; Hajdu, J., Femtosecond diffractive imaging with a soft-X-ray free-electron laser. *Nature Physics* **2006,** 2, (12), 839-843.

[31] Seibert, M. M.; Ekeberg, T.; Maia, F. R. N. C.; Svenda, M.; Andreasson, J.; Jonsson, O.; Odic, D.; Iwan, B.; Rocker, A.; Westphal, D.; Hantke, M.; DePonte, D. P.; Barty, A.; Schulz, J.; Gumprecht, L.; Coppola, N.; Aquila, A.; Liang, M.; White, T. A.; Martin, A.; Caleman, C.; Stern, S.; Abergel, C.; Seltzer, V.; Claverie, J.-M.; Bostedt, C.; Bozek, J. D.; Boutet, S.; Miahnahri, A. A.; Messerschmidt, M.; Krzywinski, J.; Williams, G.; Hodgson, K. O.; Bogan, M. J.; Hampton, C. Y.; Sierra, R. G.; Starodub, D.; Andersson, I.; Bajt, S.; Barthelmess, M.; Spence, J. C. H.; Fromme, P.; Weierstall, U.; Kirian, R.; Hunter, M.; Doak, R. B.; Marchesini, S.; Hau-Riege, S. P.; Frank, M.; Shoeman, R. L.; Lomb, L.; Epp, S. W.; Hartmann, R.; Rolles, D.; Rudenko, A.; Schmidt, C.; Foucar, L.; Kimmel, N.; Holl, P.; Rudek, B.; Erk, B.; Homke, A.; Reich, C.; Pietschner, D.; Weidenspointner, G.; Struder, L.; Hauser, G.; Gorke, H.; Ullrich, J.; Schlichting, I.; Herrmann, S.; Schaller, G.; Schopper, F.; Soltau, H.; Kuhnel, K.-U.; Andritschke, R.; Schroter, C.-D.; Krasniqi, F.; Bott, M.; Schorb, S.; Rupp, D.; Adolph, M.; Gorkhover, T.; Hirsemann, H.; Potdevin, G.; Graafsma, H.; Nilsson, B.; Chapman, H. N.; Hajdu, J., Single mimivirus particles intercepted and imaged with an X-ray laser. *Nature* **2011,** 470, (7332), 78-81.

[32] Chapman, H. N.; Fromme, P.; Barty, A.; White, T. A.; Kirian, R. A.; Aquila, A.; Hunter, M. S.; Schulz, J.; DePonte, D. P.; Weierstall, U.; Doak, R. B.; Maia, F. R. N. C.; Martin, A. V.; Schlichting, I.; Lomb, L.; Coppola, N.; Shoeman, R. L.; Epp, S. W.; Hartmann, R.; Rolles, D.; Rudenko, A.; Foucar, L.; Kimmel, N.; Weidenspointner, G.; Holl, P.; Liang, M.; Barthelmess, M.; Caleman, C.; Boutet, S.; Bogan, M. J.; Krzywinski, J.; Bostedt, C.; Bajt, S.; Gumprecht, L.; Rudek, B.; Erk, B.; Schmidt, C.; Homke, A.; Reich, C.; Pietschner, D.; Struder, L.; Hauser, G.; Gorke, H.; Ullrich, J.; Herrmann, S.; Schaller, G.; Schopper, F.; Soltau, H.; Kuhnel, K.-U.; Messerschmidt, M.; Bozek, J. D.; Hau-Riege, S. P.; Frank, M.; Hampton, C. Y.; Sierra, R. G.; Starodub, D.; Williams, G. J.; Hajdu, J.; Timneanu, N.; Seibert, M. M.; Andreasson, J.; Rocker, A.; Jonsson, O.; Svenda, M.; Stern, S.; Nass, K.; Andritschke, R.; Schroter, C.-D.; Krasniqi, F.; Bott, M.; Schmidt, K. E.; Wang, X.; Grotjohann, I.; Holton, J. M.; Barends, T. R. M.; Neutze, R.; Marchesini, S.; Fromme, R.; Schorb, S.; Rupp, D.; Adolph, M.; Gorkhover, T.; Andersson, I.; Hirsemann, H.; Potdevin, G.; Graafsma, H.;

Nilsson, B.; Spence, J. C. H., Femtosecond X-ray protein nanocrystallography. *Nature* **2011,** 470, (7332), 73-77.

[33] Koopmann, R.; Cupelli, K.; Redecke, L.; Nass, K.; DePonte, D. P.; White, T. A.; Stellato, F.; Rehders, D.; Liang, M.; Andreasson, J.; Aquila, A.; Bajt, S.; Barthelmess, M.; Barty, A.; Bogan, M. J.; Bostedt, C.; Boutet, S.; Bozek, J. D.; Caleman, C.; Coppola, N.; Davidsson, J.; Doak, R. B.; Ekeberg, T.; Epp, S. W.; Erk, B.; Fleckenstein, H.; Foucar, L.; Graafsma, H.; Gumprecht, L.; Hajdu, J.; Hampton, C. Y.; Hartmann, A.; Hartmann, R.; Hauser, G.; Hirsemann, H.; Holl, P.; Hunter, M. S.; Kassemeyer, S.; Kirian, R. A.; Lomb, L.; Maia, F. R. N. C.; Kimmel, N.; Martin, A. V.; Messerschmidt, M.; Reich, C.; Rolles, D.; Rudek, B.; Rudenko, A.; Schlichting, I.; Schulz, J.; Seibert, M. M.; Shoeman, R. L.; Sierra, R. G.; Soltau, H.; Stern, S.; Struder, L.; Timneanu, N.; Ullrich, J.; Wang, X.; Weidenspointner, G.; Weierstall, U.; Williams, G. J.; Wunderer, C. B.; Fromme, P.; Spence, J. C. H.; Stehle, T.; Chapman, H. N.; Betzel, C.; Duszenko, M., In vivo protein crystallization opens new routes in structural biology. *Nature Methods* **2012,** advance online publication.

[34] Doerr, A., Diffraction before destruction. *Nature Methods* **2011,** 8, (4), 283-283.

[35] Quiney, H. M.; Nugent, K. A., Biomolecular imaging and electronic damage using X-ray free-electron lasers. *Nature Physics* **2011,** 7, (2), 142-146.

[36] Chayen, N., Turning protein crystallisation from an art into a science. *Current Opinion in Structural Biology* **2004,** 14, (5), 577-583.

[37] Newman, J.; Egan, D.; Walter, T. S.; Meged, R.; Berry, I.; Ben Jelloul, M.; Sussman, J. L.; Stuart, D. I.; Perrakis, A., Towards rationalization of crystallization screening for small- to medium-sized academic laboratories: the PACT/JCSG+ strategy. *Acta Crystallographica Section D* **2005,** 61, (10), 1426-1431.

[38] Congreve, M.; Murray, C. W.; Blundell, T. L., Keynote review: Structural biology and drug discovery. *Drug Discovery Today* **2005,** 10, (13), 895-907.

[39] Saridakis, E.; Chayen, N. E., Systematic Improvement of Protein Crystals by Determining the Supersolubility Curves of Phase Diagrams. *Biophysical Journal* **2003,** 84, (2), 1218-1222.

[40] Naomi E, C., Methods for separating nucleation and growth in protein crystallisation. *Progress in Biophysics and Molecular Biology* **2005,** 88, (3), 329-337.

[41] Chayen, N. E.; Saridakis, E., Protein crystallization: from purified protein to diffraction-quality crystal. *Nature Methods* **2008,** 5, (2), 147-153.

[42] Govada, L.; Chayen, N. E., Crystallization by Controlled Evaporation Leading to High Resolution Crystals of the C1 Domain of Cardiac Myosin Binding Protein-C (cMyBP-C)†. *Crystal Growth & Design* **2009,** 9, (4), 1729-1732.

[43] Bolanos-Garcia, V. M.; Chayen, N. E., New directions in conventional methods of protein crystallization. *Progress in Biophysics and Molecular Biology* **2009,** 101, (1-3), 3-12.

[44] Derewenda, Z. S.; Vekilov, P. G., Entropy and surface engineering in protein crystallization. *Acta Crystallographica Section D* **2006,** 62, (1), 116-124.

[45] García-Ruiz, J. M., Nucleation of protein crystals. *Journal of Structural Biology* **2003,** 142, (1), 22-31.

[46] Vekilov, P. G., The two-step mechanism of nucleation of crystals in solution. *Nanoscale* **2010,** 2, (11), 2346-2357.

[47] Vekilov, P. G., Nucleation. *Crystal Growth & Design* **2010,** 10, (12), 5007-5019.

[48] Das, R.; Baker, D., Macromolecular Modeling with Rosetta. *Annual Review of Biochemistry* **2008,** 77, (1), 363-382.
[49] Baker, D., Prediction and design of macromolecular structures and interactions. *Philosophical Transactions of the Royal Society B: Biological Sciences* **2006,** 361, (1467), 459-463.
[50] Baker, D., An exciting but challenging road ahead for computational enzyme design. *Protein Science* **2010,** 19, (10), 1817-1819.
[51] Fold it. http://fold.it/portal/ (20.09.2011),
[52] Khatib, F.; DiMaio, F.; Cooper, S.; Kazmierczyk, M.; Gilski, M.; Krzywda, S.; Zabranska, H.; Pichova, I.; Thompson, J.; Popovic, Z.; Jaskolski, M.; Baker, D., Crystal structure of a monomeric retroviral protease solved by protein folding game players. *Nat Struct Mol Biol* **2011,** 18, (10), 1175-7.
[53] Dale, G. E.; Oefner, C.; D'Arcy, A., The protein as a variable in protein crystallization. *Journal of Structural Biology* **2003,** 142, (1), 88-97.
[54] Berne, B. J.; Pecora, R., *Dynamic Light Scattering*. ed.; John Wiley and Sons: New York, 1976; p null.
[55] Pecora, R., Doppler Shifts in Light Scattering from Pure Liquids and Polymer Solutions. *The Journal of Chemical Physics* **1964,** 40, (6), 1604.
[56] Schmitz, K. S., *An introduction to dynamic light scattering of macromolecules*. ed.; Academic Press: New York, 1990; p 472
[57] George, A.; Wilson, W. W., Predicting protein crystallization from a dilute solution property. *Acta Crystallographica Section D* **1994,** 50, (4), 361-365.
[58] Bonnete, F.; Vivares, D., Interest of the normalized second virial coefficient and interaction potentials for crystallizing large macromolecules. *Acta Crystallographica Section D* **2002,** 58, (10 Part 1), 1571-1575.
[59] Liu, J.; Yin, D.-C.; Guo, Y.-Z.; Wang, X.-K.; Xie, S.-X.; Lu, Q.-Q.; Liu, Y.-M., Selecting Temperature for Protein Crystallization Screens Using the Temperature Dependence of the Second Virial Coefficient. *PLoS ONE* **2011,** 6, (3), e17950.
[60] Yadav, S.; Scherer, T. M.; Shire, S. J.; Kalonia, D. S., Use of dynamic light scattering to determine second virial coefficient in a semidilute concentration regime. *Anal Biochem* **2011,** 411, (2), 292-6.
[61] Zhang, J.; Liu, X. Y., Effect of protein--protein interactions on protein aggregation kinetics. *The Journal of Chemical Physics* **2003,** 119, (20), 10972-10976.
[62] Li, S.; Xing, D.; Li, J., Dynamic Light Scattering Application to Study Protein Interactions in Electrolyte Solutions. *Journal of Biological Physics* **2004,** 30, (4), 313-324.
[63] Wilson, W. W., Light scattering as a diagnostic for protein crystal growth--A practical approach. *Journal of Structural Biology* **2003,** 142, (1), 56-65.
[64] Santos, N. C.; Castanho, M. A., Teaching light scattering spectroscopy: the dimension and shape of tobacco mosaic virus. *Biophysical Journal* **1996,** 71, (3), 1641-1650.
[65] Provencher, S. W., CONTIN: A general purpose constrained regularization program for inverting noisy linear algebraic and integral equations. *Computer Physics Communications* **1982,** 27, (null), 229-242.
[66] Provencher, S. W., Inverse problems in polymer characterization: Direct analysis of polydispersity with photon correlation spectroscopy. *Die Makromolekulare Chemie* **1979,** 180, (1), 201-209.

[67] Provencher, S. W., A constrained regularization method for inverting data represented by linear algebraic or integral equations. *Computer Physics Communications* **1982,** 27, (3), 213-227.
[68] Hassan, P. A.; Kulshreshtha, S. K., Modification to the cumulant analysis of polydispersity in quasielastic light scattering data. *Journal of Colloid and Interface Science* **2006,** 300, (2), 744-748.
[69] Frisken, B. J., Revisiting the Method of Cumulants for the Analysis of Dynamic Light-Scattering Data. *Applied Optics* **2001,** 40, (24), 4087-4091.
[70] Koppel, D., Analysis of Macromolecular Polydispersity in Intensity Correlation Spectroscopy: The Method of Cumulants. *The Journal of Chemical Physics* **1972,** 57, (11), 4814.
[71] Brown, W., *Dynamic light scattering: the method and some applications*. ed.; Clarendon Press: 1993; Vol. Oxford, p 735.
[72] Zimm, B., Apparatus and Methods for Measurement and Interpretation of the Angular Variation of Light Scattering; Preliminary Results on Polystyrene Solutions. *The Journal of Chemical Physics* **1948,** 16, (12), 1099.
[73] Tessier, P. M.; Johnson, H. R.; Pazhianur, R.; Berger, B. W.; Prentice, J. L.; Bahnson, B. J.; Sandler, S. I.; Lenhoff, A. M., Predictive crystallization of ribonuclease A via rapid screening of osmotic second virial coefficients. *Proteins: Structure, Function, and Bioinformatics* **2003,** 50, (2), 303-311.
[74] Baldwin, E. T.; Crumley, K. V.; Carter Jr, C. W., Practical, Rapid Screening of Protein Crystallization Conditions by Dynamic Light Scattering. *Biophysical Journal* **1986,** 49, (1), 47-48.
[75] Wilson, W. W., Monitoring crystallization experiments using dynamic light scattering: Assaying and monitoring protein crystallization in solution. *Methods* **1990,** 1, (1), 110-117.
[76] Casay, G. A.; Wilson, W. W., Laser scattering in a hanging drop vapor diffusion apparatus for protein crystal growth in a microgravity environment. *Journal of Crystal Growth* **1992,** 122, (1-4), 95-101.
[77] Wessel, T.; Ricka, J., Microvolume dynamic light scattering and simultaneous video microscopic observation for screening of protein crystal growth. *Proceedings of SPIE* **1998,** 3199, 299.
[78] Ferré-D'Amaré, A. R.; Burley, S. K., Use of dynamic light scattering to assess crystallizability of macromolecules and macromolecular assemblies. *Structure* **1994,** 2, (5), 357-359.
[79] Ferré-D'Amaré, A. R.; Burley, S. K.; Charles W. Carter, Jr., Dynamic light scattering in evaluating crystallizability of macromolecules. In *Methods in Enzymology*, Academic Press: 1997; Vol. Volume 276, pp 157-166.
[80] Georgalis, Y.; Saenger, W., Time-resolved light scattering studies on protein precrystallization fractal clusters. *Advances in Colloid and Interface Science* **1993,** 46, 165-183.
[81] Georgalis, Y.; Schüler, J.; Frank, J.; Soumpasis, M. D.; Saenger, W., Protein crystallization screening through scattering techniques. *Advances in Colloid and Interface Science* **1995,** 58, (1), 57-86.
[82] Kadima, W.; McPherson, A.; Dunn, M. F.; Jurnak, F. A., Characterization of precrystallization aggregation of canavalin by dynamic light scattering. *Biophysical Journal* **1990,** 57, (1), 125-132.
[83] Malkin, A. J.; McPherson, A., Light-scattering investigations of nucleation processes and kinetics of crystallization in macromolecular systems. *Acta Crystallographica Section D* **1994,** 50, (4), 385-395.

[84] Mikol, V.; Hirsch, E.; Giegé, R., Diagnostic of precipitant for biomacromolecule crystallization by quasi-elastic light-scattering. *Journal of Molecular Biology* **1990,** 213, (1), 187-195.
[85] Mikol, V.; Hirsch, E.; Giegé, R., Monitoring protein crystallization by dynamic light scattering. *FEBS Letters* **1989,** 258, (1), 63-66.
[86] Saridakis, E.; Dierks, K.; Moreno, A.; Dieckmann, M. W. M.; Chayen, N. E., Separating nucleation and growth in protein crystallization using dynamic light scattering. *Acta Crystallographica Section D* **2002,** 58, (10 Part 1), 1597-1600.
[87] Hanlon, A. D.; Larkin, M. I.; Reddick, R. M., Free-Solution, Label-Free Protein-Protein Interactions Characterized by Dynamic Light Scattering. *Biophysical Journal* **2010,** 98, (2), 297-304.
[88] Dierks, K.; Meyer, A.; Einspahr, H.; Betzel, C., Dynamic Light Scattering in Protein Crystallization Droplets: Adaptations for Analysis and Optimization of Crystallization Processes. *Crystal Growth & Design* **2008,** 8, (5), 1628-1634.
[89] Python. http://www.python.org/ (22.09.2011),
[90] Brown, W.; Pu, Z., Solution properties of polyisobutylene investigated by using dynamic and static light scattering and pulsed field gradient NMR. *Macromolecules* **1991,** 24, (18), 5151-5157.
[91] Brown, W., *Dynamic light scattering: the method and some applications*. ed.; Clarendon Press: Oxford, 1993; p 735.
[92] Meyer, A. Struktur-Funktions-Analyse ribosomeninaktivierender Proteine im Komplex mit nucleosidanalogen Inhibitoren. Universität Hamburg, 2008.
[93] Streets, A. M.; Quake, S. R., Ostwald Ripening of Clusters during Protein Crystallization. *Physical Review Letters* **2011,** 104, (17), 178102.
[94] Gonzalez-Ramirez, L. A.; Carrera, J.; Gavira, J. A.; Melero-Garcia, E.; Garcia-Ruiz, J. M., Granada Crystallization Facility-2: A Versatile Platform for Crystallization in Space†. *Crystal Growth & Design* **2008,** 8, (12), 4324-4329.
[95] Garcia-Ruiz, J. M.; Gonzalez-Ramirez, L. A.; Gavira, J. A.; Otalora, F., Granada Crystallisation Box: a new device for protein crystallisation by counter-diffusion techniques. *Acta Crystallographica Section D* **2002,** 58, (10 Part 1), 1638-1642.
[96] Otálora, F.; Gavira, J. A.; Ng, J. D.; García-Ruiz, J. M., Counterdiffusion methods applied to protein crystallization. *Progress in Biophysics and Molecular Biology* **2009,** 101, (1-3), 26-37.
[97] Oberthuer, D.; Melero-Garcia, E.; Dierks, K.; Meyer, A.; Betzel, C.; Garcia-Caballero, A.; Gavira, J. A., Monitoring and scoring counter-diffusion protein crystallization experiments in capillaries by in situ dynamic light scattering. *PLoS ONE* **2012,** 7, (6), e33545.
[98] García-Ruiz, J. M.; Otálora, F. n.; Novella, M. L.; Gavira, J. A.; Sauter, C.; Vidal, O., A supersaturation wave of protein crystallization. *Journal of Crystal Growth* **2001,** 232, (1-4), 149-155.
[99] Curtis, R. A.; Prausnitz, J. M.; Blanch, H. W., Protein-protein and protein-salt interactions in aqueous protein solutions containing concentrated electrolytes. *Biotechnology and Bioengineering* **1998,** 57, (1), 11-21.
[100] ANSI/SBS, ANSI/SBS 1-2004 through ANSI/SBS 4-2004. In ed.
[101] Microlytic, Crystal Former User Manual. In ed.
[102] Perbandt, M.; Burmeister, C.; Walter, R. D.; Betzel, C.; Liebau, E., Native and Inhibited Structure of a Mu class-related Glutathione S-transferase from Plasmodium falciparum. *Journal of Biological Chemistry* **2004,** 279, (2), 1336-1342.

[103] Berry, I. M.; Dym, O.; Esnouf, R. M.; Harlos, K.; Meged, R.; Perrakis, A.; Sussman, J. L.; Walter, T. S.; Wilson, J.; Messerschmidt, A., SPINE high-throughput crystallization, crystal imaging and recognition techniques: current state, performance analysis, new technologies and future aspects. *Acta Crystallographica Section D* **2006,** 62, (10), 1137-1149.
[104] Luft, J. R.; Wolfley, J.; Jurisica, I.; Glasgow, J.; Fortier, S.; DeTitta, G. T., Macromolecular crystallization in a high throughput laboratory—the search phase. *Journal of Crystal Growth* **2001,** 232, (1-4), 591-595.
[105] Raymond C, S., High-throughput protein crystallization. *Current Opinion in Structural Biology* **2000,** 10, (5), 558-563.
[106] Stewart, L.; Clark, R.; Behnke, C., High-throughput crystallization and structure determination in drug discovery. *Drug Discovery Today* **2002,** 7, (3), 187-196.
[107] Tonoli, H.; Barrett, J. C., CD82 metastasis suppressor gene: a potential target for new therapeutics? *Trends in Molecular Medicine* **2005,** 11, (12), 563-570.
[108] Annunziata, O.; Paduano, L.; Pearlstein, A. J.; Miller, D. G.; Albright, J. G., The Effect of Salt on Protein Chemical Potential Determined by Ternary Diffusion in Aqueous Solutions. *The Journal of Physical Chemistry B* **2005,** 110, (3), 1405-1415.
[109] Annunziata, O.; Payne, A.; Wang, Y., Solubility of Lysozyme in the Presence of Aqueous Chloride Salts: Common-Ion Effect and Its Role on Solubility and Crystal Thermodynamics. *Journal of the American Chemical Society* **2008,** 130, (40), 13347-13352.
[110] McPherson, A., The Growth and Preliminary Investigation of Protein and Nucleic Acid Crystals for X-ray Diffraction Analysis. In *Methods of Biochemical Analysis*, John Wiley & Sons, Inc.: 1976; pp 249-345.
[111] Garcia-Ruiz, J. M.; Carter, C. W. J.; Sweet, R. M., Counterdiffusion Methods for Macromolecular Crystallization. In *Methods in Enzymology*, Academic Press: 2003; Vol. Volume 368, pp 130-154.
[112] D'Arcy, A.; Elmore, C.; Stihle, M.; Johnston, J. E., A novel approach to crystallising proteins under oil. *Journal of Crystal Growth* **1996,** 168, (1-4), 175-180.
[113] Chayen, N. E.; Shaw Stewart, P. D.; Blow, D. M., Microbatch crystallization under oil â€" a new technique allowing many small-volume crystallization trials. *Journal of Crystal Growth* **1992,** 122, (1-4), 176-180.
[114] Chayen, N. E.; Shaw Stewart, P. D.; Baldock, P., New developments of the IMPAX small-volume automated crystallization system. *Acta Crystallographica Section D* **1994,** 50, (4), 456-458.
[115] Shah, A. K.; Liu, Z.-J.; Stewart, P. D.; Schubot, F. D.; Rose, J. P.; Newton, M. G.; Wang, B.-C., On increasing protein-crystallization throughput for X-ray diffraction studies. *Acta Crystallographica Section D* **2005,** 61, (2), 123-129.
[116] Poulter, T. C.; Ritchey, C.; Benz, C. A., The Effect of Pressure on the Index of Refraction of Paraffin Oil and Glycerine. *Physical Review* **1932,** 41, (3), 366-367.
[117] Luten, D. B., Jr., The Refractive Index of H^{2}H^{2}O; The Refractive Index and Density of Solutions of H^{2}H^{2}O in H^{1}H^{1}O. *Physical Review* **1934,** 45, (3), 161-165.
[118] Lu, H., A containerless levitation setup for liquid processing in a superconducting magnet. *Rev. Sci. Instrum.* **2008,** 79, (9), 093903.
[119] Dierks, K.; Meyer, A.; Oberthür, D.; Rapp, G.; Einspahr, H.; Betzel, C., Efficient UV detection of protein crystals enabled by fluorescence excitation at

wavelengths longer than 300 nm. *Acta Crystallographica Section F* **2010,** 66, (4), 478-484.

[120] Jamshad, M.; Rajesh, S.; Stamataki, Z.; McKeating, J. A.; Dafforn, T.; Overduin, M.; Bill, R. M., Structural characterization of recombinant human CD81 produced in *Pichia pastoris*. *Protein Expression and Purification* **2008,** 57, (2), 206-16.

[121] He, B.; Liu, L.; Cook, G. A.; Grgurevich, S.; Jennings, L. K.; Zhang, X. A., Tetraspanin CD82 Attenuates Cellular Morphogenesis through Down-regulating Integrin Î±6-Mediated Cell Adhesion. *Journal of Biological Chemistry* **2005,** 280, (5), 3346-3354.

[122] Reckel, S.; Gottstein, D.; Stehle, J.; Lohr, F.; Verhoefen, M. K.; Takeda, M.; Silvers, R.; Kainosho, M.; Glaubitz, C.; Wachtveitl, J.; Bernhard, F.; Schwalbe, H.; Guntert, P.; Dotsch, V., Solution NMR structure of proteorhodopsin. *Angew Chem Int Ed Engl* **2011,** 50, (50), 11942-6.

[123] Balasubramanian, A.; Ponnuraj, K., Crystal Structure of the First Plant Urease from Jack Bean: 83 Years of Journey from Its First Crystal to Molecular Structure. *Journal of Molecular Biology* **2010,** 400, (3), 274-283.

[124] Veerapathran, A.; Dakshinamoorthy, G.; Gnanasekar, M.; Reddy, M. V. R.; Kalyanasundaram, R., Evaluation of *Wuchereria bancrofti* GST as a Vaccine Candidate for Lymphatic Filariasis. *PLoS Neglected Tropical Diseases* **2009,** 3, (6), e457.

[125] Vitu, E.; Bentzur, M.; Lisowsky, T.; Kaiser, C. A.; Fass, D., Gain of Function in an ERV/ALR Sulfhydryl Oxidase by Molecular Engineering of the Shuttle Disulfide. *Journal of Molecular Biology* **2006,** 362, (1), 89-101.

[126] Lubkowski, J.; Bujacz, G.; Boque, L.; Peter J, D.; Tracy M, H.; Alexander, W., The structure of MCP-1 in two crystal forms provides a rare example of variable quaternary interactions. *Nature Structural and Molecular Biology* **1997,** 4, (1), 64-69.

[127] Charrin, S.; le Naour, F.; Silvie, O.; Milhiet, P. E.; Boucheix, C.; Rubinstein, E., Lateral organization of membrane proteins: tetraspanins spin their web. *Biochemical Journal* **2009,** 420, (2), 133-154.

[128] Harris, H. J.; Davis, C.; Mullins, J. G. L.; Hu, K.; Goodall, M.; Farquhar, M. J.; Mee, C. J.; McCaffrey, K.; Young, S.; Drummer, H.; Balfe, P.; McKeating, J. A., Claudin Association with CD81 Defines Hepatitis C Virus Entry. *Journal of Biological Chemistry* **2010,** 285, (27), 21092-21102.

[129] Pollmann, K.; Raff, J.; Schnorpfeil, M.; Radeva, G.; Selenska-Pobell, S., Novel surface layer protein genes in Bacillus sphaericus associated with unusual insertion elements. *Microbiology* **2005,** 151, (9), 2961-2973.

[130] Landau, E. M.; Rosenbusch, J. P., Lipidic cubic phases: A novel concept for the crystallization of membrane proteins. *Proceedings of the National Academy of Sciences* **1996,** 93, (25), 14532-14535.

[131] Drebes, J.; Perbandt, M.; Wrenger, C.; Betzel, C., Purification, crystallization and preliminary X-ray diffraction analysis of ThiM from Staphylococcus aureus. *Acta Crystallographica Section F* **2011,** 67, (4), 479-481.

[132] Shah, J. C.; Sadhale, Y.; Chilukuri, D. M., Cubic phase gels as drug delivery systems. *Advanced Drug Delivery Reviews* **2001,** 47, (2–3), 229-250.

[133] Bender, J.; Simonsson, C.; Smedh, M.; Engström, S.; Ericson, M. B., Lipid cubic phases in topical drug delivery: Visualization of skin distribution using two-photon microscopy. *Journal of Controlled Release* **2008,** 129, (3), 163-169.

[134] Li, D.; Caffrey, M., Lipid cubic phase as a membrane mimetic for integral membrane protein enzymes. *Proceedings of the National Academy of Sciences* **2011,** 108, (21), 8639-8644.
[135] Caffrey, M., Membrane protein crystallization. *Journal of Structural Biology* **2003,** 142, (1), 108-132.
[136] Höfer, N.; Aragão, D.; Lyons, J. A.; Caffrey, M., Membrane Protein Crystallization in Lipidic Mesophases. Hosting Lipid Effects on the Crystallization and Structure of a Transmembrane Peptide. *Crystal Growth & Design* **2011,** 11, (4), 1182-1192.
[137] Caffrey, M., A lipid's eye view of membrane protein crystallization in mesophases. *Current Opinion in Structural Biology* **2000,** 10, (4), 486-497.
[138] Engelhardt, H., Are S-layers exoskeletons? The basic function of protein surface layers revisited. *Journal of Structural Biology* **2007,** 160, (2), 115-124.
[139] Engelhardt, H.; Peters, J., Structural Research on Surface Layers: A Focus on Stability, Surface Layer Homology Domains, and Surface Layer-Cell Wall Interactions. *Journal of Structural Biology* **1998,** 124, (2-3), 276-302.
[140] Sara, M.; Sleytr, U. B., S-Layer Proteins. *Journal of Bacteriology* **2000,** 182, (4), 859-868.
[141] Sleytr, U. B.; Beveridge, T. J., Bacterial S-layers. *Trends in Microbiology* **1999,** 7, (6), 253-260.
[142] Hovmöller, S.; Sjögren, A.; Wang, D. N., The structure of crystalline bacterial surface layers. *Progress in Biophysics and Molecular Biology* **1988,** 51, (2), 131-163.
[143] Altschul, S. F.; Gish, W.; Miller, W.; Myers, E. W.; Lipman, D. J., Basic local alignment search tool. *Journal of Molecular Biology* **1990,** 215, (3), 403-410.
[144] Pollmann, K.; Raff, J.; Merroun, M.; Fahmy, K.; Selenska-Pobell, S., Metal binding by bacteria from uranium mining waste piles and its technological applications. *Biotechnology Advances* **2006,** 24, (1), 58-68.
[145] Sleytr, U. B.; Huber, C.; Ilk, N.; Pum, D.; Schuster, B.; Egelseer, E. M., S-layers as a tool kit for nanobiotechnological applications. *FEMS Microbiology Letters* **2007,** 267, (2), 131-144.
[146] Fahmy, K.; Merroun, M.; Pollmann, K.; Raff, J.; Savchuk, O.; Hennig, C.; Selenska-Pobell, S., Secondary Structure and Pd(II) Coordination in S-Layer Proteins from Bacillus sphaericus Studied by Infrared and X-Ray Absorption Spectroscopy. *Biophysical Journal* **2006,** 91, (3), 996-1007.
[147] Merroun, M. L.; Raff, J.; Rossberg, A.; Hennig, C.; Reich, T.; Selenska-Pobell, S., Complexation of Uranium by Cells and S-Layer Sheets of Bacillus sphaericus JG-A12. *Applied and Environmental Microbiology* **2005,** 71, (9), 5532-5543.
[148] Jing, H.; Takagi, J.; Liu, J.-h.; Lindgren, S.; Zhang, R.-g.; Joachimiak, A.; Wang, J.-h.; Springer, T. A., Archaeal Surface Layer Proteins Contain [beta] Propeller, PKD, and [beta] Helix Domains and Are Related to Metazoan Cell Surface Proteins. *Structure* **2002,** 10, (10), 1453-1464.
[149] Kern, J.; Wilton, R.; Zhang, R.; Binkowski, T. A.; Joachimiak, A.; Schneewind, O., Structure of Surface Layer Homology (SLH) Domains from Bacillus anthracis Surface Array Protein. *Journal of Biological Chemistry* **2011,** 286, (29), 26042-26049.
[150] Raff, J., Personal Communication. In E-Mail ed.; 2010.
[151] Precrystallization Test. http://hamptonresearch.com/product_detail.aspx?cid=1&sid=29&pid=10 (09.09.2011),

[152] Svergun, D., Determination of the regularization parameter in indirect-transform methods using perceptual criteria. *Journal of Applied Crystallography* **1992,** 25, (4), 495-503.
[153] ATSAS. http://www.embl-hamburg.de/biosaxs/software.html (06.10.2011),
[154] Svergun, D. I., Restoring Low Resolution Structure of Biological Macromolecules from Solution Scattering Using Simulated Annealing. *Biophysical Journal* **1999,** 76, (6), 2879-2886.
[155] Franke, D.; Svergun, D. I., DAMMIF, a program for rapid ab-initio shape determination in small-angle scattering. *Journal of Applied Crystallography* **2009,** 42, (2), 342-346.
[156] Petoukhov, M. V.; Svergun, D. I., Global Rigid Body Modeling of Macromolecular Complexes against Small-Angle Scattering Data. *Biophysical Journal* **2005,** 89, (2), 1237-1250.
[157] Laemmli, U. K., Cleavage of Structural Proteins during the Assembly of the Head of Bacteriophage T4. *Nature* **1970,** 227, (5259), 680-685.
[158] DNA http://www.dna.ac.uk/
[159] http://www.douglas.co.uk/top14.htm (11.10.2011),
[160] Uthayakumar, M.; Sowmiya, G.; Sabarinathan, R.; Udayaprakash, N.; Kirti Vaishnavi, M.; Sekar, K., BSSB: BLAST Server for Structural Biologists. *Journal of Applied Crystallography* **2011,** 44, (3), 651-654.
[161] Schrodinger, LLC, The PyMOL Molecular Graphics System, Version 1.3r1. In ed.; 2010.
[162] Arnold, K.; Bordoli, L.; Kopp, J.; Schwede, T., The SWISS-MODEL workspace: a web-based environment for protein structure homology modelling. *Bioinformatics* **2006,** 22, (2), 195-201.
[163] Dong, A.; Xu, X.; Edwards, A. M., In situ proteolysis for protein crystallization and structure determination. *Nature Methods* **2007,** 4, (12), 1019-1021.
[164] Wernimont, A.; Edwards, A., *In Situ* Proteolysis to Generate Crystals for Structure Determination: An Update. *PLoS ONE* **2009,** 4, (4), e5094.
[165] Gorrec, F., The MORPHEUS protein crystallization screen. *Journal of Applied Crystallography* **2009,** 42, (6), 1035-1042.
[166] Kapadia, S. B.; Barth, H.; Baumert, T.; McKeating, J. A.; Chisari, F. V., Initiation of Hepatitis C Virus Infection Is Dependent on Cholesterol and Cooperativity between CD81 and Scavenger Receptor B Type I. *Journal of Virology* **2007,** 81, (1), 374-383.
[167] Zhang, J.; Randall, G.; Higginbottom, A.; Monk, P.; Rice, C. M.; McKeating, J. A., CD81 Is Required for Hepatitis C Virus Glycoprotein-Mediated Viral Infection. *Journal of Virology* **2004,** 78, (3), 1448-1455.
[168] Furuse, M.; Fujita, K.; Hiiragi, T.; Fujimoto, K.; Tsukita, S., Claudin-1 and -2: Novel Integral Membrane Proteins Localizing at Tight Junctions with No Sequence Similarity to Occludin. *The Journal of Cell Biology* **1998,** 141, (7), 1539-1550.
[169] Furuse, M.; Sasaki, H.; Fujimoto, K.; Tsukita, S., A single gene product, claudin-1 or -2, reconstitutes tight junction strands and recruits occludin in fibroblasts. *The Journal of Cell Biology* **1998,** 143, (2), 391-401.
[170] Krause, G.; Winkler, L.; Mueller, S. L.; Haseloff, R. F.; Piontek, J.; Blasig, I. E., Structure and function of claudins. *Biochimica et Biophysica Acta (BBA)* **2008,** 1778, (3), 631-45.
[171] Steed, E.; Balda, M. S.; Matter, K., Dynamics and functions of tight junctions. *Trends in Cell Biology* **2010,** 20, (3), 142-149.

[172] Liu, S.; Yang, W.; Shen, L.; Turner, J. R.; Coyne, C. B.; Wang, T., Tight Junction Proteins Claudin-1 and Occludin Control Hepatitis C Virus Entry and Are Downregulated during Infection To Prevent Superinfection. *Journal of Virology* **2009,** 83, (4), 2011-2014.

[173] Meertens, L.; Bertaux, C.; Cukierman, L.; Cormier, E.; Lavillette, D.; Cosset, F.-L.; Dragic, T., The Tight Junction Proteins Claudin-1, -6, and -9 Are Entry Cofactors for Hepatitis C Virus. *Journal of Virology* **2008,** 82, (7), 3555-3560.

[174] Ploss, A.; Evans, M. J.; Gaysinskaya, V. A.; Panis, M.; You, H.; de Jong, Y. P.; Rice, C. M., Human occludin is a hepatitis C virus entry factor required for infection of mouse cells. *Nature* **2009,** 457, (7231), 882-886.

[175] Verma, S.; Lo, Y.; Chapagain, M.; Lum, S.; Kumar, M.; Gurjav, U.; Luo, H.; Nakatsuka, A.; Nerurkar, V. R., West Nile virus infection modulates human brain microvascular endothelial cells tight junction proteins and cell adhesion molecules: Transmigration across the in vitro blood-brain barrier. *Virology* **2009,** 385, (2), 425-433.

[176] Davis, C.; Harris, H. J.; McKeating, J. A.; Alan, S. L. Y., Chapter 12 - The Involvement of Tight Junction Protein Claudin-1 in Hepatitis C Virus Entry. In *Current Topics in Membranes*, Academic Press: 2010; Vol. Volume 65, pp 273-292.

[177] Krieger, S. E.; Zeisel, M. B.; Davis, C.; Thumann, C.; Harris, H. J.; Schnober, E. K.; Mee, C.; Soulier, E.; Royer, C.; Lambotin, M.; Grunert, F.; Dao Thi, V. L.; Dreux, M.; Cosset, F.-L.; McKeating, J. A.; Schuster, C.; Baumert, T. F., Inhibition of hepatitis C virus infection by anti-claudin-1 antibodies is mediated by neutralization of E2–CD81–Claudin-1 associations. *Hepatology* **2010,** 51, (4), 1144-1157.

[178] Hemler, M. E., Targeting of tetraspanin proteins - potential benefits and strategies. *Nature Reviews Drug Discovery* **2008,** 7, (9), 747-58.

[179] Tsai, Y. C.; Weissman, A. M., Dissecting the diverse functions of the metastasis suppressor CD82/KAI1. *FEBS Letters* **2011,** 585, (0), 3166-73.

[180] Liu, W. M.; Zhang, X. A., KAI1/CD82, a tumor metastasis suppressor. *Cancer Letters* **2006,** 240, (2), 183-194.

[181] Mazurov, D.; Heidecker, G.; Derse, D., The Inner Loop of Tetraspanins CD82 and CD81 Mediates Interactions with Human T Cell Lymphotrophic Virus Type 1 Gag Protein. *Journal of Biological Chemistry* **2007,** 282, (6), 3896-3903.

[182] Abe, M.; Sugiura, T.; Takahashi, M.; Ishii, K.; Shimoda, M.; Shirasuna, K., A novel function of CD82/KAI-1 on E-cadherin-mediated homophilic cellular adhesion of cancer cells. *Cancer Letters* **2008,** 266, (2), 163-170.

[183] Bass, R.; Werner, F.; Odintsova, E.; Sugiura, T.; Berditchevski, F.; Ellis, V., Regulation of Urokinase Receptor Proteolytic Function by the Tetraspanin CD82. *Journal of Biological Chemistry* **2005,** 280, (15), 14811-14818.

[184] Sridhar, S. C.; Miranti, C. K., Tetraspanin KAI1//CD82 suppresses invasion by inhibiting integrin-dependent crosstalk with c-Met receptor and Src kinases. *Oncogene* **2005,** 25, (16), 2367-2378.

[185] Rubinstein, E.; Le Naour, F.; Lagaudrière-Gesbert, C.; Billard, M.; Conjeaud, H.; Boucheix, C., CD9, CD63, CD81, and CD82 are components of a surface tetraspan network connected to HLA-DR and VLA integrins. *European Journal of Immunology* **1996,** 26, (11), 2657-2665.

[186] Hemler, M. E., Tetraspanin functions and associated microdomains. *Nature Reviews Molecular Cell Biology* **2005,** 6, (10), 801-811.

[187] Levy, S.; Shoham, T., The tetraspanin web modulates immune-signalling complexes. *Nature Reviews Immunology* **2005,** 5, (2), 136-148.

[188] Kitadokoro, K.; Bordo, D.; Galli, G.; Petracca, R.; Falugi, F.; Abrignani, S.; Grandi, G.; Bolognesi, M., CD81 extracellular domain 3D structure: insight into the tetraspanin superfamily structural motifs. *The EMBO Journal* **2001,** 20, (1/2), 12-18.

[189] Kitadokoro, K.; Ponassi, M.; Galli, G.; Petracca, R.; Falugi, F.; Grandi, G.; Bolognesi, M., Subunit Association and Conformational Flexibility in the Head Subdomain of Human CD81 Large Extracellular Loop. *Biological Chemistry* **2002,** 383, (9), 1447-1452.

[190] Min, G.; Wang, H.; Sun, T.-T.; Kong, X.-P., Structural basis for tetraspanin functions as revealed by the cryo-EM structure of uroplakin complexes at 6 Å resolution. *The Journal of Cell Biology* **2006,** 173, (6), 975-983.

[191] Bill, R. M.; Henderson, P. J. F.; Iwata, S.; Kunji, E. R. S.; Michel, H.; Neutze, R.; Newstead, S.; Poolman, B.; Tate, C. G.; Vogel, H., Overcoming barriers to membrane protein structure determination. *Nature Biotechnology* **2011,** 29, (4), 335-340.

[192] Martin, C., Membrane protein crystallization. *Journal of Structural Biology* **2003,** 142, (1), 108-132.

[193] Evans, G.; Axford, D.; Waterman, D.; Owen, R. L., Macromolecular microcrystallography. *Crystallography Reviews* **2011,** 17, (2), 105-142.

[194] Bowler, M. W.; Guijarro, M.; Petitdemange, S.; Baker, I.; Svensson, O.; Burghammer, M.; Mueller-Dieckmann, C.; Gordon, E. J.; Flot, D.; McSweeney, S. M.; Leonard, G. A., Diffraction cartography: applying microbeams to macromolecular crystallography sample evaluation and data collection. *Acta Crystallographica Section D* **2010,** 66, (8), 855-864.

[195] Moukhametzianov, R.; Burghammer, M.; Edwards, P. C.; Petitdemange, S.; Popov, D.; Fransen, M.; McMullan, G.; Schertler, G. F. X.; Riekel, C., Protein crystallography with a micrometre-sized synchrotron-radiation beam. *Acta Crystallographica Section D* **2008,** 64, (2), 158-166.

[196] Lieberman, R. L.; Culver, J. A.; Entzminger, K. C.; Pai, J. C.; Maynard, J. A., Crystallization chaperone strategies for membrane proteins. *Methods* **2011,** 55, (0), 293-302.

[197] Deniaud, A.; Moiseeva, E.; Gordeliy, V.; Pebay-Peyroula, E., Crystallography of Membrane Proteins: From Crystallization to Structure Membrane Protein Structure Determination. In *Membrane Protein Structure Determination: Methods and Protocols.*, Walker, J. M., Ed. Humana Press: 2010; Vol. 654, pp 79-103.

[198] Lorber, B.; Bishop, J. B.; DeLucas, L. J., Purification of octyl [beta]-d-glucopyranoside and re-estimation of its micellar size. *Biochimica et Biophysica Acta (BBA) - Biomembranes* **1990,** 1023, (2), 254-265.

[199] Ma, J.; Xia, D., The use of blue native PAGE in the evaluation of membrane protein aggregation states for crystallization. *Journal of Applied Crystallography* **2008,** 41, (6), 1150-1160.

[200] Laue, T. M.; Shah, B. D.; Ridgeway, T. M.; Pelletier, S. L., *Analytical ultracentrifugation in biochemistry and polymer science*. ed.; Royal Society of Chemistry: London, 1992; p 90-125.

[201] Blasig, I. E.; Winkler, L.; Lassowski, B.; Mueller, S. L.; Zuleger, N.; Krause, E.; Krause, G.; Gast, K.; Kolbe, M.; Piontek, J., On the self-association potential of transmembrane tight junction proteins. *Cellular and Molecular Life Sciences* **2006,** 63, (4), 505-514.

[202] Kovalenko, O. V.; Yang, X.; Kolesnikova, T. V.; Hemler, M. E., Evidence for specific tetraspanin homodimers: inhibition of palmitoylation makes cysteine

residues available for cross-linking. *Biochemical Journal* **2004,** 377, (2), 407-417.

[203] Kovalenko, O. V.; Yang, X. H.; Hemler, M. E., A novel cysteine cross-linking method reveals a direct association between claudin-1 and tetraspanin CD9. *Molecular and Cellular Proteomics* **2007,** 6, (11), 1855-67.

[204] Berditchevski, F., Complexes of tetraspanins with integrins: more than meets the eye. *Journal of Cell Science* **2001,** 114, (23), 4143-4151.

[205] Seigneuret, M., Complete Predicted Three-Dimensional Structure of the Facilitator Transmembrane Protein and Hepatitis C Virus Receptor CD81: Conserved and Variable Structural Domains in the Tetraspanin Superfamily. *Biophysical Journal* **2006,** 90, (1), 212-227.

9. Appendix

9.1. Python Script for Automated *in situ* DLS

```
# -*- coding: utf-8 -*-
plate = "nextal"
file = "DO_2011_030"
list = ["a1-1", "a2-1", "a3-1", "a4-1", "a5-1", "a6-1", "a7-1", "a8-1", "a9-1", "a10-1", "a11-1", "a12-1",
        "b1-1", "b2-1", "b3-1", "b4-1", "b5-1", "b6-1", "b7-1", "b8-1", "b9-1", "b10-1", "b11-1", "b12-1",
        "c1-1", "c2-1", "c3-1", "c4-1", "c5-1", "c6-1", "c7-1", "c8-1", "c9-1", "c10-1", "c11-1", "c12-1",
        "d1-1", "d2-1", "d3-1", "d4-1", "d5-1", "d6-1", "d7-1", "d8-1", "d9-1", "d10-1", "d11-1", "d12-1",
        "e1-1", "e2-1", "e3-1", "e4-1", "e5-1", "e6-1", "e7-1", "e8-1", "e9-1", "e10-1", "e11-1", "e12-1",
        "f1-1", "f2-1", "f3-1", "f4-1", "f5-1", "f6-1", "f7-1", "f8-1", "f9-1", "f10-1", "f11-1", "f12-1",
        "g1-1", "g2-1", "g3-1", "g4-1", "g5-1", "g6-1", "g7-1", "g8-1", "g9-1", "g10-1", "g11-1", "g12-1",
        "h1-1", "h2-1", "h3-1", "h4-1", "h5-1", "h6-1", "h7-1", "h8-1", "h9-1", "h10-1", "h11-1", "h12-1"]
for n in range(300):
 for drop in list:
  setpos(drop)
  wait(5)
  dls()
```

Appendix 1 Python script used for automated *in situ* DLS in HTS plates.

```
# -*- coding: utf-8 -*-
plate = "Granada"
file = "thim_cnb1_row2"
list = ["a1", "a2", "a3", "a4", "a5"]
for n in range(120):
  for drop in list:
    setpos(drop)
    for n in range(10):
      dls()
    wait(1)
    white(100)
    wait(10)
    image()
    white(0)
  wait(1360
```

Appendix 2 Python script used for automated *in situ* DLS and imaging of a crystallization experiment of ThiM within a crystallization box for space experiments.

```
plate = "MRC1"
file = "DO_2010_015"
list = ["a1-2", "a2-2", "a3-2", "a4-2", "a5-2", "a6-2", "a7-2", "a8-2", "a9-2", "a10-2", "a11-2", "a12-2",
        "b1-2", "b2-2", "b3-2", "b4-2", "b5-2", "b6-2", "b7-2", "b8-2", "b9-2", "b10-2", "b11-2", "b12-2",
        "c1-2", "c2-2", "c3-2", "c4-2", "c5-2", "c6-2", "c7-2", "c8-2", "c9-2", "c10-2", "c11-2", "c12-2",
        "d1-2", "d2-2", "d3-2", "d4-2", "d5-2", "d6-2", "d7-2", "d8-2", "d9-2", "d10-2", "d11-2", "d12-2",
        "e1-2", "e2-2", "e3-2", "e4-2", "e5-2", "e6-2", "e7-2", "e8-2", "e9-2", "e10-2", "e11-2", "e12-2",
        "f1-2", "f2-2", "f3-2", "f4-2", "f5-2", "f6-2", "f7-2", "f8-2", "f9-2", "f10-2", "f11-2", "f12-2",
        "g1-2", "g2-2", "g3-2", "g4-2", "g5-2", "g6-2", "g7-2", "g8-2", "g9-2", "g10-2", "g11-2", "g12-2",
        "h1-2", "h2-2", "h3-2", "h4-2", "h5-2", "h6-2", "h7-2", "h8-2", "h9-2", "h10-2", "h11-2", "h12-2"]
for n in range(65):
  for drop in list:
    setpos(drop)
    wait(5)
    dls()
    #image()
  wait(5)
```

Appendix 3 Python script used for automated *in situ* DLS monitoring of a detergent screen.

9.2. Self-Designed Screens

	Screen	Protein
8.2.A	PPEG	SlfB – JGA12
8.2.B	PPEG2	SlfB – JGA12
8.2.C	PPEG3	SlfB – JGA12
8.2.D	PPEG7	SlfB – JGA12
8.2.E	PPEG8	SlfB – JGA12
8.2.F	PPEG9	SlfB – JGA12
8.2.G	DO_2010_006	CD81, CD82

Additive mixture	Contents
AA-Mix	0.04 M histidine, 0.03 M arginine, 0.03 M proline
Alk-Mix	0.28 M tert-butanol, 0.28 M isopropanol, 0.28 M n-propanol, 0.28 M 1,3-propanediol
Anion-Mix	0.08 M NaCl, 0.04 M NaF, 0.04 M NaBr, 0.04 M NaI, 0.04 M Na_2SO_4
Anion-Mix2	0.07 M NaBr, 0.08 M NaI
Anion-Mix3	0.05 M NaBr, 0.05 M NaI, 0.05 M $NaNO_3$, 0.05 M sodium tartrate, 0.05 M sodium malonate
Anion-Mix5	0.05 M NH_4Cl, 0.05 M NH_4Br, 0.05 M NH_4I, 0.05 ammonium formate, 0.05 M ammonium tartrate, 0.05 M ammonium acetate, 0.05 M ammonium citrate
Anion-Mix6	0.07 M NH_4Br, 0.08 M NH_4I
Cation-Mix	0.04 M KCl, 0.02 M LiCl, 0.02 M NaCl, 0.02 M $MgCl_2$, 0.02 M $CaCl_2$

Custom PEG Screen: PPEG																				
Source	1	2	3	4		5	6	7,00		8, 17	9	10		11	12	13		14,0	15,0	16
Stock **8.2.A**	PEG2000MME	PEG4000	PEG1500	PEG3350		PEG8000	PEG10000	AS		NaOAc pH4.75	NaCitrat pH4	Isopropanol		Alk-Mix	Kation-Mix	Anion-Mix		AA-Mix	Wasser	Wasser2
Cstock	50	50	50	50		50	50	3,00		0,25	1	100		100	100	100		100,0		

Number (Destiny)	Well	Prec	Cprec	Vprec	Source	Salt	Csalt	Vsalt	Source	Buffer	Cbuffer	Vbuffer	Source	Additive	Cadditive	Vadditive		Vsum	Vwater	Source
1	A1	PEG2000MME	22	440	1	AS	0,2	66,67	7	NaOAc pH4.75	0,1	400	8	Anion Mix	5	50	13	956,7	43,3	15
2	A2	PEG2000MME	22	440	1	AS	0,2	66,67	7	NaCitrat pH4	0,1	100	9	Anion Mix	5	50	13	656,7	343,3	15
3	A3	PEG1500	22	440	3	AS	0,2	66,67	7	NaOAc pH4.75	0,1	400	8	Anion Mix	5	50	13	956,7	43,3	15
4	A4	PEG1500	22	440	3	AS	0,2	66,67	7	NaCitrat pH4	0,1	100	9	Anion Mix	5	50	13	656,7	343,3	15
5	A5	PEG3350	22	440	4	AS	0,2	66,67	7	NaOAc pH4.75	0,1	400	8	Anion Mix	5	50	13	956,7	43,3	15
6	A6	PEG3350	22	440	4	AS	0,2	66,67	7	NaCitrat pH4	0,1	100	9	Anion Mix	5	50	13	656,7	343,3	15
7	A7	PEG4000	22	440	2	AS	0,2	66,67	7	NaOAc pH4.75	0,1	400	8	Anion Mix	5	50	13	956,7	43,3	15
8	A8	PEG4000	22	440	2	AS	0,2	66,67	7	NaCitrat pH4	0,1	100	9	Anion Mix	5	50	13	656,7	343,3	15
9	A9	PEG8000	22	440	5	AS	0,2	66,67	7	NaOAc pH4.75	0,1	400	8	Anion Mix	5	50	13	956,7	43,3	15
10	A10	PEG8000	22	440	5	AS	0,2	66,67	7	NaCitrat pH4	0,1	100	9	Anion Mix	5	50	13	656,7	343,3	15
11	A11	PEG10000	22	440	6	AS	0,2	66,67	7	NaOAc pH4.75	0,1	400	8	Anion Mix	5	50	13	956,7	43,3	15
12	A12	PEG10000	22	440	6	AS	0,2	66,67	7	NaCitrat pH4	0,1	100	9	Anion Mix	5	50	13	656,7	343,3	15
13	B1	PEG2000MME	22	440	1	AS	0,22	73,33	7	NaOAc pH4.75	0,1	400	8	AA-Mix	5	50	14	963,3	36,7	15
14	B2	PEG2000MME	22	440	1	AS	0,22	73,33	7	NaCitrat pH4	0,1	100	9	AA-Mix	5	50	14	663,3	336,7	15
15	B3	PEG1500	22	440	3	AS	0,22	73,33	7	NaOAc pH4.75	0,1	400	8	AA-Mix	5	50	14	963,3	36,7	15
16	B4	PEG1500	22	440	3	AS	0,22	73,33	7	NaCitrat pH4	0,1	100	9	AA-Mix	5	50	14	663,3	336,7	15
17	B5	PEG3350	22	440	4	AS	0,22	73,33	7	NaOAc pH4.75	0,1	400	8	AA-Mix	5	50	14	963,3	36,7	15
18	B6	PEG3350	22	440	4	AS	0,22	73,33	7	NaCitrat pH4	0,1	100	9	AA-Mix	5	50	14	663,3	336,7	15
19	B7	PEG4000	22	440	2	AS	0,22	73,33	7	NaOAc pH4.75	0,1	400	8	AA-Mix	5	50	14	963,3	36,7	15
20	B8	PEG4000	22	440	2	AS	0,22	73,33	7	NaCitrat pH4	0,1	100	9	AA-Mix	5	50	14	663,3	336,7	15
21	B9	PEG8000	22	440	5	AS	0,22	73,33	7	NaOAc pH4.75	0,1	400	8	AA-Mix	5	50	14	963,3	36,7	15
22	B10	PEG8000	22	440	5	AS	0,22	73,33	7	NaCitrat pH4	0,1	100	9	AA-Mix	5	50	14	663,3	336,7	15
23	B11	PEG10000	22	440	6	AS	0,22	73,33	7	NaOAc pH4.75	0,1	400	8	AA-Mix	5	50	14	963,3	36,7	15
24	B12	PEG10000	22	440	6	AS	0,22	73,33	7	NaCitrat pH4	0,1	100	9	AA-Mix	5	50	14	663,3	336,7	15
25	C1	PEG2000MME	20	400	1	AS	0,2	66,67	7	NaOAc pH4.75	0,1	400	8			0		866,7	133,3	15
26	C2	PEG2000MME	20	400	1	AS	0,2	66,67	7	NaCitrat pH4	0,1	100	9			0		566,7	433,3	15
27	C3	PEG1500	20	400	3	AS	0,2	66,67	7	NaOAc pH4.75	0,1	400	8			0		866,7	133,3	15
28	C4	PEG1500	20	400	3	AS	0,2	66,67	7	NaCitrat pH4	0,1	100	9			0		566,7	433,3	15
29	C5	PEG3350	20	400	4	AS	0,2	66,67	7	NaOAc pH4.75	0,1	400	8			0		866,7	133,3	15
30	C6	PEG3350	20	400	4	AS	0,2	66,67	7	NaCitrat pH4	0,1	100	9			0		566,7	433,3	15
31	C7	PEG4000	20	400	2	AS	0,2	66,67	7	NaOAc pH4.75	0,1	400	8			0		866,7	133,3	15
32	C8	PEG4000	20	400	2	AS	0,2	66,67	7	NaCitrat pH4	0,1	100	9			0		566,7	433,3	15
33	C9	PEG8000	20	400	5	AS	0,2	66,67	7	NaOAc pH4.75	0,1	400	8			0		866,7	133,3	15
34	C10	PEG8000	20	400	5	AS	0,2	66,67	7	NaCitrat pH4	0,1	100	9			0		566,7	433,3	15
35	C11	PEG10000	20	400	6	AS	0,2	66,67	7	NaOAc pH4.75	0,1	400	8			0		866,7	133,3	15
36	C12	PEG10000	20	400	6	AS	0,2	66,67	7	NaCitrat pH4	0,1	100	9			0		566,7	433,3	15
37	D1	PEG2000MME	20	400	1	AS	0,22	73,33	7	NaOAc pH4.75	0,1	400	8			0		873,3	126,7	15
38	D2	PEG2000MME	20	400	1	AS	0,22	73,33	7	NaCitrat pH4	0,1	100	9			0		573,3	426,7	15
39	D3	PEG1500	20	400	3	AS	0,22	73,33	7	NaOAc pH4.75	0,1	400	8			0		873,3	126,7	15
40	D4	PEG1500	20	400	3	AS	0,22	73,33	7	NaCitrat pH4	0,1	100	9			0		573,3	426,7	15
41	D5	PEG3350	20	400	4	AS	0,22	73,33	7	NaOAc pH4.75	0,1	400	8			0		873,3	126,7	15
42	D6	PEG3350	20	400	4	AS	0,22	73,33	7	NaCitrat pH4	0,1	100	9			0		573,3	426,7	15
43	D7	PEG4000	20	400	2	AS	0,22	73,33	7	NaOAc pH4.75	0,1	400	8			0		873,3	126,7	15
44	D8	PEG4000	20	400	2	AS	0,22	73,33	7	NaCitrat pH4	0,1	100	9			0		573,3	426,7	15
45	D9	PEG8000	20	400	5	AS	0,22	73,33	7	NaOAc pH4.75	0,1	400	8			0		873,3	126,7	15
46	D10	PEG8000	20	400	5	AS	0,22	73,33	7	NaCitrat pH4	0,1	100	9			0		573,3	426,7	15
47	D11	PEG10000	20	400	6	AS	0,22	73,33	7	NaOAc pH4.75	0,1	400	8			0		873,3	126,7	15
48	D12	PEG10000	20	400	6	AS	0,22	73,33	7	NaCitrat pH4	0,1	100	9			0		573,3	426,7	15

49	E1	PEG2000MME	18	360	1	AS	0,2	66,67	7	NaOAc pH4.75	0,1	400	17	Anion Mix	10	100	13	926,7	73,3	16
50	E2	PEG2000MME	18	360	1	AS	0,2	66,67	7	NaCitrat pH4	0,1	100	9	Anion Mix	10	100	13	626,7	373,3	16
51	E3	PEG1500	18	360	3	AS	0,2	66,67	7	NaOAc pH4.75	0,1	400	17	Anion Mix	10	100	13	926,7	73,3	16
52	E4	PEG1500	18	360	3	AS	0,2	66,67	7	NaCitrat pH4	0,1	100	9	Anion Mix	10	100	13	626,7	373,3	16
53	E5	PEG3350	18	360	4	AS	0,2	66,67	7	NaOAc pH4.75	0,1	400	17	Anion Mix	10	100	13	926,7	73,3	16
54	E6	PEG3350	18	360	4	AS	0,2	66,67	7	NaCitrat pH4	0,1	100	9	Anion Mix	10	100	13	626,7	373,3	16
55	E7	PEG4000	18	360	2	AS	0,2	66,67	7	NaOAc pH4.75	0,1	400	17	Anion Mix	10	100	13	926,7	73,3	16
56	E8	PEG4000	18	360	2	AS	0,2	66,67	7	NaCitrat pH4	0,1	100	9	Anion Mix	10	100	13	626,7	373,3	16
57	E9	PEG8000	18	360	5	AS	0,2	66,67	7	NaOAc pH4.75	0,1	400	17	Anion Mix	10	100	13	926,7	73,3	16
58	E10	PEG8000	18	360	5	AS	0,2	66,67	7	NaCitrat pH4	0,1	100	9	Anion Mix	10	100	13	626,7	373,3	16
59	E11	PEG10000	18	360	6	AS	0,2	66,67	7	NaOAc pH4.75	0,1	400	17	Anion Mix	10	100	13	926,7	73,3	16
60	E12	PEG10000	18	360	6	AS	0,2	66,67	7	NaCitrat pH4	0,1	100	9	Anion Mix	10	100	13	626,7	373,3	16
61	F1	PEG2000MME	18	360	1	AS	0,22	73,33	7	NaOAc pH4.75	0,1	400	17	AA-Mix	10	100	14	933,3	66,7	16
62	F2	PEG2000MME	18	360	1	AS	0,22	73,33	7	NaCitrat pH4	0,1	100	9	Kation-Mix	5	50	12	583,3	416,7	16
63	F3	PEG1500	18	360	3	AS	0,22	73,33	7	NaOAc pH4.75	0,1	400	17	AA-Mix	10	100	14	933,3	66,7	16
64	F4	PEG1500	18	360	3	AS	0,22	73,33	7	NaCitrat pH4	0,1	100	9	Kation-Mix	5	50	12	583,3	416,7	16
65	F5	PEG3350	18	360	4	AS	0,22	73,33	7	NaOAc pH4.75	0,1	400	17	AA-Mix	10	100	14	933,3	66,7	16
66	F6	PEG3350	18	360	4	AS	0,22	73,33	7	NaCitrat pH4	0,1	100	9	Kation-Mix	5	50	12	583,3	416,7	16
67	F7	PEG4000	18	360	2	AS	0,22	73,33	7	NaOAc pH4.75	0,1	400	17	AA-Mix	10	100	14	933,3	66,7	16
68	F8	PEG4000	18	360	2	AS	0,22	73,33	7	NaCitrat pH4	0,1	100	9	Kation-Mix	5	50	12	583,3	416,7	16
69	F9	PEG8000	18	360	5	AS	0,22	73,33	7	NaOAc pH4.75	0,1	400	17	AA-Mix	10	100	14	933,3	66,7	16
70	F10	PEG8000	18	360	5	AS	0,22	73,33	7	NaCitrat pH4	0,1	100	9	Kation-Mix	5	50	12	583,3	416,7	16
71	F11	PEG10000	18	360	6	AS	0,22	73,33	7	NaOAc pH4.75	0,1	400	17	AA-Mix	10	100	14	933,3	66,7	16
72	F12	PEG10000	18	360	6	AS	0,22	73,33	7	NaCitrat pH4	0,1	100	9	Kation-Mix	5	50	12	583,3	416,7	16
73	G1	PEG2000MME	12	240	1	AS	0,2	66,67	7	NaOAc pH4.75	0,1	400	17	Isoprop	10	100	10	806,7	193,3	16
74	G2	PEG2000MME	12	240	1	AS	0,2	66,67	7	NaCitrat pH4	0,1	100	9	Isoprop	10	100	10	506,7	493,3	16
75	G3	PEG1500	12	240	3	AS	0,2	66,67	7	NaOAc pH4.75	0,1	400	17	Isoprop	10	100	10	806,7	193,3	16
76	G4	PEG1500	12	240	3	AS	0,2	66,67	7	NaCitrat pH4	0,1	100	9	Isoprop	10	100	10	506,7	493,3	16
77	G5	PEG3350	12	240	4	AS	0,2	66,67	7	NaOAc pH4.75	0,1	400	17	Isoprop	10	100	10	806,7	193,3	16
78	G6	PEG3350	12	240	4	AS	0,2	66,67	7	NaCitrat pH4	0,1	100	9	Isoprop	10	100	10	506,7	493,3	16
79	G7	PEG4000	12	240	2	AS	0,2	66,67	7	NaOAc pH4.75	0,1	400	17	Isoprop	10	100	10	806,7	193,3	16
80	G8	PEG4000	12	240	2	AS	0,2	66,67	7	NaCitrat pH4	0,1	100	9	Isoprop	10	100	10	506,7	493,3	16
81	G9	PEG8000	12	240	5	AS	0,2	66,67	7	NaOAc pH4.75	0,1	400	17	Isoprop	10	100	10	806,7	193,3	16
82	G10	PEG8000	12	240	5	AS	0,2	66,67	7	NaCitrat pH4	0,1	100	9	Isoprop	10	100	10	506,7	493,3	16
83	G11	PEG10000	12	240	6	AS	0,2	66,67	7	NaOAc pH4.75	0,1	400	17	Isoprop	10	100	10	806,7	193,3	16
84	G12	PEG10000	12	240	6	AS	0,2	66,67	7	NaCitrat pH4	0,1	100	9	Isoprop	10	100	10	506,7	493,3	16
85	H1	PEG2000MME	12	240	1	AS	0,2	66,67	7	NaOAc pH4.75	0,1	400	17	Alk-Mix	10	100	11	806,7	193,3	16
86	H2	PEG2000MME	12	240	1	AS	0,2	66,67	7	NaCitrat pH4	0,1	100	9	Alk-Mix	10	100	11	506,7	493,3	16
87	H3	PEG1500	12	240	3	AS	0,2	66,67	7	NaOAc pH4.75	0,1	400	17	Alk-Mix	10	100	11	806,7	193,3	16
88	H4	PEG1500	12	240	3	AS	0,2	66,67	7	NaCitrat pH4	0,1	100	9	Alk-Mix	10	100	11	506,7	493,3	16
89	H5	PEG3350	12	240	4	AS	0,2	66,67	7	NaOAc pH4.75	0,1	400	17	Alk-Mix	10	100	11	806,7	193,3	16
90	H6	PEG3350	12	240	4	AS	0,2	66,67	7	NaCitrat pH4	0,1	100	9	Alk-Mix	10	100	11	506,7	493,3	16
91	H7	PEG4000	12	240	2	AS	0,2	66,67	7	NaOAc pH4.75	0,1	400	17	Alk-Mix	10	100	11	806,7	193,3	16
92	H8	PEG4000	12	240	2	AS	0,2	66,67	7	NaCitrat pH4	0,1	100	9	Alk-Mix	10	100	11	506,7	493,3	16
93	H9	PEG8000	12	240	5	AS	0,2	66,67	7	NaOAc pH4.75	0,1	400	17	Alk-Mix	10	100	11	806,7	193,3	16
94	H10	PEG8000	12	240	5	AS	0,2	66,67	7	NaCitrat pH4	0,1	100	9	Alk-Mix	10	100	11	506,7	493,3	16
95	H11	PEG10000	12	240	6	AS	0,2	66,67	7	NaOAc pH4.75	0,1	400	17	Alk-Mix	10	100	11	806,7	193,3	16
96	H12	PEG10000	12	240	6	AS	0,2	66,67	7	NaCitrat pH4	0,1	100	9	Alk-Mix	10	100	11	506,7	493,3	16

Custom PEG Screen **PPEG2**																				
Source	1	2	3	4	5, 11	6	7	8,00	9	10	11									
Stock **8.2.B**	PEG3350	PEG8000	PEG10000	AS	NaOAc pH4.75	NaCitrat pH4	Anion-Mix1	Anion-Mix2	Anion-Mix3	Wasser	Wasser2									
Cstock	50	35	35	3	0,25	1	100	100,00	100											

Number (Destiny)	Well	Prec	Cprec	Vprec	Source	Salt	Csalt	Vsalt	Source	Buffer	Cbuffer	Vbuffer	Source	Additive	Cadditive	Vadditive		Vsum	Vwater	Source
1	A1	PEG3350	20	400	1	AS	0,2	66,67	4	NaOAc pH4.75	0,1	400	5	Anion Mix	10	100	7	966,67	33,33	10
2	A2	PEG3350	20	400	1	AS	0,2	66,67	4	NaCitrat pH4	0,1	100	6	Anion Mix	10	100	7	666,67	333,33	10
3	A3	PEG3350	20	400	1	AS	0,2	66,67	4	NaOAc pH4.75	0,1	400	5	Anion Mix 2	10	100	8	966,67	33,33	10
4	A4	PEG3350	20	400	1	AS	0,2	66,67	4	NaCitrat pH4	0,1	100	6	Anion Mix 2	10	100	8	666,67	333,33	10
5	A5	PEG3350	20	400	1	AS	0,2	66,67	4	NaOAc pH4.75	0,1	400	5	Anion Mix 3	10	100	9	966,67	33,33	10
6	A6	PEG3350	20	400	1	AS	0,2	66,67	4	NaCitrat pH4	0,1	100	6	Anion Mix 3	10	100	9	666,67	333,33	10
7	A7	PEG3350	20	400	1	AS	0,18	60,00	4	NaOAc pH4.75	0,1	400	5	Anion Mix	10	100	7	960,00	40,00	10
8	A8	PEG3350	20	400	1	AS	0,18	60,00	4	NaCitrat pH4	0,1	100	6	Anion Mix	10	100	7	660,00	340,00	10
9	A9	PEG3350	20	400	1	AS	0,18	60,00	4	NaOAc pH4.75	0,1	400	5	Anion Mix 2	10	100	8	960,00	40,00	10
10	A10	PEG3350	20	400	1	AS	0,18	60,00	4	NaCitrat pH4	0,1	100	6	Anion Mix 2	10	100	8	660,00	340,00	10
11	A11	PEG3350	20	400	1	AS	0,18	60,00	4	NaOAc pH4.75	0,1	400	5	Anion Mix 3	10	100	9	960,00	40,00	10
12	A12	PEG3350	20	400	1	AS	0,18	60,00	4	NaCitrat pH4	0,1	100	6	Anion Mix 3	10	100	9	660,00	340,00	10
13	B1	PEG3350	18	360	1	AS	0,2	66,67	4	NaOAc pH4.75	0,1	400	5	Anion Mix	10	100	7	926,67	73,33	10
14	B2	PEG3350	18	360	1	AS	0,2	66,67	4	NaCitrat pH4	0,1	100	6	Anion Mix	10	100	7	626,67	373,33	10
15	B3	PEG3350	18	360	1	AS	0,2	66,67	4	NaOAc pH4.75	0,1	400	5	Anion Mix 2	10	100	8	926,67	73,33	10
16	B4	PEG3350	18	360	1	AS	0,2	66,67	4	NaCitrat pH4	0,1	100	6	Anion Mix 2	10	100	8	626,67	373,33	10
17	B5	PEG3350	18	360	1	AS	0,2	66,67	4	NaOAc pH4.75	0,1	400	5	Anion Mix 3	10	100	9	926,67	73,33	10
18	B6	PEG3350	18	360	1	AS	0,2	66,67	4	NaCitrat pH4	0,1	100	6	Anion Mix 3	10	100	9	626,67	373,33	10
19	B7	PEG3350	18	360	1	AS	0,18	60,00	4	NaOAc pH4.75	0,1	400	5	Anion Mix	10	100	7	920,00	80,00	10
20	B8	PEG3350	18	360	1	AS	0,18	60,00	4	NaCitrat pH4	0,1	100	6	Anion Mix	10	100	7	620,00	380,00	10
21	B9	PEG3350	18	360	1	AS	0,18	60,00	4	NaOAc pH4.75	0,1	400	5	Anion Mix 2	10	100	8	920,00	80,00	10
22	B10	PEG3350	18	360	1	AS	0,18	60,00	4	NaCitrat pH4	0,1	100	6	Anion Mix 2	10	100	8	620,00	380,00	10
23	B11	PEG3350	18	360	1	AS	0,18	60,00	4	NaOAc pH4.75	0,1	400	5	Anion Mix 3	10	100	9	920,00	80,00	10
24	B12	PEG3350	18	360	1	AS	0,18	60,00	4	NaCitrat pH4	0,1	100	6	Anion Mix 3	10	100	9	620,00	380,00	10
25	C1	PEG3350	16	320	1	AS	0,2	66,67	4	NaOAc pH4.75	0,1	400	5	Anion Mix	10	100	7	886,67	113,33	10
26	C2	PEG3350	16	320	1	AS	0,2	66,67	4	NaCitrat pH4	0,1	100	6	Anion Mix	10	100	7	586,67	413,33	10
27	C3	PEG3350	16	320	1	AS	0,2	66,67	4	NaOAc pH4.75	0,1	400	5	Anion Mix 2	10	100	8	886,67	113,33	10
28	C4	PEG3350	16	320	1	AS	0,2	66,67	4	NaCitrat pH4	0,1	100	6	Anion Mix 2	10	100	8	586,67	413,33	10
29	C5	PEG3350	16	320	1	AS	0,2	66,67	4	NaOAc pH4.75	0,1	400	5	Anion Mix 3	10	100	9	886,67	113,33	10
30	C6	PEG3350	16	320	1	AS	0,2	66,67	4	NaCitrat pH4	0,1	100	6	Anion Mix 3	10	100	9	586,67	413,33	10
31	C7	PEG3350	16	320	1	AS	0,18	60,00	4	NaOAc pH4.75	0,1	400	5	Anion Mix	10	100	7	880,00	120,00	10
32	C8	PEG3350	16	320	1	AS	0,18	60,00	4	NaCitrat pH4	0,1	100	6	Anion Mix	10	100	7	580,00	420,00	10
33	C9	PEG3350	16	320	1	AS	0,18	60,00	4	NaOAc pH4.75	0,1	400	5	Anion Mix 2	10	100	8	880,00	120,00	10
34	C10	PEG3350	16	320	1	AS	0,18	60,00	4	NaCitrat pH4	0,1	100	6	Anion Mix 2	10	100	8	580,00	420,00	10
35	C11	PEG3350	16	320	1	AS	0,18	60,00	4	NaOAc pH4.75	0,1	400	5	Anion Mix 3	10	100	9	880,00	120,00	10
36	C12	PEG3350	16	320	1	AS	0,18	60,00	4	NaCitrat pH4	0,1	100	6	Anion Mix 3	10	100	9	580,00	420,00	10
37	D1	PEG3350	14	280	1	AS	0,2	66,67	4	NaOAc pH4.75	0,1	400	5	Anion Mix	10	100	7	846,67	153,33	10
38	D2	PEG3350	14	280	1	AS	0,2	66,67	4	NaCitrat pH4	0,1	100	6	Anion Mix	10	100	7	546,67	453,33	10
39	D3	PEG3350	14	280	1	AS	0,2	66,67	4	NaOAc pH4.75	0,1	400	5	Anion Mix 2	10	100	8	846,67	153,33	10
40	D4	PEG3350	14	280	1	AS	0,2	66,67	4	NaCitrat pH4	0,1	100	6	Anion Mix 2	10	100	8	546,67	453,33	10
41	D5	PEG3350	14	280	1	AS	0,2	66,67	4	NaOAc pH4.75	0,1	400	5	Anion Mix 3	10	100	9	846,67	153,33	10
42	D6	PEG3350	14	280	1	AS	0,2	66,67	4	NaCitrat pH4	0,1	100	6	Anion Mix 3	10	100	9	546,67	453,33	10
43	D7	PEG3350	14	280	1	AS	0,18	60,00	4	NaOAc pH4.75	0,1	400	5	Anion Mix	10	100	7	840,00	160,00	11
44	D8	PEG3350	14	280	1	AS	0,18	60,00	4	NaCitrat pH4	0,1	100	6	Anion Mix	10	100	7	540,00	460,00	11
45	D9	PEG3350	14	280	1	AS	0,18	60,00	4	NaOAc pH4.75	0,1	400	5	Anion Mix 2	10	100	8	840,00	160,00	11
46	D10	PEG3350	14	280	1	AS	0,18	60,00	4	NaCitrat pH4	0,1	100	6	Anion Mix 2	10	100	8	540,00	460,00	11
47	D11	PEG3350	14	280	1	AS	0,18	60,00	4	NaOAc pH4.75	0,1	400	5	Anion Mix 3	10	100	9	840,00	160,00	11
48	D12	PEG3350	14	280	1	AS	0,18	60,00	4	NaCitrat pH4	0,1	100	6	Anion Mix 3	10	100	9	540,00	460,00	11

49	E1	PEG8000	16	457,1	2	AS	0,2	66,67	4	NaOAc pH4.75	0,1	400	11	Anion Mix	7	70	7	993,81	6,19	11
50	E2	PEG8000	16	457,1	2	AS	0,2	66,67	4	NaCitrat pH4	0,1	100	6	Anion Mix	10	100	7	723,81	276,19	11
51	E3	PEG8000	16	457,1	2	AS	0,2	66,67	4	NaOAc pH4.75	0,1	400	11	Anion Mix 2	7	70	8	993,81	6,19	11
52	E4	PEG8000	16	457,1	2	AS	0,2	66,67	4	NaCitrat pH4	0,1	100	6	Anion Mix 2	10	100	8	723,81	276,19	11
53	E5	PEG8000	16	457,1	2	AS	0,2	66,67	4	NaOAc pH4.75	0,1	400	11	Anion Mix 3	7	70	9	993,81	6,19	11
54	E6	PEG8000	16	457,1	2	AS	0,2	66,67	4	NaCitrat pH4	0,1	100	6	Anion Mix 3	10	100	9	723,81	276,19	11
55	E7	PEG8000	15	428,6	2	AS	0,2	66,67	4	NaOAc pH4.75	0,1	400	11	Anion Mix	10	100	7	995,24	4,76	11
56	E8	PEG8000	15	428,6	2	AS	0,2	66,67	4	NaCitrat pH4	0,1	100	6	Anion Mix	10	100	7	695,24	304,76	11
57	E9	PEG8000	15	428,6	2	AS	0,2	66,67	4	NaOAc pH4.75	0,1	400	11	Anion Mix 2	10	100	8	995,24	4,76	11
58	E10	PEG8000	15	428,6	2	AS	0,2	66,67	4	NaCitrat pH4	0,1	100	6	Anion Mix 2	10	100	8	695,24	304,76	11
59	E11	PEG8000	15	428,6	2	AS	0,2	66,67	4	NaOAc pH4.75	0,1	400	11	Anion Mix 3	10	100	9	995,24	4,76	11
60	E12	PEG8000	14	400	2	AS	0,2	66,67	4	NaCitrat pH4	0,1	100	6	Anion Mix 3	10	100	9	666,67	333,33	11
61	F1	PEG8000	14	400	2	AS	0,2	66,67	4	NaOAc pH4.75	0,1	400	11	Anion Mix	10	100	7	966,67	33,33	11
62	F2	PEG8000	14	400	2	AS	0,2	66,67	4	NaCitrat pH4	0,1	100	6	Anion Mix	10	100	7	666,67	333,33	11
63	F3	PEG8000	14	400	2	AS	0,2	66,67	4	NaOAc pH4.75	0,1	400	11	Anion Mix 2	10	100	8	966,67	33,33	11
64	F4	PEG8000	14	400	2	AS	0,2	66,67	4	NaCitrat pH4	0,1	100	6	Anion Mix 2	10	100	8	666,67	333,33	11
65	F5	PEG8000	14	400	2	AS	0,2	66,67	4	NaOAc pH4.75	0,1	400	11	Anion Mix 3	10	100	9	966,67	33,33	11
66	F6	PEG8000	14	400	2	AS	0,2	66,67	4	NaCitrat pH4	0,1	100	6	Anion Mix 3	10	100	9	666,67	333,33	11
67	F7	PEG8000	13	371,4	2	AS	0,2	66,67	4	NaOAc pH4.75	0,1	400	11	Anion Mix	10	100	7	938,10	61,90	11
68	F8	PEG8000	13	371,4	2	AS	0,2	66,67	4	NaCitrat pH4	0,1	100	6	Anion Mix	10	100	7	638,10	361,90	11
69	F9	PEG8000	13	371,4	2	AS	0,2	66,67	4	NaOAc pH4.75	0,1	400	11	Anion Mix 2	10	100	8	938,10	61,90	11
70	F10	PEG8000	13	371,4	2	AS	0,2	66,67	4	NaCitrat pH4	0,1	100	6	Anion Mix 2	10	100	8	638,10	361,90	11
71	F11	PEG8000	13	371,4	2	AS	0,2	66,67	4	NaOAc pH4.75	0,1	400	11	Anion Mix 3	10	100	9	938,10	61,90	11
72	F12	PEG8000	13	371,4	2	AS	0,2	66,67	4	NaCitrat pH4	0,1	100	6	Anion Mix 3	10	100	9	638,10	361,90	11
73	G1	PEG10000	15	428,6	3	AS	0,2	66,67	4	NaOAc pH4.75	0,1	400	11	Anion Mix	10	100	7	995,24	4,76	11
74	G2	PEG10000	15	428,6	3	AS	0,2	66,67	4	NaCitrat pH4	0,1	100	6	Anion Mix	10	100	7	695,24	304,76	11
75	G3	PEG10000	15	428,6	3	AS	0,2	66,67	4	NaOAc pH4.75	0,1	400	11	Anion Mix 2	10	100	8	995,24	4,76	11
76	G4	PEG10000	15	428,6	3	AS	0,2	66,67	4	NaCitrat pH4	0,1	100	6	Anion Mix 2	10	100	8	695,24	304,76	11
77	G5	PEG10000	15	428,6	3	AS	0,2	66,67	4	NaOAc pH4.75	0,1	400	11	Anion Mix 3	10	100	9	995,24	4,76	11
78	G6	PEG10000	15	428,6	3	AS	0,2	66,67	4	NaCitrat pH4	0,1	100	6	Anion Mix 3	10	100	9	695,24	304,76	11
79	G7	PEG10000	14	400	3	AS	0,2	66,67	4	NaOAc pH4.75	0,1	400	11	Anion Mix	10	100	7	966,67	33,33	11
80	G8	PEG10000	14	400	3	AS	0,2	66,67	4	NaCitrat pH4	0,1	100	6	Anion Mix	10	100	7	666,67	333,33	11
81	G9	PEG10000	14	400	3	AS	0,2	66,67	4	NaOAc pH4.75	0,1	400	11	Anion Mix 2	10	100	8	966,67	33,33	11
82	G10	PEG10000	14	400	3	AS	0,2	66,67	4	NaCitrat pH4	0,1	100	6	Anion Mix 2	10	100	8	666,67	333,33	11
83	G11	PEG10000	14	400	3	AS	0,2	66,67	4	NaOAc pH4.75	0,1	400	11	Anion Mix 3	10	100	9	966,67	33,33	11
84	G12	PEG10000	14	400	3	AS	0,2	66,67	4	NaCitrat pH4	0,1	100	6	Anion Mix 3	10	100	9	666,67	333,33	11
85	H1	PEG10000	13	371,4	3	AS	0,2	66,67	4	NaOAc pH4.75	0,1	400	11	Anion Mix	10	100	7	938,10	61,90	11
86	H2	PEG10000	13	371,4	3	AS	0,2	66,67	4	NaCitrat pH4	0,1	100	6	Anion Mix	10	100	7	638,10	361,90	11
87	H3	PEG10000	13	371,4	3	AS	0,2	66,67	4	NaOAc pH4.75	0,1	400	11	Anion Mix 2	10	100	8	938,10	61,90	11
88	H4	PEG10000	13	371,4	3	AS	0,2	66,67	4	NaCitrat pH4	0,1	100	6	Anion Mix 2	10	100	8	638,10	361,90	11
89	H5	PEG10000	13	371,4	3	AS	0,2	66,67	4	NaOAc pH4.75	0,1	400	11	Anion Mix 3	10	100	9	938,10	61,90	11
90	H6	PEG10000	13	371,4	3	AS	0,2	66,67	4	NaCitrat pH4	0,1	100	6	Anion Mix 3	10	100	9	638,10	361,90	11
91	H7	PEG10000	12	342,9	3	AS	0,2	66,67	4	NaOAc pH4.75	0,1	400	11	Anion Mix	10	100	7	909,52	90,48	11
92	H8	PEG10000	12	342,9	3	AS	0,2	66,67	4	NaCitrat pH4	0,1	100	6	Anion Mix	10	100	7	609,52	390,48	11
93	H9	PEG10000	12	342,9	3	AS	0,2	66,67	4	NaOAc pH4.75	0,1	400	11	Anion Mix 2	10	100	8	909,52	90,48	11
94	H10	PEG10000	12	342,9	3	AS	0,2	66,67	4	NaCitrat pH4	0,1	100	6	Anion Mix 2	10	100	8	609,52	390,48	11
95	H11	PEG10000	12	342,9	3	AS	0,2	66,67	4	NaOAc pH4.75	0,1	400	11	Anion Mix 3	10	100	9	909,52	90,48	11
96	H12	PEG10000	12	342,9	3	AS	0,2	66,67	4	NaCitrat pH4	0,1	100	6	Anion Mix 3	10	100	9	609,52	390,48	11

Custom PEG Screen: **PPEG3**																				
Source	**8.2.C**	1, 14	2	3	4	5	6	7	8,00	9	10	11	12	13						
Stock		PEG3350	PEG8000	PEG10000	AS	MES pH	NaCitrat pH4	Anion-Mix1	Anion-Mix2	Anion-Mix3	Wasser	Wasser2	NaCitrat pH3	NaCitrat pH5.25						
Cstock		50	35	35	3	0,5	1	100	100,00	100			1	0,9						
Number (Destiny)	Well	Prec	Cprec	Vprec	Source	Salt	Csalt	Vsalt	Source	Buffer	Cbuffer	Vbuffer	Source	Additive	Cadditive	Vadditive		Vsum	Vwater	Source
1	A1	PEG3350	19	380	1	AS	0,2	66,67	4	NaCitrat pH3	0,1	100	12	Anion Mix	15	150	7	696,67	303,33	10
2	A2	PEG3350	19	380	1	AS	0,2	66,67	4	NaCitrat pH4	0,1	100	6	Anion Mix	15	150	7	696,67	303,33	10
3	A3	PEG3350	19	380	1	AS	0,2	66,67	4	MES pH6.5	0,1	200	5	Anion Mix	15	150	7	796,67	203,33	10
4	A4	PEG3350	19	380	1	AS	0,2	66,67	4	NaCitrat pH5,5	0,1	111,111111	13	Anion Mix	15	150	7	707,78	292,22	10
5	A5	PEG3350	19	380	1	AS	0,2	66,67	4	NaCitrat pH3	0,1	100	12	Anion Mix 2	20	200	8	746,67	253,33	10
6	A6	PEG3350	19	380	1	AS	0,2	66,67	4	NaCitrat pH4	0,1	100	6	Anion Mix 2	20	200	8	746,67	253,33	10
7	A7	PEG3350	19	380	1	AS	0,2	66,67	4	MES pH6.5	0,1	200	5	Anion Mix 2	20	200	8	846,67	153,33	10
8	A8	PEG3350	19	380	1	AS	0,2	66,67	4	NaCitrat pH5,5	0,1	111,111111	13	Anion Mix 2	20	200	8	757,78	242,22	10
9	A9	PEG3350	19	380	1	AS	0,2	66,67	4	NaCitrat pH3	0,1	100	12	Anion Mix 3	20	200	9	746,67	253,33	10
10	A10	PEG3350	19	380	1	AS	0,2	66,67	4	NaCitrat pH4	0,1	100	6	Anion Mix 3	20	200	9	746,67	253,33	10
11	A11	PEG3350	19	380	1	AS	0,2	66,67	4	MES pH6.5	0,1	200	5	Anion Mix 3	20	200	9	846,67	153,33	10
12	A12	PEG3350	19	380	1	AS	0,2	66,67	4	NaCitrat pH5,5	0,1	111,111111	13	Anion Mix 3	20	200	9	757,78	242,22	10
13	B1	PEG3350	18	360	1	AS	0,2	66,67	4	NaCitrat pH3	0,1	100	12	Anion Mix	15	150	7	676,67	323,33	10
14	B2	PEG3350	18	360	1	AS	0,2	66,67	4	NaCitrat pH4	0,1	100	6	Anion Mix	15	150	7	676,67	323,33	10
15	B3	PEG3350	18	360	1	AS	0,2	66,67	4	MES pH6.5	0,1	200	5	Anion Mix	15	150	7	776,67	223,33	10
16	B4	PEG3350	18	360	1	AS	0,2	66,67	4	NaCitrat pH5,5	0,1	111,111111	13	Anion Mix	15	150	7	687,78	312,22	10
17	B5	PEG3350	18	360	1	AS	0,2	66,67	4	NaCitrat pH3	0,1	100	12	Anion Mix 2	20	200	8	726,67	273,33	10
18	B6	PEG3350	18	360	1	AS	0,2	66,67	4	NaCitrat pH4	0,1	100	6	Anion Mix 2	20	200	8	726,67	273,33	10
19	B7	PEG3350	18	360	1	AS	0,2	66,67	4	MES pH6.5	0,1	200	5	Anion Mix 2	20	200	8	826,67	173,33	10
20	B8	PEG3350	18	360	1	AS	0,2	66,67	4	NaCitrat pH5,5	0,1	111,111111	13	Anion Mix 2	20	200	8	737,78	262,22	10
21	B9	PEG3350	18	360	1	AS	0,2	66,67	4	NaCitrat pH3	0,1	100	12	Anion Mix 3	20	200	9	726,67	273,33	10
22	B10	PEG3350	18	360	1	AS	0,2	66,67	4	NaCitrat pH4	0,1	100	6	Anion Mix 3	20	200	9	726,67	273,33	10
23	B11	PEG3350	18	360	1	AS	0,2	66,67	4	MES pH6.5	0,1	200	5	Anion Mix 3	20	200	9	826,67	173,33	10
24	B12	PEG3350	18	360	1	AS	0,2	66,67	4	NaCitrat pH5,5	0,1	111,111111	13	Anion Mix 3	20	200	9	737,78	262,22	10
25	C1	PEG3350	17	340	14	AS	0,2	66,67	4	NaCitrat pH3	0,1	100	12	Anion Mix	15	150	7	656,67	343,33	10
26	C2	PEG3350	17	340	14	AS	0,2	66,67	4	NaCitrat pH4	0,1	100	6	Anion Mix	15	150	7	656,67	343,33	10
27	C3	PEG3350	17	340	14	AS	0,2	66,67	4	MES pH6.5	0,1	200	5	Anion Mix	15	150	7	756,67	243,33	10
28	C4	PEG3350	17	340	14	AS	0,2	66,67	4	NaCitrat pH5,5	0,1	111,111111	13	Anion Mix	15	150	7	667,78	332,22	10
29	C5	PEG3350	17	340	14	AS	0,2	66,67	4	NaCitrat pH3	0,1	100	12	Anion Mix 2	20	200	8	706,67	293,33	10
30	C6	PEG3350	17	340	14	AS	0,2	66,67	4	NaCitrat pH4	0,1	100	6	Anion Mix 2	20	200	8	706,67	293,33	10
31	C7	PEG3350	17	340	14	AS	0,2	66,67	4	MES pH6.5	0,1	200	5	Anion Mix 2	20	200	8	806,67	193,33	10
32	C8	PEG3350	17	340	14	AS	0,2	66,67	4	NaCitrat pH5,5	0,1	111,111111	13	Anion Mix 2	20	200	8	717,78	282,22	10
33	C9	PEG3350	17	340	14	AS	0,2	66,67	4	NaCitrat pH3	0,1	100	12	Anion Mix 3	20	200	9	706,67	293,33	10
34	C10	PEG3350	17	340	14	AS	0,2	66,67	4	NaCitrat pH4	0,1	100	6	Anion Mix 3	20	200	9	706,67	293,33	10
35	C11	PEG3350	17	340	14	AS	0,2	66,67	4	MES pH6.5	0,1	200	5	Anion Mix 3	20	200	9	806,67	193,33	10
36	C12	PEG3350	17	340	14	AS	0,2	66,67	4	NaCitrat pH5,5	0,1	111,111111	13	Anion Mix 3	20	200	9	717,78	282,22	10
37	D1	PEG3350	16	320	14	AS	0,2	66,67	4	NaCitrat pH3	0,1	100	12	Anion Mix	15	150	7	636,67	363,33	10
38	D2	PEG3350	16	320	14	AS	0,2	66,67	4	NaCitrat pH4	0,1	100	6	Anion Mix	15	150	7	636,67	363,33	10
39	D3	PEG3350	16	320	14	AS	0,2	66,67	4	MES pH6.5	0,1	200	5	Anion Mix	15	150	7	736,67	263,33	10
40	D4	PEG3350	16	320	14	AS	0,2	66,67	4	NaCitrat pH5,5	0,1	111,111111	13	Anion Mix	15	150	7	647,78	352,22	10
41	D5	PEG3350	16	320	14	AS	0,2	66,67	4	NaCitrat pH3	0,1	100	12	Anion Mix 2	20	200	8	686,67	313,33	10
42	D6	PEG3350	16	320	14	AS	0,2	66,67	4	NaCitrat pH4	0,1	100	6	Anion Mix 2	20	200	8	686,67	313,33	10
43	D7	PEG3350	16	320	14	AS	0,2	66,67	4	MES pH6.5	0,1	200	5	Anion Mix 2	20	200	8	786,67	213,33	11
44	D8	PEG3350	16	320	14	AS	0,2	66,67	4	NaCitrat pH5,5	0,1	111,111111	13	Anion Mix 2	20	200	8	697,78	302,22	11
45	D9	PEG3350	16	320	14	AS	0,2	66,67	4	NaCitrat pH3	0,1	100	12	Anion Mix 3	20	200	9	686,67	313,33	11
46	D10	PEG3350	16	320	14	AS	0,2	66,67	4	NaCitrat pH4	0,1	100	6	Anion Mix 3	20	200	9	686,67	313,33	11
47	D11	PEG3350	16	320	14	AS	0,2	66,67	4	MES pH6.5	0,1	200	5	Anion Mix 3	20	200	9	786,67	213,33	11
48	D12	PEG3350	16	320	14	AS	0,2	66,67	4	NaCitrat pH5,5	0,1	111,111111	13	Anion Mix 3	20	200	9	697,78	302,22	11

49	E1	PEG8000	16	457,14	2	AS	0,2	66,67	4	NaCitrat pH3	0,1	100	12	Anion Mix	15	150	7	773,81	226,19	11
50	E2	PEG8000	16	457,14	2	AS	0,2	66,67	4	NaCitrat pH4	0,1	100	6	Anion Mix	15	150	7	773,81	226,19	11
51	E3	PEG8000	16	457,14	2	AS	0,2	66,67	4	MES pH6.5	0,1	200	5	Anion Mix	15	150	7	873,81	126,19	11
52	E4	PEG8000	16	457,14	2	AS	0,2	66,67	4	NaCitrat pH5,5	0,1	111,111111	13	Anion Mix	15	150	7	784,92	215,08	11
53	E5	PEG8000	16	457,14	2	AS	0,2	66,67	4	NaCitrat pH3	0,1	100	12	Anion Mix 2	20	200	8	823,81	176,19	11
54	E6	PEG8000	16	457,14	2	AS	0,2	66,67	4	NaCitrat pH4	0,1	100	6	Anion Mix 2	20	200	8	823,81	176,19	11
55	E7	PEG8000	16	457,14	2	AS	0,2	66,67	4	MES pH6.5	0,1	200	5	Anion Mix 2	20	200	8	923,81	76,19	11
56	E8	PEG8000	16	457,14	2	AS	0,2	66,67	4	NaCitrat pH5,5	0,1	111,111111	13	Anion Mix 2	20	200	8	834,92	165,08	11
57	E9	PEG8000	16	457,14	2	AS	0,2	66,67	4	NaCitrat pH3	0,1	100	12	Anion Mix 3	20	200	9	823,81	176,19	11
58	E10	PEG8000	16	457,14	2	AS	0,2	66,67	4	NaCitrat pH4	0,1	100	6	Anion Mix 3	20	200	9	823,81	176,19	11
59	E11	PEG8000	16	457,14	2	AS	0,2	66,67	4	MES pH6.5	0,1	200	5	Anion Mix 3	20	200	9	923,81	76,19	11
60	E12	PEG8000	16	457,14	2	AS	0,2	66,67	4	NaCitrat pH5,5	0,1	111,111111	13	Anion Mix 3	20	200	9	834,92	165,08	11
61	F1	PEG8000	14	400	2	AS	0,2	66,67	4	NaCitrat pH3	0,1	100	12	Anion Mix	15	150	7	716,67	283,33	11
62	F2	PEG8000	14	400	2	AS	0,2	66,67	4	NaCitrat pH4	0,1	100	6	Anion Mix	15	150	7	716,67	283,33	11
63	F3	PEG8000	14	400	2	AS	0,2	66,67	4	MES pH6.5	0,1	200	5	Anion Mix	15	150	7	816,67	183,33	11
64	F4	PEG8000	14	400	2	AS	0,2	66,67	4	NaCitrat pH5,5	0,1	111,111111	13	Anion Mix	15	150	7	727,78	272,22	11
65	F5	PEG8000	14	400	2	AS	0,2	66,67	4	NaCitrat pH3	0,1	100	12	Anion Mix 2	20	200	8	766,67	233,33	11
66	F6	PEG8000	14	400	2	AS	0,2	66,67	4	NaCitrat pH4	0,1	100	6	Anion Mix 2	20	200	8	766,67	233,33	11
67	F7	PEG8000	14	400	2	AS	0,2	66,67	4	MES pH6.5	0,1	200	5	Anion Mix 2	20	200	8	866,67	133,33	11
68	F8	PEG8000	14	400	2	AS	0,2	66,67	4	NaCitrat pH5,5	0,1	111,111111	13	Anion Mix 2	20	200	8	777,78	222,22	11
69	F9	PEG8000	14	400	2	AS	0,2	66,67	4	NaCitrat pH3	0,1	100	12	Anion Mix 3	20	200	9	766,67	233,33	11
70	F10	PEG8000	14	400	2	AS	0,2	66,67	4	NaCitrat pH4	0,1	100	6	Anion Mix 3	20	200	9	766,67	233,33	11
71	F11	PEG8000	14	400	2	AS	0,2	66,67	4	MES pH6.5	0,1	200	5	Anion Mix 3	20	200	9	866,67	133,33	11
72	F12	PEG8000	14	400	2	AS	0,2	66,67	4	NaCitrat pH5,5	0,1	111,111111	13	Anion Mix 3	20	200	9	777,78	222,22	11
73	G1	PEG10000	14	400	3	AS	0,2	66,67	4	NaCitrat pH3	0,1	100	12	Anion Mix	15	150	7	716,67	283,33	11
74	G2	PEG10000	14	400	3	AS	0,2	66,67	4	NaCitrat pH4	0,1	100	6	Anion Mix	15	150	7	716,67	283,33	11
75	G3	PEG10000	14	400	3	AS	0,2	66,67	4	MES pH6.5	0,1	200	5	Anion Mix	15	150	7	816,67	183,33	11
76	G4	PEG10000	14	400	3	AS	0,2	66,67	4	NaCitrat pH5,5	0,1	111,111111	13	Anion Mix	15	150	7	727,78	272,22	11
77	G5	PEG10000	14	400	3	AS	0,2	66,67	4	NaCitrat pH3	0,1	100	12	Anion Mix 2	20	200	8	766,67	233,33	11
78	G6	PEG10000	14	400	3	AS	0,2	66,67	4	NaCitrat pH4	0,1	100	6	Anion Mix 2	20	200	8	766,67	233,33	11
79	G7	PEG10000	14	400	3	AS	0,2	66,67	4	MES pH6.5	0,1	200	5	Anion Mix 2	20	200	8	866,67	133,33	11
80	G8	PEG10000	14	400	3	AS	0,2	66,67	4	NaCitrat pH5,5	0,1	111,111111	13	Anion Mix 2	20	200	8	777,78	222,22	11
81	G9	PEG10000	14	400	3	AS	0,2	66,67	4	NaCitrat pH3	0,1	100	12	Anion Mix 3	20	200	9	766,67	233,33	11
82	G10	PEG10000	14	400	3	AS	0,2	66,67	4	NaCitrat pH4	0,1	100	6	Anion Mix 3	20	200	9	766,67	233,33	11
83	G11	PEG10000	14	400	3	AS	0,2	66,67	4	MES pH6.5	0,1	200	5	Anion Mix 3	20	200	9	866,67	133,33	11
84	G12	PEG10000	14	400	3	AS	0,2	66,67	4	NaCitrat pH5,5	0,1	111,111111	13	Anion Mix 3	20	200	9	777,78	222,22	11
85	H1	PEG10000	12	342,86	3	AS	0,2	66,67	4	NaCitrat pH3	0,1	100	12	Anion Mix	15	150	7	659,52	340,48	11
86	H2	PEG10000	12	342,86	3	AS	0,2	66,67	4	NaCitrat pH4	0,1	100	6	Anion Mix	15	150	7	659,52	340,48	11
87	H3	PEG10000	12	342,86	3	AS	0,2	66,67	4	MES pH6.5	0,1	200	5	Anion Mix	15	150	7	759,52	240,48	11
88	H4	PEG10000	12	342,86	3	AS	0,2	66,67	4	NaCitrat pH5,5	0,1	111,111111	13	Anion Mix	15	150	7	670,63	329,37	11
89	H5	PEG10000	12	342,86	3	AS	0,2	66,67	4	NaCitrat pH3	0,1	100	12	Anion Mix 2	20	200	8	709,52	290,48	11
90	H6	PEG10000	12	342,86	3	AS	0,2	66,67	4	NaCitrat pH4	0,1	100	6	Anion Mix 2	20	200	8	709,52	290,48	11
91	H7	PEG10000	12	342,86	3	AS	0,2	66,67	4	MES pH6.5	0,1	200	5	Anion Mix 2	20	200	8	809,52	190,48	11
92	H8	PEG10000	12	342,86	3	AS	0,2	66,67	4	NaCitrat pH5,5	0,1	111,111111	13	Anion Mix 2	20	200	8	720,63	279,37	11
93	H9	PEG10000	12	342,86	3	AS	0,2	66,67	4	NaCitrat pH3	0,1	100	12	Anion Mix 3	20	200	9	709,52	290,48	11
94	H10	PEG10000	12	342,86	3	AS	0,2	66,67	4	NaCitrat pH4	0,1	100	6	Anion Mix 3	20	200	9	709,52	290,48	11
95	H11	PEG10000	12	342,86	3	AS	0,2	66,67	4	MES pH6.5	0,1	200	5	Anion Mix 3	20	200	9	809,52	190,48	11
96	H12	PEG10000	12	342,86	3	AS	0,2	66,67	4	NaCitrat pH5,5	0,1	111,111111	13	Anion Mix 3	20	200	9	720,63	279,37	11

Custom PEG Screen: **PPEG7**																							
Source	1	2	3, 24	4,0	5, 12	6	7	8,0	9	10	11	13	14	15	16	17	18	19	20	21	22	23
Stock **8.2.D**	PEG3350	PEG8000	PEG10000	AS	NaOAc pH4.75	NaCitrat pH4	Anion-Mix1	Anion-Mix2	Anion-Mix3	Wasser	Wasser2	AmNO3	NaI	NaBr	AnioMix5	AnioMix6	AmCl	AmBr	AmI	AmAc	AmFor	AmTar
Cstock	50	35	35	3,0	0,25	1	100	100,0	100			5	1	1	100	100	1	1	1	1	2	1
Vges	500																					

Number (Destiny)	Well	Prec	Cprec	Vprec	Source	Salt	Csalt	Vsalt	Source	Buffer	Cbuffer	Vbuffer	Source	Additive	Cadditive	Vadditive		Vsum	Vwater	Source		
1	A1	PEG10000	15	214,3	3	AS	0,2	33,3	4	NaCitrat pH4	0,1	50	6	Anion Mix 2	10	50	8	347,6	152,38	10		
2	A2	PEG10000	15	214,3	3	AS	0,2	33,3	4	NaCitrat pH4	0,1	50	6	Anion Mix 2	10	50	8	347,6	152,38	10		
3	A3	PEG10000	15	214,3	3	AS	0,18	30,0	4	NaCitrat pH4	0,1	50	6	Anion Mix 2	10	50	8	344,3	155,71	10		
4	A4	PEG10000	15	214,3	3	AS	0,18	30,0	4	NaCitrat pH4	0,1	50	6	Anion Mix 2	10	50	8	344,3	155,71	10		
5	A5	PEG10000	15	214,3	3	AS	0,2	33,3	4	NaCitrat pH4	0,1	50	6	NaI	0,1	50	14	347,6	152,38	10		
6	A6	PEG10000	15	214,3	3	AS	0,2	33,3	4	NaCitrat pH4	0,1	50	6	NaI	0,1	50	14	347,6	152,38	10		
7	A7	PEG10000	15	214,3	3	AS	0,18	30,0	4	NaCitrat pH4	0,1	50	6	NaI	0,1	50	14	344,3	155,71	10		
8	A8	PEG10000	15	214,3	3	AS	0,18	30,0	4	NaCitrat pH4	0,1	50	6	NaI	0,1	50	14	344,3	155,71	10		
9	A9	PEG10000	15	214,3	3	AS	0,2	33,3	4	NaCitrat pH4	0,1	50	6	NaBr	0,1	50	15	347,6	152,38	10		
10	A10	PEG10000	15	214,3	3	AS	0,2	33,3	4	NaCitrat pH4	0,1	50	6	NaBr	0,1	50	15	347,6	152,38	10		
11	A11	PEG10000	15	214,3	3	AS	0,18	30,0	4	NaCitrat pH4	0,1	50	6	NaBr	0,1	50	15	344,3	155,71	10		
12	A12	PEG10000	15	214,3	3	AS	0,18	30,0	4	NaCitrat pH4	0,1	50	6	NaBr	0,1	50	15	344,3	155,71	10		
13	B1	PEG10000	15	214,3	3	AS	0,2	33,3	4	NaCitrat pH4	0,1	50	6	AnioMix5	10	50	16	347,6	152,38	10		
14	B2	PEG10000	15	214,3	3	AS	0,2	33,3	4	NaCitrat pH4	0,1	50	6	AnioMix5	10	50	16	347,6	152,38	10		
15	B3	PEG10000	15	214,3	3	AS	0,18	30,0	4	NaCitrat pH4	0,1	50	6	AnioMix5	10	50	16	344,3	155,71	10		
16	B4	PEG10000	15	214,3	3	AS	0,18	30,0	4	NaCitrat pH4	0,1	50	6	AnioMix5	10	50	16	344,3	155,71	10		
17	B5	PEG10000	15	214,3	3	AS	0,2	33,3	4	NaCitrat pH4	0,1	50	6	AnioMix6	10	50	17	347,6	152,38	10		
18	B6	PEG10000	15	214,3	3	AS	0,2	33,3	4	NaCitrat pH4	0,1	50	6	AnioMix6	10	50	17	347,6	152,38	10		
19	B7	PEG10000	15	214,3	3	AS	0,18	30,0	4	NaCitrat pH4	0,1	50	6	AnioMix6	10	50	17	344,3	155,71	10		
20	B8	PEG10000	15	214,3	3	AS	0,18	30,0	4	NaCitrat pH4	0,1	50	6	AnioMix6	10	50	17	344,3	155,71	10		
21	B9	PEG10000	15	214,3	3	AS	0,2	33,3	4	NaCitrat pH4	0,1	50	6	AmCl	0,1	50	18	347,6	152,38	10		
22	B10	PEG10000	15	214,3	3	AS	0,2	33,3	4	NaCitrat pH4	0,1	50	6	AmCl	0,1	50	18	347,6	152,38	10		
23	B11	PEG10000	15	214,3	3	AS	0,18	30,0	4	NaCitrat pH4	0,1	50	6	AmCl	0,1	50	18	344,3	155,71	10		
24	B12	PEG10000	15	214,3	3	AS	0,18	30,0	4	NaCitrat pH4	0,1	50	6	AmCl	0,1	50	18	344,3	155,71	10		
25	C1	PEG10000	15	214,3	3	AS	0,2	33,3	4	NaCitrat pH4	0,1	50	6	AmBr	0,1	50	19	347,6	152,38	10		
26	C2	PEG10000	15	214,3	3	AS	0,2	33,3	4	NaCitrat pH4	0,1	50	6	AmBr	0,1	50	19	347,6	152,38	10		
27	C3	PEG10000	15	214,3	3	AS	0,18	30,0	4	NaCitrat pH4	0,1	50	6	AmBr	0,1	50	19	344,3	155,71	10		
28	C4	PEG10000	15	214,3	3	AS	0,18	30,0	4	NaCitrat pH4	0,1	50	6	AmBr	0,1	50	19	344,3	155,71	10		
29	C5	PEG10000	15	214,3	3	AS	0,2	33,3	4	NaCitrat pH4	0,1	50	6	AmI	0,1	50	20	347,6	152,38	10		
30	C6	PEG10000	15	214,3	3	AS	0,2	33,3	4	NaCitrat pH4	0,1	50	6	AmI	0,1	50	20	347,6	152,38	10		
31	C7	PEG10000	15	214,3	3	AS	0,18	30,0	4	NaCitrat pH4	0,1	50	6	AmI	0,1	50	20	344,3	155,71	10		
32	C8	PEG10000	15	214,3	3	AS	0,18	30,0	4	NaCitrat pH4	0,1	50	6	AmI	0,1	50	20	344,3	155,71	10		
33	C9	PEG10000	15	214,3	3	AS	0,2	33,3	4	NaCitrat pH4	0,1	50	6	AmNO3	0,1	10	13	307,6	192,38	10		
34	C10	PEG10000	15	214,3	3	AS	0,2	33,3	4	NaCitrat pH4	0,1	50	6	AmNO3	0,1	10	13	307,6	192,38	10		
35	C11	PEG10000	15	214,3	3	AS	0,18	30,0	4	NaCitrat pH4	0,1	50	6	AmNO3	0,1	10	13	304,3	195,71	10		
36	C12	PEG10000	15	214,3	3	AS	0,18	30,0	4	NaCitrat pH4	0,1	50	6	AmNO3	0,1	10	13	304,3	195,71	10		
37	D1	PEG10000	15	214,3	3	AS	0,2	33,3	4	NaCitrat pH4	0,1	50	6	AmAc	0,1	50	21	347,6	152,38	10		
38	D2	PEG10000	15	214,3	3	AS	0,2	33,3	4	NaCitrat pH4	0,1	50	6	AmAc	0,1	50	21	347,6	152,38	10		
39	D3	PEG10000	15	214,3	3	AS	0,18	30,0	4	NaCitrat pH4	0,1	50	6	AmAc	0,1	50	21	344,3	155,71	10		
40	D4	PEG10000	15	214,3	3	AS	0,18	30,0	4	NaCitrat pH4	0,1	50	6	AmAc	0,1	50	21	344,3	155,71	10		
41	D5	PEG10000	15	214,3	3	AS	0,2	33,3	4	NaCitrat pH4	0,1	50	6	AmFor	0,1	25	22	322,6	177,38	10		
42	D6	PEG10000	15	214,3	3	AS	0,2	33,3	4	NaCitrat pH4	0,1	50	6	AmFor	0,1	25	22	322,6	177,38	10		
43	D7	PEG10000	15	214,3	3	AS	0,18	30,0	4	NaCitrat pH4	0,1	50	6	AmFor	0,1	25	22	319,3	180,71	11		
44	D8	PEG10000	15	214,3	3	AS	0,18	30,0	4	NaCitrat pH4	0,1	50	6	AmFor	0,1	25	22	319,3	180,71	11		
45	D9	PEG10000	15	214,3	3	AS	0,2	33,3	4	NaCitrat pH4	0,1	50	6	AmTar	0,1	50	23	347,6	152,38	11		
46	D10	PEG10000	15	214,3	3	AS	0,2	33,3	4	NaCitrat pH4	0,1	50	6	AmTar	0,1	50	23	347,6	152,38	11		
47	D11	PEG10000	15	214,3	3	AS	0,18	30,0	4	NaCitrat pH4	0,1	50	6	AmTar	0,1	50	23	344,3	155,71	11		
48	D12	PEG10000	15	214,3	3	AS	0,18	30,0	4	NaCitrat pH4	0,1	50	6	AmTar	0,1	50	23	344,3	155,71	11		

49	E1	PEG10000	15	214,3	3	AmNO3	0,4	40,0	13	NaCitrat pH4	0,1	50	6	Anion Mix 2	10	50	8	354,3	145,71	11
50	E2	PEG10000	15	214,3	3	AmNO3	0,4	40,0	13	NaCitrat pH4	0,1	50	6	Anion Mix 2	10	50	8	354,3	145,71	11
51	E3	PEG10000	15	214,3	3	AmNO3	0,35	35,0	13	NaCitrat pH4	0,1	50	6	Anion Mix 2	10	50	8	349,3	150,71	11
52	E4	PEG10000	15	214,3	3	AmNO3	0,35	35,0	13	NaCitrat pH4	0,1	50	6	Anion Mix 2	10	50	8	349,3	150,71	11
53	E5	PEG10000	15	214,3	3	AmNO3	0,4	40,0	13	NaCitrat pH4	0,1	50	6	NaI	0,1	50	14	354,3	145,71	11
54	E6	PEG10000	15	214,3	3	AmNO3	0,4	40,0	13	NaCitrat pH4	0,1	50	6	NaI	0,1	50	14	354,3	145,71	11
55	E7	PEG10000	15	214,3	3	AmNO3	0,35	35,0	13	NaCitrat pH4	0,1	50	6	NaI	0,1	50	14	349,3	150,71	11
56	E8	PEG10000	15	214,3	3	AmNO3	0,35	35,0	13	NaCitrat pH4	0,1	50	6	NaI	0,1	50	14	349,3	150,71	11
57	E9	PEG10000	15	214,3	3	AmNO3	0,4	40,0	13	NaCitrat pH4	0,1	50	6	NaBr	0,1	50	15	354,3	145,71	11
58	E10	PEG10000	15	214,3	3	AmNO3	0,4	40,0	13	NaCitrat pH4	0,1	50	6	NaBr	0,1	50	15	354,3	145,71	11
59	E11	PEG10000	15	214,3	3	AmNO3	0,35	35,0	13	NaCitrat pH4	0,1	50	6	NaBr	0,1	50	15	349,3	150,71	11
60	E12	PEG10000	15	214,3	3	AmNO3	0,35	35,0	13	NaCitrat pH4	0,1	50	6	NaBr	0,1	50	15	349,3	150,71	11
61	F1	PEG10000	15	214,3	3	AmNO3	0,4	40,0	13	NaCitrat pH4	0,1	50	6	AnioMix5	10	50	16	354,3	145,71	11
62	F2	PEG10000	15	214,3	3	AmNO3	0,4	40,0	13	NaCitrat pH4	0,1	50	6	AnioMix5	10	50	16	354,3	145,71	11
63	F3	PEG10000	15	214,3	3	AmNO3	0,35	35,0	13	NaCitrat pH4	0,1	50	6	AnioMix5	10	50	16	349,3	150,71	11
64	F4	PEG10000	15	214,3	3	AmNO3	0,35	35,0	13	NaCitrat pH4	0,1	50	6	AnioMix5	10	50	16	349,3	150,71	11
65	F5	PEG10000	15	214,3	3	AmNO3	0,4	40,0	13	NaCitrat pH4	0,1	50	6	AnioMix6	10	50	17	354,3	145,71	11
66	F6	PEG10000	15	214,3	3	AmNO3	0,4	40,0	13	NaCitrat pH4	0,1	50	6	AnioMix6	10	50	17	354,3	145,71	11
67	F7	PEG10000	15	214,3	3	AmNO3	0,35	35,0	13	NaCitrat pH4	0,1	50	6	AnioMix6	10	50	17	349,3	150,71	11
68	F8	PEG10000	15	214,3	3	AmNO3	0,35	35,0	13	NaCitrat pH4	0,1	50	6	AnioMix6	10	50	17	349,3	150,71	11
69	F9	PEG10000	15	214,3	24	AmNO3	0,4	40,0	13	NaCitrat pH4	0,1	50	6	AmCl	0,1	50	18	354,3	145,71	11
70	F10	PEG10000	15	214,3	24	AmNO3	0,4	40,0	13	NaCitrat pH4	0,1	50	6	AmCl	0,1	50	18	354,3	145,71	11
71	F11	PEG10000	15	214,3	24	AmNO3	0,35	35,0	13	NaCitrat pH4	0,1	50	6	AmCl	0,1	50	18	349,3	150,71	11
72	F12	PEG10000	15	214,3	24	AmNO3	0,35	35,0	13	NaCitrat pH4	0,1	50	6	AmCl	0,1	50	18	349,3	150,71	11
73	G1	PEG10000	15	214,3	24	AmNO3	0,4	40,0	13	NaCitrat pH4	0,1	50	6	AmBr	0,1	50	19	354,3	145,71	11
74	G2	PEG10000	15	214,3	24	AmNO3	0,4	40,0	13	NaCitrat pH4	0,1	50	6	AmBr	0,1	50	19	354,3	145,71	11
75	G3	PEG10000	15	214,3	24	AmNO3	0,35	35,0	13	NaCitrat pH4	0,1	50	6	AmBr	0,1	50	19	349,3	150,71	11
76	G4	PEG10000	15	214,3	24	AmNO3	0,35	35,0	13	NaCitrat pH4	0,1	50	6	AmBr	0,1	50	19	349,3	150,71	11
77	G5	PEG10000	15	214,3	24	AmNO3	0,4	40,0	13	NaCitrat pH4	0,1	50	6	AmI	0,1	50	20	354,3	145,71	11
78	G6	PEG10000	15	214,3	24	AmNO3	0,4	40,0	13	NaCitrat pH4	0,1	50	6	AmI	0,1	50	20	354,3	145,71	11
79	G7	PEG10000	15	214,3	24	AmNO3	0,35	35,0	13	NaCitrat pH4	0,1	50	6	AmI	0,1	50	20	349,3	150,71	11
80	G8	PEG10000	15	214,3	24	AmNO3	0,35	35,0	13	NaCitrat pH4	0,1	50	6	AmI	0,1	50	20	349,3	150,71	11
81	G9	PEG10000	15	214,3	24	AmNO3	0,4	40,0	13	NaCitrat pH4	0,1	50	6	AmSO4	0,1	16,66667	13	321	179,05	11
82	G10	PEG10000	15	214,3	24	AmNO3	0,4	40,0	13	NaCitrat pH4	0,1	50	6	AmSO4	0,1	16,66667	13	321	179,05	11
83	G11	PEG10000	15	214,3	24	AmNO3	0,35	35,0	13	NaCitrat pH4	0,1	50	6	AmSO4	0,1	16,66667	13	316	184,05	11
84	G12	PEG10000	15	214,3	24	AmNO3	0,35	35,0	13	NaCitrat pH4	0,1	50	6	AmSO4	0,1	16,66667	13	316	184,05	11
85	H1	PEG10000	15	214,3	24	AmNO3	0,4	40,0	13	NaCitrat pH4	0,1	50	6	AmAc	0,1	50	21	354,3	145,71	11
86	H2	PEG10000	15	214,3	24	AmNO3	0,4	40,0	13	NaCitrat pH4	0,1	50	6	AmAc	0,1	50	21	354,3	145,71	11
87	H3	PEG10000	15	214,3	24	AmNO3	0,35	35,0	13	NaCitrat pH4	0,1	50	6	AmAc	0,1	50	21	349,3	150,71	11
88	H4	PEG10000	15	214,3	24	AmNO3	0,35	35,0	13	NaCitrat pH4	0,1	50	6	AmAc	0,1	50	21	349,3	150,71	11
89	H5	PEG10000	15	214,3	24	AmNO3	0,4	40,0	13	NaCitrat pH4	0,1	50	6	AmFor	0,1	25	22	329,3	170,71	11
90	H6	PEG10000	15	214,3	24	AmNO3	0,4	40,0	13	NaCitrat pH4	0,1	50	6	AmFor	0,1	25	22	329,3	170,71	11
91	H7	PEG10000	15	214,3	24	AmNO3	0,35	35,0	13	NaCitrat pH4	0,1	50	6	AmFor	0,1	25	22	324,3	175,71	11
92	H8	PEG10000	15	214,3	24	AmNO3	0,35	35,0	13	NaCitrat pH4	0,1	50	6	AmFor	0,1	25	22	324,3	175,71	11
93	H9	PEG10000	15	214,3	24	AmNO3	0,4	40,0	13	NaCitrat pH4	0,1	50	6	AmTar	0,1	50	23	354,3	145,71	11
94	H10	PEG10000	15	214,3	24	AmNO3	0,4	40,0	13	NaCitrat pH4	0,1	50	6	AmTar	0,1	50	23	354,3	145,71	11
95	H11	PEG10000	15	214,3	24	AmNO3	0,35	35,0	13	NaCitrat pH4	0,1	50	6	AmTar	0,1	50	23	349,3	150,71	11
96	H12	PEG10000	15	214,3	24	AmNO3	0,35	35,0	13	NaCitrat pH4	0,1	50	6	AmTar	0,1	50	23	349,3	150,71	11

Custom PEG Screen: **PPEG8**																								
Source		1	2	3, 24	4	5, 12	6	7	8,0	9	10	11	13	14	15	16	17	18	19	20	21	22	23
Stock	**8.2.E**	PEG3350	PEG8000	PEG10000	AS	NaOAc pH4.75	NaCitrat pH4	Anion-Mix1	Anion-Mix2	Anion-Mix3	Wasser	Wasser2	AmNO3	NaI	NaBr	AnioMix5	AnioMix6	AmCl	AmBr	AmI	AmAc	AmFor	AmTar
Cstock		50	35	35	3	1	1	100	100,0	100			5	1	1	100	100	1	1	1	1	2	1
Vges		500																						
Number (Destiny)	Well	Prec	Cprec	Vprec	Source	Salt	Csalt	Vsalt	Source	Buffer	Cbuffer	Vbuffer	Source	Additive	Cadditive	Vadditive		Vsum	Vwater	Source				
1	A1	PEG10000	15	214,3	3	AS	0,2	33,3	4	NaCitrat pH4	0,1	50	6	AmI	0,1	50	20	347,6	152,38	10				
2	A2	PEG10000	15	214,3	3	AS	0,2	33,3	4	NaCitrat pH4	0,1	50	6	AmI	0,15	75	20	372,6	127,38	10				
3	A3	PEG10000	15	214,3	3	AS	0,2	33,3	4	NaCitrat pH4	0,1	50	6	AmI	0,2	100	20	397,6	102,38	10				
4	A4	PEG10000	15	214,3	3	AS	0,2	33,3	4	NaOAc pH4.75	0,1	50	5	AmI	0,1	50	20	347,6	152,38	10				
5	A5	PEG10000	15	214,3	3	AS	0,2	33,3	4	NaOAc pH4.75	0,1	50	5	AmI	0,15	75	20	372,6	127,38	10				
6	A6	PEG10000	15	214,3	3	AS	0,2	33,3	4	NaOAc pH4.75	0,1	50	5	AmI	0,2	100	20	397,6	102,38	10				
7	A7	PEG10000	15	214,3	3	AS	0,19	31,7	4	NaCitrat pH4	0,1	50	6	AmI	0,1	50	20	346	154,05	10				
8	A8	PEG10000	15	214,3	3	AS	0,19	31,7	4	NaCitrat pH4	0,1	50	6	AmI	0,15	75	20	371	129,05	10				
9	A9	PEG10000	15	214,3	3	AS	0,19	31,7	4	NaCitrat pH4	0,1	50	6	AmI	0,2	100	20	396	104,05	10				
10	A10	PEG10000	15	214,3	3	AS	0,19	31,7	4	NaOAc pH4.75	0,1	50	5	AmI	0,1	50	20	346	154,05	10				
11	A11	PEG10000	15	214,3	3	AS	0,19	31,7	4	NaOAc pH4.75	0,1	50	5	AmI	0,15	75	20	371	129,05	10				
12	A12	PEG10000	15	214,3	3	AS	0,19	31,7	4	NaOAc pH4.75	0,1	50	5	AmI	0,2	100	20	396	104,05	10				
13	B1	PEG10000	15	214,3	3	AS	0,18	30,0	4	NaCitrat pH4	0,1	50	6	AmI	0,1	50	20	344,3	155,71	10				
14	B2	PEG10000	15	214,3	3	AS	0,18	30,0	4	NaCitrat pH4	0,1	50	6	AmI	0,15	75	20	369,3	130,71	10				
15	B3	PEG10000	15	214,3	3	AS	0,18	30,0	4	NaCitrat pH4	0,1	50	6	AmI	0,2	100	20	394,3	105,71	10				
16	B4	PEG10000	15	214,3	3	AS	0,18	30,0	4	NaOAc pH4.75	0,1	50	5	AmI	0,1	50	20	344,3	155,71	10				
17	B5	PEG10000	15	214,3	3	AS	0,18	30,0	4	NaOAc pH4.75	0,1	50	5	AmI	0,15	75	20	369,3	130,71	10				
18	B6	PEG10000	15	214,3	3	AS	0,18	30,0	4	NaOAc pH4.75	0,1	50	5	AmI	0,2	100	20	394,3	105,71	10				
19	B7	PEG10000	15	214,3	3	AS	0,17	28,3	4	NaCitrat pH4	0,1	50	6	AmI	0,1	50	20	342,6	157,38	10				
20	B8	PEG10000	15	214,3	3	AS	0,17	28,3	4	NaCitrat pH4	0,1	50	6	AmI	0,15	75	20	367,6	132,38	10				
21	B9	PEG10000	15	214,3	3	AS	0,17	28,3	4	NaCitrat pH4	0,1	50	6	AmI	0,2	100	20	392,6	107,38	10				
22	B10	PEG10000	15	214,3	3	AS	0,17	28,3	4	NaOAc pH4.75	0,1	50	5	AmI	0,1	50	20	342,6	157,38	10				
23	B11	PEG10000	15	214,3	3	AS	0,17	28,3	4	NaOAc pH4.75	0,1	50	5	AmI	0,15	75	20	367,6	132,38	10				
24	B12	PEG10000	15	214,3	3	AS	0,17	28,3	4	NaOAc pH4.75	0,1	50	5	AmI	0,2	100	20	392,6	107,38	10				
25	C1	PEG10000	14	200	3	AS	0,2	33,3	4	NaCitrat pH4	0,1	50	6	AmI	0,1	50	20	333,3	166,67	10				
26	C2	PEG10000	14	200	3	AS	0,2	33,3	4	NaCitrat pH4	0,1	50	6	AmI	0,15	75	20	358,3	141,67	10				
27	C3	PEG10000	14	200	3	AS	0,2	33,3	4	NaCitrat pH4	0,1	50	6	AmI	0,2	100	20	383,3	116,67	10				
28	C4	PEG10000	14	200	3	AS	0,2	33,3	4	NaOAc pH4.75	0,1	50	5	AmI	0,1	50	20	333,3	166,67	10				
29	C5	PEG10000	14	200	3	AS	0,2	33,3	4	NaOAc pH4.75	0,1	50	5	AmI	0,15	75	20	358,3	141,67	10				
30	C6	PEG10000	14	200	3	AS	0,2	33,3	4	NaOAc pH4.75	0,1	50	5	AmI	0,2	100	20	383,3	116,67	10				
31	C7	PEG10000	14	200	3	AS	0,19	31,7	4	NaCitrat pH4	0,1	50	6	AmI	0,1	50	20	331,7	168,33	10				
32	C8	PEG10000	14	200	3	AS	0,19	31,7	4	NaCitrat pH4	0,1	50	6	AmI	0,15	75	20	356,7	143,33	10				
33	C9	PEG10000	14	200	3	AS	0,19	31,7	4	NaCitrat pH4	0,1	50	6	AmI	0,2	100	20	381,7	118,33	10				
34	C10	PEG10000	14	200	3	AS	0,19	31,7	4	NaOAc pH4.75	0,1	50	5	AmI	0,1	50	20	331,7	168,33	10				
35	C11	PEG10000	14	200	3	AS	0,19	31,7	4	NaOAc pH4.75	0,1	50	5	AmI	0,15	75	20	356,7	143,33	10				
36	C12	PEG10000	14	200	3	AS	0,19	31,7	4	NaOAc pH4.75	0,1	50	5	AmI	0,2	100	20	381,7	118,33	10				
37	D1	PEG10000	14	200	3	AS	0,18	30,0	4	NaCitrat pH4	0,1	50	6	AmI	0,1	50	20	330	170	10				
38	D2	PEG10000	14	200	3	AS	0,18	30,0	4	NaCitrat pH4	0,1	50	6	AmI	0,15	75	20	355	145	10				
39	D3	PEG10000	14	200	3	AS	0,18	30,0	4	NaCitrat pH4	0,1	50	6	AmI	0,2	100	20	380	120	10				
40	D4	PEG10000	14	200	3	AS	0,18	30,0	4	NaOAc pH4.75	0,1	50	5	AmI	0,1	50	20	330	170	10				
41	D5	PEG10000	14	200	3	AS	0,18	30,0	4	NaOAc pH4.75	0,1	50	5	AmI	0,15	75	20	355	145	10				
42	D6	PEG10000	14	200	3	AS	0,18	30,0	4	NaOAc pH4.75	0,1	50	5	AmI	0,2	100	20	380	120	10				
43	D7	PEG10000	14	200	3	AS	0,17	28,3	4	NaCitrat pH4	0,1	50	6	AmI	0,1	50	20	328,3	171,67	11				
44	D8	PEG10000	14	200	3	AS	0,17	28,3	4	NaCitrat pH4	0,1	50	6	AmI	0,15	75	20	353,3	146,67	11				
45	D9	PEG10000	14	200	3	AS	0,17	28,3	4	NaCitrat pH4	0,1	50	6	AmI	0,2	100	20	378,3	121,67	11				
46	D10	PEG10000	14	200	3	AS	0,17	28,3	4	NaOAc pH4.75	0,1	50	5	AmI	0,1	50	20	328,3	171,67	11				
47	D11	PEG10000	14	200	3	AS	0,17	28,3	4	NaOAc pH4.75	0,1	50	5	AmI	0,15	75	20	353,3	146,67	11				
48	D12	PEG10000	14	200	3	AS	0,17	28,3	4	NaOAc pH4.75	0,1	50	5	AmI	0,2	100	20	378,3	121,67	11				
49	E1	PEG10000	15	214,3	3	AS	0,2	33,3	4	NaCitrat pH4	0,1	50	6	AmNO3	0,1	10	13	307,6	192,38	11				

50	E2	PEG10000	15	214,3	3	AS	0,2	33,3	4	NaCitrat pH4	0,1	50	6	AmNO3	0,15	15	13	312,6	187,38	11
51	E3	PEG10000	15	214,3	3	AS	0,2	33,3	4	NaCitrat pH4	0,1	50	6	AmNO3	0,2	20	13	317,6	182,38	11
52	E4	PEG10000	15	214,3	3	AS	0,2	33,3	4	NaOAc pH4.75	0,1	50	5	AmNO3	0,1	10	13	307,6	192,38	11
53	E5	PEG10000	15	214,3	3	AS	0,2	33,3	4	NaOAc pH4.75	0,1	50	5	AmNO3	0,15	15	13	312,6	187,38	11
54	E6	PEG10000	15	214,3	3	AS	0,2	33,3	4	NaOAc pH4.75	0,1	50	5	AmNO3	0,2	20	13	317,6	182,38	11
55	E7	PEG10000	15	214,3	3	AS	0,19	31,7	4	NaCitrat pH4	0,1	50	6	AmNO3	0,1	10	13	306	194,05	11
56	E8	PEG10000	15	214,3	3	AS	0,19	31,7	4	NaCitrat pH4	0,1	50	6	AmNO3	0,15	15	13	311	189,05	11
57	E9	PEG10000	15	214,3	3	AS	0,19	31,7	4	NaCitrat pH4	0,1	50	6	AmNO3	0,2	20	13	316	184,05	11
58	E10	PEG10000	15	214,3	3	AS	0,19	31,7	4	NaOAc pH4.75	0,1	50	5	AmNO3	0,1	10	13	306	194,05	11
59	E11	PEG10000	15	214,3	3	AS	0,19	31,7	4	NaOAc pH4.75	0,1	50	5	AmNO3	0,15	15	13	311	189,05	11
60	E12	PEG10000	15	214,3	3	AS	0,19	31,7	4	NaOAc pH4.75	0,1	50	5	AmNO3	0,2	20	13	316	184,05	11
61	F1	PEG10000	15	214,3	3	AS	0,18	30,0	4	NaCitrat pH4	0,1	50	6	AmNO3	0,1	10	13	304,3	195,71	11
62	F2	PEG10000	15	214,3	3	AS	0,18	30,0	4	NaCitrat pH4	0,1	50	6	AmNO3	0,15	15	13	309,3	190,71	11
63	F3	PEG10000	15	214,3	3	AS	0,18	30,0	4	NaCitrat pH4	0,1	50	6	AmNO3	0,2	20	13	314,3	185,71	11
64	F4	PEG10000	15	214,3	3	AS	0,18	30,0	4	NaOAc pH4.75	0,1	50	5	AmNO3	0,1	10	13	304,3	195,71	11
65	F5	PEG10000	15	214,3	24	AS	0,18	30,0	4	NaOAc pH4.75	0,1	50	5	AmNO3	0,15	15	13	309,3	190,71	11
66	F6	PEG10000	15	214,3	24	AS	0,18	30,0	4	NaOAc pH4.75	0,1	50	5	AmNO3	0,2	20	13	314,3	185,71	11
67	F7	PEG10000	15	214,3	24	AS	0,17	28,3	4	NaCitrat pH4	0,1	50	6	AmNO3	0,1	10	13	302,6	197,38	11
68	F8	PEG10000	15	214,3	24	AS	0,17	28,3	4	NaCitrat pH4	0,1	50	6	AmNO3	0,15	15	13	307,6	192,38	11
69	F9	PEG10000	15	214,3	24	AS	0,17	28,3	4	NaCitrat pH4	0,1	50	6	AmNO3	0,2	20	13	312,6	187,38	11
70	F10	PEG10000	15	214,3	24	AS	0,17	28,3	4	NaOAc pH4.75	0,1	50	5	AmNO3	0,1	10	13	302,6	197,38	11
71	F11	PEG10000	15	214,3	24	AS	0,17	28,3	4	NaOAc pH4.75	0,1	50	5	AmNO3	0,15	15	13	307,6	192,38	11
72	F12	PEG10000	15	214,3	24	AS	0,17	28,3	4	NaOAc pH4.75	0,1	50	5	AmNO3	0,2	20	13	312,6	187,38	11
73	G1	PEG10000	14	200	24	AS	0,2	33,3	4	NaCitrat pH4	0,1	50	6	AmNO3	0,1	10	13	293,3	206,67	11
74	G2	PEG10000	14	200	24	AS	0,2	33,3	4	NaCitrat pH4	0,1	50	6	AmNO3	0,15	15	13	298,3	201,67	11
75	G3	PEG10000	14	200	24	AS	0,2	33,3	4	NaCitrat pH4	0,1	50	6	AmNO3	0,2	20	13	303,3	196,67	11
76	G4	PEG10000	14	200	24	AS	0,2	33,3	4	NaOAc pH4.75	0,1	50	5	AmNO3	0,1	10	13	293,3	206,67	11
77	G5	PEG10000	14	200	24	AS	0,2	33,3	4	NaOAc pH4.75	0,1	50	5	AmNO3	0,15	15	13	298,3	201,67	11
78	G6	PEG10000	14	200	24	AS	0,2	33,3	4	NaOAc pH4.75	0,1	50	5	AmNO3	0,2	20	13	303,3	196,67	11
79	G7	PEG10000	14	200	24	AS	0,19	31,7	4	NaCitrat pH4	0,1	50	6	AmNO3	0,1	10	13	291,7	208,33	11
80	G8	PEG10000	14	200	24	AS	0,19	31,7	4	NaCitrat pH4	0,1	50	6	AmNO3	0,15	15	13	296,7	203,33	11
81	G9	PEG10000	14	200	24	AS	0,19	31,7	4	NaCitrat pH4	0,1	50	6	AmNO3	0,2	20	13	301,7	198,33	11
82	G10	PEG10000	14	200	24	AS	0,19	31,7	4	NaOAc pH4.75	0,1	50	5	AmNO3	0,1	10	13	291,7	208,33	11
83	G11	PEG10000	14	200	24	AS	0,19	31,7	4	NaOAc pH4.75	0,1	50	5	AmNO3	0,15	15	13	296,7	203,33	11
84	G12	PEG10000	14	200	24	AS	0,19	31,7	4	NaOAc pH4.75	0,1	50	5	AmNO3	0,2	20	13	301,7	198,33	11
85	H1	PEG10000	14	200	24	AS	0,18	30,0	4	NaCitrat pH4	0,1	50	6	AmNO3	0,1	10	13	290	210	11
86	H2	PEG10000	14	200	24	AS	0,18	30,0	4	NaCitrat pH4	0,1	50	6	AmNO3	0,15	15	13	295	205	11
87	H3	PEG10000	14	200	24	AS	0,18	30,0	4	NaCitrat pH4	0,1	50	6	AmNO3	0,2	20	13	300	200	11
88	H4	PEG10000	14	200	24	AS	0,18	30,0	4	NaOAc pH4.75	0,1	50	5	AmNO3	0,1	10	13	290	210	11
89	H5	PEG10000	14	200	24	AS	0,18	30,0	4	NaOAc pH4.75	0,1	50	5	AmNO3	0,15	15	13	295	205	11
90	H6	PEG10000	14	200	24	AS	0,18	30,0	4	NaOAc pH4.75	0,1	50	5	AmNO3	0,2	20	13	300	200	11
91	H7	PEG10000	14	200	24	AS	0,17	28,3	4	NaCitrat pH4	0,1	50	6	AmNO3	0,1	10	13	288,3	211,67	11
92	H8	PEG10000	14	200	24	AS	0,17	28,3	4	NaCitrat pH4	0,1	50	6	AmNO3	0,15	15	13	293,3	206,67	11
93	H9	PEG10000	14	200	24	AS	0,17	28,3	4	NaCitrat pH4	0,1	50	6	AmNO3	0,2	20	13	298,3	201,67	11
94	H10	PEG10000	14	200	24	AS	0,17	28,3	4	NaOAc pH4.75	0,1	50	5	AmNO3	0,1	10	13	288,3	211,67	11
95	H11	PEG10000	14	200	24	AS	0,17	28,3	4	NaOAc pH4.75	0,1	50	5	AmNO3	0,15	15	13	293,3	206,67	11
96	H12	PEG10000	14	200	24	AS	0,17	28,3	4	NaOAc pH4.75	0,1	50	5	AmNO3	0,2	20	13	298,3	201,67	11

Custom PEG Screen: **PPEG9**																									
Source		1	2	3, 24	4	5, 12	6	7	8	9	10	11	13	14	15	16	17	18	19	20	21	22	23	25,0	26	27
Stock	**8.2.F**	PEG3350	PEG8000	PEG10000	AS	NaOAc pH4.75	NaCitrat pH4	Anion-Mix1	Anion-Mix2	Anion-Mix3	Wasser	Wasser2	AmNO3	NaI	NaBr	AnioMix5	AnioMix6	AmCl	AmBr	AmI	AmAc	AmFor	AmTar	Glycerin	KI	KNO3
Cstock		50	35	35	3	1	1	100	100	100			5	1	1	100	100	1	1	1	1	2	1	44,0	2	2
Vges		500																								

Number (Destiny)	Well	Prec	Cprec	Vprec	Source	Salt	Csalt	Vsalt	Source	Buffer	Cbuffer	Vbuffer	Source	Additive	Cadditive	Vadditive		Cryo	Cadditive	Vadditive	Source	Vsum	Vwater	Source	
1	A1	PEG10000	15	214,3	3	AS	0,18	30	4	NaCitrat pH4	0,1	50	6	AmI	0,1	50	20	Glycerol	10	113,636	25	457,9	42,1	10	
2	A2	PEG10000	15	214,3	3	AS	0,18	30	4	NaCitrat pH4	0,1	50	6	AmI	0,1	50	20	Glycerol	10	113,636	25	457,9	42,1	10	
3	A3	PEG10000	15	214,3	3	AS	0,18	30	4	NaCitrat pH4	0,1	50	6	AmI	0,1	50	20	Glycerol	10	113,636	25	457,9	42,1	10	
4	A4	PEG10000	15	214,3	3	AS	0,18	30	4	NaCitrat pH4	0,1	50	6	AmI	0,1	50	20	Glycerol	10	113,636	25	457,9	42,1	10	
5	A5	PEG10000	15	214,3	3	AS	0,18	30	4	NaCitrat pH4	0,1	50	6	AmI	0,1	50	20	Glycerol	12	136,364	25	480,6	19,4	10	
6	A6	PEG10000	15	214,3	3	AS	0,18	30	4	NaCitrat pH4	0,1	50	6	AmI	0,1	50	20	Glycerol	12	136,364	25	480,6	19,4	10	
7	A7	PEG10000	15	214,3	3	AS	0,18	30	4	NaCitrat pH4	0,1	50	6	AmI	0,1	50	20	Glycerol	12	136,364	25	480,6	19,4	10	
8	A8	PEG10000	15	214,3	3	AS	0,18	30	4	NaCitrat pH4	0,1	50	6	AmI	0,1	50	20	Glycerol	12	136,364	25	480,6	19,4	10	
9	A9	PEG10000	15	214,3	3	AS	0,18	30	4	NaCitrat pH4	0,1	50	6	AmI	0,1	50	20	Glycerol	13,5	153,409	25	497,7	2,3	10	
10	A10	PEG10000	15	214,3	3	AS	0,18	30	4	NaCitrat pH4	0,1	50	6	AmI	0,1	50	20	Glycerol	13,5	153,409	25	497,7	2,3	10	
11	A11	PEG10000	15	214,3	3	AS	0,18	30	4	NaCitrat pH4	0,1	50	6	AmI	0,1	50	20	Glycerol	13,5	153,409	25	497,7	2,3	10	
12	A12	PEG10000	15	214,3	3	AS	0,18	30	4	NaCitrat pH4	0,1	50	6	AmI	0,1	50	20	Glycerol	13,5	153,409	25	497,7	2,3	10	
13	B1	PEG10000	15	214,3	3	AS	0,18	30	4	NaCitrat pH4	0,1	50	6	AmI	0,1	50	20					344,3	155,7	10	
14	B2	PEG10000	15	214,3	3	AS	0,18	30	4	NaCitrat pH4	0,1	50	6	AmI	0,1	50	20					344,3	155,7	10	
15	B3	PEG10000	15	214,3	3	AS	0,18	30	4	NaCitrat pH4	0,1	50	6	AmI	0,1	50	20					344,3	155,7	10	
16	B4	PEG10000	15	214,3	3	AS	0,18	30	4	NaCitrat pH4	0,1	50	6	AmI	0,1	50	20					344,3	155,7	10	
17	B5	PEG10000	15	214,3	3	AS	0,18	30	4	NaCitrat pH4	0,1	50	6	AmI	0,1	50	20					344,3	155,7	10	
18	B6	PEG10000	15	214,3	3	AS	0,18	30	4	NaCitrat pH4	0,1	50	6	AmI	0,1	50	20					344,3	155,7	10	
19	B7	PEG10000	15	214,3	3	AS	0,18	30	4	NaCitrat pH4	0,1	50	6	AmI	0,1	50	20					344,3	155,7	10	
20	B8	PEG10000	15	214,3	3	AS	0,18	30	4	NaCitrat pH4	0,1	50	6	AmI	0,1	50	20					344,3	155,7	10	
21	B9	PEG10000	15	214,3	3	AS	0,18	30	4	NaCitrat pH4	0,1	50	6	AmI	0,1	50	20					344,3	155,7	10	
22	B10	PEG10000	15	214,3	3	AS	0,18	30	4	NaCitrat pH4	0,1	50	6	AmI	0,1	50	20					344,3	155,7	10	
23	B11	PEG10000	15	214,3	3	AS	0,18	30	4	NaCitrat pH4	0,1	50	6	AmI	0,1	50	20					344,3	155,7	10	
24	B12	PEG10000	15	214,3	3	AS	0,18	30	4	NaCitrat pH4	0,1	50	6	AmI	0,1	50	20					344,3	155,7	10	
25	C1	PEG10000	15	214,3	3	AS	0,18	30	4	NaCitrat pH4	0,1	50	6	KI	0,1	25	26	Glycerol	10	113,636	25	432,9	67,1	10	
26	C2	PEG10000	15	214,3	3	AS	0,18	30	4	NaCitrat pH4	0,1	50	6	KI	0,1	25	26	Glycerol	10	113,636	25	432,9	67,1	10	
27	C3	PEG10000	15	214,3	3	AS	0,18	30	4	NaCitrat pH4	0,1	50	6	KI	0,1	25	26	Glycerol	10	113,636	25	432,9	67,1	10	
28	C4	PEG10000	15	214,3	3	AS	0,18	30	4	NaCitrat pH4	0,1	50	6	KI	0,1	25	26	Glycerol	10	113,636	25	432,9	67,1	10	
29	C5	PEG10000	15	214,3	3	AS	0,18	30	4	NaCitrat pH4	0,1	50	6	KI	0,1	25	26	Glycerol	13	147,727	25	467	33,0	10	
30	C6	PEG10000	15	214,3	3	AS	0,18	30	4	NaCitrat pH4	0,1	50	6	KI	0,1	25	26	Glycerol	13	147,727	25	467	33,0	10	
31	C7	PEG10000	15	214,3	3	AS	0,18	30	4	NaCitrat pH4	0,1	50	6	KI	0,1	25	26	Glycerol	13	147,727	25	467	33,0	10	
32	C8	PEG10000	15	214,3	3	AS	0,18	30	4	NaCitrat pH4	0,1	50	6	KI	0,1	25	26	Glycerol	13	147,727	25	467	33,0	10	
33	C9	PEG10000	15	214,3	3	AS	0,18	30	4	NaCitrat pH4	0,1	50	6	KI	0,1	25	26	Glycerol	15	170,455	25	489,7	10,3	10	
34	C10	PEG10000	15	214,3	3	AS	0,18	30	4	NaCitrat pH4	0,1	50	6	KI	0,1	25	26	Glycerol	15	170,455	25	489,7	10,3	10	
35	C11	PEG10000	15	214,3	3	AS	0,18	30	4	NaCitrat pH4	0,1	50	6	KI	0,1	25	26	Glycerol	15	170,455	25	489,7	10,3	10	
36	C12	PEG10000	15	214,3	3	AS	0,18	30	4	NaCitrat pH4	0,1	50	6	KI	0,1	25	26	Glycerol	15	170,455	25	489,7	10,3	10	
37	D1	PEG10000	15	214,3	3	AS	0,18	30	4	NaCitrat pH4	0,1	50	6	KI	0,1	25	26					319,3	180,7	10	
38	D2	PEG10000	15	214,3	3	AS	0,18	30	4	NaCitrat pH4	0,1	50	6	KI	0,1	25	26					319,3	180,7	10	
39	D3	PEG10000	15	214,3	3	AS	0,18	30	4	NaCitrat pH4	0,1	50	6	KI	0,1	25	26					319,3	180,7	10	
40	D4	PEG10000	15	214,3	3	AS	0,18	30	4	NaCitrat pH4	0,1	50	6	KI	0,1	25	26					319,3	180,7	10	
41	D5	PEG10000	15	214,3	3	AS	0,18	30	4	NaCitrat pH4	0,1	50	6	KI	0,1	25	26					319,3	180,7	10	
42	D6	PEG10000	15	214,3	3	AS	0,18	30	4	NaCitrat pH4	0,1	50	6	KI	0,1	25	26					319,3	180,7	10	
43	D7	PEG10000	15	214,3	3	AS	0,18	30	4	NaCitrat pH4	0,1	50	6	KI	0,1	25	26					319,3	180,7	11	
44	D8	PEG10000	15	214,3	3	AS	0,18	30	4	NaCitrat pH4	0,1	50	6	KI	0,1	25	26					319,3	180,7	11	
45	D9	PEG10000	15	214,3	3	AS	0,18	30	4	NaCitrat pH4	0,1	50	6	KI	0,1	25	26					319,3	180,7	11	
46	D10	PEG10000	15	214,3	3	AS	0,18	30	4	NaCitrat pH4	0,1	50	6	KI	0,1	25	26					319,3	180,7	11	
47	D11	PEG10000	15	214,3	3	AS	0,18	30	4	NaCitrat pH4	0,1	50	6	KI	0,1	25	26					319,3	180,7	11	
48	D12	PEG10000	15	214,3	3	AS	0,18	30	4	NaCitrat pH4	0,1	50	6	KI	0,1	25	26					319,3	180,7	11	

49	E1	PEG10000	15	214,3	3	AS	0,18	30	4	NaCitrat pH4	0,1	50	6	AmNO3	0,1	10	13	Glycerol	10	113,636	25	417,9	82,1	11
50	E2	PEG10000	15	214,3	3	AS	0,18	30	4	NaCitrat pH4	0,1	50	6	AmNO3	0,1	10	13	Glycerol	10	113,636	25	417,9	82,1	11
51	E3	PEG10000	15	214,3	3	AS	0,18	30	4	NaCitrat pH4	0,1	50	6	AmNO3	0,1	10	13	Glycerol	10	113,636	25	417,9	82,1	11
52	E4	PEG10000	15	214,3	3	AS	0,18	30	4	NaCitrat pH4	0,1	50	6	AmNO3	0,1	10	13	Glycerol	10	113,636	25	417,9	82,1	11
53	E5	PEG10000	15	214,3	3	AS	0,18	30	4	NaCitrat pH4	0,1	50	6	AmNO3	0,1	10	13	Glycerol	13	147,727	25	452	48,0	11
54	E6	PEG10000	15	214,3	3	AS	0,18	30	4	NaCitrat pH4	0,1	50	6	AmNO3	0,1	10	13	Glycerol	13	147,727	25	452	48,0	11
55	E7	PEG10000	15	214,3	3	AS	0,18	30	4	NaCitrat pH4	0,1	50	6	AmNO3	0,1	10	13	Glycerol	13	147,727	25	452	48,0	11
56	E8	PEG10000	15	214,3	3	AS	0,18	30	4	NaCitrat pH4	0,1	50	6	AmNO3	0,1	10	13	Glycerol	13	147,727	25	452	48,0	11
57	E9	PEG10000	15	214,3	3	AS	0,18	30	4	NaCitrat pH4	0,1	50	6	AmNO3	0,1	10	13	Glycerol	15	170,455	25	474,7	25,3	11
58	E10	PEG10000	15	214,3	3	AS	0,18	30	4	NaCitrat pH4	0,1	50	6	AmNO3	0,1	10	13	Glycerol	15	170,455	25	474,7	25,3	11
59	E11	PEG10000	15	214,3	3	AS	0,18	30	4	NaCitrat pH4	0,1	50	6	AmNO3	0,1	10	13	Glycerol	15	170,455	25	474,7	25,3	11
60	E12	PEG10000	15	214,3	3	AS	0,18	30	4	NaCitrat pH4	0,1	50	6	AmNO3	0,1	10	13	Glycerol	15	170,455	25	474,7	25,3	11
61	F1	PEG10000	15	214,3	3	AS	0,18	30	4	NaCitrat pH4	0,1	50	6	AmNO3	0,1	10	13					304,3	195,7	11
62	F2	PEG10000	15	214,3	3	AS	0,18	30	4	NaCitrat pH4	0,1	50	6	AmNO3	0,1	10	13					304,3	195,7	11
63	F3	PEG10000	15	214,3	3	AS	0,18	30	4	NaCitrat pH4	0,1	50	6	AmNO3	0,1	10	13					304,3	195,7	11
64	F4	PEG10000	15	214,3	3	AS	0,18	30	4	NaCitrat pH4	0,1	50	6	AmNO3	0,1	10	13					304,3	195,7	11
65	F5	PEG10000	15	214,3	24	AS	0,18	30	4	NaCitrat pH4	0,1	50	6	AmNO3	0,1	10	13					304,3	195,7	11
66	F6	PEG10000	15	214,3	24	AS	0,18	30	4	NaCitrat pH4	0,1	50	6	AmNO3	0,1	10	13					304,3	195,7	11
67	F7	PEG10000	15	214,3	24	AS	0,18	30	4	NaCitrat pH4	0,1	50	6	AmNO3	0,1	10	13					304,3	195,7	11
68	F8	PEG10000	15	214,3	24	AS	0,18	30	4	NaCitrat pH4	0,1	50	6	AmNO3	0,1	10	13					304,3	195,7	11
69	F9	PEG10000	15	214,3	24	AS	0,18	30	4	NaCitrat pH4	0,1	50	6	AmNO3	0,1	10	13					304,3	195,7	11
70	F10	PEG10000	15	214,3	24	AS	0,18	30	4	NaCitrat pH4	0,1	50	6	AmNO3	0,1	10	13					304,3	195,7	11
71	F11	PEG10000	15	214,3	24	AS	0,18	30	4	NaCitrat pH4	0,1	50	6	AmNO3	0,1	10	13					304,3	195,7	11
72	F12	PEG10000	15	214,3	24	AS	0,18	30	4	NaCitrat pH4	0,1	50	6	AmNO3	0,1	10	13					304,3	195,7	11
73	G1	PEG10000	15	214,3	24	AS	0,18	30	4	NaCitrat pH4	0,1	50	6	KNO3	0,1	25	27	Glycerol	10	113,636	25	432,9	67,1	11
74	G2	PEG10000	15	214,3	24	AS	0,18	30	4	NaCitrat pH4	0,1	50	6	KNO3	0,1	25	27	Glycerol	10	113,636	25	432,9	67,1	11
75	G3	PEG10000	15	214,3	24	AS	0,18	30	4	NaCitrat pH4	0,1	50	6	KNO3	0,1	25	27	Glycerol	10	113,636	25	432,9	67,1	11
76	G4	PEG10000	15	214,3	24	AS	0,18	30	4	NaCitrat pH4	0,1	50	6	KNO3	0,1	25	27	Glycerol	10	113,636	25	432,9	67,1	11
77	G5	PEG10000	15	214,3	24	AS	0,18	30	4	NaCitrat pH4	0,1	50	6	KNO3	0,1	25	27	Glycerol	13	147,727	25	467	33,0	11
78	G6	PEG10000	15	214,3	24	AS	0,18	30	4	NaCitrat pH4	0,1	50	6	KNO3	0,1	25	27	Glycerol	13	147,727	25	467	33,0	11
79	G7	PEG10000	15	214,3	24	AS	0,18	30	4	NaCitrat pH4	0,1	50	6	KNO3	0,1	25	27	Glycerol	13	147,727	25	467	33,0	11
80	G8	PEG10000	15	214,3	24	AS	0,18	30	4	NaCitrat pH4	0,1	50	6	KNO3	0,1	25	27	Glycerol	13	147,727	25	467	33,0	11
81	G9	PEG10000	15	214,3	24	AS	0,18	30	4	NaCitrat pH4	0,1	50	6	KNO3	0,1	25	27	Glycerol	15	170,455	25	489,7	10,3	11
82	G10	PEG10000	15	214,3	24	AS	0,18	30	4	NaCitrat pH4	0,1	50	6	KNO3	0,1	25	27	Glycerol	15	170,455	25	489,7	10,3	11
83	G11	PEG10000	15	214,3	24	AS	0,18	30	4	NaCitrat pH4	0,1	50	6	KNO3	0,1	25	27	Glycerol	15	170,455	25	489,7	10,3	11
84	G12	PEG10000	15	214,3	24	AS	0,18	30	4	NaCitrat pH4	0,1	50	6	KNO3	0,1	25	27	Glycerol	15	170,455	25	489,7	10,3	11
85	H1	PEG10000	15	214,3	24	AS	0,18	30	4	NaCitrat pH4	0,1	50	6	KNO3	0,1	25	27					319,3	180,7	11
86	H2	PEG10000	15	214,3	24	AS	0,18	30	4	NaCitrat pH4	0,1	50	6	KNO3	0,1	25	27					319,3	180,7	11
87	H3	PEG10000	15	214,3	24	AS	0,18	30	4	NaCitrat pH4	0,1	50	6	KNO3	0,1	25	27					319,3	180,7	11
88	H4	PEG10000	15	214,3	24	AS	0,18	30	4	NaCitrat pH4	0,1	50	6	KNO3	0,1	25	27					319,3	180,7	11
89	H5	PEG10000	15	214,3	24	AS	0,18	30	4	NaCitrat pH4	0,1	50	6	KNO3	0,1	25	27					319,3	180,7	11
90	H6	PEG10000	15	214,3	24	AS	0,18	30	4	NaCitrat pH4	0,1	50	6	KNO3	0,1	25	27					319,3	180,7	11
91	H7	PEG10000	15	214,3	24	AS	0,18	30	4	NaCitrat pH4	0,1	50	6	KNO3	0,1	25	27					319,3	180,7	11
92	H8	PEG10000	15	214,3	24	AS	0,18	30	4	NaCitrat pH4	0,1	50	6	KNO3	0,1	25	27					319,3	180,7	11
93	H9	PEG10000	15	214,3	24	AS	0,18	30	4	NaCitrat pH4	0,1	50	6	KNO3	0,1	25	27					319,3	180,7	11
94	H10	PEG10000	15	214,3	24	AS	0,18	30	4	NaCitrat pH4	0,1	50	6	KNO3	0,1	25	27					319,3	180,7	11
95	H11	PEG10000	15	214,3	24	AS	0,18	30	4	NaCitrat pH4	0,1	50	6	KNO3	0,1	25	27					319,3	180,7	11
96	H12	PEG10000	15	214,3	24	AS	0,18	30	4	NaCitrat pH4	0,1	50	6	KNO3	0,1	25	27					319,3	180,7	11

DO_2010_006	CD81/82	Lipids	20°C				
19.02.2010		FOS14 || 0.5 mM in every Reservoir (50 µL)			FOS18 || 0.5 mM in every Reservoir (50 µL)		
8.2.G	**Reservoir: 1 mL**	**1**	**2**	**3**	**4**	**5**	**6**
CD82 // fil-frozen	**A**	1,6-Hexandiole 3.6M 10mM CaCl2	1,6-Hexandiole 3.8M 10mM CaCl2	1,6-Hexandiole 4M 10mM CaCl2	1,6-Hexandiole 3.6M 10mM CaCl2	1,6-Hexandiole 3.8M 10mM CaCl2	1,6-Hexandiole 4M 10mM CaCl2
	B	38 % PEG 400 10 mM CaCl2 4% MPD	40 % PEG 400 10 mM CaCl2 4% MPD	42 % PEG 400 10 mM CaCl2 4% MPD	38 % PEG 400 10 mM CaCl2 4% MPD	40 % PEG 400 10 mM CaCl2 4% MPD	42 % PEG 400 10 mM CaCl2 4% MPD
CD81 // frozen-fil	**C**	1,6-Hexandiole 3.6M 10mM CaCl2	1,6-Hexandiole 3.8M 10mM CaCl2	1,6-Hexandiole 4M 10mM CaCl2	1,6-Hexandiole 3.6M 10mM CaCl2	1,6-Hexandiole 3.8M 10mM CaCl2	1,6-Hexandiole 4M 10mM CaCl2
	D	38 % PEG 400 10 mM CaCl2 4% MPD	40 % PEG 400 10 mM CaCl2 4% MPD	42 % PEG 400 10 mM CaCl2 4% MPD	38 % PEG 400 10 mM CaCl2 4% MPD	40 % PEG 400 10 mM CaCl2 4% MPD	42 % PEG 400 10 mM CaCl2 4% MPD
Stock:	**Hexandiole 5.6 M**	**200 mM CaCl2**	**100% PEG 400**	**40 % MPD**	**10 mM FOS**		
		1,6-Hexandioel 3.6M 10mM CaCl2	1,6-Hexandiole 3.8M 10mM CaCl2	1,6-Hexandiole 4M 10mM CaCl2	38 % PEG 400 10 mM CaCl2 4% MPD	40 % PEG 400 10 mM CaCl2 4% MPD	42 % PEG 400 10 mM CaCl2 4% MPD
FOS 14	**Res-solution (3x):**	1.928 mL 7M Hexandiol 150 µL CaCl2 150 µL FOS14 772 µL Water	2.036 mL 7M Hexandiol 150 µL CaCl2 150 µL FOS14 664µL Water	2.14 mL 7M Hexandiol 150 µL CaCl2 150 µL FOS14 560 µL Water	1,14 mL PEG 400 150 µL CaCl2 150µL FOS14 300 µL MPD 1,260 mL Water	1.2 mL PEG 400 150 µL CaCl2 150µL FOS14 300 µL MPD 1.2 mL Water	1.26 mL PEG 400 150 µL CaCl2 150µL FOS14 300 µL MPD 1,160 mL Water
FOS 18	**Res-solution (3x):**	1.928 mL 7M Hexandiol 150 µL CaCl2 150 µL FOS18 772 µL Water	2.036 mL 7M Hexandiol 150 µL CaCl2 150 µL FOS18 664µL Water	2.14 mL 7M Hexandiol 150 µL CaCl2 150 µL FOS18 560 µL Water	1,14 mL PEG 400 150 µL CaCl2 150µL FOS18 300 µL MPD 1,260 mL Water	1.2 mL PEG 400 150 µL CaCl2 150µL FOS18 300 µL MPD 1.2 mL Water	1.26 mL PEG 400 150 µL CaCl2 150µL FOS18 300 µL MPD 1,160 mL Water

10. Instrumentation and Chemicals

10.1. Instrumentation

Beamlines	a) **X12**, EMBL, HASYLAB, DESY, Hamburg • Synchrotron source Bending magnet • Wavelength 0.7 – 2.1 Å • Focal spot 2 mm x 0.4 mm (varies with energy) Detector MARMosaic, 225 mm b) **X13**, consortiums beamline, HASYLAB, DESY, Hamburg: • Synchrotron source Bending magnet • Wavelength 0.81 Å • Focal spot 2 mm x 0.4 mm • Detector MARCCD 165 mm c) **X33**, SAXS beamline, EMBL, HASYLAB, DESY, Hamburg • Synchrotron source DORIS bending magnet Wavelength 1.5 A • Focal spot 2 mm x 0.6 mm • Large automated sample changer • Detectors Photon counting Pilatus 1M-W pixel detector; Photon counting Pilatus 300K-W pixel detector; Mar345 image plate (345 mm^2)
Centrifuges	a) Centrifuge 5804R (Eppendorf, Germany) b) Centrifuge 5415R (Eppendorf, Germany) c) Centrikon T-1065 (Kontron, Germany)

Crystallization robots	a) Honeybee 961 (Genomic Solutions, USA) b) IMPAX (Douglas Instruments, UK)
DLS instrumentation	a) *Spectro*SIZE 300 (Nabitec, Germany) b) *Spectro*LIGHT 500 (Nabitec, Germany)
Imaging	a) CrystalScore (Diversified Scientific, USA) b) Microscope SZX12 with camera DP10 (both Olympus, Japan)
Incubator	Crystallization experiments at 4°C and 20°C were stored in RUMED 3001 (Rubarth, Germany) incubators
Microbalance	Sartorius CP224S-OCE (Sartorius, Germany)
pH Meter	Five Easy FE20 (Mettler-Toledo, Switzerland
Photospectrometry / Absorption Spectroscopy	Nanodrop 2000c (ThermoScientific, Peqlab, Germany)
Pipetting robots	Lissy (Zinsser, Germany)
SDS-PAGE	Consort EV265
UV-light source	*Crystal*LIGHT 100 (Nabitec, Germany)

10.2. Chemicals and Formulations

10.2.1. Chemicals Used *(Including GHS Classification and Hazard and Precautionary Statements)*

Compound	CAS-No.	Supplier	GHS hazard	Hazard Statements	Precautionary Statements
$(NH_4)_2SO_4$	7283-20-2	Carl Roth	-	-	-
1,3-Propanediol	504-63-2	Merck	-	-	-
1,6-Hexanediol	629-11-8	Merck	-	-	-
1-Propanol	71-23-8	Carl Roth	**GHS02 GHS05 GHS07**	H225, H318, H336	P210, P233, P305+351+338
Acetic acid	64-19-7	Chem-solute	**GHS02 GHS05**	H226, H314	P280, P305+351+338, P310
Acrylamide 30%	79-06-1	Carl Roth	**GHS06 GHS08**	H301, H312, H316, H317, H319, H332, H340, H350, H361f, H372	P201, P280, P301+310, P305+351+338, P308+313
APS	7727-54-0	Carl Roth	**GHS03 GHS07 GHS08**	H272, H302, H315, H317, H319, H334; H335	P280, P305+351+338, P302+352, P304+341, P342+311
Arginine	74-79-3	Fluka	**-**	-	-
$BaCl_2$	10361-37-2	Merck	**GHS06**	H301, H332	P301+310
Bromphenol blue	115-39-9	Applichem	**-**	-	-
$CaCl_2$	10043-52-4	Merck	**GHS07**	H319	P305+351+338
CaOAc	5743-26-0	Merck	**GHS07**	H315, H319, H335	P261, P305+351+338
$CdCl_2$	10108-64-2	Sigma	**GHS06 GHS08 GHS09**	H350, H340, H360FD, H330, H301, H372, H410	P201, P260, P273, P284, P301+310, P310
CHEMS	102601-49-0	Anatrace	**-**	-	-
Citric acid	77-92-9	Sigma	**GHS05**	H318	P305+351+338, P311
$CuSO_4$	7758-98-7	Merck	**GHS07 GHS09**	H302, H315, H319, H410	P273, P305+351+338, P302+352
D-mannose	3458-28-4	Carl Roth	**-**	-	-
DTT	3483-12-3	Applichem	**GHS07**	H302, H315, H319, H335	P302+352, P305+351+338
EDTA	60-00-4	Sigma	**GHS07**	H319	P305+351+338
Ethanol	64-17-5	Carl Roth	**GHS02**	H225	P210
Ethylene glycol	107-21-1	Merck	**GHS07**	H302	-

Compound	CAS-No.	Supplier	GHS hazard	Hazard Statements	Precautionary Statements
FOS14	77733-28-9	Anatrace	**GHS07**	H302+312+322	P260, P280, P305
FOS18	65956-63-0	Anatrace	**GHS07**	H302+312+322	P260, P280, P305
Galactose	59-23-4	Sigma	**-**	-	-
Glutathione	70-18-8	Carl Roth	**-**	-	-
Glycerol	56-81-5	Sigma	**-**	-	-
Glycine	56-40-6	Applichem	**-**	-	-
Hepes	7365-45-9	Sigma Aldrich	**-**	-	-
Histidine	71-00-1	Sigma	**-**	-	-
Hydrochloric acid >25 %	7647-01-0	Merck	**GHS05 GHS07**	H314, H335	P261, P280, P310, P305+351+338
Isopropanol	67-63-0	Carl Roth	**GHS02 GHS07**	H225, H319, H336	P210, P233, P305+351+338
KCl	7447-40-7	Carl Roth	**-**	-	-
Li_2SO_4	10102-25-7	Merck	**GHS07**	H302	-
LiCl	7447-41-8	Merck	**GHS07**	H302; H315, H319, H335	P302+352, P305+351+338
$Mg(HCOO)_2$	6150-82-9	Fluka	**-**	-	-
$MgCl_2$	7786-30-3	Carl Roth	**-**	-	-
MgOAc	16674-78-5	Merck	**-**	-	-
$MgSO_4$	7487-88-9	Merck	**-**	-	-
MO	111-03-5	Sigma	**-**	-	-
Mops	1132-61-2	Serva	**GHS07**	H315, H319, H335	P261, P305+351+338
MPD	107-41-5	Carl Roth	**GHS07**	H315, H319	-
NaBr	7647-15-6	Merck	**-**	-	-
NaCl	7647-14-5	Carl Roth	**-**	-	-
NaF	7681-49-4	Merck	**GHS06**	EUH032, H301, H315, H319	P264, P280, P301+310
NaI	7681-82-5	Applichem	**GHS07**	H315, H318	P264, P280, P302+P352, P305+351+338, P321, P332+P313, P362
$NaNO_3$	7631-99-4	Merck	**GHS03 GHS07**	H302, H315, H319, H335	P220, P261, P305+351+338
NaOAc	127-09-3	Applichem	**-**	-	-
NaOH	1310-73-2	Merck	**GHS05**	H314	P280, P310, P305+351+338
NH_4Br	12124-97-9	Applichem	**-**	-	-
NH_4I	12027-06-4	Sigma	**GHS07**	H315, H319, H335	P261, P305+351+338
NH_4NO_3	6484-52-2	Applichem	**GHS03 GHS07**	H315, H319, H335	P220, P261, P305+351+338
NH_4OAc	631-61-8	Applichem	**-**	-	-
Paraffin	8002-74-2	Applichem	**-**	-	-
PEG 10000	25322-68-3	Merck	**-**	-	-

Compound	CAS-No.	Supplier	GHS hazard	Hazard Statements	Precautionary Statements
PEG 1500	25322-68-3	Fluka	**-**	-	-
PEG 2000 MME	25322-68-3	Fluka	**-**	-	-
PEG 300	25322-68-3	Applichem	**-**	-	-
PEG 3350	25322-68-3	Sigma	**-**	-	-
PEG 400	25322-68-3	Sigma	**-**	-	-
PEG 4000	25322-68-3	Merck	**-**	-	-
PEG 8000	25322-68-3	Sigma	**-**	-	-
Proline	147-85-3	Sigma	**-**	-	-
SDS	151-21-3	Sigma	**GHS02 GHS06**	H228, H302, H311, H315, H319, H335	P210, P261, P280, P312, P305+351+338
Sodium citrate	6132-05-4	Sigma	**-**	-	-
Sodium malonate	141-95-7	Sigma	**-**	-	-
Sodium tartrate	868-18-8	Applichem	**-**	-	-
$SrCl_2$	10476-85-4	Merck	**GHS05 GHS07**	H315, H318, H335	P261, P280, P305+351+338
TEMED	110-18-9	Merck	**GHS02 GHS05 GHS07**	H225, H302, H314, H332	P261, P280, P305+351+338
tert-Butanol	75-65-0	AppliChem	**GHS02 GHS07**	H225, H319, H332, H335	P210, P305+351+338, P403+233
Tris	1185-53-1	Fluka	**GHS07**	H315, H319, H335	P261 P305+351+338
$ZnSO_4$	7446-20-0	Aldrich	**GHS05 GHS07 GHS09**	H302, H318, H410	P273, P280, P501 P305+351+338
β-OG	29836-26-8	Carl Roth	**-**	-	-

10.2.2. Formulations and Buffers

10.2.2.1. Commercial Protein Screens and Kits

Name	Supplier	Risk label	Risk phrases	Safety phrases
PCT	Hampton	-	-	-
pH Screen	Hampton	**Xn**	R38, R20/21/22	S26, S46, S24/25
Floppy Choppy	Jena Bio Science	**C, Xn, Xi**	R35, R41, R42, R36/37/38	S22, S26, S45, S24/25, S36/37/39:
Macrosol	Molecular Dimensions	**T, N**	R10, R45, R46, R60, R61, R25, R36/37/38, R48/20/22, R51/53	S20, S26, S45, S53, S61, S36/37/39
Morpheus	Molecular Dimensions	**T, N**	R10, R45, R46, R60, R61, R63, R23/25, R36/37/38, R48/20/22, R51/53	S20, S26, S45, S53, S61, S36/37/39
PACT premier	Molecular Dimensions	**T**	R23/25, R52/53	S20, S36, S45, S61

Name	Supplier	Risk label	Risk phrases	Safety phrases
PGA Screen	Molecular Dimensions	**Xn**	R20, R21, R22	S20, S26, S46, S24/25
Stura / Footprint*	Molecular Dimensions	**T, N**	R10, R45, R46, R60, R61, R25, R36/37/38, R48/20/22, R51/53	S20, S26, S45, S53, S61, S36/37/39
AmSO4 Suite	Qiagen	**T+, N**	R10, R25, R26, R45, R46, R60, R61, R48/23/25, R51/53	S45, S53, S61, S36/37.
Anions Suite	Qiagen	**Xn, O**	R8, R22, R36	S15, S16, S26, S36/37/39
Classic Suite	Qiagen	**T, N**	R10, R45, R46, R60, R61, R23/25, R36/37/38, R48/20/22, R51/53	S20, S26, S45, S53, S36/37/39. ,
ComPAS Suite	Qiagen	**T**	R10, R45, R23/24/25, R36/38, R39/23/24/25, R51/53	S13, S26, S45, S53, S61, S36/37/39.
Cryos Suite	Qiagen	**T, N**	R10, R45, R46, R60, R61, R23/25, R36/37/38, R48/20/22, R51/53	S20, S26, S45, S53, S61, S36/37/39.
JCSG+ Suite	Qiagen	**T, N**	R10, R21, R41, R45, R23/25, R37/38, R51/53	S13, S20, S26, S45, S53, S36/37/39
MbClass II Suite	Qiagen	**N**	R51/53	S61
MbClass Suite	Qiagen	**N, Xi**	R10, R36/38, R51/53	S26, S61
MPD Suite	Qiagen	**T, N**	R10, R22, R23, R43, R45, R46, R60, R61, R36/38, R48/20/22, R51/53	S26, S45, S53, S61, S36/37
pH Clear Suite	Qiagen	**Xi**	R10, R36	S26
pH Clear II suite	Qiagen	**Xi**	R36/38	S26

10.2.2.2. Buffers, Formulations and SDS-PAGE

If not stated differently buffer pH was adjusted by titration against 1 M NaOH or 1 M HCl solutions. For NaOAc/HOAc-buffer pH was adjusted by addition of acetic acid to avoid contamination with Cl^-. For 100 mL of 250 mM buffer 56.5 mL NaOAc solution (250 mM) was mixed with 10.9 mL acetic acid (1 M) and water was added to 100 mL.

Concentrations of solutions are always in relation to the final volume, e.g. for a 50 % (w/v) solution of PEG, 50 g of the respective PEG were dissolved in water and then water was added to a total volume of 100 mL.

Protein concentration was estimated before every experiment by analysis of the absorption at a wavelength of 280 nm applying a Nanodrop 2000c (Fisher Scientific, Peqlab, Germany)

A 7% SDS-PAGE was prepared by mixing (in that particular order) 5 mL water, 2.5 mL buffer (1.5 M Tris, pH 8.8), 100 µL SDS solution (10 % (w/v) in water), 2.31 mL acrylamide (30 % solution), 10 µL TEMED and 50 µL APS (15 % (w/v) solution in water). The stacking gel (4%) was prepared by mixing 6.1 mL water, 2.5 mL buffer (0.5 M Tris, pH 6.8), 100 µL SDS solution (10 % (w/v) in water), 1.3 mL acrylamide (30 % solution), 10 µL TEMED and 50 µL APS (15 % (w/v) solution in water). Protein bands were stained with Coomassie blue solution (250 mL isopropanol, 100 mL acetic acid, 1 g Coomassie blue, 1000 mL water) and destained in 16.7 % (v/v) acetic acid. For the estimation of molecular mass protein weight marker SM0431 (Fermentas, Germany) was used.

Unless stated else, water was deionized by a SG ion exchange (Omnilab, Germany) system prior to use.

10.2.3. GHS and Risk Symbols and Information about Hazard-, Risk-, Safety- and Precaution- Statements

Figure 84: GHS pictograms (source: http://www.unece.org/trans/danger/publi/ghs/pictograms.html).

GHS Hazard Statements	
EUH032	Contact with acids liberates very toxic gas
H 225	Highly flammable liquid and vapour
H 226	Flammable liquid and vapour
H 228	Flammable solid
H 272	May intensify fire; oxidizer
H 301	Toxic if swallowed
H 302	Harmful if swallowed
H 311	Toxic in contact with skin
H 312	Harmful in contact with skin
H 314	Causes severe skin burns and eye damage
H 315	Causes skin irritation
H 316	Causes mild skin irritation
H 317	May cause an allergic skin reaction

GHS Hazard Statements	
H 318	Causes serious eye damage
H 319	Causes serious eye irritation
H 330	Fatal if inhaled
H 332	Harmful if inhaled
H 334	May cause allergy or asthma symptoms or breathing difficulties if inhaled
H 335	May cause respiratory irritation
H 336	May cause drowsiness or dizziness
H 340	May cause genetic defects
H 350	May cause cancer
H 360	May damage fertility or the unborn child
H 361	Suspected of damaging fertility or the unborn child
H 372	Causes damage to organs through prolonged or repeated exposure
H 410	Very toxic to aquatic life with long lasting effects

GHS Precautionary Statements	
P201	Obtain special instructions before use
P210	Keep away from heat/sparks/open flames/hot surfaces – No smoking
P233	Keep container tightly closed
P260	Do not breathe dust/fume/gas/mist/vapors/spray
P261	Avoid breathing dust/fume/gas/mist/vapors/spray
P264	Wash … thoroughly after handling
P273	Avoid release to the environment
P280	Wear protective gloves/protective clothing/eye protection/face protection
P284	Wear respiratory protection
P310	Immediately call a POISON CENTER or doctor/physician
P311	Call a POISON CENTER or doctor/physician
P321	Specific treatment (see respective MSDS)
P362	Take off contaminated clothing and wash before reuse
P301+310	IF SWALLOWED: Immediately call a POISON CENTER or doctor/physician
P308+313	IF exposed or concerned: Get medical advice/attention
P403+233	Store in a well-ventilated place. Keep container tightly closed
P304+341	IF INHALED: If breathing is difficult, remove victim to fresh air and keep at rest in a position comfortable for breathing
P332+313	If skin irritation occurs: Get medical advice/attention
P342+311	Call a POISON CENTER or doctor/physician
P302+352	IF ON SKIN: Wash with soap and water
P305+351+338	IF IN EYES: Rinse cautiously with water for several minutes. Remove contact lenses if present and easy to do – continue rinsing

Figure 85: Hazard symbols for formulations and respective risk labels (Source: http://de.wikipedia.org/wiki/Gefahrensymbol).

Risk Statements	
R8	Contact with combustible material
R10	May cause fire
R20	Flammable
R21	Harmful by inhalation
R22	Harmful in contact with skin
R25	Harmful if swallowed
R35	Toxic if swallowed
R36	Causes severe burns
R38	Irritating to eyesIrritating to skin
R41	Risk of serious damage to eyes
R42	May cause sensitisation by inhalation
R43	May cause sensitisation by skin contact
R45	May cause cancer
R46	May cause heritable genetic damage
R60	May impair fertility
R61	May cause harm to the unborn child
R39/23/24/25	Toxic: danger of very serious irreversible effects through inhalation, in contact with skin and if swallowed
R36/37/38	Irritating to eyes, respiratory system and skin
R23/24/25	Toxic by inhalation, in contact with skin and if swallowed
R20/21/22	Harmful by inhalation, in contact with skin and if swallowed
R48/20/22	Harmful: danger of serious damage to health by prolonged exposure through inhalation and if swallowed
R23/25	Toxic by inhalation and if swallowed
R36/38	Irritating to eyes and skin
R51/53	Toxic to aquatic organisms, may cause long-term adverse effects in the aquatic environment
R37/38	Irritating to respiratory system and skin

Safetey Statements	
S13	Keep away from food, drink and animal foodstuffs
S15	Keep away from heat
S16	Keep away from sources of ignition - No smoking
S20	When using do not eat or drink. Do not breathe dust
S22	In case of contact with eyes, rinse immediately with plenty of water and

Safetey Statements	
	seek medical advice
S26	In case of accident or if you feel unwell seek medical advice immediately (show the label where possible).
S45	If swallowed, seek medical advice immediately and show this container or label
S46	Avoid exposure - obtain special instructions before use
S53	Avoid release to the environment
S61	Refer to special instructions/safety data sheet
S24/25	Avoid contact with skin and eyes
S36/37	Wear suitable protective clothing and gloves
S36/37/39	Wear suitable protective clothing, gloves and eye/face protection

11. Acknowledgements

Zunächst möchte ich mich bei Prof. Ch. Betzel für die Überlassung des spannenden Themas, die Möglichkeit diese Arbeit in seinem Arbeitskreis durchzuführen, die jederzeit exzellente Betreuung und die Anleitung zum selbständigen wissenschaftlichen Arbeiten herzlich bedanken. Prof. R. Bredehorst danke ich für die Übernahme des Zweitgutachtens dieser Arbeit.

Allen Menschen im Arbeitskreis gilt mein Dank für die tolle Atmosphäre, die Hilfsbereitschaft und die Unterstützung. Es war eine schöne Zeit mit euch. Ich werde die Kaffee- und Teerunden mit z.B. Dirk, Anne, Lars, Madeleine, Arne, Markus, Birgitta, Bara, Julia, Marko, Svetlana, Petra und Raphael vermissen. I especially enjoyed the internationality in our group, it certainly widened my mind and I am grateful to have had nice conversations with you all, discussing differences and things in common and to get to know in practice that it is the individual person that matters most and not “culture” or “ethnicity”. Thank you Afshan, Ahmed, Aisha, Amr, Arif, Hidayat, Liu, Mohammed, Monika (muito obrigado também para a possibilidade de falar portugues contigo), Nasser, Prince, Rana, Rodrigo, Rossana and Sadaf.

Für die Einführung in Theorie und Praxis von Lichtstreuexperimenten und die gemeinsame Zeit im „Erfinderbüro“ möchte ich Dr. Arne Meyer und Dr. Karsten Dierks besonders danken. Dr. Markus Perbandt hat mir geholfen zu lernen, wie Proteine zu kristallisieren sind, wie mit diesen Kristallen an der Beamline Diffraktionsbilder erzeugt werden können und wie anschließend Strukturen gelöst werden ohne an den Programmen zu verzweifeln. Vielen Dank dafür.

Julia Drebes und Raphael Eberle danke ich für die großartige Zusammenarbeit im Rahmen des China-Projektes. A project which would not have been possible without the help of Prof. Cang, Prof. Yin Da-Chuan and Dr. Hu-Ling Cao, thank you very much, 谢谢. Special thanks go to Dr. Yong Yu, who has become a great friend and whose help during research in Beijing was immeasurably valuable, 多谢 .

I would like to thank all members of the *OptiCryst* consortium for the great work together. It was wonderful to be part of this international collaboration. Special thanks to Dr. Roslyn Bill and Dr. Nicklas Bonander for the fine collaboration in the project regarding the membrane proteins CD81, CD82 and Claudin-1, to Dr. José A.

Gavira and Dr. Emilio M. Garcia, to Prof. R. Hilgenfeld and Robert Wrase and Dr. Sahir Khurschid and Prof. N. Chayen.

Dr. Johannes Raff und Ulrike Weinert danke ich für die Zusammenarbeit im Rahmen des Surface-Layer Projektes. For further collaborations I would like to thank Dr. K. Petratos and Dr. Prince Prabhu. Dr. Charly Förster danke ich für die sehr tolle Zusammenarbeit im Bereich der Strukturaufklärung von RNA/LNA.

Julia Drebes, Raphael Eberle und Madeleine Künz danke ich für das sorgfältige Korrekturlesen und die wertvollen Hinweise zu Form und Inhalt. Etwaige verbliebene Fehler habe ich zu verantworten.

Bei meinen Freundinnen und Freunden muss ich mich zunächst für die wenige Zeit entschuldigen, die ich in den vergangenen Jahren für euch hatte. Ich danke für die nötige Ablenkung von der Arbeit, schönes Zusammensein und schöne Zeiten.

Ohne die Unterstützung durch meine Eltern (und auch meine Schwestern) in den vergangenen fast 32 Jahren wäre diese Arbeit nicht möglich gewesen. Ich danke Euch dafür, dass ihr es mir ermöglicht und gefördert habt kritisch und kreativ zu denken.

Birte und Lasse habe ich diese Arbeit gewidmet: Es erfüllt mich mit unsagbarer Freude Lasse aufwachsen zu sehen. Birte war in den vergangenen fünfeinhalb Jahren immer für mich da, der Dank dafür ist mit Worten nicht auszudrücken. Ich freue mich auf das Leben mit euch.

12. Curriculum Vitae

entfällt aus datenschutzrechtlichen Gründen

entfällt aus datenschutzrechtlichen Gründen

Eidesstattliche Erklärung

Hiermit erkläre ich an Eides statt, diese Arbeit selbstständig und ohne fremde Hilfe verfasst, sowie keine anderen, als die von mir angegebenen Hilfsmittel verwendet zu haben.

Ferner versichere ich, dass ich noch keine Promotionsversuche an anderen Universitäten unternommen habe.

Hamburg, 01. März 2012

_____

(Dominik Oberthür)